Electronic and Magnetic Structure of Some Ferrites

A Thesis

Submitted for the award of Ph.D. degree

In Physics
(Faculty of Science)

To the

University of Kota

By

Kalpana Panwar

Under the Supervision of

Dr. N. L. Heda

(Assistant Professor of Physics)

DEPARTMENT OF PURE & APPLIED PHYSICS
UNIVERSITY OF KOTA
KOTA (RAJASTHAN)

MARCH 2020

Department of Pure & Applied Physics

University of Kota, Kota

M.B.S. Marg, Kabir Circle, Kota

Dr. N.L. Heda

E-mail: nlheda@uok.ac.in **Assistant Professor of Physics**

CERTIFICATE

I feel great pleasure in certifying that the thesis entitled **"Electronic and Magnetic Structure of Some Ferrites"** embodies a record of the results of investigations carried out by **Mrs. Kalpana Panwar** under my guidance. She has completed the following requirements as per Ph.D. regulations of the University.

(a) Course work as per the University rules.

(b) Residential requirements of the University.

(c) Submitted annual progress report.

(d) Presented her work in the departmental committee.

(e) Published/accepted minimum of one research paper in a referred research journal.

I recommend the submission of thesis.

Date: **(Dr. N.L. Heda)**

Assistant Professor of Physics

Department of Pure and Applied Physics

University of Kota, Kota

ANTI-PLAGIARISM CERTIFICATE

It is certified that Ph.D. thesis entitled, **"Electronic and Magnetic Structure of Some Ferrites"** by **Mrs. Kalpana Panwar** has been examined by us with the following anti-plagiarism tools. We undertake the follows:

a. Thesis has significant new work/knowledge as compared already published or are under consideration to be published elsewhere. No sentence, equation, diagram, table, paragraph or section has been copied verbatim from previous work unless it is placed under quotation mark and duly referenced.

b. The work presented is original and own work of the author (i.e. there is no plagiarism). No ideas, processes, results or words of the others have been presented as author's own work.

c. There is no fabrication of data or results which has been compiled and analyzed.

d. There is no falsification by manipulating research materials, equipment or processes, or changing or omitting data or results such that the research is not accurately represented in the research record.

e. The thesis has been checked using 'URKUND' Software and found within limits as per HEC plagiarism Policy and instructions issued from time to time.

(Mrs. Kalpana Panwar) **(Dr. N.L. Heda)**

(Name & Signature of Research Scholar) (Name & Signature and seal of Research Supervisor)

Place: Kota Place: Kota

Date: Date:

Abstract

Ferrites belong to a special class of magnetic materials consisting of metal oxides and ferric oxides as their main compositions. The nonmagnetic (Zn and Cd) and magnetic impurity (Ni, Cr and Fe) doped ferrimagnetic oxides, MFe_2O_4 (M = Fe, Ni, Cr, Zn, and Cd) are new engineered materials for advanced applications like microwave-integrated and magnetoelectric devices etc. The main interest in doped ferrite materials is due to their role in spin barriers used in conjunction with spin filters. Compton spectroscopy has been recognized as a well defined technique to calculate the electronic properties of the material. It has also been utilized to validate the *ab-initio* calculations with different exchange and correlation energies. In the present thesis, we report the systematic study of experimental and theoretical Compton profiles (CPs) of some ferrites namely Fe_3O_4, $NiFe_2O_4$, $ZnFe_2O_4$ and $CdFe_2O_4$. For the CP measurements of $TMFe_2O_4$ (TM = Fe, Ni, Zn and Cd), we have used First Indian 20 Ci ^{137}Cs Compton spectrometer while the theoretical CPs have been calculated using linear combination of atomic orbitals (LCAO) approximations. Further, the CP of Fe_3O_4 have also been measured using first ever shortest geometry and lowest intensity based 100 mCi ^{241}Am Compton spectrometer and compared the results with LCAO based CPs. In addition, we have also prepared bulk $Ni_{1-x}Cr_xFe_2O_4$ (x= 0.00, 0.02 and 0.05) using solid state reaction (SSR) method and $Ni_{1-x}Cr_xFe_2O_4$ (x= 0.02 and 0.05) thin films using pulsed laser deposition (PLD) method. The characterization of these samples have been done by X-ray diffraction (XRD), X-ray photoemission spectroscopy (XPS), Raman spectroscopy (RS), superconducting quantum interface device-vibration sample magnetometer (SQUID-VSM) and Fourier transform infrared (FTIR) spectroscopic measurements. Further, the LCAO schemes have been employed with pure density functional theory (DFT) and hybrid (HF+DFT) theory to compute majority- and minority-spin energy bands and density of states (DOS), Mulliken population (MP), band gap, magnetic moment and CP, etc. for Fe_3O_4, $NiFe_2O_4$, $ZnFe_2O_4$ and $CdFe_2O_4$.

In the **first chapter**, we have reported the basic aspects of the experimental techniques employed in the present thesis work, namely XRD, XPS, RS and Compton scattering (CS). A detailed review of the earlier studies on relevant ferrites during last two decades has also been incorporated in the chapter.

We have divided **second chapter** into two parts. In the first part, we have presented the details of SSR and PLD techniques along with the important experimental features of XRD, XPS, RS, SQUID-VSM and FTIR measurements. We have also presented salient features of 20 Ci ^{137}Cs and 100 mCi ^{241}Am Compton spectrometer along with the data correction process to extract the true CP. In the second part, we have incorporated theoretical aspects of LCAO approximations and DFT computations within local density approximation (LDA), generalized gradient approximation (GGA), second order GGA (SOGGA) and also the hybrid schemes (B3LYP, B3PW, PBE0, PBESOL0, WC1LYP and B1WC).

The **third chapter** describes the study of structural, electronic and magnetic properties of PLD thin films of $Ni_{1-x}Cr_xFe_2O_4$ (x = 0.02 and 0.05) on Si (111) and Si (100) substrates. Here, the films show single phase, polycrystalline structure with a better crystalline quality on Si (111) substrate than to Si (100) substrate. The reported XPS studies show the mixed spinel structure and suggests that Ni and Fe ions exist in 2+ and 3+ states, respectively. The deviation from the inverse spinel leads to modified magnetic properties. It is also seen that saturation magnetization drastically drops compared to the expected saturation value for inverse spinel structure. Strain in the films and lattice distortion produced by the Cr doping also appear to influence the magnetic properties [The third chapter is based on our published research paper entitled "The effect of Cr substitution on the structural, electronic and magnetic properties of pulsed laser deposited $NiFe_2O_4$ thin films", **J. Mag. Mag. Mat. 421 (2017) 25–30**]

In the **fourth chapter**, the LCAO calculations have been employed to compute MP, energy bands, partial and total DOS and CPs of $TMFe_2O4$ (TM = Zn and Cd). The LCAO calculations have been performed within pure and hybrid DFT calculations and DFT calculations have been performed within LDA and GGA along with hybrid approximations (B3LYP and PBE0). The validation of hybrid

functionals have accomplished using CP measurements (661.65 keV γ-rays from ^{137}Cs source) for both the ferrites. Chi-square test indicates an overall better agreement of experimental CP data with LCAO-B3LYP scheme based momentum densities leading to usefulness of hybrid functionals in predicting electronic and magnetic response of such ferrites. Whereas, LCAO-B3LYP based majority- and minority-spin energy bands and DOS for $ZnFe_2O_4$ and $CdFe_2O_4$ predict semiconducting nature in both the ferrites. In addition, MP data and equal-valence-electron-density scaled EMDs indicate more covalent character of $ZnFe_2O_4$ than that of $CdFe_2O_4$. A reasonable agreement of magnetic moments of both the ferrites with available data unambiguously promotes the use of Gaussian-type orbitals in LCAO scheme in exploring magnetic properties of such ferrites [The fourth chapter is based on our published research paper entitled "Performance of hybrid functional in linear combination of atomic orbitals scheme in predicting electronic response in spinel ferrites $ZnFe_2O_4$ and $CdFe_2O_4$", **J. Mater. Sci. 55 (2020) 3912–3925**].

In the **fifth chapter**, we have presented structural and magnetic response of $Ni_{1-x}Cr_xFe_2O_4$ (x = 0.00 and 0.05) using XRD, RS, FTIR spectroscopy and SQUID magnetometer. The single phase of both the compositions is confirmed using Rietveld refinement method and the absence of any impurity is further cinched using structural sensitive techniques, namely FTIR and RS. Further, we have reported magnetic moment, MP, partial and total DOS and CPs for $NiFe_2O_4$ using LCAO scheme with and without hybrid functional. The theoretical CPs have also been validated using isotropic CP measurement with 662 keV photons for $NiFe_2O_4$. Among the considered exchange-correlation potentials within LCAO, the B3LYP scheme based momentum densities show better agreement with the experimental CP. The majority- and minority-spin DOS have confirmed the insulating nature of $NiFe_2O_4$. Peculiarities of presently deduced MP data and magnetic moments are also discussed [The fifth chapter is based on our research paper entitled "Structural, magnetic and electronic properties of nickel ferrites: Experiment and LCAO calculations, **Communicated to J. Alloys Compounds (2020) Revised**].

The **sixth chapter** is also divided into two parts. The part-I is devoted to the CP measurements of Fe_3O_4 using 100 mCi ^{241}Am Compton spectrometer at a resolution of 0.55 a.u. (fwhm). The experimental CP has been analyzed using LCAO-DFT with LDA and GGA approximations. It is observed that the DFT-GGA scheme gives the better agreement than to DFT-LDA. In addition, we have also reported the MP and DOS using the DFT-GGA scheme. MP data shows the charge transfer from Fe to O atoms whiles DOS have predicted the half metallic character of Fe_3O_4. Whereas the part-II deals with the CP measurements of Fe_3O_4 at higher resolution (0.34 a.u., fwhm) using 20 Ci ^{137}Cs Compton spectrometer to validate the hybrid potentials derived using B3LYP. It is found that B3LYP scheme gives a better agreement with experimental data than the DFT-GGA scheme. Also, spin dependent DOS using LCAO-B3LYP scheme have also confirmed the half metallic character of Fe_3O_4, while the large value of MP data (4.72 e^-) predicts the dominancy of ionic nature in the studied compound [The part-I of chapter 6 is based on our published research paper entitled "Electronic properties of Fe_3O_4: LCAO calculations and Compton spectroscopy" **AIP Conf. Proc. (USA) 1942 (2018) 090032-1–090032-4]**.

In the **seventh chapter**, we have reported the summary of work done and suggestions for future possibilities. Among the future possibilities, the high resolution directional CP measurements may further be attempted to compare the present theoretical anisotropies in the momentum densities of Fe_3O_4, $NiFe_2O_4$, $ZnFe_2O_4$ and $CdFe_2O_4$. Also, the high resolution magnetic Compton profile measurements of these ferrites using synchrotron radiations may be helpful to deduce site-specific magnetic moments to further validation of our LCAO calculations in reproducing the origin of magnetic response of such ferrites. The energy bands, DOS, CPs and magnetic moment using full-potential linearized augmented plane wave (FP-LAPW) and spin-polarized-relativistic Korringa-Kohn-Rostoker (SPR-KKR) is also suggested as a part of future scope.

Besides above chapters, we have also included one **Appendix** which reports CP measurements for $Ni_{1-x}Cr_xFe_2O_4$ (x = 0.2 and 0.5) and $NiCr_xFe_{2-x}O_4$ (x = 0.2 and 0.5) using 20 Ci ^{137}Cs Compton spectrometer and their comparison with free atom CP. Negligible difference in experimental and free atom profile in the momentum

range $p_z \geq 3.0$ a.u. for all the reported compositions show an accuracy of the measurements and the data reduction.

CANDIDATE'S DECLARATION

I, hereby, certify that the work, which is being presented in the thesis, entitled, **"Electronic and Magnetic Structure of Some Ferrites"** in partial fulfilment of the requirement for the award of the Degree of Doctor of Philosophy, carried under the supervision of **Dr. N.L. Heda**, Assistant Professor and submitted to the Department of Pure & Applied Physics, University of Kota, Kota, represents my ideas in my own words and where others ideas or words have been included. I have adequately cited and referenced the original sources. The work presented in this thesis has not been submitted elsewhere for the award of any other degree or diploma from any Institutions. I also declare that I have adhered to all principles of academic honesty and integrity and have not misrepresented or fabricated or falsified any idea/data/fact/source in my submission. I understand that any violation of the above will cause for disciplinary action by the University and can also evoke penal action from the sources which have thus not been properly cited or from whom proper permission has not been taken when needed.

Date: **(Kalpana Panwar)**

This is to certify that the above statement made by **Kalpana Panwar** (Registration No. RS/2066/17 dated 21.03.2017) is correct to the best of my knowledge.

Date:

Dr. N.L. Heda
(Research Supervisor)
Assistant Professor of Physics
Department of Pure and Applied Physics
University of Kota, Kota

ACKNOWLEDGEMENTS

Words cannot express my deep sense of gratitude for my supervisor Dr. N.L. Heda, Assistant Professor of Physics, Department of Pure & Applied Physics, University of Kota, Kota. He provided me valuable guidance, inspiration, support, encouragement and innovative ideas, thus engaging me in a scholastic aptitude throughout my doctoral study. Without his proper and timely guidance my scholarly endeavors would not have taken the present shape. His truly scientific intuition has made him as a constant oasis of ideas and passions in science, which exceptionally inspire and enrich my growth as a student and a researcher.

I am thankful to Head, Department of Pure and Applied Physics, University of Kota, Kota and authorities of University of Kota, Kota for providing me the essential facilities. I also thank all faculty members of our Pure & Applied Physics Department namely Prof. N.K. Jaiman, Dr. Saurabh Dalela, Dr. Ghanshyam Sharma, Dr. Namrata Sengar, Prof. K.P. Maheshwari and Sh. B.L. Suthar for their valuable support. Further, the help of Research section of our University is also acknowledged.

I express my debt of gratitude to our collaborator Prof. B.L. Ahuja, M.L. Sukhadia University, Udaipur for motivating me towards the research. I also express my regards to Prof. Ahuja for providing me the experimental and theoretical facilities.

I also owe my gratitude to Dr. Shailja Tiwari, Department of Physics, Govt. Women Engineering College, Ajmer for her valuable guidance and support during the Ph.D. work.

I am thankful to Prof. R. Dovesi and CRYSTAL support team for the CRYSTAL14 code to our collaborator Prof. B.L. Ahuja. I express my sincere thank to Prof. D.M. Phase, Dr. R.J. Choudhary and the authority of UGC- DAE- CSR, Indore for helping me in the characterization of the samples. I am also thankful to UGC-DAR-CSR, Indore and SERB, DST, New Delhi for granting the research projects to our collaborators Prof. B.L. Ahuja and Dr. Shailja Tiwari, which help me in experimental and theoretical work.

It is a pleasure to express my gratitude to Dr. Komal Bapana, Dr. Gunjan Arora, Mr. Lekhraj Meena, Dr. Kishor Kumar, Dr. Pooja Bhoumik, Ms. Seema Kumari Meena, Mr. Mahesh Suthar, Ms. Deepika Mali, Ms. Pooja Joshi, Mr. Hukmi Chand Suthar, Mr. Om Prakash Soni and Mrs. Nusrat Naz for their academic, moral support and help during the work.

I also express my deepest regard to my parents (Mr. Ummed Singh Panwar and Mrs. Raj Kunwar Panwar), my brother Mr. Lakshya Raj Singh Panwar and my sister Mrs. Jyotsana Panwar for their love, support and encouragement throughout my life. Endless encouragement and everlasting inspiration of my husband (Mr. Yuvraj Singh Ranawat) and my in-laws enabled me to complete this task which I sincerely acknowledge from the core of my heart.

Last but not the least, I express my thanks to everybody who has directly or indirectly helped or supported me in the completion of this work.

Finally, I thank the God for blessings at every stage of my life.

(Kalpana Panwar)

CONTENTS

LIST OF TABLES

LIST OF FIGURES

ABBREVIATION

- CS : Compton scattering
- CP : Compton profile
- EMD : Electron momentum density
- LCAO : Linear combination of atomic orbitals
- HF : Hartree-Fock
- DFT : Density functional theory
- LDA : Local density approximation
- GGA : Generalized gradient approximation
- SOGGA : Second order GGA
- MP : Mulliken populations
- DOS : Density of states
- SSR : Solid state reaction
- PLD : Pulsed laser deposition
- XRD : X-ray diffraction
- XPS : X-ray photon spectroscopy
- RS : Raman spectroscopy
- FTIR : Fourier-transform infrared spectroscopy
- SQUID : Superconducting quantum interference device
- VSM : Vibrating sample magnetometer
- EVED : Equal-valence-electron-density

Constants and Units used in Compton Spectroscopy

In the analysis of Compton profiles, we have mainly used atomic units (a.u.), wherein

1 a.u. of momentum = 1.9929×10^{-24} kg m s^{-1}

1 a.u. of energy = 1 Hartree = 27.212 eV

1 a.u. of length = 5.2918×10^{-11} m

($\hbar = m = e = 1,\ c = 137.036$)

Chapter 1

Introduction and Review

The chapter is divided into two parts. The first part describes the theoretical introduction of characteristic techniques namely x-ray diffraction (XRD), x-ray photoelectron spectroscopy (XPS) and Raman spectroscopy (RS) along with the basics of Compton scattering (CS) techniques. Whereas the second part presents the review related to the proposed samples and earlier relevant CS studies.

1.1. X-ray Diffraction:

XRD is well known technique to characterize the structure of polycrystalline materials (lattice parameter, stress, strain, particle size, orientations, etc.) [1,2]. In such process, when the x-ray beam incidents on the material then the electrons of the atom oscillate and emit a radiation of the same frequency. Such emission is subjected to the fulfilment of the Bragg's law, defined as:

$$2d \sin\theta = n\lambda \quad (1.1)$$

where θ and λ are diffraction angle and the wavelength of incident x-ray, respectively, while n and d are the order of the diffraction and inter-planer spacing, respectively. In Fig. 1.1., we have sketched the schematic diagram of the XRD process. Here, the monochromatic photon (incident x-ray) falls on the material and the scattered x-rays are detected by the x-ray detector. Here, the scattering angle (between the incident and scattered x-rays) is found to be 2θ. Further, we plot a spectrum between the intensity of scattered x-rays and 2θ. The spectrum contains various informations like lattice parameters, inter-planar spacing, grain size, etc. Since the first order diffraction takes place at a specific value of 2θ for the particular set of planes and λ. Hence, we can confirm the phase of the sample by analysing peak position using standard data.

1.2. X-ray Photoemission Spectroscopy:

XPS is usually employed to study the electronic and chemical states, composition of elements and empirical formula of the sample [3,4]. It is basically a photo electric effect in which a photon of energy $h\upsilon$ interacts with an electron of material surface. Here, $h\upsilon$ is greater than to the binding energy (BE) of photon. In such process, the kinetic energy (KE) of the emitted electron is defined as:

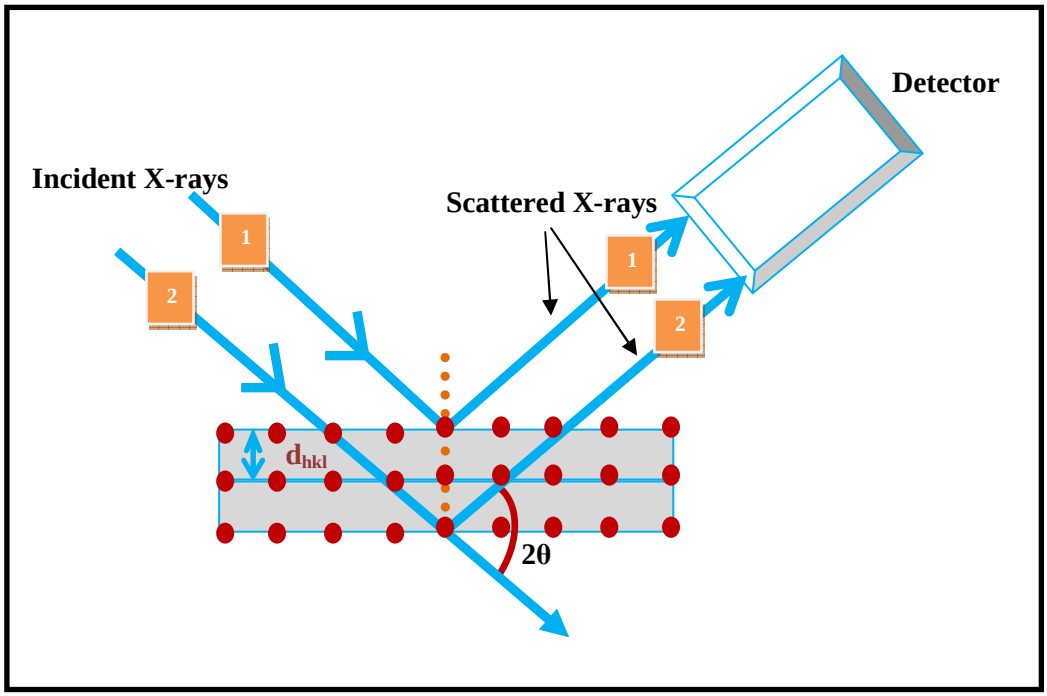

Fig. 1.1: Schematic diagram of X-ray diffraction (XRD).

$$KE = h\upsilon - BE - \phi \quad (1.2)$$

where ϕ is the work function of the experimental sample. In Fig. 1.2, we have shown the schematic sketch of XPS. It is known that every element (atom) has its characteristic BE hence the characteristic set of peaks of the photoelectron spectra of XPS can be used to calculate the KE.

1.3. Raman Spectroscopy:

RS is an important technique to characterize the material as it informs about the composition of the materials through molecular vibrations. It is basically the inelastic scattering of photon (may be taken from laser source) as the frequency of the monochromatic light changes with the interaction of the material. Here, the incident photons are first absorbed by the material and then further re-emitted with change (increase or decrease) in frequency. As shown in Fig. 1.3, the various possible types of scatterings are:

- Rayleigh scattering: If the incident and scattered light have the same frequency.
- Stokes scattering: If the frequency of the incident light is greater than that of scattered light.
- Anti-stokes scattering: If the frequency of the scattered light is greater than that of incident light.

In RS, stokes scattering is considered and Raman spectra is basically the curve between the intensity of shifted light and energy (i.e. frequency). This curve is used for the identification of the molecules [5,6].

1.4. Compton Scattering:

A.H. Compton has reported Compton effect (CE) [7] for which he was honoured by the Nobel prize in Physics in 1927. In CE, the electron at rest collides with the photon and the scattered photon is detected at an angle θ. The process is shown in Fig. 1.4, where Compton wavelength shift ($\Delta\lambda$) is defined as:

$$\Delta\lambda = \lambda_2 - \lambda_1 = \frac{h}{m_0 c}(1 - \cos\theta) \quad (1.3)$$

here λ_1 (λ_2) : wavelength of incident (scattered) photon; m_0: rest mass of electron; h: Planck's constant; c: velocity of light.

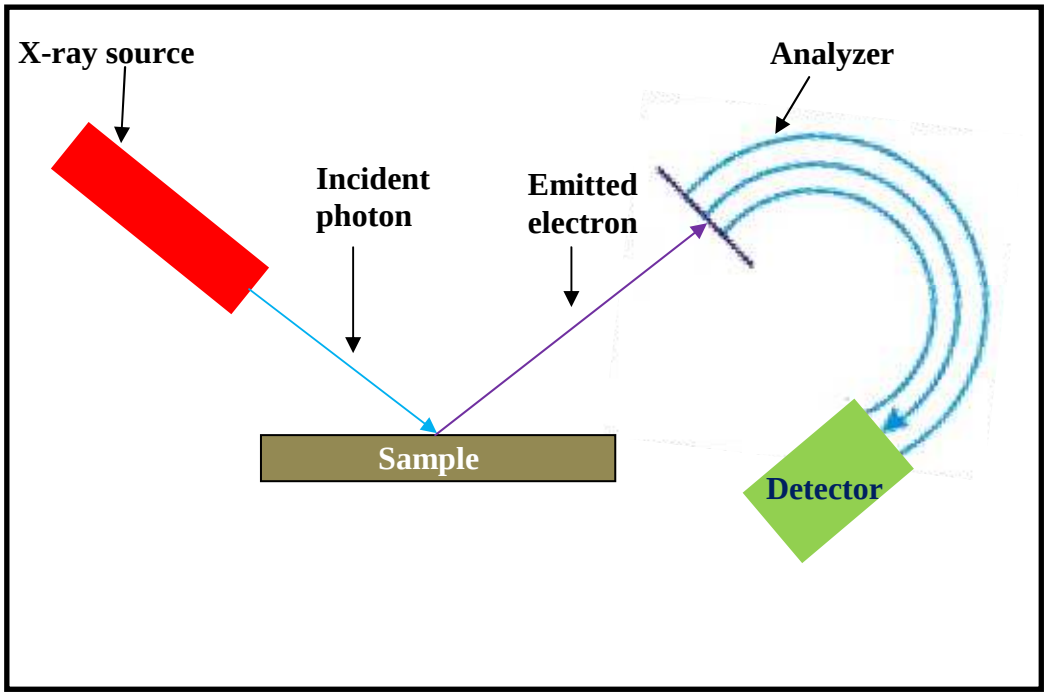

Fig. 1.2: Schematic diagram of X-ray photoelectron spectroscopy (XPS).

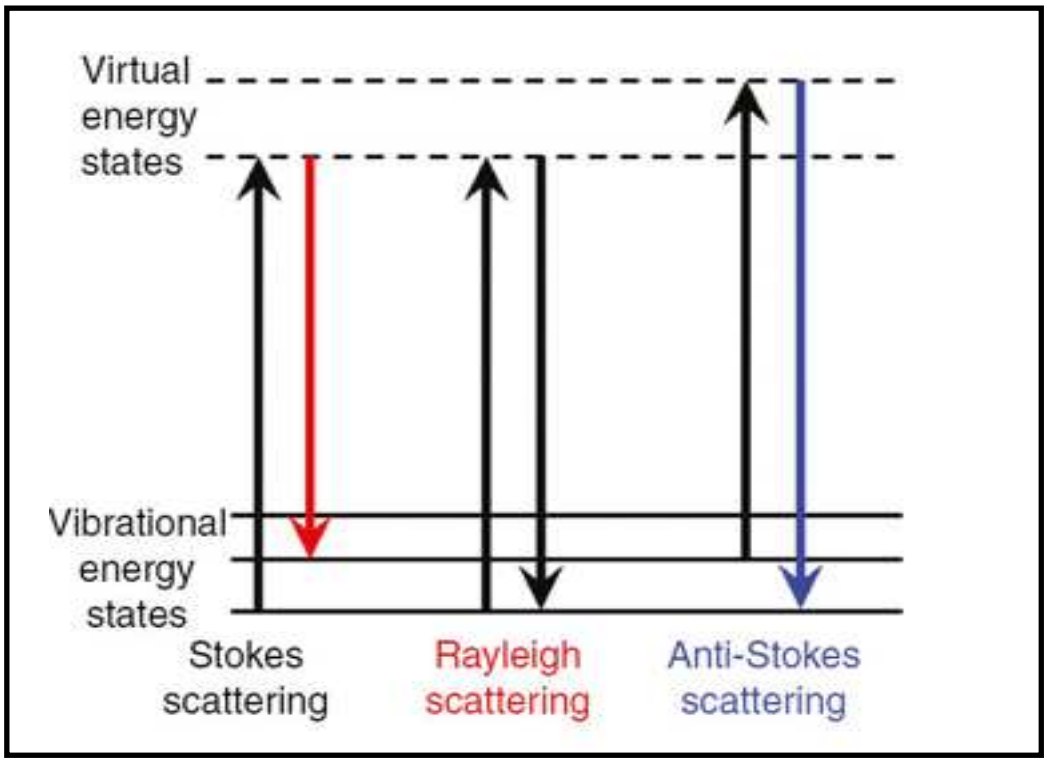

Fig. 1.3: Representative energy level diagram for Rayleigh scattering, Stokes Raman scattering and anti-Stokes Raman scattering.

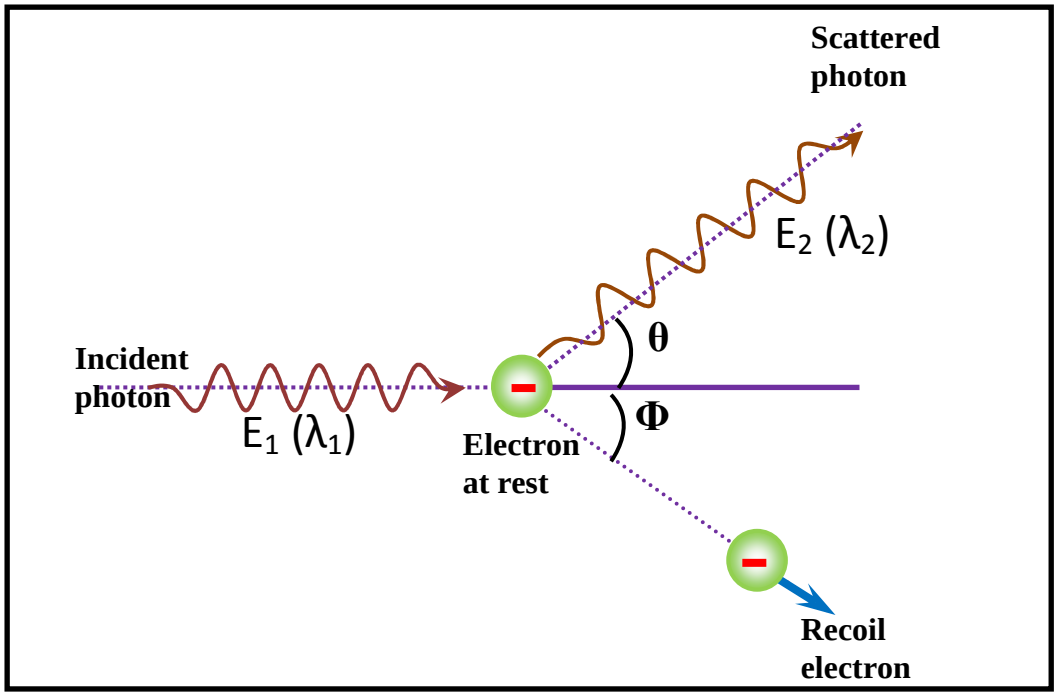

Fig. 1.4: Schematic diagram of Compton effect [7]. Here, E_1 (λ_1) and E_2 (λ_2) are the incident energy (wave length) and scattering energy (wave length) of the photons, respectively and θ is scattering angle.

From last four decades, CS (a technique sensitive to the valence electrons) has been recognized as a unique and versatile tool to predict the ground state properties and other related parameters of the materials [8-12]. It is worth while mentioning that CS is not very sensitive to the purity of the material, which puts CS into an advantage mode than that of rival techniques like positron annihilation, etc. In terms of incident and scattered energy (E_1 and E_2, respectively), Eq. (1.3) can be scaled as:

$$E_2 = \frac{E_1}{1 + \frac{E_1}{m_0 c^2}(1 - \cos\theta)} \tag{1.4}$$

In real materials the electrons are neither free or nor at rest. In Fig. 1.5, we have shown the CS process in real materials. If the motion of electrons is also considered in conservation laws of energy and momentum then Eq. (1.3) takes the following shape,

$$\Delta\lambda = \lambda_2 - \lambda_1 = \frac{h}{mc}(1 - \cos\theta) + 2(\lambda_1\lambda_2)^{1/2}\left(p_z/mc\right)\sin\left(\theta/2\right) \tag{1.5}$$

where p_z is the linear component of momentum along z-axis. Here, the first term in the right hand side represents the Compton peak position whereas the second term predicts the broadening in Compton line and is called Doppler broadening (DB). Such DB spectra in CS is known as Compton profile (CP), $J(p_z)$, which is also the projection of the electron momentum density (EMD) along the resultant (or scattering) vector direction and is usually taken along z-axis [9]. Here the CP in real material is subjected to the fulfilment of following two impulse approximations (IA) conditions:

(i) For the electron to be treated as free with same momentum: The incident energy of photons should be much-much higher than that of the BE of the electron in material. This is because a very short time should be spent in photon-electron collision so that electron does not get sufficient time to change its potential leading to its ground state properties.

(ii) For the electron to be treated at rest: It is well approximated when the interaction is impulsive.

.

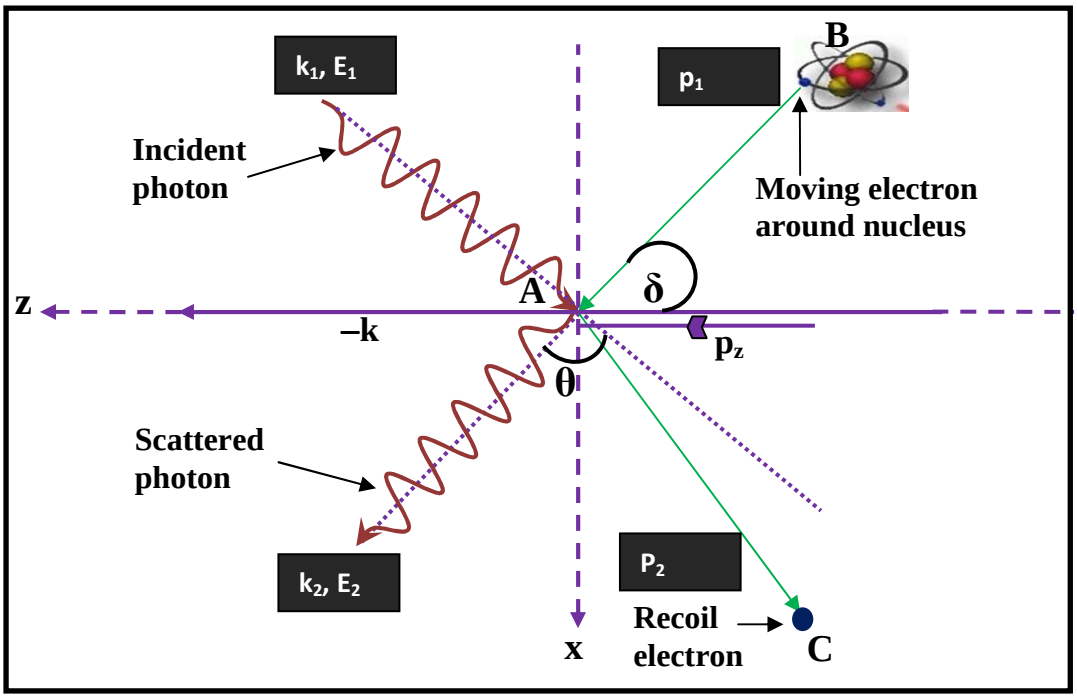

Fig. 1.5: Schematic diagram of Compton scattering. Here, E_1 (k_1) and E_2 (k_2) are the respective energy (wave vector) of incident and scattered photon and θ is the scattering angle. While p_1 and p_2 are the momentum of electron before and after scattering, respectively.

1.4.1. Measurement of CP:

Experimentally, the CP can be calculated by measuring the double differential Compton scattering (DDCS) cross section for a momentum transfer **k** (=$\mathbf{k_1}$–$\mathbf{k_2}$). Here, the DDCS cross-section $\left(d^2\sigma/d\Omega dE_2\right)$ is given by the multiplication of the standard Thomson scattering cross-section, $\left(d\sigma/d\Omega\right)_{Thom.}$, and dynamical structure factor, $S(k,E)$, as:

$$\frac{d^2\sigma}{d\Omega dE_2} = \left(\frac{d\sigma}{d\Omega}\right)_{Thom.} \times S(k, E = E_1 - E_2) \tag{1.6}$$

Mathematically, DDCS cross-section and CP are directly proportional to each other and can be connected through a proportionality constant, $C(E_1, E_2, \theta, p_z)$ as:

$$\frac{d^2\sigma}{d\Omega dE_2} = C(E_1, E_2, \theta, p_z) J(p_z) \tag{1.7}$$

here $C(E_1, E_2, \theta, p_z)$ is defined by Eisenberger and Reed [13], wherein C parameter is:

$$C(E_1, E_2, \theta, p_z) = \left(\frac{e}{4\pi\pi m}\right)^4 \left[\frac{E_1\left(1 - p_z/mc\right)}{E_2\left(1 + p_z/mc\right)} + \frac{E_2\left(1 - p_z/mc\right)}{E_1\left(1 + p_z/mc\right)}\right] \times \frac{E_2 mc}{2E_1\left(E_1^2 + E_2^2 - 2E_1E_2\cos\Phi\right)^{\frac{1}{2}} + p_z\left(\frac{E_1 - E_2}{mc}\right)} \tag{1.8}$$

1.4.2. Why CP is helpful ?

Theoretically, CP, $J(p_z)$, is defined as [8-12]:

$$J(p_z) = \iint \rho(\vec{p})\, dp_x dp_y \tag{1.9}$$

Here $\rho(\vec{p})$ denotes the probability distribution of EMDs and is calculated as:

$$\rho(\vec{p}) = \sum^{Occupied} \left|\chi_i(\vec{p}) = \frac{1}{(2\pi\hbar)^{\frac{3}{2}}} \int \psi(\vec{r}) \exp\left(-i\frac{\vec{p}\cdot\vec{r}}{\hbar}\right) d^3\vec{r}\right|^2 \tag{1.10}$$

where $\chi_i(\vec{p})$ is the momentum space wave function and it is calculated from the Fourier transform of the real space wave functions, $\psi(\vec{r})$, as shown in Eq. (1.10). Also, CP measurement has a powerful utility for the validation of the different solid state wave functions. Here, the normalization of CP is defined as:

$$\int_{-\infty}^{+\infty} J(p_z) dp_z = \text{Number of electron participat ing in the CS phenomena } (N) \tag{1.11}$$

REVIEW OF LITERATURE

In this part of the chapter, we present review of earlier work related to the proposed samples and relevant CS studies of last two decades. It is worth mentioning that earlier systematic review on CS studies is available in literature [10-12]. Following classification based abbreviations have been used in the present tabulated review:

- FO : Fe_3O_4
- NFO : $NiFe_2O_4$
- ZFO : $ZnFe_2O_4$
- CFO : $CdFe_2O_4$
- CoFO : $CoFe_2O_4$
- CS : Compton scattering
- MCS : Magnetic Compton scattering
- EMD : Electron momentum density
- CP : Compton profile
- MCP : Magnetic Compton profile
- CO : Charge ordering
- MO : Magnetic ordering
- LCAO : Linear combination of atomic orbitals
- HF : Hartree-Fock
- DFT : Density functional theory
- PP : Pseudopotential
- LDA : Local density approximation
- LSDA : Local spin density approximation
- SIC–LSDA : Self interaction corrected LSDA
- GGA : Generalised gradient approximation
- SOGGA : Second order GGA
- B3LYP/B3PW/PBE0/PBESOL0/WC1LYP/B1WC : Different hybrid (HF+DFT) schemes
- LMTO : Linear muffin-tin orbitals
- TB-LMTO : Tight binding LMTO

- LAPW : Linearized augmented plane wave
- FP-LAPW : Full potential LAPW
- mBJ: Modified Becke-Johnson
- MP : Mulliken population
- DOS : Density of states
- VCD : Valence charge density
- SSR : Solid state reaction
- PLD : Pulsed laser deposition
- RS : Raman spectroscopy
- FTIR : Fourier-transform infrared spectroscopy
- SQUID : Superconducting quantum interference device
- VSM : Vibrating sample magnetometer
- EDXS : Energy dispersive X-ray spectroscopy
- XRD : X-ray diffraction
- XRR : X-ray reflectivity
- XAS : X-ray absorption spectroscopy
- MNS : Magnetic neutron scattering
- MS : Mössbauer spectroscopy
- SEM : Scanning electron microscopy
- TEM : Transmission electron microscopy
- HRTEM : High resolution TEM
- AFM : Atomic force microscopy
- XPS : X-ray photon spectroscopy
- XMLD : X-ray magnetic linear dichroism
- XMCD : X-ray magnetic circular dichroism
- PPMS : Physical properties measurement system
- ECM : Electrical conductivity measurements
- EVED : Equal-valence-electron-density
- MM : Magnetic moment
- M-H : Magnetization vs magnetic field
- M-T : Magnetization vs temperature
- NRM : Neutron reflectometry measurements

Authors	**Experimental techniques and/or theoretical methods**	**Salient features**
Zhang et al. [14]	XRD, AFM and M-H measurements	Illustrated the effect of Ni^{2+} doping in CoFO films in terms of film structure and magnetic properties.
Wright et al. [15]	XRD and neutron power diffraction	Reported crystal structure of FO below 122 K (Verwey transition temperature) and discussed CO.
Antonov et al. [16]	Full relativistic Dirac LMTO-LSDA+U	Elucidated optical and magneto-optical spectra of CO in FO. Also discussed the band structure and DOS of pure and Mg^{+2}/Al^{+3} doped FO.
Singh et al. [17]	LAPW-DFT with LSDA and GGA	Presented electronic and magnetic properties of spinel ZFO and observed an insulating antiferromagnetic state of the compound.
Jeng and Guo [18]	LMTO-DFT-LSDA	Explained the magneto crystalline anisotropic energy in NFO and calculated uni-axial anisotropy constant.
Yamada et al. [19]	Classical Heisenberg spin model	Performed a theoretical description of neutron scattering in ZFO and discussed the magnetic interactions in the compounds.
El-Sayed [20]	XRD, infra-red (IR) absorption spectra and SEM	Prepared $Ni_{0.6}Zn_{0.4}Cr_xFe_{2-x}O_4$ (x = 0.00 to 0.25 at the interval of 0.05) using ceramic process and analyzed in terms of lattice parameter, density, porosity and shrinkage.
Nikumbh et al. [21]	XRD, MS, electrical conductivity, thermoelectric and M-H measurements	Synthesized $Cd_{1-x}Ni_xFe_2O_4$ ($0\leq x\leq 1$ at the step of 0.2) using tartarate precursor and reported XRD, MS, IR electrical conductivity and thermoelectric measurements along with saturation magnetization and MM.
Singh et al. [22]	LAPW-DFT	Explored $TMFe_2O_4$ (TM=Zn and Mn) for electronic and magnetic properties and shown ZFO as a small gap insulator while $MnFe_2O_4$ is reported as half metallic compound in the fully ordered state.
Szotek et al. [23]	SIC-LSDA	Calculated and discussed the electronic properties (like spin dependent DOS, MM, etc.) and possible CO in FO in two phases namely cubic and ortho-rhombic.
El-Sayed [24]	ECM	Synthesized $Ni_{1-x}Zn_xFe_2O_4$ ($0.1\leq x\leq 0.9$) and $Ni_{0.6}Zn_{0.4}Cr_yFe_{2-y}O_4$ ($0.0\leq y\leq 0.25$) using ceramic method and performed ECM at variable and constant frequency.

Kamazawa et al. [25]	MNS	Undertaken MNS measurements of ZFO single crystals to discuss geometrical frustration and unusual character of the compound.
Antonov et al. [26]	Fully relativistic Dirac LMTO with LSDA and LSDA+U	Explored electronic properties like DOS, XMCD spectra and MM calculations in pure and Mn-, Co- and Ni-substituted FO compounds.
Kamazawa et al. [27]	MNS	Investigated geometrical frustration in CFO and resembled the data with ZFO to discuss ferro- and anti-ferro magnetic interactions among the nearest neighbors.
Huang et al. [28]	SQUID and XMCD	Analyzed orbital and spin MM in FO and observed non-integer spin and larger orbital contributions in the compounds due to 3d electrons of Fe.
Caltun [29]	XRD, SEM, EDX, PLD and AFM	Grown and characterized NFO film and explored the role of the post annealing conditions on magnetic properties.
Horng et al. [30]	XRD, M-H and M-T measurements	Synthesized FO and CoFO thin films using molecular beam epitaxy and studied magnetic anisotropic properties of both the compounds.
Leonov et al. [31]	TB-LMTO-LSDA+U	Highlighted the charge and orbital ordering in FO and discussed the role of Anderson criterion and Kugel-Khomskii theory.
Wang et al. [32]	XRD, AFM and M-H measure-ments	Deposited CoFO films on SiO_2 single-crystal substrate and characterized by XRD. Also reported that magnetic properties depend on annealing temperature, duration of annealing and film thickness.
Rais et al. [33]	XRD, MS and VSM measurements	Illustrated the role of cation occupancy and magnetic character in $NiCr_xFe_{2-x}O_4$ ($0 \leq x \leq 1.4$) and discussed the results in view of Neel's molecular field theory.
Gismelseed and Yousif [34]	XRD and MS	Elucidated the structural and magnetic character of spinel $NiCr_xFe_{2-x}O_4$ ($0 \leq x \leq 1.4$) system and discussed the cation distribution.
Caltun [35]	XRD, SEM, EDXS, VSM and AFM	Synthesized and characterized the thin film of $Ni_{0.5}Zn_{0.5}Fe_2O_4$ using PLD and studied the electronic and magnetic properties of the compound.
Madsen and Novak [36]	LAPW-DFT with LDA and LDA+U	Compared the results of LDA and LDA+U calculations with experimental data of CO in FO and predicted the applicability of LDA+U calculation.

Cheng [37]	DFT-GGA	Interpreted structural and magnetic properties of FO surface and discussed the results in the framework of four model formalism.
Lüders et al. [38]	XRD, AFM, XPS and VSM	Demonstrated the growth of NFO thin film and discussed MM and conductive phenomena in spinel structure.
Sorescua et al. [39]	XRD and SQUID	Used laser deposition method to synthesize nano-scale Ni-Zn and Zn ferrite films on Si (100) substrate and presented a systematic comparison between magnetization data of bulk and thin film along with their characterization. Also reported the applicability of ferrite films as prime candidates in thin-film high frequency microwave devices.
Singh et al. [40]	XRD, XPS and IR spectra measurements	Presented thin film of $NiCr_xFe_{2-x}O_4$ ($0 \leq x \leq 1$) using precipitation method and studied physic-chemical and electro-catalytic character of the compounds.
Phase et al. [41]	XRD and RS	Shaded light on the growth of FO thin film using PLD and discussed RS measurements (85–300 K) along with their characterization through XRD.
Piekarz et al. [42]	DFT with GGA and GGA+U	Studied electronic properties and phonon spectrum in FO for the induced phase transition from cubic (high temperature state) to monoclinic (low temperature state) phase along with the role of Fe-3d electrons.
Zhu et al. [43]	DFT with LDA+U and GGA	Calculated total and partial DOS for bulk and surface FO and observed the half-metallic properties in both the states of the compound.
Devan et al. [44]	XRD, SEM, DC resistivity and AC conductivity measurements	Prepared $Ni_{0.95-x}Co_xCu_{0.05}Fe_2O_4$ (x= 0.01, 0.02 and 0.03) using ceramic technique and studied the effect of Co substitution on Ni site in $Ni_{0.95}Cu_{0.05}Fe_2O_4$ through different experimental techniques.
Szotek et al. [45]	SIC-LSDA	Reported electronic and magnetic properties in $TMFe_2O_4$ (TM = Mn, Fe, Co and Ni) and observed the increase in spin MM with the transition metal doping in the order Mn→Fe→Co→Ni.
Nakashima et al. [46]	FP-LAPW+lo (local orbitals) with DFT	Prepared ZFO thin film using sputtering method and reproduced the theoretical x-ray absorption near-edge structures (XANES) by the measured data.

Piekarz et al. [47]	DFT with GGA and GGA+U	Discussed Verwey phase transition using group theory along with the crystal structure and electronic properties of FO.
Perron et al. [48]	DFT with LSDA and GGA	Compared the magnetic structure results using LSDA and GGA scheme along with the experimental data for NFO and reported the applicability of GGA than that of LSDA scheme.
Singhal and Chandra [49]	XRD, VSM and MS	Described the preparation of Cr doped NFO using aerosol method and studied the cation distribution and magnetic properties to discuss the role of Cr substitution in NFO.
Chinnasamy et al. [50]	XRD and VSM	Deposited thin film of NFO on MgO substrate using PLD method to see the effect of growth temperature on magnetic, microwave and cation inversion properties.
Ramalho et al. [51]	XRD and MS	Synthesized NFO using combustion reaction method and the cation distribution was studied by Rietveld method with synchrotron radiations and MS.
Tiwari et al. [52]	XRD, XPS, RS and four probe resistivity measurements	Grown FO thin films on Si (111), GaAs (100), Al_2O_3 (001) and amorphous float glass substrates using PLD at 450 °C and analyzed by XRD, XPS and RS along with ac magnetic susceptibility and resistivity measurements.
Tiwari et al. [53]	RS and VSM	Synthesized FO thin films on Si substrate in (111), (110) and (100) orientations using PLD method and single phase was confirmed by RS. Also reported that mag-netization in films was saturated at 0.2 T.
Bhame and Joy [54]	M-H measurements	Prepared $Co_{1-x}Mn_xFe_2O_4$ ($0 \leq x \leq 0.4$) using ceramic method and discussed in terms of magnetic and magneto-striction properties. Also, reported that $Co_{0.7}Mn_{0.3}Fe_2O_4$ has highest magneto-striction properties, results its utility in many applications.
Bharathi et al. [55]	XRD, VSM and strain gauge method	Prepared $NiFe_{1.925}Dy_{0.075}O_4$ by SSR method and reported that Dy substitution on Fe site decreases the saturation magnetization. Also revealed the dispersion in relaxation time through dielectric constant with frequency.
Cheng [56]	DFT with GGA and GGA+U	Discussed electronic properties of ZFO and CFO in terms of Fe-Fe interactions and reported the anti ferromagnetic nature of both the compounds.

Cheng and Liu [57]	DFT with LDA, GGA, LDA+U and GGA+U	Explained electronic structure in ZFO and CFO using DOS and band gaps in normal and inverse spinel structure.
Kulkarni et al. [58]	XRD, FTIR and SEM	Produced $Ni_xZn_{1-x}Fe_2O_4$ film using co-precipitation method and performed permi-ttivity and permeability measurements along with dielectric constant.
Winell et al. [59]	XRD and MS	Prepared 10 composition of $NiCr_xFe_{2-x}O_4$ ($0 \leq x \leq 1.8$) in single phase and observed inverted spinel structure for $x \leq 0.6$. Also for higher value of x, the complicated ordering is observed.
Tiwari et al. [60]	XRD, XPS and RS	Synthesized FO thin films of different thickness on Si and MgO substrates and reported the non existence of anti-phase boundaries in the films.
Gabal and Al Angari [61]	XRD, FTIR, MS and dielectric constant measurements	Reported $Ni_{1-x}Zn_xFe_2O_4$ ($0.0 \leq x \leq 1.0$) using thermal decomposition method and studied the effect of Zn doping in NFO in terms of structural, electrical and magnetic properties.
Kambale et al. [62]	XRD, M-H and DC resistivity measurements	Presented five composition of Co doped NFO (at the interval of 0.2) at Ni site using ceramic method and seen the decrease in resistivity, increase in saturation magneti-sation and decrease in coercive field with increase of Co doping at room temperature.
Tiwari et al. [63]	XRD, XPS and RS	Prepared FO thin films using PLD in 350 to 550 °C temperature range and studied the structural and transport properties.
Patil and Chougule [64]	XRD, dielectric properties and M-H measurement	Synthesized $Ni_{1-x}Cu_xFe_2O_4$ (x= 0.0, 0.1 and 0.2) using ceramic method and phase identification was done by XRD. Also, studied in terms of dielectric properties and magnetization saturation.
Rowan et al. [65]	DFT-GGA and B3LYP	Employed pure and hybrid DFT approximation to compute electronic properties (energy bands, DOS, MP data and charge density) and phonon frequencies for FO and compared their results with the experimental data.
Bharathi et al. [66]	XRD and VSM	Reported Gd and Nd doped NFO using SSR method and studied for its magnetoelectric properties and reported that the MM decreases with small substitution of Nd and Gd at Fe site.

Shirsath et al. [67]	XRD, magnetization and susceptibility measurements	Presented In doped NFO (0.0 to 0.30 at the step of 0.05) and confirmed their single phase by XRD. Also observed the increase in saturation magnetization and magneto number with increasing In doping concentration.
Ramos et al. [68]	XRD, VSM, PPMS and NRM	Prepared FO/CoFO bilayers systems using oxygen plasma-assisted molecular beam epitaxy and explored with M-H, magneto-transport and NRM to demonstrate the artificial anti-phase boundary in the compound.
Dixit et al. [69]	XRD, RS, SEM and VSM	Synthesized NFO thin films on Si (100) substrate using PLD method and reported that the annealing temperature controls the structural and magnetic properties of the film.
Jacob and Khadar [70]	XRD, MS, FTIR, RS and VSM	Reported single crystalline NFO by co-precipitation technique in inverse spinel structure along with its XRD, RS, MS, FTIR and magnetization measurements.
Fritsch and Ederer [71]	DFT with LSDA+U and GGA+U	Applied LSDA+U and GGA+U within DFT scheme to see the effect of epitaxial strain on the magnetic properties of NFO and CoFO. Also compared their results with the experimental data.
Datta et al. [72]	TEM and HRTEM	Deposited NFO thin films on different substrates using PLD method and studied by TEM and HRTEM.
Anjum et al. [73]	XRD, TEM, SEM, XPS and VSM	Synthesized NFO thin film by PLD and studied for the effect of vacancies in transport and magnetic properties of films through different experimental techniques.
Ma et al. [74]	EDXS and AFM	Employed PLD technique to grow NFO and CoFO films in the temperature range 175–690 °C and characterized by EDXS and AFM.
Zhou and Ceder [75]	DFT-GGA+U	Studied CO, orbital ordering and ionic displacement in FO using DFT with GGA+U approximation.
Ivanov et al. [76]	RS	Measured Raman spectra for NFO single crystal and compared the results with pure and Ni-Zn (Ni=0.7 and Zn = 0.3) doped FO in terms of short range B-site ordering.
Ahuja et al. [77]	MCS	Measured MCPs of $Bi_xCo_{2-x}MnO_4$ (x= 0 and 0.03) at different temperature and 2.5 T magnetic field and reported the reversal behavior of orbital MM with Bi doping.

Duffy et al. [78]	MCS	Performed MCS measurements of single crystal of FO along [100], [110] and [111] directions at 100 K and 2.5 T and calculated spin and orbital MM.
Patange et al. [79]	XRD and electrical resistivity measurement	Prepared nano particles of $NiAl_xFe_{2-x}O_4$ ($0 \leq x \leq 1$) using co-precipitation method and characterized by XRD. Also calculated AC and DC electrical resistivity to discuss switching properties of the compounds.
Shirsath et al. [80]	XRD, SEM, VSM and susceptibility measurements	Produced $Ni_{1-2x}Ce_xFe_2O_4$ ($0 \leq x \leq 0.25$) using SSR method and studied interms of lattice distortion, strain, bulk density, saturation magnetization and Curie temperature.
Bharathi et al. [81]	XRD, XRR and Ultra violet (UV) spectra	Fabricated $NiFe_{1.925}Dy_{0.075}O_4$ thin films using sputter deposition technique and studied for its structural and optical properties and observed the significance of grain size and lattice expansion effect on optical properties.
Soliman et al. [82]	DFT with LDA and GGA+U	Analyzed electronic properties (energy bands, DOS and ground state energy) of ZFO and observed superiority of GGA+U calculations over LDA approximation.
Tang et al. [83]	Quantum-mechanical approximation	Employed quantum mechanical method to discuss the cation distribution and MM of $TMFe_2O_4$ (TM= Mn, Fe, Co, Ni and Cu) and $TM_{1-x}Zn_xFe_2O_4$ (TM = Mn, Fe, Co, Ni and Cu; x = 0.2, 0.4, 0.6, 0.8 and 1.0).
Fritsch and Ederer [84]	DFT-GGA+U	Studied the effect on cation distribution by epitaxial strain in NFO and CoFO and observed cation inversion tendency, which is in accordance with the experimental data.
Prasad et al. [85]	XRD, electrical resistivity and magnetization measurements	Prepared $Ni_{0.65-x}Cd_xZn_{0.35}Fe_2O_4$ ($0 \leq x \leq 0.2$; at the interval of 0.04) using ceramic method and studied crystal structure, electric and magnetic properties.
Atif et al. [86]	XRD, M-H, dielectric permittivity and ac conductivity measurements	Applied sol-gel method to synthesize Zn-doped NFO ($Ni_{1-x}Zn_xFe_2O_4$; $0 \leq x \leq 0.6$) and observed the increase in saturation magnetization with increase of Zn doping up to x = 0.4. Also calculated dielectric permittivity, AC conductivity and dielectric loss as a function of frequency.
Noor et al. [87]	XRD, dc electrical resistivity and dielectric measurements	Prepared $Co_{1-x}Cd_xFe_2O_4$ (x= 0.0 to 1.0 at the step of 0.1) using ceramic method to investigate the effect of Cd substitution on the structural and transport properties of CoFO.

Ahuja et al. [88]	MCS	Measured MCP of Co_2MnO_4 at 10 K to calculate the spin moment of the compound.
Choudhary et al. [89]	CS and DFT-LDA/ GGA, B3LYP and B3PW	Performed ^{137}Cs based CP measurements of CdO and HgO to compare with the theoretical data of LCAO scheme and observed the best agreement with B3LYP scheme. Also discussed energy bands, DOS and EVED of both the oxides.
Tiwari et al. [90]	XRD, PPMS and four probe measurements	Applied SSR method to prepare 6 compositions of $La_{0.7}Ca_{0.3}Mn_{1-x}Al_xO_3$ ($0 \leq x \leq 1$) and characterized by XRD. Also, attempted field and zero filed cooled PPMS (four probes) measurements in 10-300 K at 0.05 T (5-300 K at 2.5 T).
Ahuja et al. [91]	MCS and VSM	Performed MCPs and M-H measurements of $La_{0.7}Ca_{0.3}Mn_{1-x}Al_xO_3$ (x = 0, 0.02 and 0.06) to analyzed spin and MM on the basis of 3d state of Mn.
Mund et al. [92]	EDXS, MCS and VSM	Prepared CoFO using SSR method and confirmed homogeneity through EDXS. Also measured MCP of the compound at 8 and 300 K to decompose into its constituent elements along with spin moment calculations through MCP and M-H measurements.
Raghunathan et al. [93]	XRD, EDXS, SEM and VSM	Grown CoFo thin films on SiO_2/ Si(100) substrates using PLD method to see the influence of reactive atmosphere on magnetic properties.
Rama Krishna et al. [94]	XRD, EDXS, SEM and VSM	Presented the synthesis of six composition of $Ni_{1-x}Zn_xFe_2O_4$ ($0 \leq x \leq 1$) at 180 °C using combustion process and characterized by XRD, EDXS and SEM measurements. Also, reported the saturation magnetization and MM of the compositions.
Fritsch and Ederer [95]	DFT-GGA+U	Attempted electron beam deposition technique to prepare NFO and CoFO thin film and applied to calculate magnetoelastic and magnetostriction coefficients and obtained a good agreement with the available experimental data.
Rai et al. [96]	XRD, AFM and absorption spectra measurements	Deposited NFO and CoFO thin film using electron beam decomposition method to study the electronic and optical properties of the films.

Yu et al. [97]	DFT-GGA+U	Calculated electronic properties, stabilities and magnetic properties of three FO surfaces to discuss the on-site Coulomb interaction among Fe-3d electrons.
Singh et al. [98]	XRD, AFM, SEM, EDXS and VSM	Deposited thin film of Ni, NiFe and NFO using magnetron sputtering and employed different experimental techniques for structural and magnetic response.
Dixit et al. [99]	PLD, XRD, RS, FTIR , VSM and UV reflectance spectra measurements	Grown NFO thin films on Si(100) substrate by PLD in various thicknesses (62 to 76 nm) and characterized by XRD, RS and FTIR. Also reported the increase in saturation magnetization with decrease in thickness and the non-dependence of optical band gap on the thickness.
Patange et al. [100]	XRD, MS and VSM	Reported $NiCr_xFe_{2-x}O_4$ ($0 \leq x \leq 1$ in step of 0.2) in nano crystalline form by co-precipitation method and characterized by XRD and RS. Also, reported the decrease in saturation magnetization with increasing Cr contribution.
Li et al. [101]	XRD, SEM and VSM	Grown $Ni_{0.5}Zn_{0.5}Fe_2O_4$ thin film using ceramic method and annealing temperature effect was studied in terms of magnetic properties, phase structure and micro-structure. Also discussed coercivity by stress model.
Jaffari et al. [102]	XRD, SEM, XPS and VSM	Synthesized NFO thin film using PLD method and carried out various measure-ments to see the effect of oxygen vacancies on electronic and magnetic properties.
Seifikar et al. [103]	XRD, SEM, TEM and SQUID	Fabricated NFO thin film on Si(111) through sol-gel processing and achieved uniaxial texture with decrease in thickness of the film and proposed the improvement in the magnetization and coercivity.
Zabotto et al. [104]	XRD, SEM, M-H and M-T measurements	Prepared NFO using SSR method to assess various electric and magnetic properties and also observed that coercive field decreases with increase in grain size.
Sun et al. [105]	DFT-LSDA+U and HSE06	Reported the indirect band gap character of NFO using the minority spin energy bands and DOS along with the comparative study of theoretical and experimental value of dielectric constant.
Tiwari et al. [106]	XRD, RS, XPS and resistivity measurements	Grown $Mo_{1-x}Fe_xO_2$ (x = 0 and 0.05) thin film by PLD technique and studied XRD, XPS, RS and resistivity measurements.

Ahuja et al. [107]	MCS	$Ni_{1-x}Zn_xFe_2O_4$ (x = 0, 0.1 and 0.2) was prepared by SSR method and employed for MCP measurements at 8 and 300 K at 2.5 T. Also decompose MCP into its component element to calculate the site specification MM of the compounds.
Bhamu et al. [108]	CS and DFT with LDA, GGA and SOGGA	Discussed the nature of bonding in $ATiO_3$ (A = Ca and Sr) using experimental and theoretical CPs and MP data. Also calculated, the energy bands and DOS to discuss the semiconducting nature of the compound along with the validation of DFT-SOGGA based CP with 661.65 keV based CS measurements.
Mohammed et al. [109]	CS and LCAO-PP with DFT-LDA/GGA/ SOGGA	Performed CP measurements of Nd_2O_3 using ^{137}Cs isotope and compared the data with different approximations under PP-DFT scheme and reported the better agreement with PP-DFT-GGA. Also discussed the semiconducting nature of the compound through energy bands and DOS.
Caffrey et al. [110]	SIC-LSDA	Presented energy bands and DOS of NFO and CoFO to discuss the spin filtering efficiency.
O'Brien et al. [111]	DFT-GGA	Used effective chemical potentials to calculate the free energy of ZFO and NFO from 300 to 600 K at 155 bar pressure.
Sharma and Singhal [112]	XRD, FTIR, TEM and M-H measurements	Synthesized $Zn_xNi_{1-x}Fe_2O_4$ (x= 0, 0.2, 0.4, 0.6, 0.8 and 1) using sol-gel method and employed different measurements to discuss their structural, electrical and magnetic properties.
Varshney and Verma [113]	XRD, RS and dielectric properties measurements	Prepared pure and 5 % Zn and Mg doped NFO using co-precipitation method and confirmed their single phase by XRD and RS. Also, discussed frequency dependence of dielectric constant of the compounds.
Himcinschi et al. [114]	XRD, AFM and RS	Deposited NFO and CoFO epitaxial films using PLD method and confirmed the good crystalline quality by XRD and AFM. Also, observed a larger number of phonon bands through Raman spectra which confirms the cubic spinel structure of the compounds.
Cheng [115]	DFT-GGA	Employed DFT-GGA approximations to compute the lowest energy phase, DOS and band gap of NFO and reported the spin-tronic applications of the compound.

Bengtson et al. [116]	DFT-GGA+U	Performed DFT with GGA+U calculation to discuss Fe spin state and MO in FO using DOS along with the variation of enthalpy with pressure and volume.
Heda and Ahuja [117]	CS, LCAO and FP-LAPW	Measured CP of WO_3 using ^{137}Cs radio-isotope and validated DFT-GGA scheme. Also discussed the charge transfer through MP analysis and bond distances along with the semiconducting nature using LCAO and FP-LAPW approximations through energy bands and DOS.
Ahuja et al. [118]	CS and LCAO	Applied CS method to measure EMDs of RDX and HMX using 661.65 keV photons and reported the applicability of DFT-GGA scheme along with the semiconducting nature of both the compounds. The causes of being the explosive nature of both the compounds were also reported using MP analysis.
Mohammed et al. [119]	CS and LCAO-DFT within LDA, GGA and SOGGA	Performed CP measurements of $CaCO_3$ using 59.55 keV and validated the DFT-GGA scheme. Also reported the semi-conducting nature of the compound using energy bands and DOS.
Dashora et al. [120]	MCS, VSM and PPMS	Prepared $LaFe_{1-x}Ni_xO_3$ (x = 0.4 and 0.5) using SSR method and performed MCP measurements using 182 keV synchrotron radiations along with M-T data using PPMS measurements. Also, discussed site specific spin moments in terms of Fe and Ni contribution.
Mund et al. [121]	XPS and MCS	Synthesized $CoFe_{2-x}RE_xO_4$ (RE = Dy and Gd; x= 0 and 0.05) using SSR method and employed MCP and XPS measurements for data analysis. Also MCPs decomposed for site specification moments of individual components.
Holinsworth et al. [122]	PP-PAW-DFT with LDA+U and GGA+U along with optical measurements	Prepared CoFO films using PLD and performed optical measurements in reflectance and transmittance modes to calculate the band gap. Also computed indirect (1.2 eV) and direct (2.7 eV) band gap using DFT scheme and compared their results with NFO at high temperature.

Zhi-Feng et al. [123]	XRD, EDXS, SEM and PPMS	Prepared $Co_{1-x}Cr_xFe_2O_4$ ($0 \leq x \leq 1$) using hydrothermal method to discuss the cation distribution using MM. Also reported that saturation magnetization decreases with increase of Cr component in CoFO.
Odkhuu et al. [124]	DFT with GGA and GGA+U	Discussed effect of CO in FO and CoFO through DFT and calculated the band gap, lattice constant, MM and magnetostriction.
Matzen et al. [125]	TEM, XMCD, XAS and VSM	Grown NFO (111) layers using oxygen assisted molecular beam and explored for structural and magnetic characterizations.
Jesus et al. [126]	XRD, M-H and susceptibility measurements	Prepared ZFO using SSR method and reported various properties using XRD, magnetization vs temperature and magnetic susceptibility vs temperature.
Lang et al. [127]	XRD, M-H and quantum mechanical potential barrier (QMPB) model	Prepared $TM_xNi_{1-x}Fe_2O_4$ (TM = Cr and Co; $0 \leq x \leq 0.3$) using co-precipitation method and analyzed structural and magnetic response using XRD and M-H measurements. Also calculated the site specific MM using QMPB model.
Klewe et al. [128]	PLD, XRD, XRR, XPS, AFM, XAS, XMCD and XMLD	Grown NFO thin films on $MgAl_2O_4$ (001) substrate using PLD method at different temperature were analyzed for structural and surface topography along with characteristics and transport properties through various experimental techniques.
Meinert and Reiss [129]	FP-LAPW-DFT-LDA with mBJ	Explored electronic and optical properties of inverse spinel NFO. The mBJ exchange potentials scheme has reproduced the experimental optical absorption spectra and the indirect band gap was reported as 1.53 eV in minority spin states through energy bands and DOS.
Heda et al. [130]	FP-LAPW and LCAO based DFT-GGA	Analyzed MP data in WO_3 using LCAO-DFT-GGA scheme along with energy bands and DOS using FP-LAPW-DFT-GGA scheme. Also, explained DOS in terms of MP data and observed the CP difference (between convoluted theory and experiment) within the experimental error.
Sahariya et al. [131]	MCS and VSM	Measured temperature dependent MCPs of $NiFe_{2-x}RE_xO_4$ (x = 0 and 0.05; RE = Dy and Gd) and reported similar spin moment of Dy and Gd doped and pure NFO. Also compared the MCP based MM with the M-H measurements.

Sharma et al. [132]	CS and DFT within LDA, GGA and SOGGA	Attempted EMD measurements using 662 keV γ-rays to validate the DFT-GGA based CP of La_2O_3. Also reported the semi-conducting nature through energy bands and DOS along with the nature of bonding through MP and VCDs of the compound.
Şabikoğlu et al. [133]	XRD, SEM, FTIR, SQUID and MS	Prepared Nd doped NFO using SSR method to see the effect of Nd substitution on structural and magnetic properties of NFO. Such studies indicate the existence of two different phases and discussed in terms of tetrahedral and octahedral positions.
Masrour et al. [134]	FP-LAPW-DFT with GGA	Applied DFT-GGA within FP-LAPW approximation to calculate spin projected DOS, magnetic susceptibility and MM of FO and also discussed Fe-Fe interactions using mean field theory.
Hoppe et al. [135]	PLD, XRD, XRR, XPS, XMCD and SQUID	Synthesized NFO thin films using PLD method and investigated the structural, electronic and magnetic properties of films using different experimental techniques.
Zaari et al. [136]	FP-LAPW-DFT with mBJ and GGA+U	Calculated DOS along with optical and XMCD properties of CFO using mBJ and GGA+U calculations within DFT framework. Both the approximations predict the results well while comparing with the experimental data.
Heda and Ahuja [137]	CS and LCAO-DFT with LDA, GGA, SOGGA	Presented CP measurements of WO_2 using 662 keV photons and found in accordance with DFT-GGA data. The metal-like behavior was confirmed by energy bands and DOS while MP data and EVED based CPs have reported increasing order of ionic character in iso-electronic compounds as $WSe_2 \rightarrow WS_2 \rightarrow WO_2$.
Sharma et al. [138]	CS and LCAO	Computed MP, energy bands, DOS and CPs of Sm_2O_3 in cubic and monoclinic phases using LCAO-DFT approximations and validated the GGA scheme through CP measurements at 0.34 a.u.
Meena et al. [139]	CS and LCAO-DFT with LDA and GGA	Employed CS to measure the CP of AWO_4 (A = Zn and Cd) and reported the utility of DFT-GGA with PBESol potentials. Also analyzed the semiconducting nature of both the compounds along with the more covalent character in $ZnWO_4$ than that of $CdWO_4$ using MP and EVED scaled CPs.

Sharma et al. [140]	CS, LCAO and FP-LAPW	Checked the performance of PBESol approximations within LCAO scheme with CP measurements of RuO_2. Also reported metallic character using LCAO and FP-LAPW within DFT-GGA-PBESol approximations. The MP data, Fermi surfaces and optical properties have also been discussed.
Jahan et al. [141]	XRD and resistivity measurements	Ceramic method was applied to prepare $NiCr_xFe_{2-x}O_4$ ($0.0 \leq x \leq 1$) and single phase has been confirmed by XRD. Also performed dc resistivity measurements through two probe method and predicted the semiconducting nature of the compositions.
Jong et al. [142]	DFT-GGA+U	Reported theoretical investigations of ferri-magnetism and ferro-electricity in NFO and discussed p-d hybridization in the compound.
Quintero et al. [143]	MS and FP-LAPW-DFT-GGA+U	Presented theoretical and experimental investigations in ZFO in terms of hyperfine parameters, MM and magnetic alignment.
Abdul Khader et al. [144]	XRD and SEM	Synthesized $Ni_xCr_{1-x}Fe_2O_4$ (x = 0, 0.25, 0.50, 0.75 and 1.0) nano-particles using combustion method and studied structural and dielectric properties of the compounds using XRD, SEM and dielectric measurements.
Meena et al. [145]	LCAO within B3LYP, B3PW and PBE0	Calculated MP analysis, energy bands, DOS and EMDs of $CdWO_4$ and reported the applicability of B3LYP along with the semiconducting nature of the compound.
Meena et al. [146]	CS along with LCAO with DFT-LDA, DFT-GGA, B3LYP and PBE0	Computed MP and CPs of AWO_4 (A= CO, Ni and Cu) using pure and hybrid DFT within LCAO schemes and analyzed by CP measurements at 0.34 a.u. momentum resolution. Also discussed the role of 3d electrons of Co/Ni/Cu in these compounds using equally normalized scale profiles.
Ahuja et al. [147]	CS and LCAO	Calculated energy bands, DOS, MP, VCDs, CPs, dielectric function, absorption coefficient and refractive index of A_2O_3 (A= Sc and Y) using LCAO and FP-LAPW schemes. These theoretical CPs have also been analyzed by experimental CPs at 0.34 momentum resolution.
Ahuja and Dashora [148]	CS and LCAO	Reported the basic aspects of CP measurements along with the data reduction part and discussed various applications in frame work of different compounds.

Sharma et al. [149]	CS, LCAO and FP-LAPW-mBJ	Undertook CP measurements of $AMoO_4$ (A = Zn and Cd) to interpret the LCAO based CP data. Also calculated accurate energy bands and DOS using FP-LAPW-mBJ along with the discussion of relative nature of bonding using CP and MP data in these compounds.
Bapna et al. [150]	XRD, XPS and UV spectra	Prepared nano particles of N-doped TiO_2 using sol-gel method and characterized by XRD, XPS and UV spectra measurements.
Sharma et al. [151]	XRD, XPS, VSM and MCS	Studied spin-dependent EMDs of $CoGa_xFe_{2-x}O_4$ (x = 0.2 and 0.3) at 8 K to see the effect of Ga doping in electronic and magnetic properties of the compositions.
Mund and Ahuja [152]	XRD, FTIR, RS and VSM	Synthesized 6 compositions of nano particles of $Co_{1-x}Mg_xFe_2O_4$ using sol-gel method and characterized by XRD, FTIR and RS. Also performed the magnetization measurements and reported the increase of MM with Mg doping at Co site.
Shan et al. [153]	PLD and SQUID	Synthesized NFO thin films of 40 and 450 nm thickness using PLD and analyzed magnon spin transport phenomena.
Mahmood et al. [154]	FP-LAPW with mBJ	Explored electronic, magnetic, optical and thermoelectric character of CFO using mBJ and PBESol potentials. Here, mBJ reports metallic character while PBESol led to the semiconducting nature of the compound.
Quintero et al. [155]	FP-LAPW-DFT with GGA and GGA+U	Presented theoretical investigations of ZFO in terms of MO, spin projected DOS, MM and hyperfine parameters.
Meena et al. [156]	CS and LCAO	Compared theoretical and experimental CPs of $BaTiO_3$ to compare various exchange-correlation potentials. The calculated energy bands and DOS confirmed the indirect semiconducting nature of the compound using B3PW scheme.
Meena et al. [157]	LCAO, B1WC and WC1LYP	Employed hybrid approximations (B1WC and WC1LYP) to compute MP and EMDs of AWO_4 (A = Co, Ni, Cu and Zn) and discussed the applicability of WC1LYP scheme. Also, explored the role of 3d electrons of Co/Ni/Cu/Zn in terms of equally normalized CPs and MP data.
Quintero et al. [158]	MS and FP-LAPW +lo with DFT-GGA	Approximated structural, electronic and magnetic properties along with the role of defects on the magnetic response of ZFO and described the hyperfine properties at Fe

		sites using MS measurements at 4 and 300 K.
Yaremiy et al. [159]	XRD	Prepared $NiCr_xFe_{2-x}O_4$ ($0 \leq x \leq 0.5$) nano particles using sol-gel auto-combustion method and reported the cubic phase of the compounds. Also reported the decrease in lattice parameter with increase of the Cr component in NFO at Fe site.
Meena et al. [160]	CS along with DFT-LDA/ GGA/ SOGGA and WC1LYP	Validated computed CPs (DFT with LDA, GGA and SOGGA along with WClLYP) with experimental CPs for $BaTiO_3$ and observed WC1LYP as a good approxi-mation among other considered approximations. Also, the semi-conducting nature is discussed through bands and DOS along with the relative trend of nature of bonding through MP data and EVED scale as $CaTiO_3 \rightarrow BaTiO_3 \rightarrow SrTiO_3$.
Meena et al. [161]	CS along with DFT-LDA/GGA /SOGGA and PBESOL0	Checked the performance of PBESOL0 scheme using CP measurements for Ag_2TMO_4 (TM = Cr and Mo). Also discussed energy bands, DOS, MP and EVED based CPs for semiconducting and bonding nature in these compounds.
Ikram et al. [162]	XRD, SEM, VSM and FTIR	Synthesized La^{+3} doped Ni-Zn-CFO nano-structured compounds using sol-gel combustion method and studied structure, magnetic and optical properties of the compounds using different experimental tools.
Dashora et al. [163]	MCS and SPR-KKR	Measured temperature dependent MCPs of $CoCr_{1.6}Fe_{0.4}O_4$ and $CoCrFeO_4$ using synchrotron radiations. Also calculated MCPs and band structure using Green function formalism.
Ghasemi et al. [164]	XRD, TEM, M-H measurements	Characterized the impact of Cu doping in CFO nano particles, which were prepared by co-precipitation method. Also reported the magnetic response and MM of the compounds.
Ulpe and Bredow [165]	DFT-GGA	Different GW approximations within many body perturbation theory are employed to calculate the band gap and optical spectra of ZFO to see the effect of cation distribution.

References

1. B.D. Cullity (Ed.), Elements of X-rays Diffraction, Addison Wesley Publication Company, 1978.

2. M. Birkholz, Thin Film Analysis by X-Ray Scattering, Wiley-VCH Weinheim, 2006.

3. C.D. Wagner, W.M. Riggs, L.E. Davis, J.F. Moulder, Handbook of X-ray Photoemission Spectroscopy, G.E. Muilenberg (Ed.), Perkin Elmer, Minnesota, USA, 1978.

4. C.N. Benwell, E.M. McCash, Fundamental of Molecular Spectroscopy, Tata McGraw Hill, 4th Edition, 1995.

5. A. Barone (Ed.), Principles and Applications of Superconducting Quantum Interference Devices, World Scientific Publishing 1992.

6. J.P. Wright, J.P. Attfield, P.G. Radaelli, Phys. Rev. Lett. 87 (2001) 266401-1–266401-4.

7. A.H. Compton, Phys. Rev. 21 (1923) 409–413; ibid Phys. Rev. 21 (1923) 483–502.

8. B.G. Williams, Compton Scattering, McGraw-Hill, London, 1977.

9. M.J. Cooper, Rep. Prog. Phys. 48 (1985) 415–481 and references therein.

10. M.J. Cooper, P.E. Mijnarends, N. Shiotani, N. Sakai, A. Bansil, X-ray Compton Scattering, Oxford Science Publications, Oxford University Press, New York, 2004 and references therein.

11. W. Schülke, Electron Dynamics by Inelastic X-ray Scattering, Oxford Science Publications, Oxford University Press, New York, 2007.

12. B.L. Ahuja (Ed.), Recent Trends in Radiation Physics Research, Himanshu Publications, New Delhi, India, 2010.

13. P. Eisenberger, W.A. Reed, Phys. Rev. B 9 (1974) 3237–3241.

14. F. Zhang, Y. Kitamoto, M. Abe, M. Naoe, J. Appl. Phys. 87 (2000) 6881–6883.

15. J.P. Wright, J.P. Attfield, P.G. Radaelli, Phys. Rev. Lett. 87 (2001) 266401-1–266401-4.

16. V.N. Antonov, B.N. Harmon, V.P. Antropov, A.Ya. Perlov, A.N. Yaresko, Phys. Rev. B 64 (2001) 134410-1–134410-12.

17. D.J. Singh, M. Gupta, R. Gupta, Phys. Rev. B 63 (2001) 205102-1–205102-5.

18. H.-T. Jeng, G.Y. Guo, J. Mag. Mag. Mat. 240 (2002) 436–438.

19. Y. Yamada, K. Kamazawa, Y. Tsunoda, Phys. Rev. B 66 (2002) 064401-1–064401-7.

20. A.M. El-Sayed, Ceram. Inter. 28 (2002) 651–655.

21. A.K. Nikumbh, A.V. Nagawade, G.S. Gugale, M.G. Chaskar, P.P. Bakare, J. Mater. Sci. 37 (2002) 637–647.

22. D.J. Singh, M. Gupta, R. Gupta, J. Appl. Phys. 91 (2002) 7370–7372.

23. Z. Szotek, W.M. Temmerman, A. Svane, L. Petit, G.M. Stocks, H. Winter, Phys. Rev. B 68 (2003) 054415-1–054415-9.

24. A.M. El-Sayed, Mater. Chem. Phys. 82 (2003) 583–587.

25. K. Kamazawa, Y. Tsunoda, H. Kadowaki, K. Kohn, Phys. Rev. B 68 (2003) 024412-1–024412-9.

26. V.N. Antonov, B.N. Harmon, A.N. Yaresko, Phys. Rev. B 67 (2003) 024417-1–024417-14.

27. K. Kamazawa, S. Park, S.-H. Lee, T.J. Sato, Y. Tsunoda, Phys. Rev. B 70 (2004) 024418-1–024418-5.

28. D.J. Huang, C.F. Chang, H.-T. Jeng, G.Y. Guo, H.-J. Lin, W.B. Wu, H.C. Ku, A. Fujimori, Y. Takahashi, C.T. Chen, Phys. Rev. Lett. 93 (2004) 077204-1–077204-4.

29. O.F. Caltun, J. Optoelectro. Adv. Mater. 6 (2004) 935–938.

30. L. Horng, G. Chern, M.C. Chen, P.C. Kang, D.S. Lee, J. Mag. Mag. Mat. 270 (2004) 389–396.

31. I. Leonov, A.N. Yaresko, V.N. Antonov, M.A. Korotin, V.I. Anisimov, Phys. Rev. Lett. 93 (2004) 146404-1–146404-4.

32. Y.C. Wang, J. Ding, J.B. Yi, B.H. Liu, T. Yu, Z.X. Shen, Appl. Phys. Lett. 84 (2004) 2596–2598.

33. A. Rais, A.M. Gismelseed, I.A. Al-Omari, Phys. Stat. Sol. (b) 242 (2005) 1497–1503.

34. A.M. Gismelseed, A.A. Yousif, Physica B 370 (2005) 215–222.

35. O.F. Caltun, J. Optoelectro. Adv. Mater. 7 (2005) 739–744.

36. G.K.H. Madsen, P. Novak, Europhys. Lett. 69 (2005) 777–783.

37. C. Cheng, Phys. Rev. B 71 (2005) 052401-1–052401-4.

38. U. Lüders, M. Bibes, J.-F. Bobo, M. Cantoni, R. Bertacco, J. Fontcuberta, Phys. Rev. B 71 (2005) 134419-1–134419-7.

39. M. Sorescua, L. Diamandescu, R. Swaminathan, M.E. McHenry, M. Feder, J. Appl. Phys. 97 (2005) 10G105-1–10G105-3.

40. R.N. Singh, J.P. Singh, B. Lal, M.J.K. Thomas, S. Bera, Electrochim. Acta 51 (2006) 5515–5523.

41. D.M. Phase, S. Tiwari, R. Prakash, A. Dubey, V.G. Sathe, R.J. Choudhary, J. Appl. Phys. 100 (2006) 123703-1–123703-5.

42. P. Piekarz, K. Parlinski, A.M. Oles, Phys. Rev. Lett. 97 (2006) 156402-1–156402-4.

43. L. Zhu, K.L. Yao, Z.L. Liu, Phys. Rev. B 74 (2006) 035409-1–035409-10.

44. R.S. Devan, Y.D. Kolekar, B.K. Chougule, J. Phys.: Condens. Matter 18 (2006) 9809–9821.

45. Z. Szotek, W.M. Temmerman, D. Ködderitzsch, A. Svane, L. Petit, H. Winter, Phys. Rev. B 74 (2006) 174431-1–174431-12.

46. S. Nakashima, K. Fujita, K. Tanaka, K. Hirao, T. Yamamoto, I. Tanaka, Phys. Rev. B 75 (2007) 174443-1–174443-8.

47. P. Piekarz, K. Parlinski, A.M. Oleś, Phys. Rev. B 76 (2007) 165124-1–165124-16.

48. H. Perron, T. Mellier, C. Domain, J. Roques, E. Simoni, R. Drot, H. Catlette, J. Phys.: Condens. Matter 19 (2007) 346219-1–346219-10.

49. S. Singhal, K. Chandra, J. Solid State Chem. 180 (2007) 296–300.

50. C.N. Chinnasamy, S.D. Yoon, A. Yang, A. Baraskar, C. Vittoria, V.G. Harris, J. App. Phys. 101 (2007) 09M517-1–09M517-3.

51. M.A.F. Ramalho, L. Gama, S.G. Antonio, C.O. Paiva-Santos, E.J. Miola, R.H.G.A. Kiminami, A.C.F.M. Costa, J. Mater. Sci. 42 (2007) 3603–3606.

52. S. Tiwari, R. Prakash, R.J. Choudhary, D.M. Phase, J. Phys. D: Appl. Phys. 40 (2007) 4943–4947.

53. S. Tiwari, R.J. Choudhary, R. Prakash, D.M. Phase, J. Phys.: Condens. Matter 19 (2007) 176002-1–176002-7.

54. S.D. Bhame, P.A. Joy, J. Phys. D: Appl. Phys. 40 (2007) 3263–3267.

55. K. Bharathi, K. Balamurugan, P.N. Santhosh, M. Pattabiraman, G. Markandeyulu, Phys. Rev. B 77 (2008) 172401-1–172401-4.

56. C. Cheng, Phys. Rev. B 78 (2008) 132403-1–132403-4.

57. C. Cheng, C.-S. Liu, J. Phys.: Conf. Ser. 145 (2009) 012028-1–012028-4.

58. D.C. Kulkarni, S.P. Patil, V. Puri, Microelect. J. 39 (2008) 248–252.

59. S. Winell, Ö. Amcoff, T. Ericsson, Phys. Stat. Sol. (b) 245 (2008) 1635–1640.

60. S. Tiwari, D.M. Phase, R.J. Choudhary, Appl. Phys. Lett. 93 (2008) 234108-1–234108-3.

61. M.A. Gabal, Y.M. Al Angari, Mater. Chem. Phys. 115 (2009) 578–584.

62. R.C. Kambale, P.A. Shaikh, S.S. Kamble, Y.D. Kolekar, J. Alloys Compounds 478 (2009) 599–603.

63. S. Tiwari, R.J. Choudhary, D.M. Phase, Thin Solid Films 517 (2009) 3253–3256.

64. D.R. Patil, B.K. Chougule, Mater. Chem. Phys. 117 (2009) 35–40.

65. A.D. Rowan, C.H. Patterson, L.V. Gasparov, Phys. Rev. B 79 (2009) 205103-1–205103-18.

66. K.K. Bharathi, J.A. Chelvane, G. Markandeyulu, J. Mag. Mag. Mat. 321 (2009) 3677–3680.

67. S.E. Shirsath, B.G. Toksha, K.M. Jadhav, Mater. Chem. Phys. 117 (2009) 163–168.

68. A.V. Ramos, S. Matzen, J. Moussy, F. Ott, M. Viret, Phys. Rev. B 79 (2009) 014401-1–014401-8.

69. G. Dixit, J.P. Singh, R.C. Srivastava, H.M. Agrawal, R.J. Choudhary, A. Gupta, Surf. Inter. Analysis 42 (2010) 151–156.

70. J. Jacob, M.A. Khadar, J. Appl. Phys. 107 (2010) 114310-1–114310-10.

71. D. Fritsch, C. Ederer, Phys. Rev. B 82 (2010) 104117-1–104117-11.

72. R. Datta, S. Kanuri, S.V. Karthik, D. Mazumdar, J.X. Ma, A. Gupta, Appl. Phys. Lett. 97 (2010) 071907-1–071907-3.

73. S. Anjum, G.H. Jaffari, A.K. Rumaiz, M.S. Rafique, S.I. Shah, J. Phys. D: Appl. Phys. 43 (2010) 265001-1–265001-7.

74. J.X. Ma, D. Mazumdar, G. Kim, H. Sato, N.Z. Bao, A. Gupta, J. Appl. Phys. 108 (2010) 063917-1–063917-5.

75. F. Zhou, G. Ceder, Phys. Rev. B 81 (2010) 205113-1–205113-6.

76. V.G. Ivanov, M.V. Abrashev, M.N. Iliev, M.M. Gospodinov, J. Meen, M.I. Aroyo, Phys. Rev. B 82 (2010) 024104-1–024104-8.

77. B.L. Ahuja, A. Dashora, N.L. Heda, S. Tiwari, N.E. Rajeevan, M. Itou, Y. Sakurai, R. Kumar, Appl. Phys. Lett. 97 (2010) 212502-1–212502-3.

78. J.A. Duffy, J.W. Taylor, S.B. Dugdale, C. Shenton-Taylor, M.W. Butchers, S.R. Giblin, M.J. Cooper, Y. Sakurai, M. Itou, Phys. Rev. B 81 (2010) 134424-1–134424-5.

79. S.M. Patange, S.E. Shirsath, K.S. Lohar, S.S. Jadhav, N. Kulkarni, K.M. Jadhav, Physica B 406 (2011) 663–668.

80. S.E. Shirsath, S.S. Jadhav, B.G. Toksha, S.M. Patange, K.M. Jadhav, J. Appl. Phys. 110 (2011) 013914-1–013914-8.

81. K.K. Bharathi, R.S. Vemuri, C.V. Ramana, Chem. Phys. Lett. 504 (2011) 202–205.

82. S. Soliman, A. Elfalaky, G.H. Fecher, C. Felser, Phys. Rev. B 83 (2011) 085205-1–085205-6.

83. G.D. Tang, D.H. Ji, Y.X. Yao, S.P. Liu, Z.Z. Li, W.H. Qi, Q.J. Han, X. Hou, D.L. Hou, Appl. Phys. Lett. 98 (2011) 072511-1–072511-3.

84. D. Fritsch, C. Ederer, Appl. Phys. Lett. 99 (2011) 081916-1–081916-3.

85. M.S.R. Prasad, B.B.V.S.V. Prasad, B. Rajesh, K.H. Rao, K.V. Ramesh, J. Mag. Mag. Mat. 323 (2011) 2115–2121.

86. M. Atif, M. Nadeem, R. Grössinger, R.S. Turtelli, J. Alloys Compounds 509 (2011) 5720–5724.

87. S. Noor, M.M. Rahman, S.S. Sikder, M.A. Hakim, Jahangirnagar Univ. J. Sci. 34 (2011) 1–11.

88. B.L. Ahuja, A. Dashora, N.L. Heda, S. Tiwari, R. Kumar, M. Itou, Y. Sakurai, AIP Conf. Proc. 1347 (2011) 202–205.

89. G. Choudhary, V. Raykar, S. Tiwari, A. Dashora, B.L. Ahuja, Phys. Stat. Sol. (b) 248 (2011) 212–219.

90. S. Tiwari, D.M. Phase, R.J. Choudhary, H.S. Mund, B.L. Ahuja, J. Appl. Phys. 109 (2011) 033911-1–033911-5.

91. B.L. Ahuja, S. Tiwari, A. Dashora, H.S. Mund, J. Sahariya, D.M. Phase, R.J. Choudhary, A. Banerjee, M. Itou, Y. Sakurai, Appl. Phys. Lett. 99 (2011) 062515-1–062515-3.

92. H.S. Mund, S. Tiwari, J. Sahariya, M. Itou, Y. Sakurai, B.L. Ahuja, J. Appl. Phys. 110 (2011) 073914-1–073914-4.

93. A. Raghunathan, D.C. Jiles, J.E. Synder, J. Appl. Phys. 109 (2011) 083922-1–083922-4.

94. K. Rama Krishna, D. Ravinder, K. Vijaya Kumar, C.A. Lincon, World J. Condens. Matter Phys. 2 (2012) 153–159.

95. D. Fritsch, C. Ederer, Phys. Rev. B 86 (2012) 014406-1–014406-10.

96. R.C. Rai, S. Wilser, M. Guminiak, B. Cai, M.L. Nakarmi, Appl. Phys. A 106 (2012) 207–211.

97. X. Yu, C.-F. Huo, Y.-W. Li, J. Wang, H. Jiao, Surf. Sci. 606 (2012) 872–879.

98. J. Singh, S.K. Gupta, A.K. Singh, P. Kothari, R.K. Kotnala, J. Akhtar, J. Mag. Mag. Mat. 324 (2012) 999–1005.

99. G. Dixit, J.P. Singh, R.C. Srivastava, H.M. Agrawal, R.J. Choudhary, Adv. Mater. Lett. 3 (2012) 21–28.

100. S.M. Patange, S.E. Shirsath, S.S. Jadhav, K.M. Jadhav, Phys. Stat. Sol. A 209 (2012) 347–352.

101. J. Li, Z. Yu, K. Sun, X. Jiang, Z. Xu, Z. Lan, J. Alloys Compounds 513 (2012) 606–609.

102. G.H. Jaffari, A.K. Rumaiz, J.C. Woicik, S.I. Shah, J. Appl. Phys. 111 (2012) 093906-1–093906-6.

103. S. Seifikar, A. Tabei, E. Sachet, T. Rawdanowicz, N. Bassiri-Gharb, J. Schwartz, J. Appl. Phys. 112 (2012) 063908-1–063908-6.

104. F.L. Zabotto, A.J. Gualdi, J.A. Eiras, A.J.A. de Oliveira, D. Garcia, Mater. Res. 15 (2012) 428–433.

105. Q.-C. Sun, H. Sims, D. Mazumdar, J.X. Ma, B.S. Holinsworth, K.R. O'Neal, G. Kim, W.H. Butler, A. Gupta, J.L. Musfeldt, Phys. Rev. B 86 (2012) 205106-1–205106-5.

106. S. Tiwari, R. Master, R.J. Choudhary, D.M. Phase, B.L. Ahuja, J. Appl. Phys. 111 (2012) 083905-1–083905-6.

107. B.L. Ahuja, H.S. Mund, S. Tiwari, J. Sahariya, A. Dashora, M. Itou, Y. Sakurai, Appl. Phys. Lett. 100 (2012) 132410-1–132410-4.

108. K.C. Bhamu, A. Dashora, G. Arora, B.L. Ahuja, Rad. Phys. Chem. 81 (2012) 728–734.

109. F.M Mohammed, A.M. Ghaleb, J. Sahariya, B.L. Ahuja, K.C. Bhamu, Nat. Sci. 4 (2012) 797–802.

110. N.M. Caffrey, D. Fritsch, T. Archer, S. Sanvito, C. Ederer, Phys. Rev. B 87 (2013) 024419-1–024419-7.

111. C.J. O'Brien, Z. Rák, D.W. Brenner, J. Phys.: Condens. Matter 25 (2013) 445008-1–445008-17.

112. R. Sharma, S. Singhal, Physica B 414 (2013) 83–90.

113. D. Varshney, K. Verma, Mater. Chem. Phys. 140 (2013) 412–418.

114. C. Himcinschi, I. Vrejoiu, G. Salvan, M. Fronk, A. Talkenberger, D.R.T. Zahn, D. Rafaja, J. Kortus, J. Appl. Phys. 113 (2013) 084101-1–084101-8.

115. C. Cheng, J. Mag. Mag. Mat. 325 (2013) 144–146.

116. A. Bengtson, D. Morgan, U. Becker, Phys. Rev. B 87 (2013) 155141-1–155141-13.

117. N.L. Heda, B.L. Ahuja, Comp. Mater. Sci. 72 (2013) 49–53.

118. B.L. Ahuja, P. Jain, J. Sahariya, N.L. Heda, P. Soni, J. Phys. Chem. A 117 (2013) 5685–5692.

119. S.F. Mohammed, F.M. Mohammed, J. Sahariya, H.S. Mund, K.C. Bhamu, B.L. Ahuja, App. Rad. Isotopes. 72 (2013) 64–67.

120. A. Dashora, J. Sahariya, R.J. Choudhary, D.M. Phase, M. Itou, Y. Sakurai, B.L. Ahuja, Appl. Phys. Lett. 102 (2013) 142403-1–142403-4.

121. H.S. Mund, J. Sahariya, R.J. Choudhary, D.M. Phase, A. Dashora, M. Itou, Y. Sakurai, B.L. Ahuja, Appl. Phys. Lett. 102 (2013) 232403-1–232403-4.

122. B.S. Holinsworth, D. Mazumdar, H. Sims. Q.-C. Sun, M.K. Yurtisigi, S.K. Sarker, A. Gupta, W.H. Bulter, J.L. Musfeldt, Appl. Phys. Lett. 103 (2013) 082406-1–082406-4.

123. S. Zhi-Feng, Q. Wei-Hua, J. Deng-Hui, X. Jing, T. Gui-De, Z. Xaio-Yun, L. Zhuang-Zhi, L. Li-Li, Chin. Phys. B 10 (2014) 107503-1–107503-10.

124. D. Odkhuu, P. Taivansaikhan, W.S. Yun, S.C. Hong, J. Appl. Phys. 115 (2014) 17A916-1–17A916-3.

125. S. Matzen, J.-B. Moussy, P. Wei, C. Gatel, J.C. Cezar, M.A. Arrio, P. Sainctavit, J.S. Moodera, Appl. Phys. Lett. 104 (2014) 182404-1–182404-5.

126. C.B.R. Jesus, E.C. Mendonça, L.S. Silva, W.S.D. Folly, C.T. Meneses, J.G.S. Duque, J. Mag. Mag. Mat. 350 (2014) 47–49.

127. L.L. Lang, J. Xu, W.H. Qi, Z.Z. Li, G.D. Tang, Z.F. Shang, X.Y. Zhang, L.Q. Wu, L.C. Xue, J. Appl. Phys. 116 (2014) 123901-1–123901-10.

128. C. Klewe, M. Meinert, A. Boehnke, K. Kuepper, E. Arenholz, A. Gupta, J.M. Schmalhorst, T. Kuschel, G. Reiss, J. Appl. Phys. 115 (2014) 123903-1–123903-7.

129. M. Meinert, G. Reiss, J. Phys.: Condens. Matter 26 (2014) 115503-1–115503-4.

130. N.L. Heda, A. Dashora, J. Sahariya, B.L. Ahuja, Solid State Phenomena 209 (2014) 156–159.

131. J. Sahariya, H.S. Mund, A. Sharma, A. Dashora, M. Itou, Y. Sakurai, B.L. Ahuja, J. Mag. Mag. Mat. 360 (2014) 113–117.

132. S. Sharma, J. Sahariya, G. Arora, B.L. Ahuja, Physica B 450 (2014) 25–29.

133. İ. Sabikoğlu, L. Parali, O. Malina, P. Novak, J. Kaslik, J. Tucek, J. Pechousek, J. Navarik, O. Schneeweiss, Prog. Nat. Sci.: Mater. Inter. 25 (2015) 215–221.

134. R. Masrour, E.K. Hlil, M. Hamedoun, A. Benyoussef, O. Mounkachi, H. El Moussaoui, J. Mag. Mag. Mat. 378 (2015) 37–40.

135. M. Hoppe, S. Döring, M. Gorgoi, S. Cramm, M. Muller, Phys. Rev. B 91 (2015) 054418-1–054418-7.

136. H. Zaari, A.G. El hachimi, A. Benyoussef, A. El Kenz, J. Mag. Mag. Mat. 393 (2015) 183–187.

137. N.L. Heda, U. Ahuja, Rad. Phys. Chem. 106 (2015) 33–39.

138. S. Sharma, N.L. Heda, K.K. Suthar, S. Bhatt, K. Sharma, B.L. Ahuja, Comp. Mater. Sci. 104 (2015) 205–211.

139. B.S. Meena, N.L. Heda, H.S. Mund, B.L. Ahuja, Rad. Phys. Chem. 117 (2015) 93–101.

140. K. Sharma, J. Sahariya, B.L. Ahuja, J. Alloys Compounds 645 (2015) 414–420.

141. N. Jahan, F. Chowdhury, A.K.M. Zakaria, Mater. Sci. Poland 34 (2016) 185–191.

142. U.-G. Jong, C.-J. Yu, Y.-S. Park, C.-S. Ri, Phys. Lett. A 380 (2016) 3302–3306.

143. J.J.M. Quintero, K.L.S. Rodríguez, G.A. Pasquevich, P.M. Zélis, S.J. Stewart, C.E.R. Torres, L.A. Errico, Hyperfine Interact. 63 (2016) 237-1–237-7.

144. S. Abdul Khader, S. Mohamed Shariff, N. Firdous, J. Basawaraja, H. Madanakumara, M.S. Thyagaraj, J. Chem. Pharm. Sci. 9 (2016) 993–997.

145. B.S. Meena, N.L. Heda, H.S. Mund, B.L. Ahuja, AIP Conf. Proc. 1731 (2016) 090016-1–090016-3.

146. B.S. Meena, N.L. Heda, K. Kumar, S. Bhatt, H.S. Mund, B.L. Ahuja, Physica B 484 (2016) 1–6.

147. B.L. Ahuja, S. Sharma, N.L. Heda, S. Tiwari, K. Kumar, B.S. Meena, S. Bhatt, J. Phys. Chem. Solids 92 (2016) 53–63.

148. B.L. Ahuja, A. Dashora, Compton Scattering, Reference Module in Materials Science and Materials Engineering. Oxford: Elsevier; 2016. pp. 1–8.

149. K. Sharma, H.S. Mund, K. Kumar, S. Talreja, B.L. Ahuja, Phys. Stat. Sol. (b) 253 (2016) 1743–1753.

150. K. Bapna, R.J. Choudhary, D.M. Phase, S. Shastri, R. Prasad, B.L. Ahuja, AIP Conf. Proc. 1728 (2016) 020462-1–020462-3.

151. A. Sharma, H.S. Mund, K. Bapna, S. Tiwari, M. Itou, Y. Sakurai, B.L. Ahuja, J. Mater. Sci. 52 (2017) 4568–4574.

152. H.S. Mund, B.L. Ahuja, Mater. Res. Bull. 85 (2017) 228–233.

153. J. Shan, A.V. Singh, L. Liang, L.J. Cornelissen, Z. Galazka, A. Gupta, B.J. van Wees, T. Kuschel, Appl. Phys. Lett. 113 (2018) 162403-1–162403-5.

154. Q. Mahmood, M. Yaseen, K.C. Bhamu, A. Mahmood, Y. Javed, S.M. Ramay, Chin. Phys. B 27 (2018) 037103-1-037103-8.

155. J.J.M. Quintero, C.E.R. Torres, L.A. Errico, J. Alloys Compounds 741 (2018) 746–755.

156. S.K. Meena, K. Bapna, N.L. Heda, B.L. Ahuja, AIP Conf. Proc. 1942 (2018) 090033-1–090033-4.

157. B.S. Meena, N.L. Heda, B.L. Ahuja, AIP Conf. Proc. 1953 (2018) 140135-1–140135-4.

158. J.J.M. Quintero, K.L.S. Rodríguez, C.E.R. Torres, L.A. Errico, J. Alloys Compounds 775 (2019) 1117–1128.

159. I.P. Yaremiy, V.S. Bushkova, N.I. Bushkov, S.I. Yaremiy, J. Nano Elect. Phys. 11 (2019) 04020-1–04020-8.

160. S.K. Meena, A. Dashora, N.L. Heda, B.L. Ahuja, Rad. Phys. Chem. 158 (2019) 46–52.

161. S.K. Meena, N.L. Heda, G. Arora, L. Meena, B.L. Ahuja, Physica B 560 (2019) 236–243.

162. S. Ikram, J. Jacob, M.I. Arshad, K. Mahmood, A. Ali, N. Sabir, N. Amin , S. Hussain, Ceram. Inter. 45 (2020) 3563–3569.

163. A. Dashora, M. Suthar, K. Kumar, R.J. Choudhary, H. Sakurai, N. Tsuji, Y. Sakurai, B.L. Ahuja, J. Alloys Compounds 824 (2020) 153883-1–153883-6.

164. R. Ghasemi, J. Echeverría, J.I. Pérez-Landazábal, J.J. Beato-Lopez, M. Naseri, C. Gómez-Polo, J. Mag. Mag. Mat. 499 (2020) 166201.

165. A. Ulpe, T. Bredow, Chem. Phys. Chem. 21 (2020) 1–7.

Chapter 2

Experimental Methodologies and Ab-initio Approximation

(i) Experimental methodologies

In the first part of the chapter, features about the various experimental techniques employed in present investigations, namely preparation of bulk samples using solid state reaction (SSR), thin film deposition using pulsed laser deposition (PLD), X-ray diffraction (XRD), X-ray photoemission spectroscopy (XPS), Raman spectroscopy (RS), superconducting quantum interference device-vibrating sample magnetometer (SQUID-VSM) and Fourier transform infrared (FTIR) spectroscopy are incorporated. Moreover, description of 100 mCi ^{241}Am and 20 Ci ^{137}Cs Compton spectrometer are also reported along with the data corrections to extract the true Compton profile (CP).

2.1. Preparation of Bulk Samples using Solid State Reaction Technique:

The SSR method has been employed to prepare the bulk samples namely $Ni_{1-x}Cr_xFe_2O_4$ (x= 0.00, 0.02 and 0.05) for the present thesis work. The advantages with SSR method are that we get the final product in a solid form with quite accurate structure and desired properties. For the sample preparation, the powders of high purity base materials (Fe_2O_3, NiO and Cr_2O_3) have firstly been mixed as per their stoichiometric ratio and desired composition through the agate mortar and pestle. Then, the muffle furnace is employed to heat the grinded mixture of each composition around 600-700 ºC in presence of air (calcination). Afterwards, the calcination process is further repeated two or three times. It is worth while mentioning that we have grinded the mixture after every process and temperature is also taken in higher side than that of the previous process. Here, the uniform and compact pellet is formed by sintering it at suitable high temperature as the composition, nature and properties of the desired composition depend on the high temperature and sintering time [1]. The data on these measurements are discussed in Chapter 3 and 5.

2.2. Pulsed Laser Deposition Technique for Thin Film Deposition:

We have used PLD technique for the thin film growth of $Ni_{1-x}Cr_xFe_2O_4$ (x= 0.02 and 0.05). It is worth mentioning that the thin film properties are quite different than that of bulk form and PLD is known as unique and powerful technique for thin film deposition [2]. The prepared bulk powder of $Ni_{1-x}Cr_xFe_2O_4$ (x= 0.02 and 0.05) were used for the thin film growth of both the compounds. In Fig. 2.1, we have shown the schematic diagram of PLD technique. It is to state that we have used the PLD experimental set-up at University Grant Commission (UGC)-Department of Atomic Energy (DAE)-Council for Scientific Research (CSR), Indore. Here, the pulsed laser beam (wave length = 248 nm and pulse width = 20 ns) from excimer laser source (KrF) is allowed to hit the target through the beam reflector, focusing lens and quartz window. The target was kept in a deposition chamber which is facilitated by rotating assembly and vacuum system. During the growth, the temperature and pressure of the substrate were 700 °C and $5x10^{-6}$ Torr, respectively. Here, the temperature was measured by the thermocouple, which was mounted on the backside of the substrate holder. It has been ensured that no other gas could pass in the chamber during the film growth. Further, the deposited film was cooled at same pressure. The data on these measurements are discussed in Chapter 3.

2.3. X-ray Diffraction:

It is known that XRD technique is most commonly used technique to characterize the structure of the samples i.e. crystal structure, lattice parameters, stress, strain, particle size, orientation in polycrystalline arrangement, etc. [3,4]. The theoretical aspects of XRD have already been discussed in Chapter 1. We have performed XRD measurements at UGC-DAE-CSR, Indore. In Fig. 2.2, we have shown the schematic diagram of XRD technique. The XRD measurements for thin films of $Ni_{1-x}Cr_xFe_2O_4$ (x= 0.02 and 0.05) and bulk $Ni_{1-x}Cr_xFe_2O_4$ (x= 0.00 and 0.05) were carried out using Brooker D2-Phaser with Cu-K_α source (wave length = 1.54184 Å) and θ–2θ geometry in the range of 20°–80°. The data on these measurements are discussed in Chapters 3 and 5.

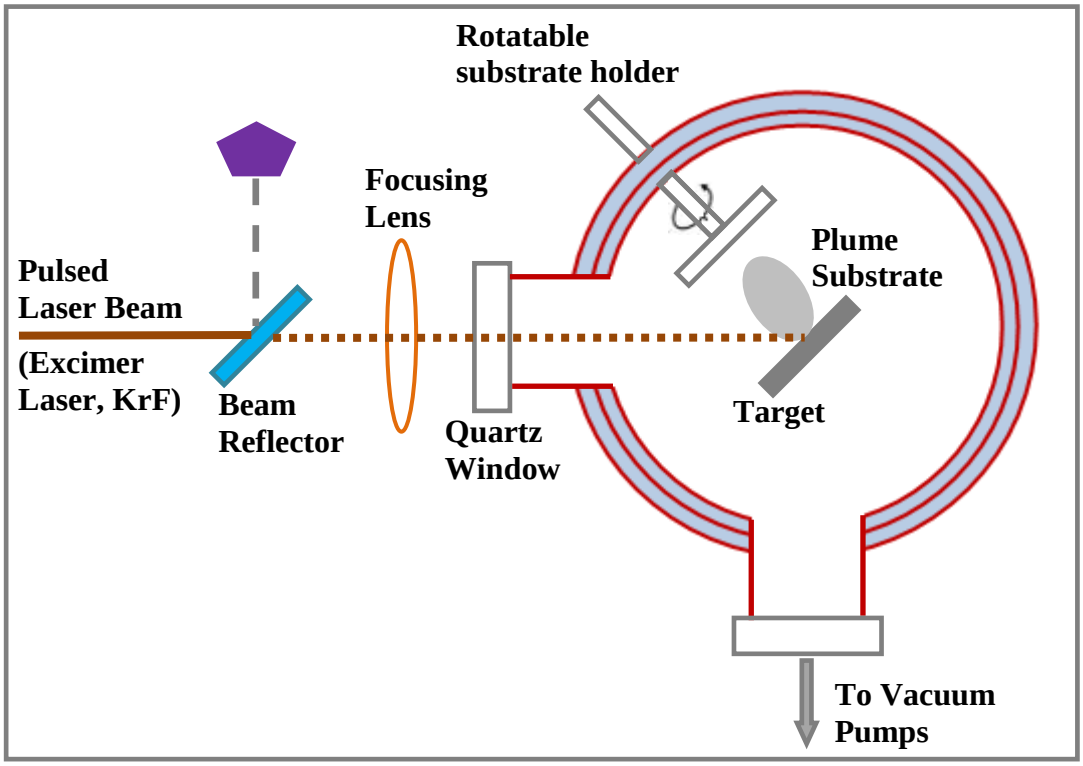

Fig. 2.1: Schematic diagram of pulsed laser deposition (PLD) technique.

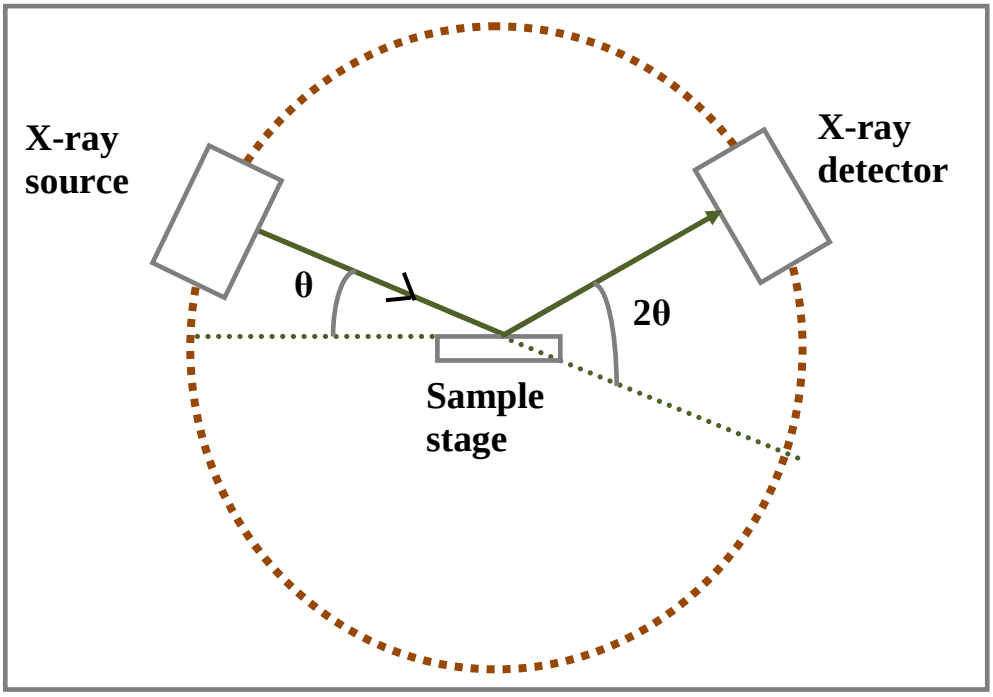

Fig. 2.2: Representative diagram of X-ray diffraction (XRD) technique.

2.4. X-ray Photoemission Spectroscopy:

It is known that XPS has been identified as a powerful tool to study the electronic and chemical states, composition of elements and empirical formula of the sample [5,6]. The theoretical aspects of XPS have already been reported in Chapter 1. The schematic diagram of XPS is reported in Fig. 2.3. We have performed XPS measurements for thin films of $Ni_{1-x}Cr_xFe_2O_4$ (x= 0.02 and 0.05) at UGC-DAE-CSR, Indore. The XPS measurements were undertaken using Omicron energy analyzer (EA 125, Germany) with Al-Kα source (energy = 1486.6 eV). Here, 1486.7 eV photons were employed to target the sample and the energy of ejected photoelectrons were analyzed by a combination of an electrostatic lens and an electrostatic hemispherical analyzer. A computer based data system is used to scan the electron energy and accumulates counts (detected electrons), which generates the photoelectron spectrum. The data on these measurements are discussed in Chapter 3.

2.5. Raman Spectroscopy:

It has been recognized that RS is used to measure molecular vibration to identify the sample along with the full characterization of element composition [7,8]. The theoretical details of RS have already been mentioned in Chapter 1. We have performed RS measurements for thin films of $Ni_{1-x}Cr_xFe_2O_4$ (x= 0.02 and 0.05) and bulk $Ni_{1-x}Cr_xFe_2O_4$ (x= 0.00 and 0.05) at UGC-DAE-CSR, Indore. Here, HR800 Jobin-Yvon spectrometer was employed to measure the Raman spectra at room temperature in backscattering configuration. The spectrometer has resolution of 1 cm^{-1} and 632.8 nm photon (He-Ne laser) were employed on the sample at a power of 9 mW. The data on these measurements are discussed in Chapters 3 and 5.

2.6. Superconducting Quantum Interference Device-Vibrating Sample Magnetometer:

We have used SQUID-VSM experimental set-up at UGC-DAE-CSR, Indore for M-T and M-H measurements of thin films ($Ni_{1-x}Cr_xFe_2O_4$; x= 0.02 and 0.05) and

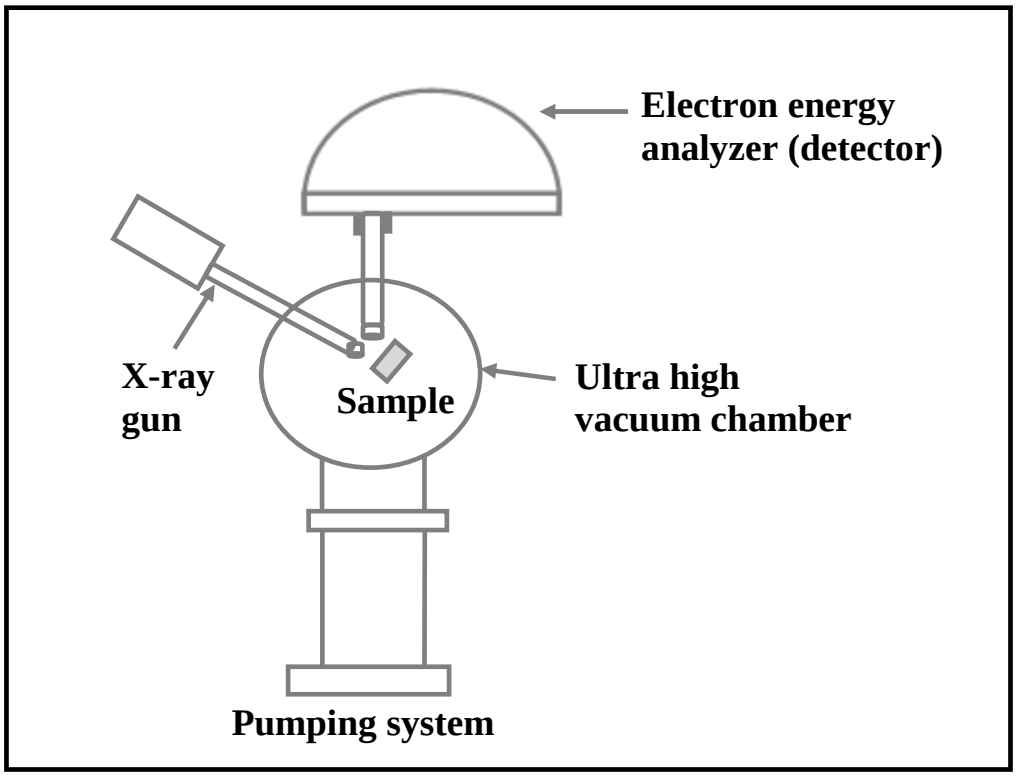

Fig. 2.3: Diagram of X-ray photoemission spectroscopy (XPS) technique.

bulk samples ($Ni_{1-x}Cr_xFe_2O_4$; x= 0.00 and 0.05). For this purpose, a commercial 7-Tesla SQUID-VSM (SVSM; Quantum Design Inc., USA) was employed. Here, SQUID consists of two superconductors which were separated by thin insulating layers for parallel Josephson junction formation. Further, the sample is also allowed to vibrate at a known frequency about the centre of the detection coils, which generates a SQUID signal [9]. The data on these measurements are discussed in Chapters 3 and 5.

2.7. Fourier Transform Infrared Spectroscopy:

It is worth while mentioning that FTIR measurements give us an infrared spectrum of emission, absorption, transmission and photoconductivity of the sample. It also provides information about the growth of the target on any substrate and the fingerprints of the chemical composition of the sample. We have performed FTIR measurement of thin films ($Ni_{1-x}Cr_xFe_2O_4$; x= 0.02 and 0.05) and bulk samples ($Ni_{1-x}Cr_xFe_2O_4$; x= 0.00 and 0.05) using Bruker model vertex 70 at UGC-DAE-CSR, Indore. The data on these measurements are discussed in Chapters 3 and 5.

2.8. 20 Ci ^{137}Cs Compton Spectrometer:

Despite the usual characterization measurements, we have employed first Indian 20 Ci ^{137}Cs Compton spectrometer [10,11] to measure the CP of Fe_3O_4, $NiFe_2O_4$, $ZnFe_2O_4$ and $CdFe_2O_4$. The spectrometer is available at M.L. Sukhadia University (MLSU), Udaipur. In Figs. 2.4 (a,b), we have shown the layout and respective laboratory view of the ^{137}Cs based spectrometer. The spectrometer can be divided into three essential parts as:

- **Scattering chamber:** The dimensions of the scattering chamber (left hand side of Fig. 2.4a) are 800 × 400 × 350 mm^3. This chamber contains sample holder, vacuum port for evacuation and window for scattering at 90^o. Here, the sample is placed vertically in the sample holder.
- **Source chamber:** The main components of the chamber are ^{137}Cs source, high purity germanium detector (HPGe) detector capsule and collimators. Here, the

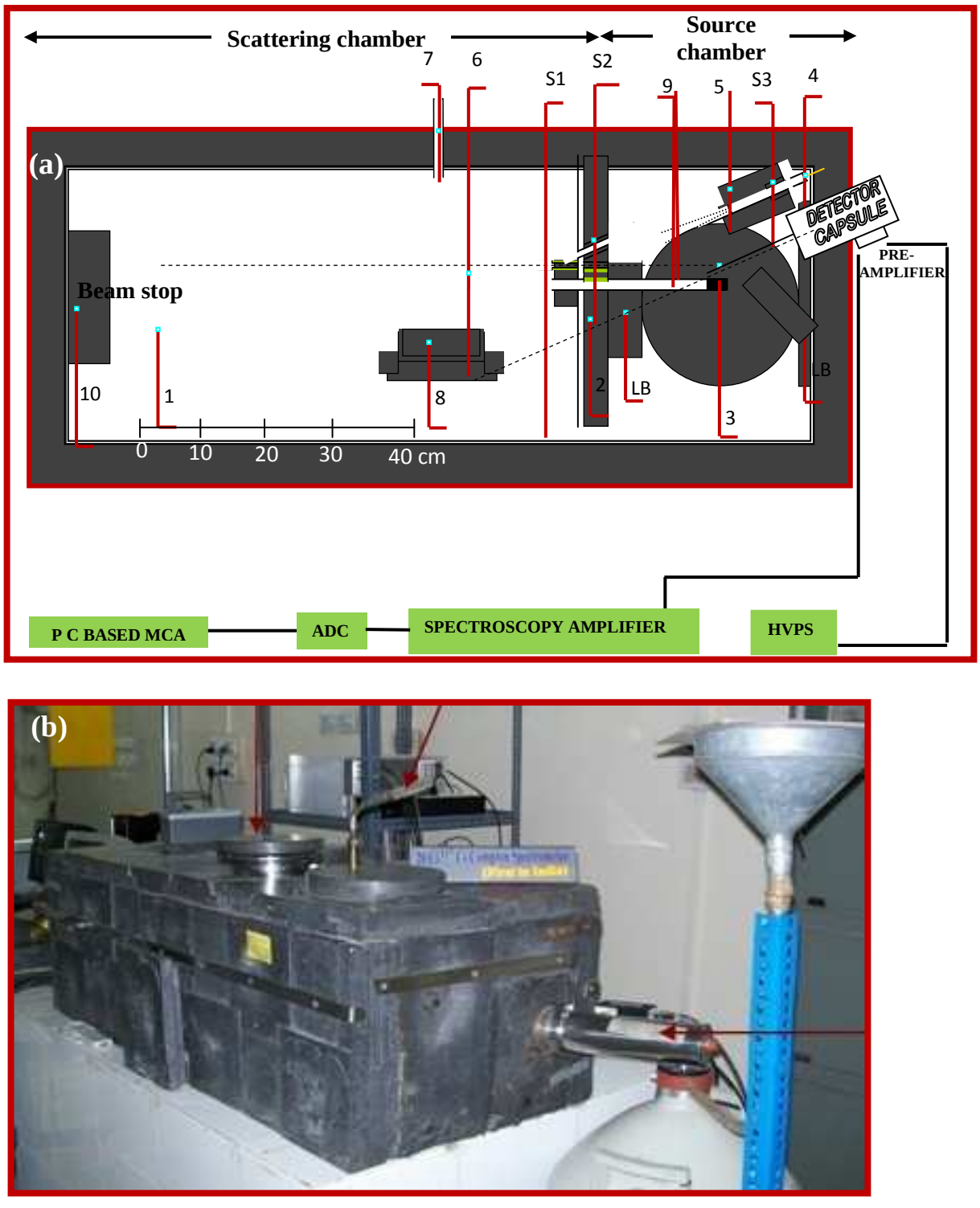

Fig. 2.4: (a) Layout of 20 Ci ^{137}Cs Compton spectrometer. (1)-Steel chamber 1150 x 350 × 400 mm; (2)-lead partition; (3)-^{137}Cs source; (4)-Solid state Ge detector crystal, (5)-detector collimator, (6)-sample; (7)-port for evacuation; (8)-additional window for scattering at 90º; (9)-volume seen by detector; (10)-beam dump. Collimating slits (S1, S2 and S3) and lead bricks (LB) are also shown. (b) Laboratory view of the spectrometer at M.L. Sukhadia University, Udaipur, as employed in the present work.

^{137}Cs-isotope is placed in a cylindrical lead block of 220 × 220 mm with source dimensions as 23.3 × 36.7 mm. The source-sample (so-sa), sample-detector (sa-de) and source-detector (so-de) distances in the geometry are 380, 548 and 238 mm, respectively where as the best possible scattering angle is $160^{o}\pm0.6^{o}$. Here, 10 mm and 500 mm^2 are the thickness and cross-sectional area of Ge crystal, respectively and the intrinsic characters of Ge crystal are maintained by cooling it at 77 K using liquid nitrogen environment.

- **Detection system:** This part contains pre-amplifier, high voltage power supply (HVPS), spectroscopy amplifier, analog-to-digital converter (ADC), multichannel analyser (MCA), etc. Here, −800 V bias is applied from HVPS to operate the detector.

In CP measurements, 661.65 keV photons are allowed to incident on sample and scattered photons were detected by HPGe detector. Now, these collated charge pulses are integrated and converted into voltage pluses by pre-amplifier and further amplification is done by spectroscopy amplifier. Further the digital conversion of these pluses is done by ADC and registered by MCA. Also, the stability of the experimental set-up is monitored from time-to-time by weak isotopes (^{57}Co and ^{133}Ba). The overall momentum resolution of 20 Ci ^{137}Cs Compton spectrometer is found to be 0.34 a.u. (full width at half maximum). In Fig. 2.5 (a-d), we have reported the measured raw data for Fe_3O_4, $NiFe_2O_4$, $ZnFe_2O_4$ and $CdFe_2O_4$, respectively which is further discussed in chapters 4-6.

2.9. 100 mCi ^{241}Am Compton Spectrometer:

In addition to the CP measurements by ^{137}Cs spectrometer, we have also employed first ever shortest geometry and lowest intensity based 100 mCi ^{241}Am Compton spectrometer [12,13] for the CP measurements of Fe_3O_4. In Fig. 2.6 (a,b), we have shown the layout and respective laboratory view of 100 mCi ^{241}Am Compton spectrometer. This spectrometer is available at MLSU, Udaipur. Here, the active diameter and length of the ^{241}Am radio-isotope are 4 and 1.2 mm, respectively, while the sample chamber is made by brass pipe with 300 mm length and 5 mm thickness. In the present set-up, the beam spot diameter at sample

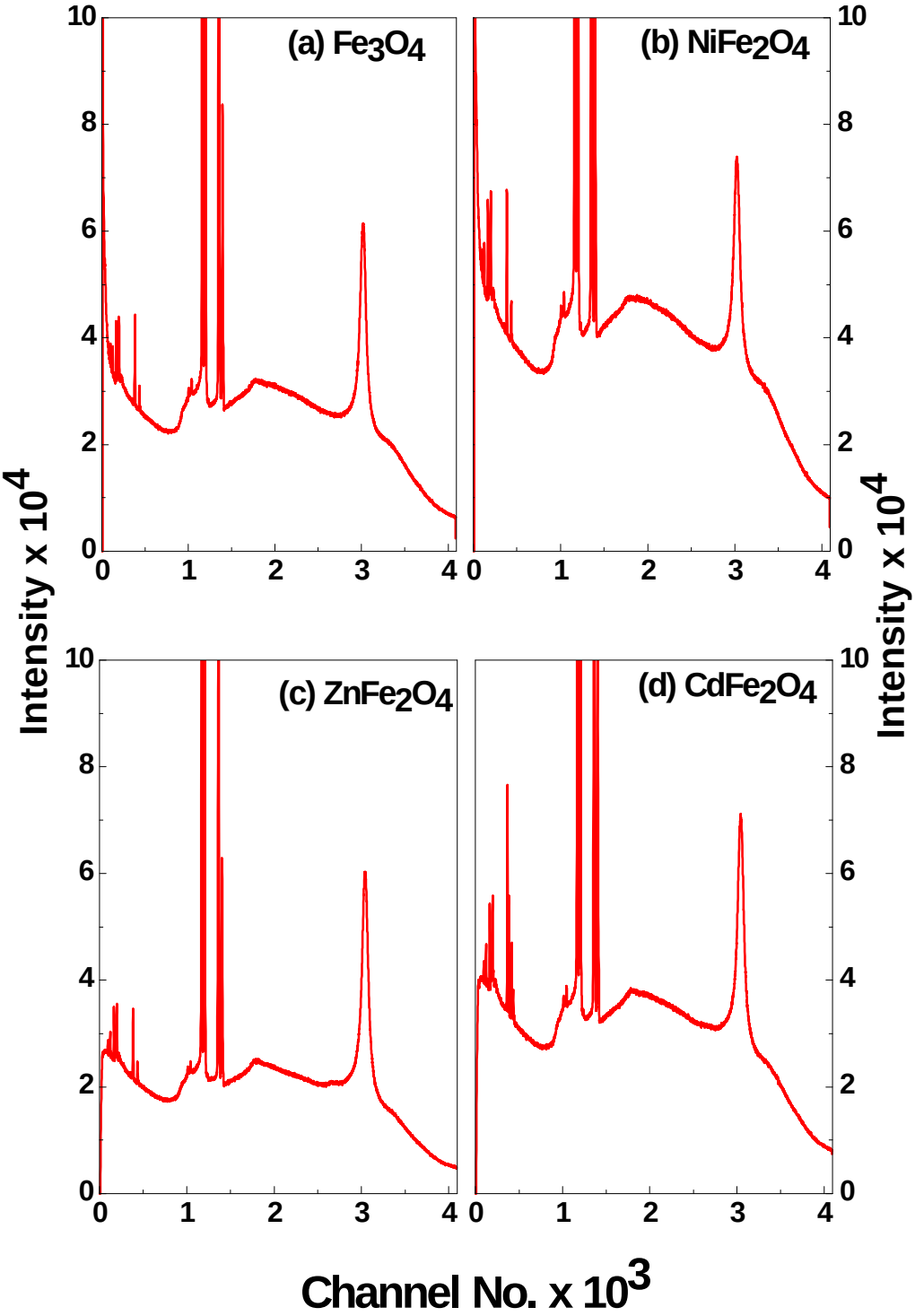

Fig. 2.5: Raw data for (a) Fe_3O_4, (b) $NiFe_2O_4$, (c) $ZnFe_2O_4$ and (d) $CdFe_2O_4$ as measured using 20 Ci ^{137}Cs Compton spectrometer. The peak towards right hand side is raw Compton profile.

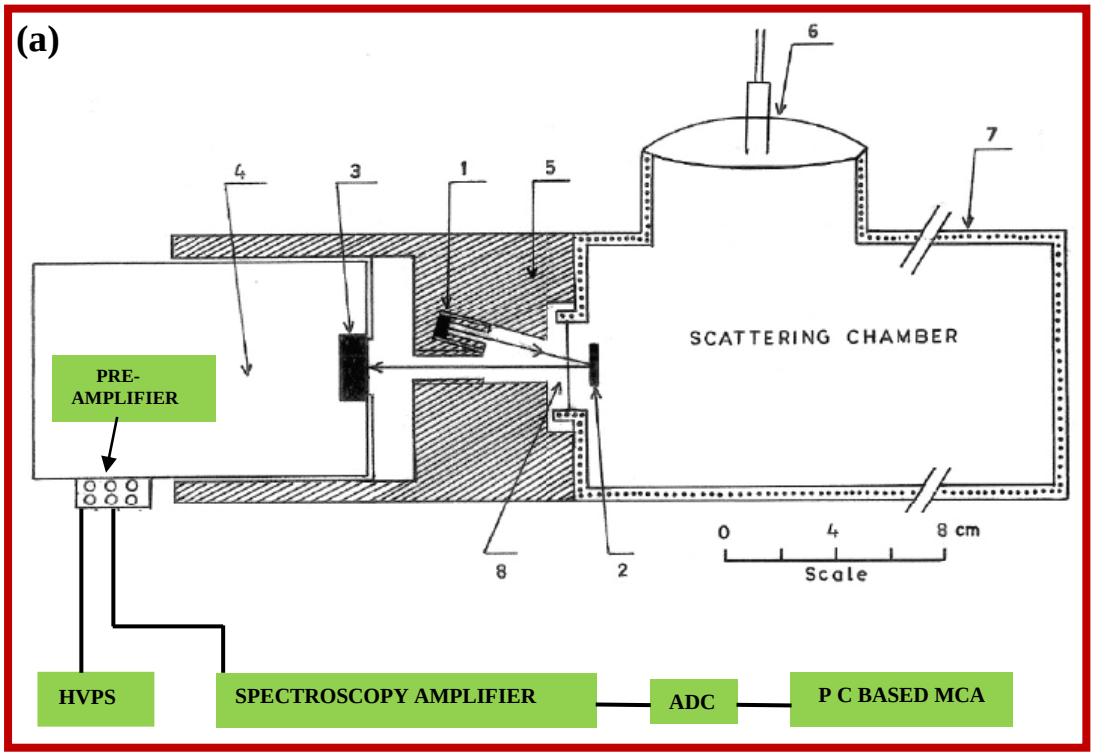

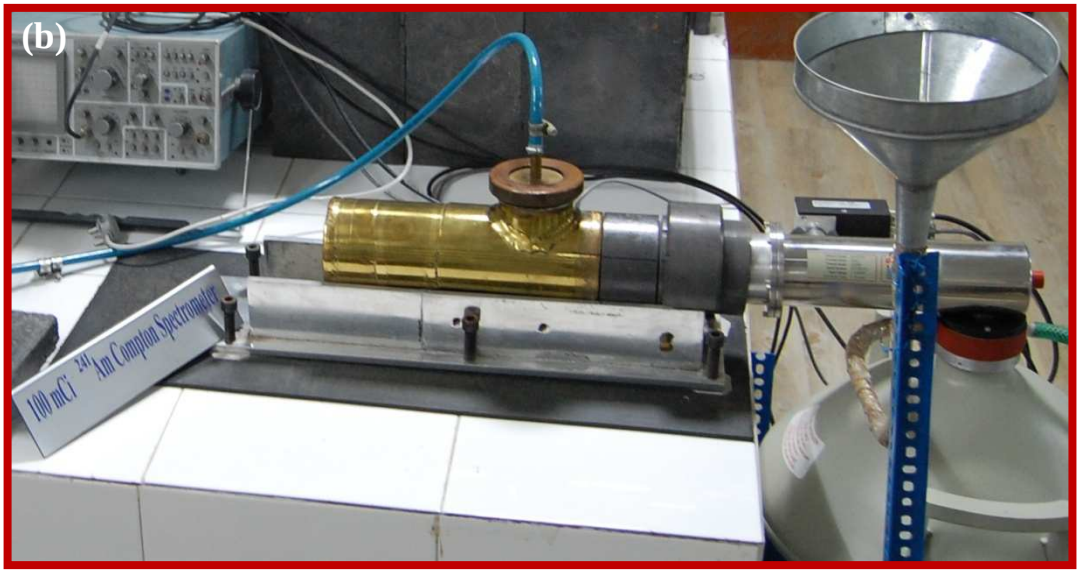

Fig. 2.6: (a) Layout of 100 mCi ^{241}Am Compton spectrometer. (1)-^{241}Am-isotope; (2)-sample position; (3)-Ge crystal; (4)-HPGe detector capsule; (5)-lead shielding around source and detector; (6)- port for evacuation connected to rotary oil pump; (7)-scattering chamber made of brass; and (8)-mylar foil (25 μm) to evacuate scattering chamber. (b) Laboratory view of the spectrometer at M.L. Sukhadia University, Udaipur.

position is 8 mm. For the CP measurements, 59.54 keV γ-rays are allowed to incident on the sample and scattered photons are collated at $165^{o}\pm1.5^{o}$ angle.
Here, so-sa, sa-de and so-de distances are 57, 88 and 36 mm, respectively while the overall momentum resolution is calculated as 0.55 a.u. (FWHM). During the measurements, the stability of the spectrometer is also monitored time-to-time by weak ^{241}Am source. The detection system was similar as 20 Ci ^{137}Cs spectrometer, except the cross-sectional area of Ge crystal, which is 200 mm^2. The raw data of Fe_3O_4 using ^{241}Am spectrometer is plotted in Fig. 2.7 and discussed in chapter 6.

2.10. Data Reduction to Obtain True Compton Profile:

The measured raw data from both spectrometers are processed for various data corrections to deduce the true CP [14,15]. In Fig. 2.8, we have reported a flow chart of different corrections required for the true CP calculations along with input and output files and the nomenclature of executive files as per the Timms et al. [14]. Briefly, the different corrections are as follow:

- **Background corrections**: The raw data is initially employed to remove the background contribution (BGC). The various factors for BGC are photons scattering from wall of scattering/source chamber, air within chamber, cosmic rays, mylar foil and ampoule in sample holder, etc. These contributions are measured by running the spectrometer without the sample and further subtracted from the measured sample (raw) data after proper point-by-point time scaling.
- **Partial deconvolution (tail stripping)**: HPGe detector does not perform the complete charge collections in the active region of the Ge crystal which results to the long tail in the low energy side [16]. The raw data needs to be corrected for removal of low energy tail to have a symmetric profile as suggested by Copper et al. [17].

Detector efficiency correction: We need to correct the profile by detector efficiency correction (DEC) because the probability of absorption of scattered photon in the detector decreases as the energy of incident photons increases. Usually, the efficiency is calculated as:

$$\text{Efficiency} = \frac{\text{Number of photons absorbed by the detector crystal}}{\text{Number of photons entered in the detector crystal}} \qquad (2.1)$$

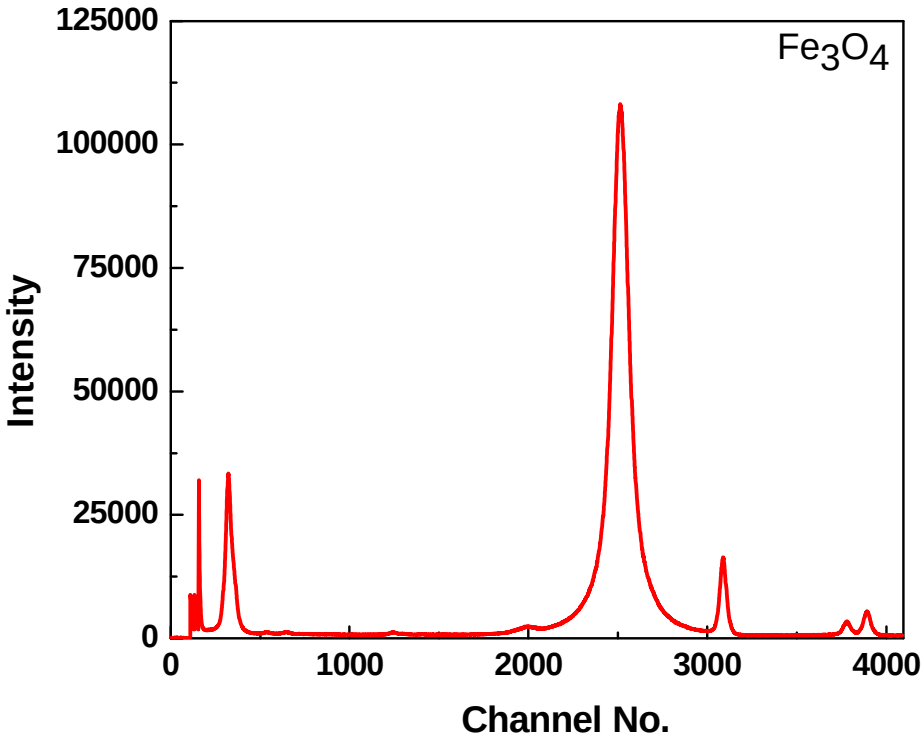

Fig. 2.7: Raw data for Fe_3O_4 using 100 mCi ^{241}Am Compton spectrometer. The broad and most intense peak is raw Compton profile.

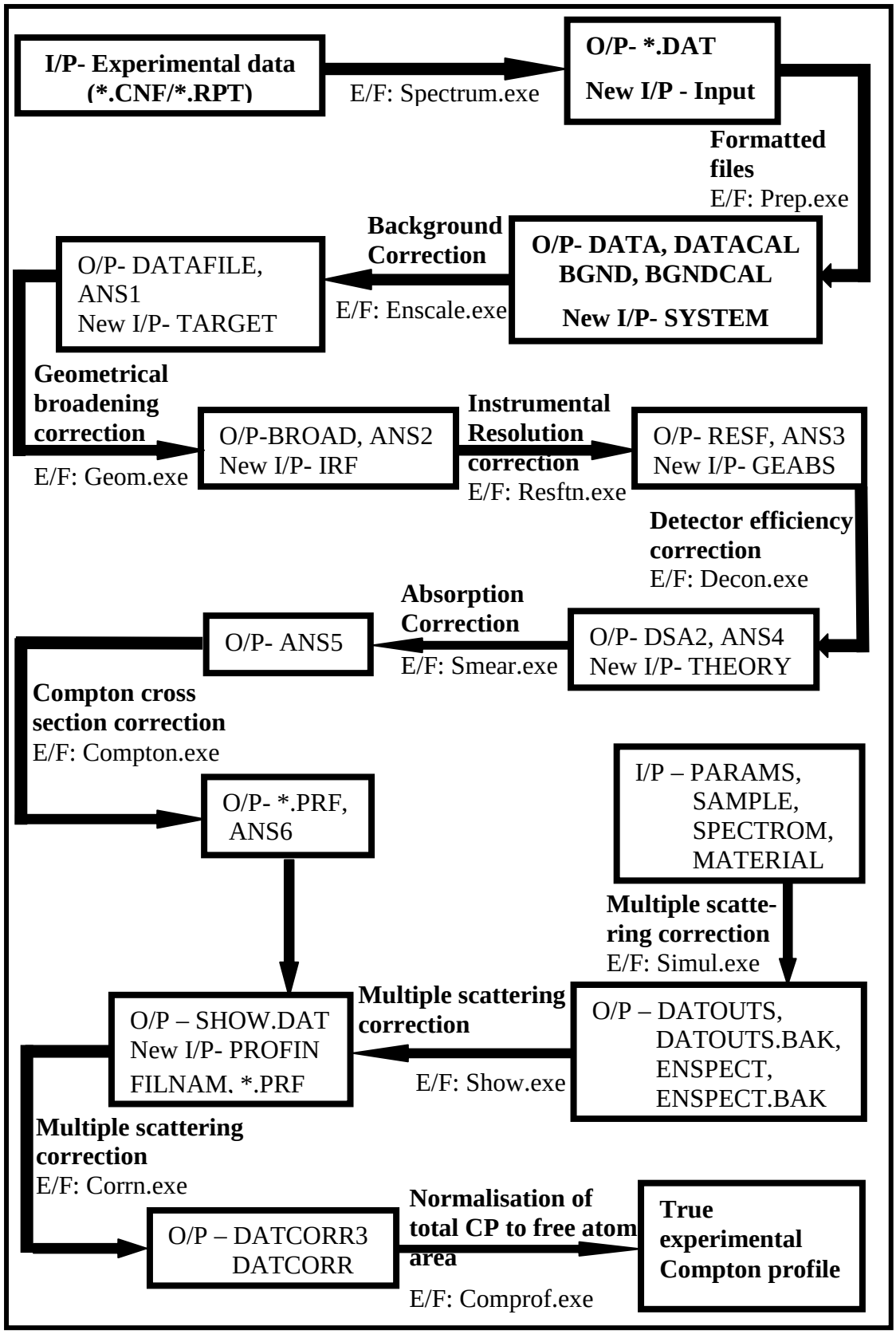

Fig. 2.8: Input (I/P) and output (O/P) files along with name of correction and corresponding executing file (E/F) for data corrections as facilitated in the data correction package.

Specially, the profile from ^{137}Cs (662 keV) spectrometer needs to be corrected by DEC. Needless to mention that the DEC is applicable for ^{137}Cs spectrometer data as the efficiency of detector is almost 100 % in case of ^{241}Am Compton spectrometer (due to scattered photon energy in the range 44-52 keV).

- **Sample absorption correction**: In the present measurements, the sample can absorb both kind of radiation (incident and scattered photons). Such absorption depends upon the energy and thickness of sample. Hence, we need to correct the profile by sample absorption correction (SAC). For the SAC, the data is multiplied by $A_{absorption}$, which is defined as [18,19]:

$$A_{absorption} = \frac{\left(\frac{\mu'}{\cos\alpha} + \frac{\mu''}{\cos\beta}\right)}{\left[1 - \exp\left\{-l\left(\frac{\mu'}{\cos\alpha} + \frac{\mu''}{\cos\beta}\right)\right\}\right]} \quad (2.2)$$

Here μ' and μ'' are linear absorption coefficients for incident and scattered radiations and α and β are the angles between sample face with incident and scattered radiations, respectively.

- **Compton cross-section correction**: Now, the data needs to be corrected for Compton cross-section correction (CCSC) as one measures the double differential Compton cross-section (DDCCS) [17]. As discussed in Chapter 1, we can calculate CP by using DDCCS [17,20] as:

$$\text{DDCCS} = \text{Proportionality Constant} \times \text{CP} \quad (2.3)$$

- **Compton profile in momentum scale**: After CCSC, the energy scale is converted into the momentum scale with the following relation as:

$$J(E_2)\Delta E_2 = J(p_z)\Delta p_z \quad (2.4)$$

here width in momentum scale (Δp_z) corresponds to channel width (ΔE_2).

- **Normalisation**: Now the CP in momentum scale is normalized to the corresponding free atom (FA) CP area using the CP data of Biggs et al. [21]. The normalisation is required to compare our experimental CP with the calculated or available theoretical or experimental CP data.

- **Multiple scattering correction**: Since, we need the CP from the singly contributed photons contribution only hence the CP needs to be further corrected by multiple scattering correction (MSC). For the MSC, we have used a computer

code based on Monte Carlo simulation as developed by Felsteiner et al. [22]. This code calculates the contribution of single, double and triple scattered photons. In Fig. 2.9, we have reported the contribution of single, double and triple scattered radiations for $NiFe_2O_4$ (NFO) with ^{137}Cs geometry.

To visualise the shape of the CP after the various corrections, we have shown the corrected CPs at different stages along with the raw and background data for NFO in Fig. 2.10.

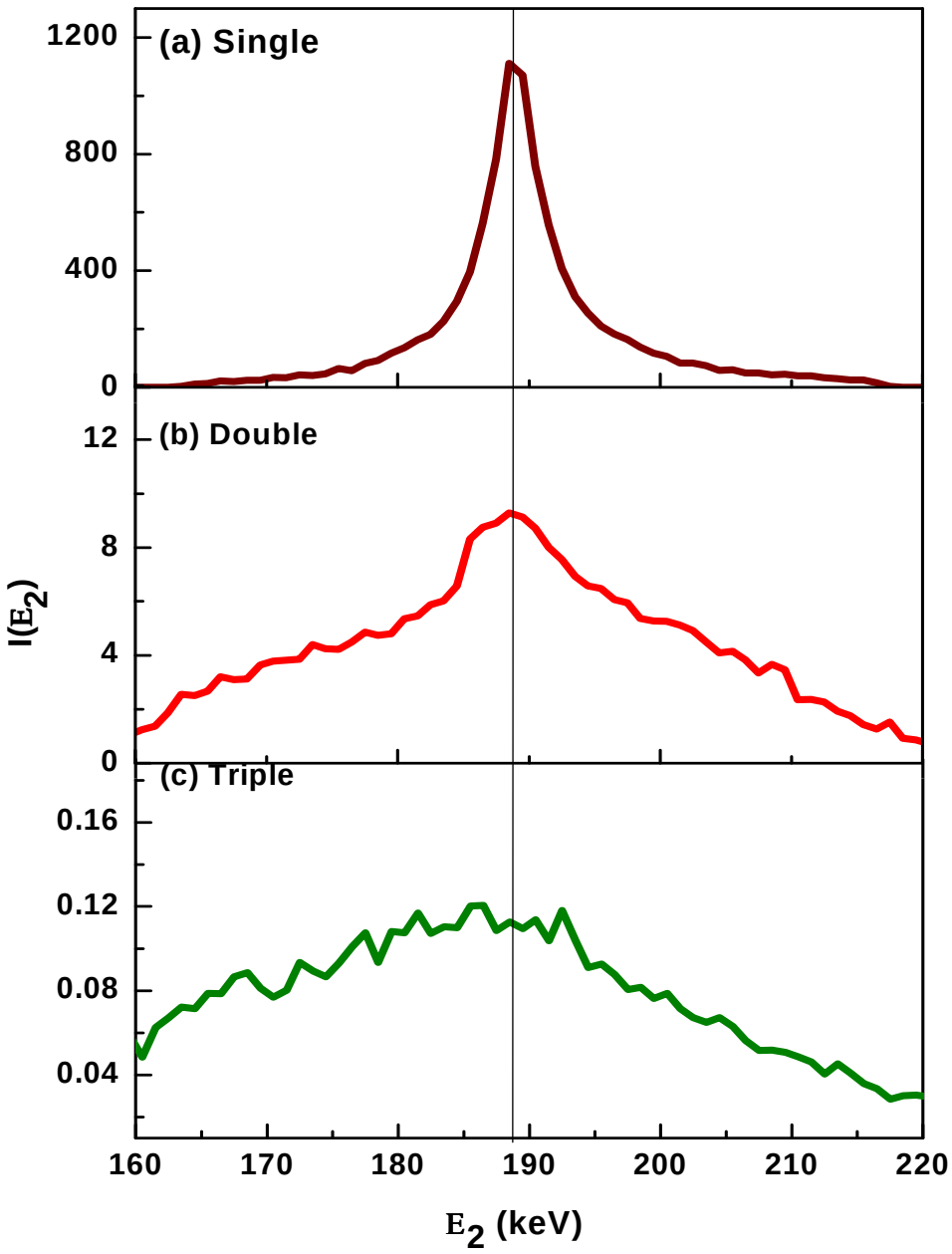

Fig. 2.9: Monte Carlo based (a) single (b) double and (c) triple scattered radiation spectra for $NiFe_2O_4$ (NFO) with ^{137}Cs geometry.

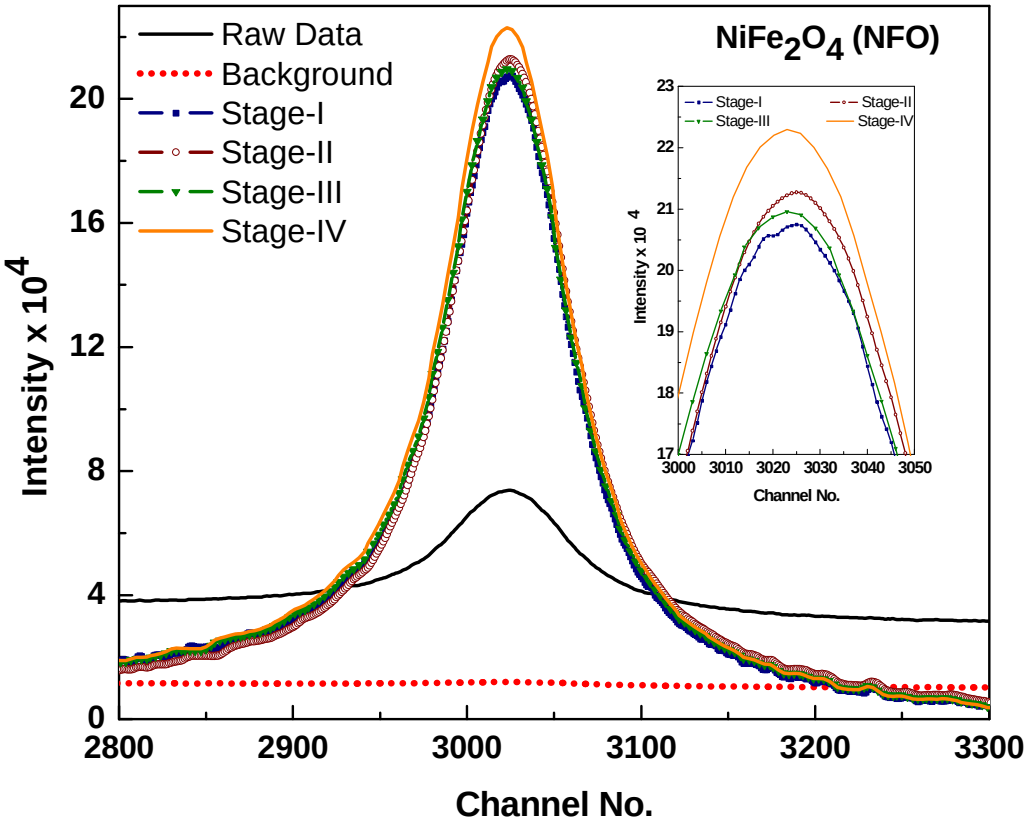

Fig. 2.10: Compton profile (CP) shape of $NiFe_2O_4$ (NFO) at different stages during data corrections as. Stage-I: CP after background correction (DATAFILE); Stage-II: CP after background, partial deconvolution and detector efficiency correction (DSA2); Stage-III: CP after background, partial deconvolution, detector efficiency, sample absorption and Compton cross-section correction (*.PRF) and Stage-IV: CP after background, partial deconvolution, detector efficiency, sample absorption, Compton cross-section and multiple scattering correction (DATCORR3). In inset, the amplified region near the peak is shown for clarity.

(ii) Ab-initio approximation

2.11. Linear Combination of Atomic Orbitals:

Linear combination of atomic orbitals (LCAO) approximations based CRYSTAL14 computer code [23] has been utilized to calculate the electronic properties of various ferrites (Fe_3O_4, $NiFe_2O_4$, $ZnFe_2O_4$ and $CdFe_2O_4$). Here, the calculations of Mulliken's population (MP), energy bands, partial and total density of states (DOS), isotropic and directional CPs and magnetic properties of the ferrites have been performed. In LCAO approximation, the key aim is to solve the Schrödinger equation to calculate the crystal wave function for individual particle as:

$$\hat{H}\,\Psi = E\Psi \tag{2.5}$$

here $\hat{H}$ is the Hamiltonian energy operator while the wave function and total energy are denoted by Ψ and E, respectively. Needless to mention that Ψ must follow the Bloch theorem as:

$$\Psi(\vec{r}+\vec{g}) = \Psi(\vec{r})\, e^{i\,\vec{k}.\vec{g}} \tag{2.6}$$

here $\vec{k}$ and $\vec{g}$ are the generating vector and crystal translation. Such electronic wave functions have been calculated by taking the linear combination of Bloch functions (BF) and BF are basically the linear combination of local functions. Here, the local functions are the linear combination of Gaussian type functions (GTF) for s, p, d and f electrons with coefficients (d_j) and exponents (α_j). The set of d_j and α_j are called the basis sets. It is worth mentioning that LCAO approximation has various options namely Hartree-Fock (HF), density functional theory (DFT), their hybridisation (HF+DFT) and pseudopotential (PP). These schemes are differentiable on the basis of the definition of $\hat{H}$. In case of HF/DFT, $\hat{H}$ is defined as:

$$\hat{H}^{HF/DFT} = \hat{T} + \hat{V} + \hat{J} + \hat{K}_X^{HF} / \hat{K}_{XC}^{DFT} \tag{2.7}$$

here first three terms ($\hat{T}, \hat{V}$ and $\hat{J}$) in the right hand side of Eq. 2.7 are corresponding to kinetic energy, external potential and Coulomb potential, respectively. While $\hat{K}_X^{HF}$ is the exact HF exchange operator i.e. HF approximation is free from the correlation effect. Since the real atoms always have certain

contributions of the correlation impact of electron hence wave function of HF scheme may not contain the proper symmetry during the interchanging of particles. Further, $\hat{K}_{XC}^{DFT}$ is the exchange correlation energy operator in DFT calculation and basically defined as the first order partial density derivative of exchange-correlation density functional energy (E_{XC}) as:

$$\hat{K}_{XC}^{DFT} = \frac{\partial E_{XC}[\rho(\vec{r})]}{\partial \rho(\vec{r})} \tag{2.8}$$

DFT schemes also have various options namely local density approximation (LDA), generalized gradient approximation (GGA) and the second order GGA (SOGGA). In these sub divisions, the E_{XC} is defined differently as:

$$E_{XC}^{DFT-LDA}[\rho(\vec{r})] = \int \rho(\vec{r}) \varepsilon_{xc}[\rho(\vec{r})] d\vec{r} \tag{2.9}$$

$$E_{XC}^{DFT-GGA}[\rho(\vec{r})] = \int \rho(\vec{r}) \varepsilon_{xc}[\rho(\vec{r}), |\nabla\rho(\vec{r})|] d\vec{r} \tag{2.10}$$

$$E_{XC}^{DFT-SOGGA}[\rho(\vec{r})] = \int \varepsilon_{XC}^{LDA}[r_s(\vec{r})] F_{XC}[r_s(\vec{r}), s(\vec{r})] d\vec{r} \tag{2.11}$$

here ε_{xc} is the exchange-correlation energy per particle for uniform electron gas and $\rho(\vec{r})$ is the electron density. In Eq. 2.11, the F_{XC} (r_s,s) is defined as:

$$F_{xc}(r_s, s) = F_x(s) + F_c(r_s, s) \tag{2.12}$$

where r_s and s are Wigner-Seitz radius and reduced density gradient, respectively. While F_x(s) within Perdew-Burke-Ernzerhof (PBE) [24] exchange potential for GGA is defined as:

$$F_x^{GGA}(s) = 1 + k - \frac{k^2}{k + \mu s^2} \tag{2.13}$$

and for SOGGA, the F_x(s) is given as [25],

$$F_x^{SOGGA}(s) = 1 + k - \frac{1}{2}\left(\frac{k^2}{k + \mu s^2}\right) - \frac{k}{2}\left(e^{-(\mu/k)s^2}\right) \tag{2.14}$$

In Eq. 2.13 and 2.14, μ and k are the constants. Further, the standard hybridized functions within CRYSTAL14 code [23] are named as B3LYP, B3PW, PBE0, PBESOL0, WC1LYP and B1WC. In these approximations, E_{XC} is defined as:

$$E_{XC}^{LCAO-B3LYP/B3PW} = 0.80 * E_X^{LDA} + 0.72 * \Delta E_X^{BECKE} + 0.20 * E_X^{HF} + 0.81 * E_C^{LYP/PWGGA} + 0.19 E_C^{VWN} \tag{2.15}$$

$$E_{XC}^{LCAO-PBE0/PBESol0} = 0.25 * E_X^{HF} + 0.75 * E_X^{PBE/PBESol} + E_C^{PBE/PBESol} \quad (2.16)$$

$$E_{XC}^{LCAO-WC1LYP/B1WC} = 0.16 * E_X^{HF} + 0.84 * E_X^{WC} + E_C^{LYP/PWGGA} \quad (2.17)$$

Here X and C stand for exchange and correlation parts, respectively. While the details of other keywords as mentioned in Eqns. 2.15-2.17 are reported in Table 2.1 [23-36]. The input for CRYSTAL14 can be divided input following four parts as,

- **Geometry Input:** This part of input is facilitated by the details of the geometrical input of the sample which includes space group, lattice parameters and atomic positions (individual) in the primitive cell. Here, we have not performed the geometrical optimization due to well defined geometrical inputs for Fe_3O_4, $NiFe_2O_4$, $ZnFe_2O_4$ and $CdFe_2O_4$.
- **Basis-sets Input:** This section of input contains the numerical values of d_j and α_j (basis sets) for s, p and d electrons. It is worth mentioning that the choice of basis sets may affect the results or level of accuracy. In the present thesis, we have considered the basis sets for individual constituent atoms and further optimized using BILLY software for Fe_3O_4, $NiFe_2O_4$, $ZnFe_2O_4$ and $CdFe_2O_4$ environment. The numerical values of the optimized basis sets are reported in the respective chapter. In present LCAO calculations, the linear combination of d_j and α_j are used to compute the wave functions as discussed earlier.
- **Hamiltonian and computational parameters Input:** This part of input section contains the possible exchange and correlation functionals, as incorporated in Table 2.1. In another words, we can say that this section dictates the nature of the approximations viz. HF or DFT within LDA/GGA/SOGGA or hybrid (HF+DFT). The inputs related to spin dependent calculations are also incorporated in this section.
- **Self-consistent field calculation Input:** This part of Input contains the details of the parameters for self-consistent field (SCF) calculations. The SCF calculation process is described in Fig. 2.11.

Table 2.1: Different exchange and correlation functionals available in CRYSTAL14 code.

(a) Exchange

Functional	Type	Keyword in CRYSTAL14	Reference
Dirac-Slater	LDA	LDA	Dovesi et al. [23]
von Barth-Hedin	LDA	VBH	von-Barth and Hedin [26]
Becke (1988)	GGA	BECKE	Becke [27]
Perdew-Burke-Ernzerhof (PBE) (1996)	GGA	PBE	Perdew et al. [24]
PBE functional revised for solids	GGA	PBESOL	Perdew et al. [28]
Perdew-Wang 91	GGA	PWGGA	Perdew et al. [29]
Second order GGA	GGA	SOGGA	Zhao and Truhlar [25]
Wu-Cohen	GGA	WCGGA	Wu and Cohen [30]

(b) Correlation

Functional	Type	Keyword in CRYSTAL14	Reference
Perdew-Zunger	LDA	PZ	Perdew and Zunger [31]
von Barth-Hedin	LDA	VBH	von-Barth and Hedin [26]
Vosko-Wilk-Nusair (1980)	LDA	VWN	Vosko et al. [32]
Lee-Yang-Parr (1988)	GGA	LYP	Lee et al. [33]
Perdew (1986)	GGA	P86	Perdew [34]
Perdew-Burke-Ernzerhof (1996)	GGA	PBE	Perdew et al. [24]
PBE functional revised for solids	GGA	PBESOL	Perdew et al. [28]
Perdew-Wang 91	GGA	PWGGA	Perdew et al. [29]
Perdew-Wang (1992)	LDA	PWLSD	Perdew and Wang [35]
Wilson-Levy	GGA	WL	Wilson and Levy [36]

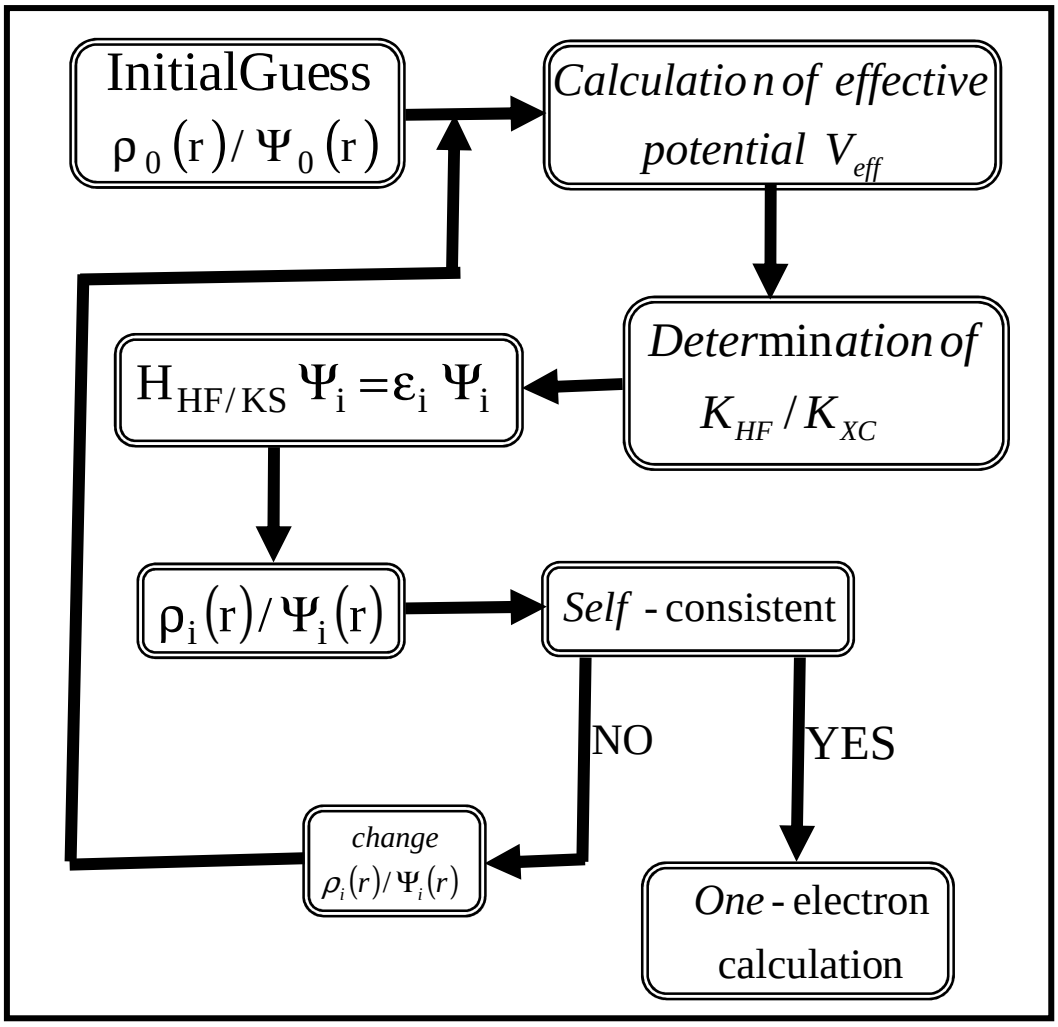

Fig. 2.11: The diagram for self consistent field (SCF) calculations process.

References

1. A.R. West, Solid State Chemistry and its Applications, John Wiley & Sons, Asia, 2003.

2. R. Eason (Ed.), Pulsed Laser Deposition of Thin Films, Wiley Inter Science, New Jersey, 2007.

3. B.D. Cullity (Ed.), Elements of X-ray Diffraction, Addison Wesley Publication Company, 1978.

4. M. Birkholz, Thin Film Analysis by X-Ray Scattering, Wiley-VCH Weinheim, 2006.

5. C.D. Wagner, W.M. Riggs, L.E. Davis, J.F. Moulder, Handbook of X-ray Photoemission Spectroscopy, G.E. Muilenberg (Ed.), Perkin Elmer, Minnesota, USA, 1978.

6. S. Huffner, Photoelectron Spectroscopy, Springer, Berlin, 1996.

7. E.N. Kaufmann, Characterization of Materials, John Wiley & Sons, 2003.

8. C.N. Benwell, E.M. McCash, Fundamental of Molecular Spectroscopy, Tata McGraw Hill, 4th addition, 1995.

9. Magnetic Property Measurement System SQUID-VSM, User's Manual, Quantum Design, USA, 2010.

10. B.L. Ahuja, M. Sharma, S. Mathur, Nucl. Instrum. Methods B 244 (2006) 419–426.

11. B.L. Ahuja, M. Sharma, Pramana-J. Phys. 65 (2005) 137–145.

12. B.L. Ahuja, N.L. Heda, Pramana-J. Phys. 68 (2007) 843–850.

13. B.L. Ahuja, V. Sharma, A. Rathor, A.R. Jani, B.K. Sharma, Nucl. Instrum. Methods B 262 (2007) 391–398.

14. D.N. Timms, Compton Scattering Studies of Spin and Momentum Densities (Ph.D. Thesis), University of Warwick, UK 1989 (unpublished).

15. B.G. Williams, Compton Scattering, McGraw Hill, New York, 1977.

16. R.C.H. Cheng, B.G. Williams, M.J. Cooper, Phil. Mag. 23 (1971) 115–133.

17. M.J. Cooper, P.E. Mijnarends, N. Shiotani, N. Sakai, A. Bansil, X-ray Compton Scattering, Oxford Science Publications, New York, 2004.

18. W.H. McMaster, G.N. KerrDel, J.H. Mallett, J.H. Hubble, Compilation of X-ray Cross Sections, Section I, Lawrence Radiation Laboratory, University of California, Livermore, USA, UCRL-50174, Sec. I, 1979.

19. J.A. Victoreen, J. Appl. Phys. 20 (1949) 1141–1147.

20. P. Eisenberger, W.A. Reed, Phys. Rev. B 9 (1973) 3237–3241.

21. F. Biggs, L.B. Mendelsohn, J.B. Mann, At. Data Nucl. Data Tables 16 (1975) 201–308.

22. J. Felsteiner, P. Pattison, M.J. Cooper, Phil. Mag. 30 (1974) 537–548.

23. R. Dovesi, V.R. Saunders, C. Roetti, R. Orlando, C.M. Zicovich-Wilson, F. Pascale, B. Civalleri, K. Doll, N.M. Harrison, I.J. Bush, Ph. D'Arco, M. Llunell, M. Causa, Y. Neol, CRYSTAL14 User's Manual, University of Torino, Torino, 2014, and references therein.

24. J.P. Perdew, K. Burke, M. Ernzerhof, Phys. Rev. Lett. 77 (1996) 3865–3868.

25. Y. Zhao, D.G. Truhlar, J. Chem. Phys. 128 (2008) 184109-1–184109-8.

26. U. von Barth, L. Hedin, J. Phys. C: Solid State Phys. 5 (1972) 1629–1642.

27. A.D. Becke, Phys. Rev. A 38 (1988) 3098–3100.

28. J.P. Perdew, A. Ruzsinszky, G.I. Csonka, O.A. Vydrov, G.E. Scuseria, L.A. Constantin, X. Zhou, K. Burke, Phys. Rev. Lett. 100 (2008) 136406-1–136406-4.

29. J.P. Perdew, J.A. Chevary, S.H. Vosko, K.A. Jackson, M.R. Pederson, D.J. Singh, C. Fiolhais, Phys. Rev. B 46 (1992) 6671–6686.

30. Z. Wu, R.E. Cohen, Phys. Rev. B 73 (2006) 235116-1–235116-6.

31. J.P. Perdew, A. Zunger, Phys. Rev. B 23 (1981) 5048–5079.

32. S.H. Vosko, L. Wilk, M. Nusair, Can. J. Phys. 58 (1980) 1200–1211.

33. C. Lee, W. Yang, R.G. Parr, Phys. Rev. B 37 (1988) 785–789.

34. J.P. Perdew, Phys. Rev. B 33 (1986) 8822–8824.

35. J.P. Perdew, Y. Wang, Phys. Rev. B 45 (1992) 13244–13249.

36. L.C. Wilson, M. Levy, Phys. Rev. B 41 (1990) 12930–12932.

Chapter 3

The Effect of Cr Substitution on the Structural, Electronic and Magnetic Properties of Pulsed Laser Deposited $NiFe_2O_4$ Thin Films

Based on:

Kalpana Panwar, S. Tiwari, K. Bapna, N.L. Heda, R.J. Choudhary, D.M. Phase, B.L. Ahuja, J. Mag. Mag. Mat. 421 (2017) 25-30

3.1. Introduction:

AFe_2O_4 ("A" being transition metal cation) based spinel ferrites have attracted tremendous attention among condensed matter physicists owing to their wide range of physical properties. Such ferrites have huge relevancies in contemporary technologies such as spintronics, high-density data storage, microwave absorption, catalysis, hydrogen production, batteries, magneto-caloric refrigeration, as magneto-strictive phase in multilayer magnetoelectric composites, etc. [1-6]. Besides these technological implications, these materials are also a source of abundant fundamental physics related to magnetization as well as catalytic properties. Among many spinel based ferrites, $NiFe_2O_4$ (NFO) has been widely studied because of the low eddy current loss, low magneto-striction and rather high Curie temperature which makes it suitable candidate for soft magnets and low loss materials at high frequency. To further extend its application domain, efforts are being made to modulate its structural, electrical and magnetic properties by doping of magnetic or non-magnetic impurity, where the dopant ions are expected to modify the exchange interaction among Ni and Fe ions of the host matrix [7-10]. NFO is mostly considered to be an inverse spinel structured ferrimagnetic material where the tetrahedral (A) sites are occupied by half of the Fe^{3+}cations, and the octahedral (B) sites are occupied by the rest of Fe^{3+} and Ni^{2+} ions. However, it has been found that in such spinel ferrites, the cationic distribution can deviate from perfect inverse spinel depending upon the growth parameters. It is to be noted that the magnetic moments of transition metal ions at the A and B sites interact antiferromagnetically, while the ions at the same site have a ferromagnetic interaction. It suggests that the magnetic property is immensely governed by the distribution of Ni and Fe ions at the A or B sites. Any alteration in distribution of these ions at these sites would hence affect the various functional magnetic features such as Curie temperature, saturation magnetization, magnetic anisotropy constant, coercivity, remanent magnetization, etc. [5-13].

Most of the previous studies are related to the nanoparticles of NFO, which show super paramagnetic behaviour [14-17]. However, for better prospects in devices, study on thin film based structure of NFO is crucial. In thin film form, the structure of these ferrites depends upon the technique used for deposition, type of

substrate, strain in the film, substrate temperature etc. [18-22]. Moreover, its integration with technologically important Si substrate will be a key to realize its relevance in device. In spite of this, there are few reports in literature related to growth and properties of NFO films on Si substrate [3,18,22]. However, there are large discrepancies regarding the cation distributions among the various sites and the observed magnetic moments in these reports.

In this chapter, which is also published by us in J. Mag. Mag. Mat. 421 (2017) 25-30, we present structural and magnetic study of effect of Cr doping in $NiFe_2O_4$ thin films on the same substrate with different orientation; Si (100) and Si (111).

3.2. Experiment:

The bulk target of $Ni_{1-x}Cr_xFe_2O_4$ (x = 0.02 and 0.05) (NCFO) in pellet form used for the deposition was synthesized by standard conventional solid state route. NCFO films were deposited on chemically cleaned Si (100) and Si (111) substrates using pulsed laser deposition (PLD) technique. As mentioned in chapter 2, KrF excimer laser source (λ =248 nm, pulse width = 20 ns) was used for growing the films. During growth, substrate temperature was kept at 700°C and base pressure was kept as the growth pressure. No addition gas was passed in the chamber. The temperature of the substrate was measured by thermocouple, mounted on the back side of the substrate holder. The substrate to target distance was fixed at 5 cm. The base pressure was kept to be $5x10^{-6}$ Torr. After the deposition, film was cooled under the same pressure. Thickness of the films was measured by Talystep profilometer and found to be ~ 70 nm. Further, as mentioned in chapter 2 also, θ-2θ X-ray diffraction (XRD) measurement was carried out using Brooker D2-Phaser with Cu-K_α source. Fourier transform infrared spectroscopy (FTIR) measurement was performed using Bruker model vertex 70. X-ray photoemission spectroscopy (XPS) was performed using Omicron energy analyzer (EA 125, Germany) with Al-K_α lab source (hν=1486.6 eV). Raman spectroscopy consisting of 200mW Ar- laser (488nm) was also used to characterise the films. Magnetization measurements as a function of temperature and magnetic field were carried out by employing a commercial 7-

Tesla SQUID-vibrating sample magnetometer (SVSM; Quantum Design Inc., USA).

3.3. Results and Discussion:

In Fig. 3.1, we show the XRD patterns of $Ni_{1-x}Cr_xFe_2O_4$ (x = 0.02 and 0.05) films grown on Si (100) and Si (111) substrates. Mainly three intense peaks are observed which correspond to planes of $NiFe_2O_4$ structure as reported in PCPDF card (PCPDF No – 862267), while other remaining peaks match well with the Si substrates. Here, if we compare the growth of Cr doped NFO on Si substrates with the growth of magnetite (Fe_3O_4) which also has a cubic inverse spinel structure consisting of Fe^{2+} and Fe^{3+} ions, it turns out that the growth nature of NCFO films are different than that of Fe_3O_4. Fe_3O_4 grows along [111] direction irrespective of the choice of orientation of Si substrate [18] whereas, in the present case, of NCFO films, it turns out to be a polycrystalline growth of the films on both orientations of Si substrate. Further, when we compare the patterns of films on Si (100) and Si (111) substrates, it is revealed that for both the doping concentrations, full width at half maxima (FWHM) of the peaks is smaller for the films grown on Si (111) substrate than that of Si (100), suggesting larger grain size in films grown on Si (111) than the corresponding films on Si (100). FWHM values given in Table 3.1 correspond to the most intense peak (111) in θ-2θ scan lying between 18° to 19° as shown in inset of Fig. 3.1.

After confirmation of phase, we calculated the grain size (D) of the films by following the Debye-Scherrer formula,

$$D = 0.94 \times \lambda/(B \cos\theta) \quad (3.1)$$

where, λ is the wavelength of the x-ray source and B is the FWHM of individual peak at 2θ (where θ is Bragg angle). Lattice strain (T) in the material also causes broadening of diffraction peak, which can be represented by the relationship

$$T \tan\theta = (\lambda / D \cos\theta) - B \quad (3.2)$$

Various XRD based parameters for the present films are given in Table 3.1. Consequently, it is revealed that grain size decreases with Cr doping for films on both the substrates. It is also observed that films deposited on Si (111) substrate

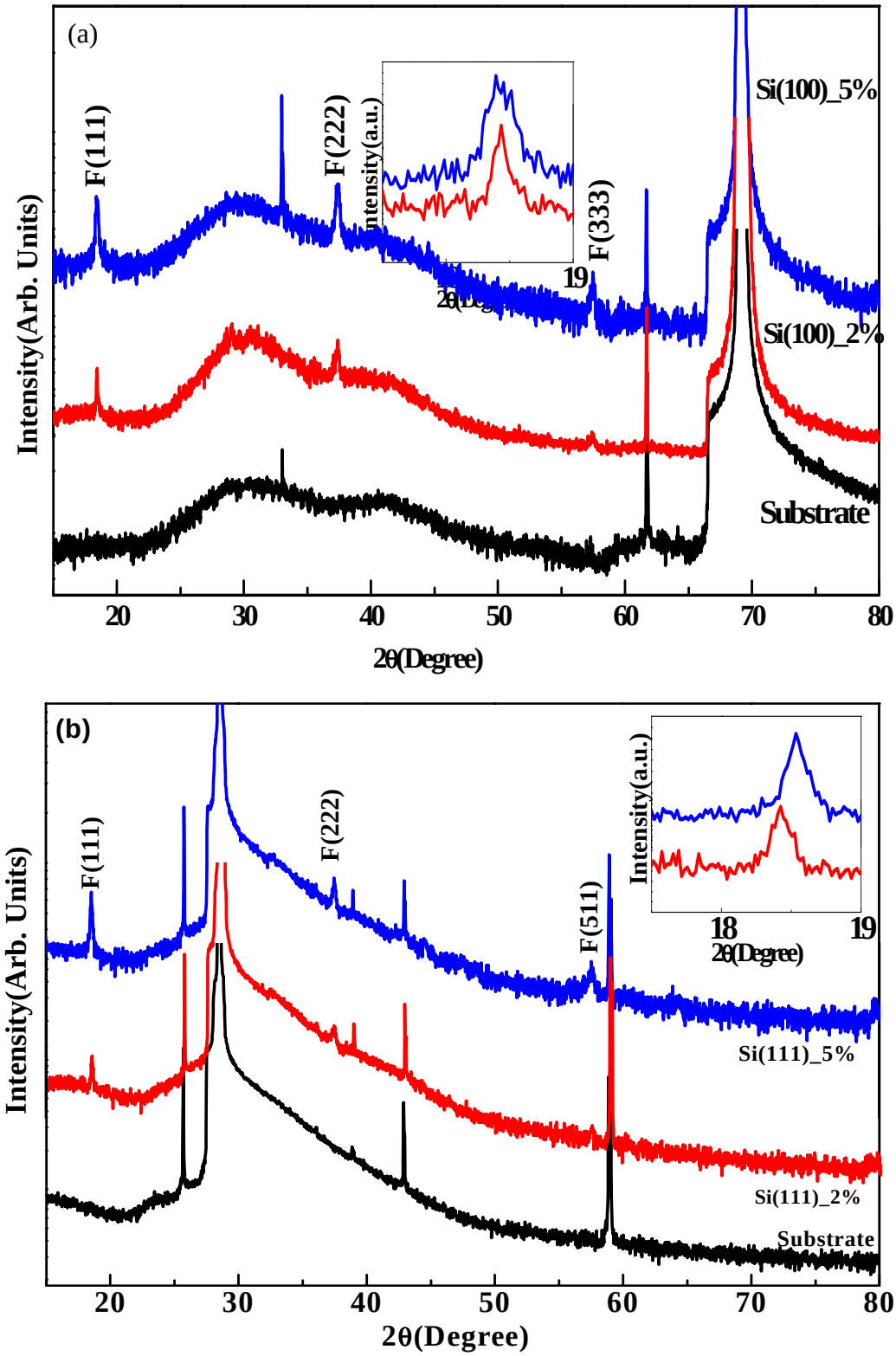

Fig. 3.1: The XRD patterns of $Ni_{1-x}Cr_xFe_2O_4$ (x = 0.02 and 0.05) films grown on (a) Si (100) and (b) Si (111) substrates along with those of the bare substrates. Here F corresponds to the peaks arising from the film. The inset shows a zoomed view of the most intense film peak (111).

Table 3.1: XRD method based lattice parameters and other parameters of Cr doped $Ni_{1-x}Cr_xFe_2O_4$ (x = 0.02, 0.05) films grown on Si (111) and Si (100) substrates.

Substrate	**Doping % (x)**	**Lattice constant (Å) (±0.003)**	**FWHM (degree)**	**Grain size (Å)**	**Strain**
Si(100)	0.02	8.330	0.43	324	5×10^{-3}
Si(111)	0.02	8.325	0.22	425	3.4×10^{-3}
Si(100)	0.05	8.345	0.91	167	12×10^{-3}
Si(111)	0.05	8.330	0.20	293	5.7×10^{-3}

for both the doping concentration reveal larger grain size value than the respective films grown on Si (100) substrate.

We shall like to mention here that initially we tried to deposit the films at lower temperature also, but single phase was not observed. We could get the single phase of $NiFe_2O_4$ (undoped as well as doped) at 700 °C only. Substrate temperature is used to provide sufficient kinetic energy to the adsorbent atoms/ions so that they can diffuse at the substrate surface and get into a crystalline form with the required phase.

To find out the thickness of the films, we have performed x-ray reflectivity (XRR) measurement. As an example, the XRR patterns of 2% Cr doped NFO film on Si (111) substrate is shown in inset of Fig. 3.2. After fitting the spectra, thickness of the film was calculated to be ~ 67 nm. Similar spectra were observed for the other films also. To re-confirm the structure of the films, we have also undertaken FTIR spectroscopy measurements. NFO has a cubic inverse spinel structure, and the full unit cell contains 56 atoms, but the smallest Bravais cell contains only 14 atoms. As a result, one should expect 39 (3N-3) vibrational modes. From group theory, considering the space group O_h^7 (Fd3m) one can predict the following modes within irreducible representation [3].

$$\Gamma = A_{1g}(R) + E_g(R) + T_{1g}(in) + 3T_{2g}(R) + 2A_{2u}(in) + 2E_u(in) + 4T_{1u}(IR) + 2T_{2u}(in) \quad (3.3)$$

Among these modes A_{1g}, E_g, $3T_{2g}$ are Raman active modes and only T_{1u} type vibrations are infrared active modes. Other modes T_{1g}, A_{2u}, E_u and T_{2u} are silent. In four infrared spectral bands, first two bands 560-630 cm^{-1} and 390-525 cm^{-1} are assigned to vibration of the tetrahedron and octahedron sublattices, respectively [3]. FTIR spectra of NCFO films on Si (100) and Si (111) substrates are shown in Fig. 3.2. The observed mode positions match well with the predicted vibrational modes, which further confirm the growth of NFO phase on both the substrates. From Fig. 3.2, it appears that there are two IR active modes at 561 cm^{-1} and 610 cm^{-1}. These bands are in tetrahedral region and represent Fe-O bond at tetrahedral site. A hump like feature is also seen at ~ 500 cm^{-1}, which is assigned to octahedral metal stretching vibration. The intense absorption band observed around ~ 610 cm^{-1} occurs due to proportional distribution of metal ions at A and B sites, which is generally expected for the inverse spinel structure. However, with

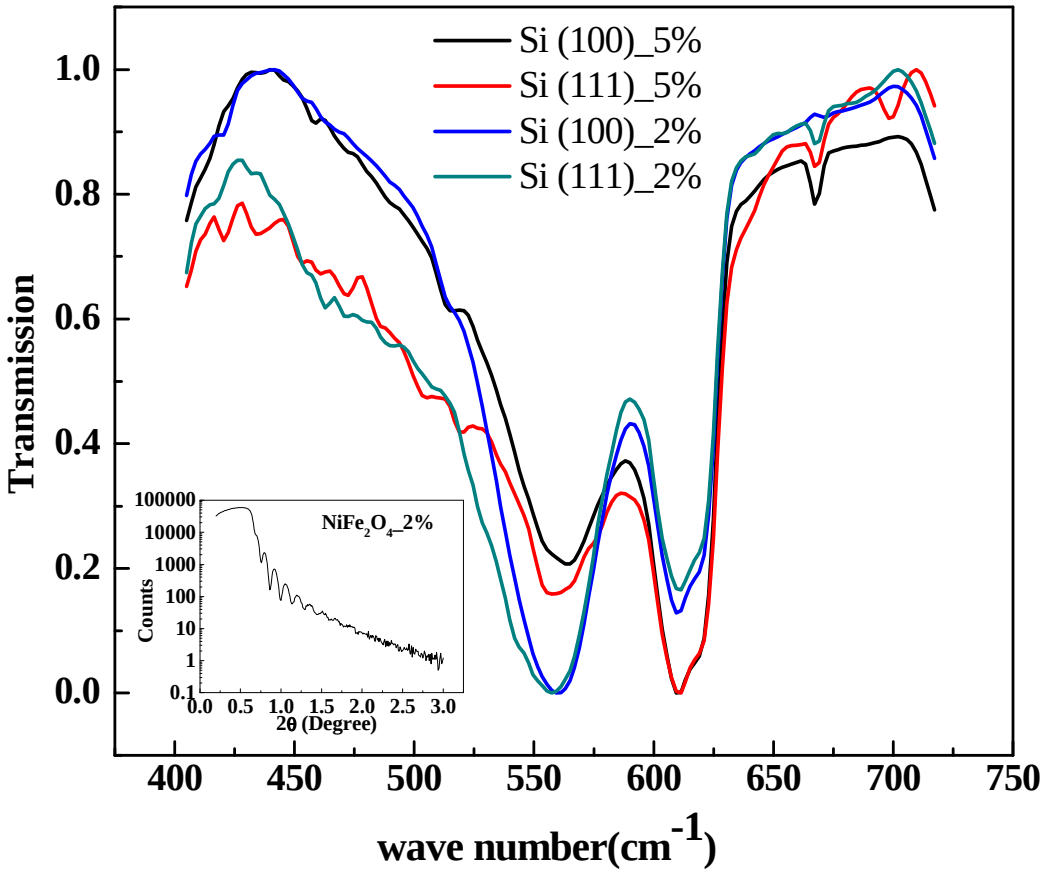

Fig. 3.2: FTIR spectra of $Ni_{1-x}Cr_xFe_2O_4$ (x = 0.02 and 0.05) films grown on Si (111) and Si (100) substrates. The inset shows XRR patterns of 2% Cr doped NFO film on Si (111) substrate.

increase in dopant percentage of Cr, it is observed that the intensity trend of bands 561 and 610 cm^{-1} is reversed, suggesting the redistribution of metal cations among octahedral and tetrahedral sites. Hence, the observed characteristic absorption bands in the FTIR spectra suggest that the NCFO films grown on Si (111) and Si (100) substrates have mixed spinel structure.

Figs. 3.3 (a) and (b) show the Raman spectra of $Ni_{0.95}Cr_{0.05}Fe_2O_4$ and $Ni_{0.98}Cr_{0.02}Fe_2O_4$ films respectively on Si (111) substrate. From Fig. 3.3(a), it is observed that the vibrational bands appear at ~ 336, 487, 587, 665 and 701 cm^{-1}, which are characteristics bands of $NiFe_2O_4$. In these bands, the peak at ~336 cm^{-1} corresponds to E_g symmetry and band at high frequency 701 cm^{-1} is due to A_{1g} symmetry and corresponds to stretching of oxygen atom with metal/ Fe ion at tetrahedral site. The bands with vibrational frequency lesser than 600 cm^{-1} are due to oxygen stretching at octahedral sites. Similar Raman spectrum is also observed for other films, suggesting their single phase nature [23].

Moreover to probe the mixed spinel nature of NCFO films and also to explore the oxidation states of cations Ni and Fe, we have performed XPS measurements. Cr concentration being only 2 and 5 %, Cr 2p core level spectra could not be accurately recorded. Ni 2p and Fe 2p core level XPS spectra of the grown films are shown in Figs. 3.4 and 3.5, respectively. These spectra were fitted with combined Gaussian-Lorentzian functions. Figs. 3.4 (a) and (b) show the Ni 2p core level XPS spectra of $Ni_{0.98}Cr_{0.02}Fe_2O_4$ films on both substrates. Probing the chemical states of Ni ions using the Ni $2p_{3/2}$ core level binding energy position with a possibility of their distribution among tetrahedral (T_d) and octahedral(O_h) sites is a challenging job due to their corresponding features occurring at close binding energy values, which can be easily mistaken for other chemical state of Ni ions. However, appearance of satellite peaks can be used to probe the chemical state. It is found that the main peak of Ni 2p core level actually consists of two features, corresponding to its distribution between O_h and T_d sites. The other components in the spectra arise because of shake-up satellite features of Ni $2p_{3/2}$ and Ni $2p_{1/2}$ peaks. Accordingly the Ni $2p_{3/2}$ feature can be fitted very well with two peaks at energies of ~ 854eV (labelled as O_h) and ~ 856eV (labelled as T_d) which belong to distribution of Ni^{2+} ions at O_h and T_d

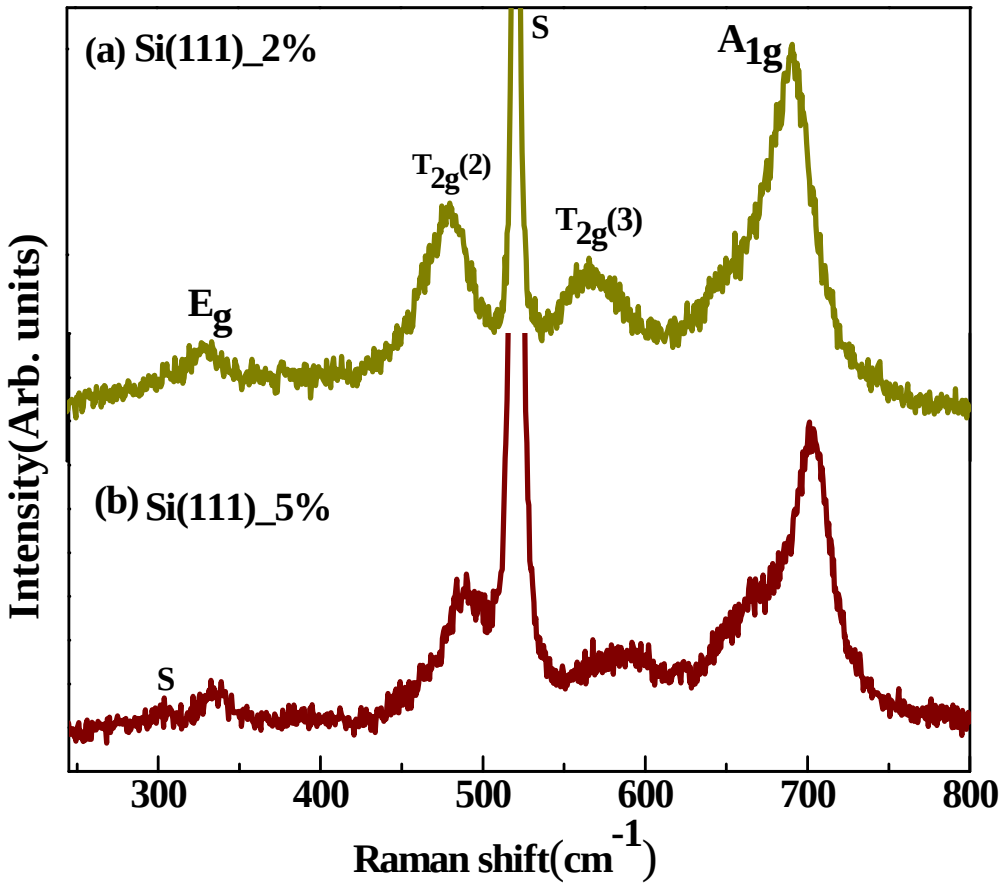

Fig. 3.3: Raman spectra of $Ni_{1-x}Cr_xFe_2O_4$ for (a) x = 0.02 and (b) x = 0.05 films grown on Si (111) substrates.

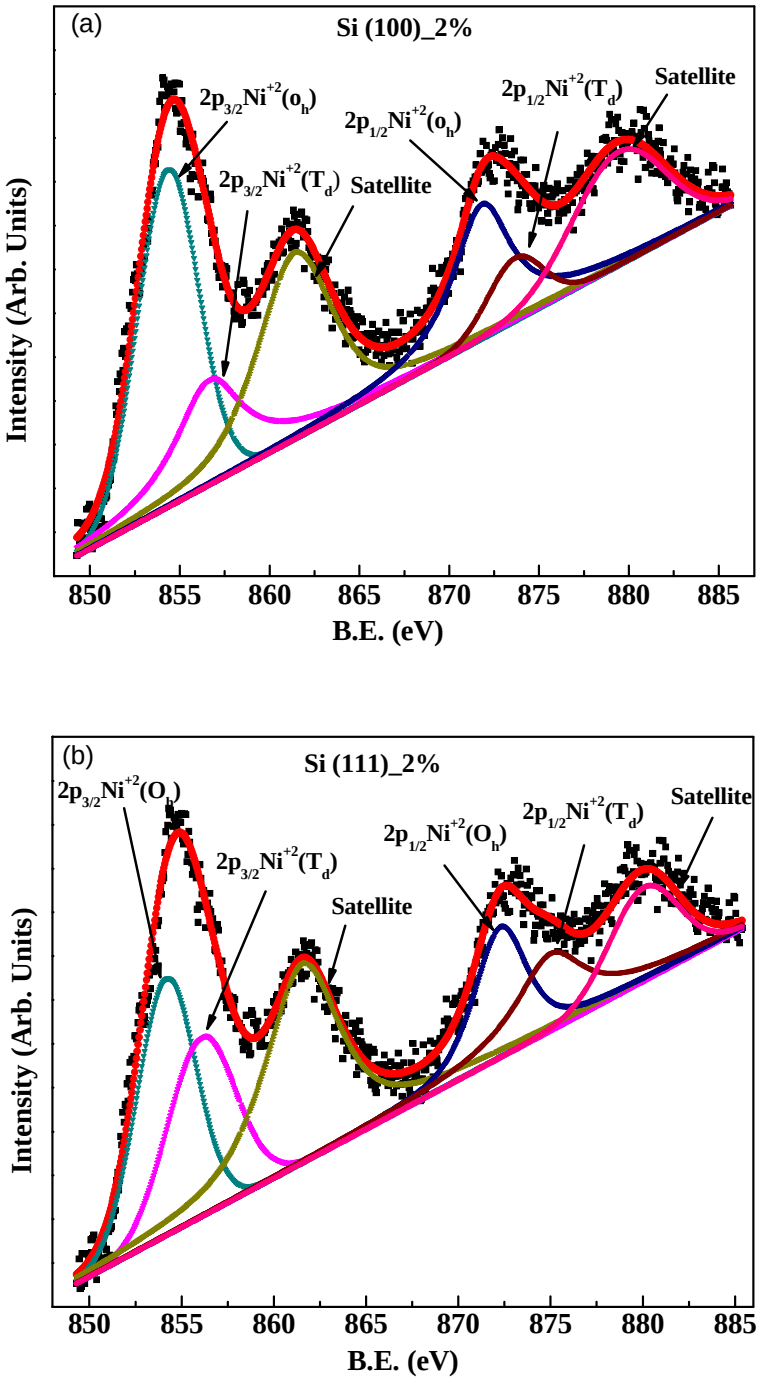

Fig. 3.4: Ni-2p core level x-ray photoelectron spectra of $Ni_{1-x}Cr_xFe_2O_4$ (x= 0.02) film grown on (a) Si (100) and (b) Si (111) substrates.

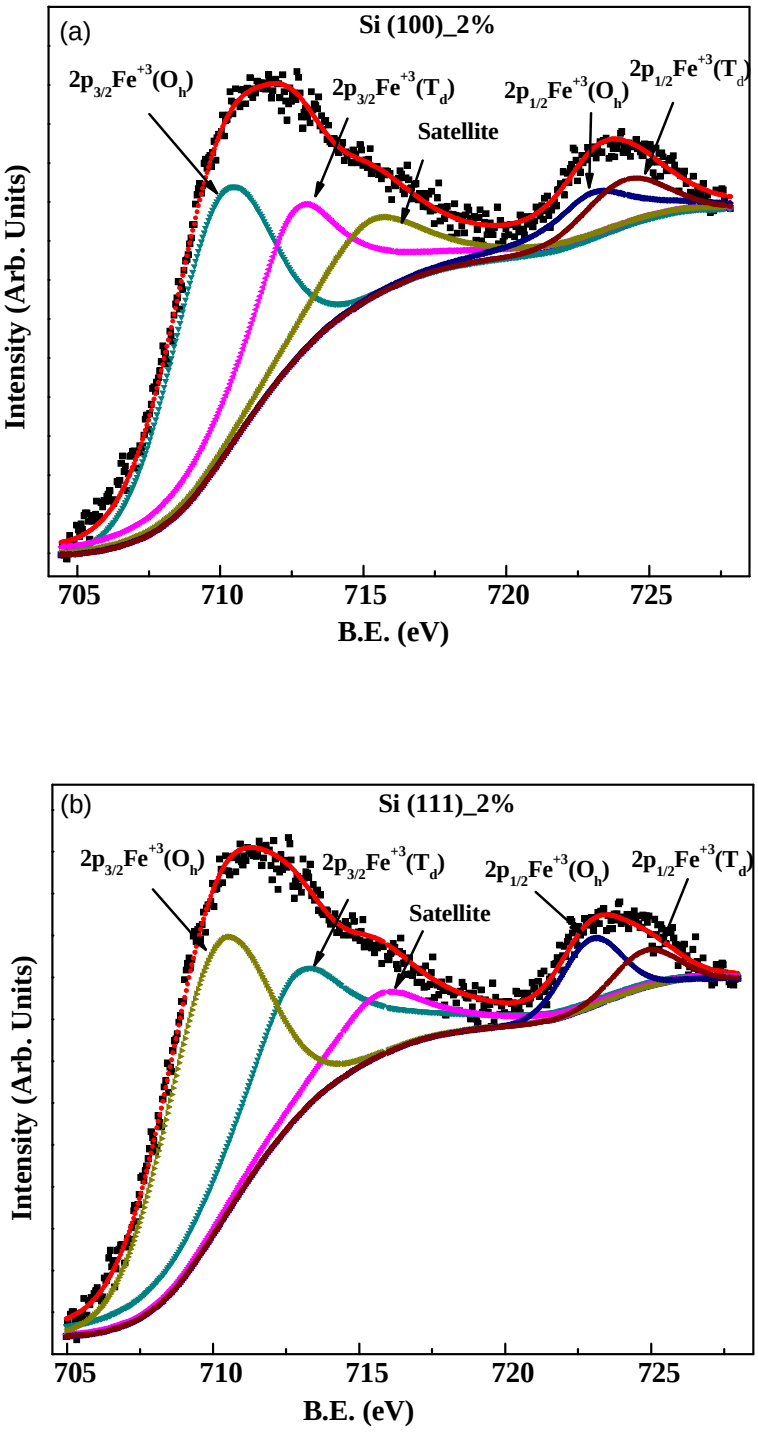

Fig. 3.5: Fe 2p core level x-ray photoelectron spectra of $Ni_{1-x}Cr_xFe_2O_4$ (x = 0.02) film grown on (a) Si (100) and (b) Si (111) substrates.

sites, respectively [22]. These binding energy positions suggest Ni to be present in 2+ states distributed between O_h and T_d sites. Similar spectra for Ni 2p core level are observed in other films also.

Similarly Fe 2p core level spectra as shown in Fig. 3.5(a) and (b) of $Ni_{0.98}Cr_{0.02}Fe_2O_4$ films on both substrates suggest that Fe ions are in 3+ valence state and that they are also distributed at T_d and O_h sites. As the magnetic properties of NFO are hugely dependent upon the cation distribution among O_h and T_d sites, we estimated the $Ni^{2+}{}_{Oh}/Ni^{2+}{}_{Td}$ and $Fe^{3+}{}_{Oh}/Fe^{3+}{}_{Td}$ ratio for all the films by evaluating the area under the corresponding T_d and O_h features. Thus obtained O_h/T_d values for both the ions are listed in Table 3.2 for all the films. It is evident from the Table 3.2 that the studied films have mixed spinel structure, as also revealed from the FTIR spectra. It is also observed that O_h/T_d ratio of Ni and Fe ions increases with Cr concentration, though the change is very small (since Cr doping concentration is also very low). Although small, an increase in O_h/T_d value for Fe and Ni ions with Cr doping suggests that Cr ions possibly substitute for Ni^{2+} at T_d sites and consequently distortion produced by Cr ions at T_d sites forces Fe^{3+} ions to move towards O_h sites. Hence the O_h /T_d ratio increases lightly for Fe^{3+} ions also. However, if we look into the O_h/T_d values for the different substrates, effect of substrate orientation is observed to be more pronounced on the cationic distribution than the Cr doping. It may be due to different strain produced by the substrates as revealed from XRD data. XPS technique, though it is surface sensitive, has provided us a qualitative behaviour of cationic distribution.

In Figs. 3.6 (a) and (b), we show the magnetization versus temperature (M-T) behaviour of the grown films measured in the field cooled protocol. The samples were cooled down to 10 K in 500 Oe magnetic field and the measurement was performed in the warming cycle. It is clear from the M-T behavior that the films magnetic transition temperature is beyond room temperature. To further understand this behaviour, M-H measurement is performed at room temperature for all the films. Fig. 3.6 (c) shows magnetic hysteresis loop of $Ni_{1-x}Cr_xFe_2O_4$ (x= 0.02, 0.05) thin films on Si (100) and Si (111) substrates at room temperature. We observe that all the films show clear hysteresis behaviour with different coercivity

Table 3.2: Octa/tetra ratio of Ni 2p and Fe 2p spectra for $Ni_{1-x}Cr_xFe_2O_4$ (x= 0.02, 0.05) thin films grown on Si (100) and Si (111) substrates.

Substrate	**Doping % (x)**	**(O_h/T_d ratio)**	**Calculated M_S (μ_B/FU)**
Si(100)	0.02	Ni: 1.15	0.85
		Fe: 1.17	
Si(100)	0.05	Ni: 1.27	0.88
		Fe: 1.18	
Si(111)	0.02	Ni: 1.21	0.80
		Fe: 1.14	
Si(111)	0.05	Ni: 1.22	0.84
		$Fe_{(Oh/Td\ ratio)}$: 1.18	

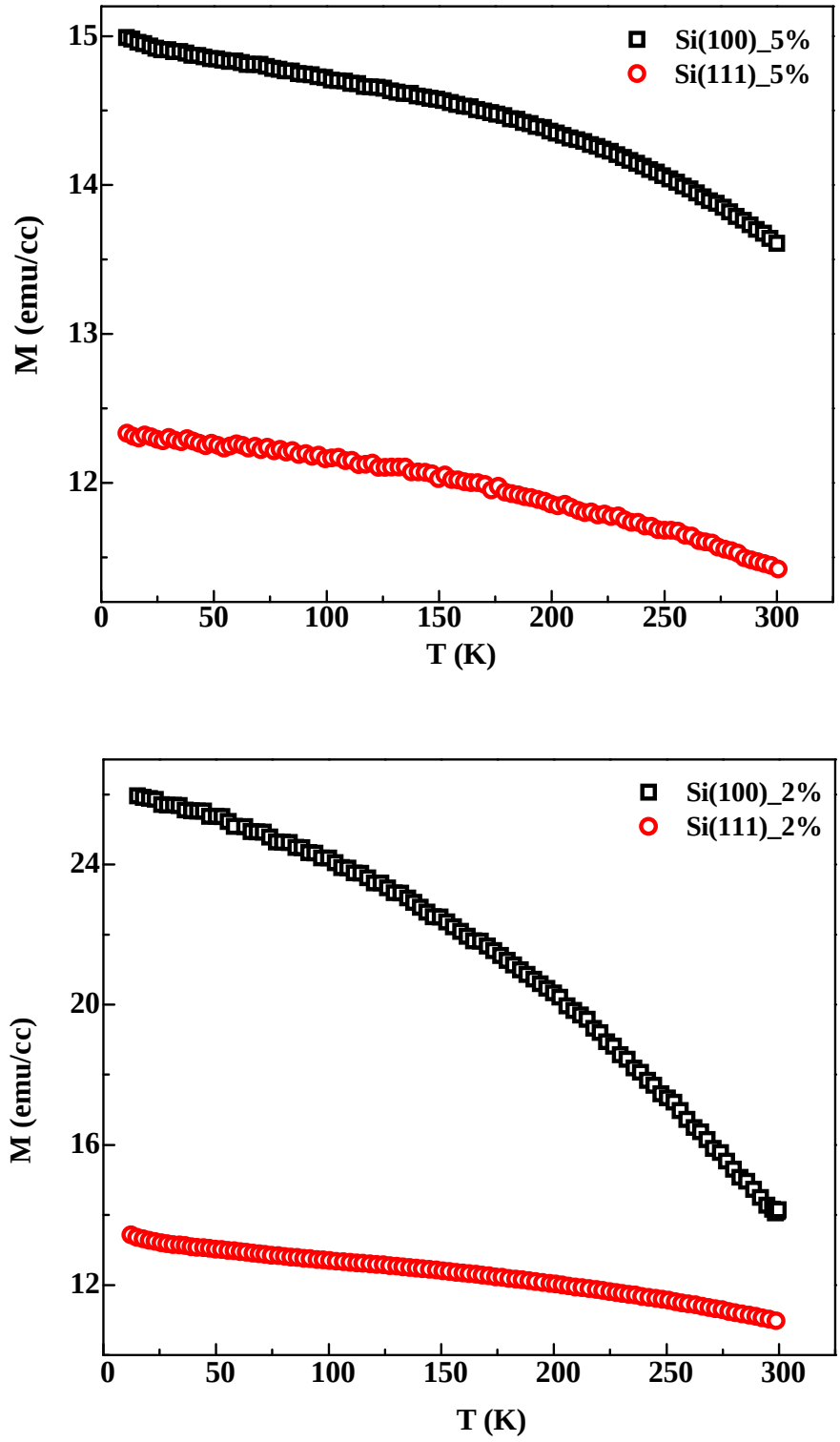

Fig. 3.6: Magnetization-versus temperature behavior of (a) $Ni_{0.95}Cr_{0.05}Fe_2O_4$ films grown on Si (100) and Si (111) substrates and (b) $Ni_{0.98}Cr_{0.02}Fe_2O_4$ films grown on Si (100) and Si (111) substrates.

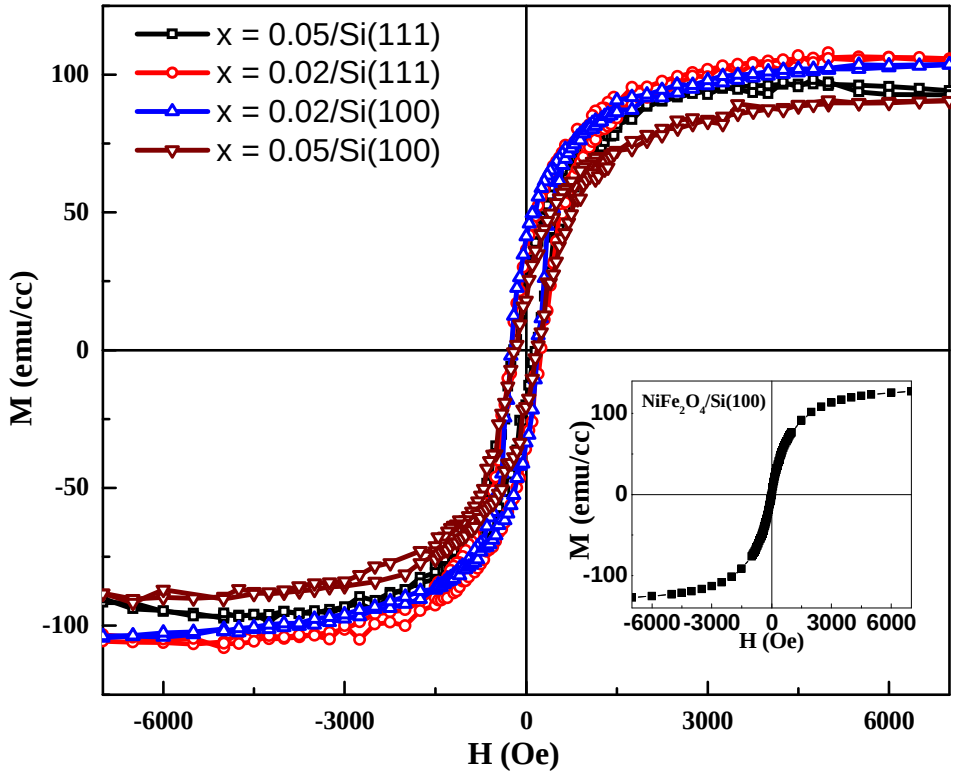

Fig. 3.6 (c): The magnetic hysteresis loop of $Ni_{1-x}Cr_xFe_2O_4$ (x = 0.02 and 0.05) thin films on Si (100) and Si (111) substrates. Inset shows M-H curve of undoped $NiFe_2O_4$ thin film grown on Si (100) substrate.

values. However, the magnetic moment values are much smaller than bulk Cr doped $NiFe_2O_4$ (~2μ_B/FU), as reported by Lang et al. [13]. It should be noted that $NiFe_2O_4$ is a ferrimagnetic compound due to antiferromagnetic exchange interaction between unequal magnetic moments at T_d and O_h sites. The observed lower saturation magnetic moment for these Cr doped films could be due to various reasons. One of the important factors is the ratio of distribution of cations between the T_d and O_h sites. It should be noted here that Lang et al. [13] have estimated the cation distribution in NCFO on a theoretical ground with various possible combinations of ionic valency for Cr, Fe and Ni at T_d and O_h sites [13]. In the present study, however, as discussed earlier, FTIR and XPS results suggested that the studied films are not in inverse spinel structure, rather they are in mixed spinel structure with the possible ionic states of Fe^{3+} and Ni^{2+} as determined by XPS. Therefore, the magnetic interaction among the T_d and O_h sites will be accordingly modified and the observed saturation magnetization would be different than as observed in bulk NCFO samples.

It should be noted here that the electronic configurations for Ni^{2+}, Fe^{3+} and Cr^{3+} are $3d^8$, $3d^5$ and $3d^3$, respectively. In the O_h and T_d crystal field, these degenerate d levels will split in to triply degenerate t_{2g} and doubly degenerate e_g levels. The energy positions of t_{2g} and e_g will be lower or higher depending on the field strength due to O_h or T_d crystal field, respectively. Therefore, electronic configurations of Ni^{2+} and Fe^{3+} in the O_h ligand field will be $3d^8$: $t_{2g}^6\ e_g^2$ and $3d^5$: $t_{2g}^3 e_g^2$, respectively. Considering the distribution ratio of Ni and Fe ions at O_h and T_d sites obtained from XPS analysis, we write 2% Cr doped NFO (for example) film on Si(100) as: $(Fe^{3+}_{0.92}Ni^{2+}_{0.46}Cr^{3+}_{0.02})_{tetra}(Fe^{3+}_{1.08}Ni^{2+}_{0.52})_{octa}O_4$. After considering the magnetic interactions, it turns out that now the magnetic moment is ~0.85μB/FU only. This value is considerably lower than the saturation moment one would observe if the structure had inverse spinel structure. Our experimentally obtained magnetic saturation value from magnetization measurements for this sample ~ 110 emu/cc (0.73μB/FU) is much lower than the theoretically calculated value, concomitant with the mixed spinel magnetic structure as observed from XPS analysis.

The calculated magnetic moment values using XPS data for all other films also, as shown in Table 3.2, qualitatively match with saturation magnetization values obtained from magnetization data. The larger moment in films on Si (100) in both samples could also be due to larger strain in the film than on Si (111), which may hinder the antiferromagnetic interaction between the T_d and O_h ions [23]. There are reports on $NiFe_2O_4$ nano-particles, where the saturation magnetization was found to be much lower than 300 emu/cc and was attributed to the defects, surface pinning effect, etc. [14,16]. Jaffari et al. [22] attributed the decrease in magnetic moment in non-stoicheometric NFO films to the weakening of super exchange interaction as a result of missing oxygen atoms. To get an insight of these values with respect to the undoped $NiFe_2O_4$ film, we performed M-H behaviour of undoped film also, which was grown under similar condition as used for the Cr doped samples on Si(100) substrate, shown in the inset of Fig. 3.6(c). It is observed that the saturation magnetization in undoped sample also is only ~130 emu/cc, again much lower than the expected theoretical value for ideal cationic distribution. It is also noted that the observed saturation magnetization in the studied Cr doped NFO films are lesser than those reported for other dopants in NFO [24,25]. Therefore, from the present study, the rather larger decrease in moment value for the NCFO films than its bulk counterpart suggests that besides the Cr doping, strain produced by substrate is also an important parameter to influence the cationic distribution at O_h and T_d sites and hence the magnetic properties of NFO based compounds. Since the cationic distribution is dependent on the method of preparation, different reports on saturation magnetization values differ considerably from each other.

3.4. Conclusions:

Thin films of $Ni_{1-x}Cr_xFe_2O_4$ (x = 0.02 and 0.05) are grown on Si (111) and Si (100) substrates using pulsed laser deposition. It is seen that films on Si (111) substrate have larger grain size than those on Si (100) substrate. Though XRD and FTIR results confirm the single phase growth of the films, their cationic distribution in the formula unit deviates considerably from inverse spinel structure, as revealed by XPS analysis. It is found that Ni^{2+} ions are distributed not

only at octahedral site, as expected for inverse spinel structure, but also at the tetrahedral sites, suggesting the mixed spinel structure. This leads to considerably decreased saturation magnetization arising because of enhanced magnetic moment at tetrahedral site and decreased magnetic moment at octahedral site, which interact antiferromagnetically. Different cationic distribution of Ni and Fe ions between O_h and T_d sites are attributed to the different strain produced by the substrates and lattice distortion produced by the Cr doping. The magnetic transition temperature of the studied films is above room temperature. The present study suggests that the magnetic property in this class of materials is mainly controlled by the cationic distribution at different sites, which may be controlled by defect density, strain in the film, doping of magnetic or non-magnetic ions.

References

1. S. Winell, Ö. Amcoff, T. Ericsson, Phys. Stat. Sol. (b) 245 (2008) 1635–1640.

2. C. Himcinschi, L. Vrejoiu, G. Salvan, M. Fronk, A. Talkenberger, D.R.T. Zahn, D. Rafaja, J. Kortus, J. Appl. Phys. 113 (2013) 084101-1–084101-8.

3. G. Dixit, J.P. Singh, R.C. Srivastava, H.M. Agrawal, R.J. Choudhary, Adv. Mater. Lett. 3 (2012) 21–28.

4. V.G. Ivanov, M.V. Abrashev, M.N. Iliev, M.M. Gospodinov, J. Meen, M.I. Aroyo, Phys. Rev. B 82 (2010) 024104-1– 024104-8.

5. J. Kulawik, D. Szwagierczak, P. Guzdek, J. Mag. Mag. Mat. 324 (2012) 3052–3057.

6. P. Guzdek, J. Mag. Mag. Mat. 349 (2014) 219–223.

7. M. Meinert, G. Reiss, J. Phys.: Condens. Matter 26 (2014) 115503-1–115503-4.

8. J.X. Ma, D. Mazumdar, G. Kim, H. Sato, N.Z. Bao, A. Gupta, J. Appl. Phys. 108 (2010) 063917-1–063917-5.

9. B.S. Holinsworth, D. Mazumdar, H. Sims, Q.C. Sun, M.K. Sarker, A. Gupta, W.H. Bulter, J.L. Musfeldt, Appl. Phys. Lett. 103 (2013) 082406-1–082406-4.

10. U. Luders, M. Bides, J.F. Bobo, M. Cantoni, R. Bertacco, J. Fontcuberta, Phys. Rev. B 71 (2005) 134419-1–134419-7.

11. S.M. Patange, S.E. Shirsath, S.S. Jadhav, K.S. Lohar, D.R Mane, K.M. Jadhav, Mater. Lett. 64 (2010) 722–724.

12. S. Singhal, K. Chandra, J. Solid State Chem. 180 (2006) 296–300.

13. L.L. Lang, J. Xu, W.H. Qi, Z.Z. Li, G.D. Tang, Z.F. Shang, X.Y. Zhang, L.Q. Wu, L.C. Xue, J. Appl. Phys. 116 (2014) 123901-1–123901-10.

14. C.N. Chinnasamy, A. Narayanasamy, N. Ponpandian, K. Chattopadhyay, K. Shinoda, B. Jeyadevan, K. Tohji, K. Nakatsuka, T. Furubayashi, I. Nakatani, Phys. Rev. B 63 (2001) 184108-1–184108-8.

15. S. Phumying, S. Labuayai, E. Swatsitang, V. Amornkitbamrung, S. Maensiri, Mater. Res. Bull. 48 (2013) 2060–2065.

16. C.N. Chinnasamy, A. Narayanasamy, N. Ponpandian, R.J. Joseyphus, B. Jeyadevan, K. Tohji, K. Chattopadhyay, J. Mag. Mag. Mat. 238 (2002) 281–287.

17. V. Sepelak, I. Bergmann, A. Feldhoff, P. Heitjans, F. Krumeich, D. Menzel, F.J. Letterst, S.J. Campobell, K.D. Becker, J. Phys. Chem. C 111 (2007) 5025 –5033.

18. S. Tiwari, R.J. Choudhary, R. Prakash, D.M. Phase, J. Phys.: Condens. Matter 19 (2007) 176002-1–176002-7.

19. C.N. Chinnasamy, S.D. Yoon, A. Yang, A. Baraskar, C. Vittoria, V.G. Harris, J. Appl. Phys. 101 (2007) 09M517-1–09M517-3.

20. O.F. Caltum, J. Optoelec. Adv. Mater. 7 (2005) 739–744.

21. S. Seifikar, A. Tabei, E. Sachet, T. Rawdanowicz, N. Bassiri-Gharb, J. Schwartz, J. Appl. Phys. 112 (2012) 063908-1–063908-6.

22. G.H. Jaffari, A.K. Rumaiz, J.C. Woicik, S.I. Shah, J. Appl. Phys. 111 (2012) 093906-1–093906-6.

23. M.N. Iliev, D. Mazumdar, J.X. Ma, A. Gupta, F. Rigato, J. Fontcuberta, Phys. Rev. B 83 (2011) 014108-1–014108-6.

24. P. Guzdek, J. Kulawik, K. Zaraska, A. Bienkowski, J. Mag. Mag. Mat. 322 (2010) 2897–2901.

25. L. Li, X. Tu, L. Peng, X. Zhu, J. Alloy Compounds 545 (2012) 67–69.

Chapter 4

Performance of Hybrid Functional in Linear Combination of Atomic Orbitals Scheme in Predicting Electronic Response in Spinel Ferrites $ZnFe_2O_4$ and $CdFe_2O_4$

Based on:

N.L. Heda, Kalpana Panwar, K. Kumar,
B.L. Ahuja, J. Mater. Sci. 55 (2020) 3912–3925

4.1. Introduction:

Zinc and cadmium ferrites ($ZnFe_2O_4$ and $CdFe_2O_4$) crystallize in cubic spinel structure and are classified as important functional materials due to their peculiar electronic and magnetic properties [1-4]. Regarding earlier studies, Evans et al. [1] have employed Mössbauer spectroscopy (MS) to calculate nuclear quadrupole coupling constants and isomer shifts. Temperature dependent electric-field gradients of both the ferrites were studied using time differential perturbed angular correlation technique by Pasquevich and Shitu [2]. Further, density functional theory (DFT) with generalized gradient approximation (GGA) and GGA plus one side Coulomb interaction (GGA+U) schemes were applied to highlight Fe-Fe interactions [3]. DFT within local density approximation (LDA), GGA, LDA+U and GGA+U schemes were employed by Cheng and Liu [4] to discuss the cation distribution effect in both the compounds. Electronic and magnetic properties of $ZnFe_2O_4$ were reported using DFT schemes with different approximations namely atomic-sphere approximations [5], general potential linearized augmented plane wave method (LAPW) [6], plane wave pseudopotential (PWP) [7] and full potential (FP)-LAPW [8]. On the experimental side, structural and magnetic properties of $ZnFe_2O_4$ were explored by neutron diffraction, MS, X-ray diffraction (XRD), scanning electron microscopy, energy dispersive spectroscopy, vibrating sample magnetometer and Fourier transform infrared (FTIR) measurements [9-11]. Also, Quintero et al. [12,13] have studied $ZnFe_2O_4$ using FP-LAPW method and MS measurements to visualize effect of defects on structural, electronic, hyperfine and magnetic properties. In case of $CdFe_2O_4$, Mahmood et al. [14] have used DFT with Perdew-Becke-Ernzerhof (PBE) revised for solids (PBESol) with modified Becke–Johnson (mBJ) exchange-correlations potentials to explain optical, magnetic and thermoelectric properties. Measurements on $CdFe_2O_4$ which include XRD, electrical conductivity, thermoelectric power, magnetic hysteresis, initial magnetic susceptibility, infrared spectroscopy and MS, inelastic neutron scattering and structural and transport properties have been reported by different groups [15-17]. In addition, density of states (DOS) along with optical and X-ray magnetic

circular dichroism properties of $CdFe_2O_4$ were discussed by Zaari et al. [18] using FP-LAPW-DFT with mBJ potentials.

It is well known that Compton scattering (CS) measurements can be uniquely applied in testing various exchange-correlation potentials through electron momentum densities (EMDs) [19,20 and chapter 1]. The projection of EMD along the z-axis (scattering vector direction) is measured in CS experiment and is defined as Compton profile (CP), $J(p_z)$. Mathematically,

$$J(p_z) = \int_{p_x=-\infty}^{+\infty} \int_{p_y=-\infty}^{+\infty} \rho\left(\overrightarrow{p_x}, \overrightarrow{p_y}, \overrightarrow{p_z}\right) d\,\overrightarrow{p_x} d\overrightarrow{p_y} \quad (4.1)$$

Here, $\rho\left(\overrightarrow{p_x}, \overrightarrow{p_y}, \overrightarrow{p_z}\right)$ represents the momentum distribution of the electrons while $\overrightarrow{p_x}$, $\overrightarrow{p_y}$ and $\overrightarrow{p_z}$ are the components of electron linear momentum ($\vec{p}$) along x, y and z-directions of the Cartesian coordinate system, respectively. Experimentally, we deduce CP from the measured double differential Compton cross-section using the relations,

$$J(p_z) = \frac{\text{Double differential Compton cross-section}}{C\,(E_1, E_2, \theta, p_z)} \quad (4.2)$$

Here $C\,(E_1, E_2, \theta, p_z)$ depends on the experimental setup with E_1 and E_2 being the incident and scattered energies of photons and θ is the photon scattering angle. The variable C in Eq. 4.2 depends on the experimental geometry also.

In the present chapter, which is also published by us in J. Mater. Sci. 55 (2020) 3912–3925, we have employed CRYSTAL14 code [21 and chapter 2] to compute Mullikan population (MP), energy bands, DOS and CPs for $TMFe_2O_4$ (TM= Zn and Cd). The purpose of present CP measurements is hands-on validation of various types of exchange and correlation potentials and hybrid functionals for reliable electronic properties under the frame work of linear combination of atomic orbitals (LCAO). We have also scaled the experimental and theoretical CP on equal-valence-electron-density (EVED) to predict a relative nature of bonding in these iso-electronic compounds. Furthermore, trend of bonding in both the ferrites has also been validated by the present MP analysis. Going beyond CPs, energy bands, DOS, band gaps and magnetic moments of both the compounds have been compared with the available data which enables to conclude about applicability of different types of exchange-correlation energy and hybrid schemes in such type of ferrites.

4.2. Methodologies:

4.2.1. Theory:

LCAO calculations have been performed within the hypothesis of DFT and hybridizations of Hartree-Fock (HF) to DFT (so called B3LYP and PBE0) as embodied in the CRYSTAL14 software [21 and chapter 2]. We have adopted the LDA and GGA under the DFT scheme. In LCAO calculations, one solves the one electron Schrodinger equation ($\widehat{H}\Psi = E\Psi$) to obtain the crystal wave functions. The Hamiltonian energy operator ($\widehat{H}$) includes kinetic energy, electrostatic potential (arising due to interaction of nuclei with electrons), electrostatic repulsion between electrons and exchange-correlation density functional energy($\mathrm{E_{XC}}$). First three part of $\widehat{H}$ are same in DFT-LDA, DFT-GGA, B3LYP and PBE0 approximations, whereas differences among these approximations occur in terms of $\mathrm{E_{XC}}$. In case of DFT within LDA or GGA, $\mathrm{E_{XC}}$ is defined as,

$$\mathrm{E_{XC}^{LCAO-DFT-LDA/GGA}}\left\{\rho(\bar{r})\right\} = \int \rho(\bar{r})\ \varepsilon_{xc}\ \left\{\rho(\bar{r})/(\rho(\bar{r}), \left|\nabla\rho(\bar{r})\right|)\right\} d\vec{r} \qquad (4.3)$$

In Eq. 4.3, ε_{xc} is known as exchange-correlation energy per particle in uniform electron gas and $\rho(\bar{r})$ is the electron density. In case of LCAO-DFT-LDA scheme, we have adopted exchange and correlation potentials of Dirac-Slater [21] and Perdew and Zunger [22], respectively. While the exchange and correlation energies of PBESol [23] were considered for LCAO-DFT-GGA approximations. In case of hybridized (HF+DFT) approximations (B3LYP and PBE0), $\mathrm{E_{XC}}$ is defined as:

$$\mathrm{E_{XC}^{LCAO-B3LYP}} = \mathrm{A} * \mathrm{E_X^{LDA}} + \mathrm{B} * \Delta\mathrm{E_X^{BECKE}} + (1-\mathrm{A}) * \mathrm{E_X^{HF}} + \mathrm{C} * \mathrm{E_C^{LYP}} + (1-\mathrm{C}) * \mathrm{E_C^{VWN}} \qquad (4.4)$$

$$\mathrm{E_{XC}^{LCAO-PBE0}} = \mathrm{D} * \mathrm{E_X^{HF}} + (1-\mathrm{D}) * \mathrm{E_X^{PBE}} + \mathrm{E_C^{PBE}} \qquad (4.5)$$

The standard values of A, B, C and D are 0.80, 0.72, 0.81 and 0.25, respectively [24,25]. Further $\mathrm{E_X^{HF}}$, $\mathrm{E_X^{LDA}}$, $\mathrm{E_X^{BECKE}}$ and $\mathrm{E_X^{PBE}}$ are the exchange energies corresponding to HF [21], Dirac Slater [21], Becke [26] and Perdew et al. [27]. $\mathrm{E_C^{LYP}}$, $\mathrm{E_C^{VWN}}$ and $\mathrm{E_C^{PBE}}$ are the correlation energies of Lee et al. [28], Vosko et al. [29] and Perdew et al. [27], respectively.

Further, all electron basis sets of Zn, Cd, Fe and O atoms [30] were used after the re-optimization for the lowest energy of both the ferrites using BILLY code [21]. The optimized basis sets Zn (Cd), Fe and O atoms in $ZnFe_2O_4$ ($CdFe_2O_4$)

environment are tabulated in Table 4.1 (Table 4.2). The lattice parameters, position of atoms and space group of spinel $ZnFe_2O_4$ and $CdFe_2O_4$ were adopted from Quintero et al. [13] and Zaari et al. [18], respectively. The self consistent field (SCF) calculations for both the compounds were performed with 29 **k** points in the irreducible Brillouin zone (BZ). The unit cell in cubic spinel structure for $ZnFe_2O_4$ is plotted using XCrysden visualization software of Kokalj [31] (Fig. 4.1a) and the corresponding first BZ structure is sketched in Fig. 4.1b.

4.2.2. Experiment:

To ratify the choice of exchange and correlation potentials through reconciliation of theoretical and experimental CPs, we have employed 20 Ci ^{137}Cs Compton spectrometer [32 and chapter 2] to measure CPs of $TMFe_2O_4$ (TM = Zn and Cd). In the present measurements an absolute momentum resolution (Gaussian full width at half maximum) of the experimental setup was 0.34 a.u. Due to difficulties in growing large size single crystals (15mm diameter and 2 mm thickness) and to discuss the relative nature of bonding on EVED scale of $ZnFe_2O_4$ and $CdFe_2O_4$, we have taken pallets of high purity (> 99 %) polycrystalline powder of both the ferrites. Further, γ-radiations of energy 661.65 keV were allowed to incident on pallets of individual ferrite and the scattered radiations (160±0.6° scattering angle) were energy analyzed by a high purity Ge detector (GL0510P, Canberra made). During the exposure time of 162.4 (273.8) h for $ZnFe_2O_4$ ($CdFe_2O_4$), the integrated Compton intensity was found to be 3.17×10^7 (4.44×10^7) counts. The stability of the acquisition system was monitored from time-to-time by two weak radio-isotopes namely ^{57}Co and ^{133}Ba. To obtain absolute CP, the raw Compton spectra (as shown in Figs. 2.5(c-d) in chapter 2) of both the ferrites were corrected for systematic corrections (background, detector efficiency, sample absorption, stripping-off the low energy tail and CS cross-section) with computer code of Warwick group [33]. To obtain true singly scattered photon profile, we have also corrected the data for the effect upto triple scattering using Monte Carlo method [34]. Each Compton line was normalized to corresponding free atom (FA) CP area using the tabulated values of Biggs et al. [35]. The value of FA CP area for $ZnFe_2O_4$ ($CdFe_2O_4$) was 51.62 (57.77) e^- in the momentum range 0 to 7 a.u.

Table 4.1: Optimized basis-sets, Gaussian exponents (in a.u.$^{-2}$) and contraction coefficients for Zn, Fe and O in case of $ZnFe_2O_4$. Asterisks represent unoccupied atomic orbitals at the beginning of the self consistent field (SCF) process.

Atom	Orbitals	Exponents	Coefficients		
			s	p	d
Zn	s	417016.5	0.00023		
		60504.2	0.00192		
		12907.9	0.01101		
		3375.74	0.04978		
		1018.11	0.16918		
		352.55	0.36771		
		138.19	0.40244		
		57.851	0.14386		
	sp	1079.2	-0.00620	0.00889	
		256.52	-0.07029	0.06384	
		85.999	-0.13721	0.22039	
		34.318	0.26987	0.40560	
		14.348	0.59918	0.41370	
		4.7769	0.32239	0.34974	
	sp	60.891	0.00679	-0.00895	
		25.082	-0.08468	-0.03333	
		10.620	-0.34709	0.08119	
		4.3076	0.40633	0.56518	
	sp	1.6868	1.0	1.0	
	sp*	0.62679	1.0	1.0	
	sp*	0.15033	1.0	1.0	
	d	57.345			0.02857
		16.082			0.15686
		5.3493			0.38663
		1.7548			0.47766
	d*	0.51592			1.0
Fe	s	315379.0	0.000227		
		45690.0	0.0019		
		9677.3	0.0111		
		2520.88	0.0501		
		759.746	0.1705		
		262.964	0.36924		
		102.801	0.4033		
		42.9733	0.1434		
	sp	798.262	-0.0052	0.00850	
		191.162	-0.068	0.0608	
		63.6885	-0.1314	0.2114	
		25.3625	0.2517	0.3944	
		10.7338	0.6433	0.398	
		3.764	0.2825	0.2251	

	sp	48.1434	0.0122	-0.0215	
		17.4579	-0.2278	-0.085	
		6.9972	-0.8801	0.201	
		3.0791	0.9755	1.3024	
	sp	1.2989	1.0	1.0	
	sp*	0.5430	1.0	1.0	
	d	31.3296			0.058
		8.7866			0.263
		3.1008			0.5017
		1.1377			0.5656
	d*	0.3594			1.0
O	s	8020.0	0.00108		
		1338.0	0.00804		
		255.4	0.05324		
		69.22	0.1681		
		23.90	0.3581		
		9.264	0.3855		
		3.851	0.1468		
		1.212	0.0728		
	sp	47.7145	-0.0102	0.0098	
		10.47	-0.0908	0.0692	
		3.2817	-0.0434	0.2052	
		1.241	0.3984	0.3263	
	sp*	0.466	1.0	1.0	
	sp*	0.183	1.0	1.0	

Table 4.2: Optimized basis-sets, Gaussian exponents (in a.u.$^{-2}$) and contraction coefficients for Cd, Fe and O in case of $CdFe_2O_4$. Asterisks represent unoccupied atomic orbitals at the beginning of the self consistent field (SCF) process.

Atom	Orbitals	Exponents	Coefficients		
			s	p	d
Cd	s	3806666.0	0.0000487		
		569411.9375	0.000383		
		123127.648438	0.00225		
		31268.371094	0.0112		
		8980.700195	0.0465		
		2854.445801	0.1554		
		1009.196594	0.3515		
		399.020874	0.4266		
		166.670609	0.1854		
	sp	11112.272461	-0.000306	0.00103	
		2561.287109	-0.00635	0.00954	
		781.066467	-0.0543	0.0567	
		275.585419	-0.1473	0.2179	
		110.071716	0.1462	0.4549	
		50.098621	0.6198	0.43	
		24.000904	0.4052	0.1757	
	sp	240.497849	0.00642	-0.0146	
		93.222374	-0.0339	-0.0698	
		39.301212	-0.3249	0.0368	
		17.460880	0.0259	0.8806	
		8.100710	0.9324	1.2846	
		3.815374	0.4064	0.4154	
	d	331.966			0.0123
		98.8574			0.0861
		36.9351			0.2829
		15.2038			0.4621
		6.5373			0.3394
		2.6577			0.0612
	sp	6.2065	-4.4517	-0.073	
		2.9451	1.9018	0.5548	
		1.2793	9.8763	0.8933	
	sp	0.1739	1.0	1.0	
	sp*	0.5375	1.0	1.0	
	d	4.6812			0.1891
		1.8023			0.4956
		0.6875			0.4544
	d*	0.2588			1.0

Fe	s	315379.0	0.000227		
		45690.0	0.0019		
		9677.3	0.0111		
		2520.88	0.0501		
		759.746	0.1705		
		262.964	0.36924		
		102.801	0.4033		
		42.9733	0.1434		
	sp	798.262	-0.0052	0.00850	
		191.162	-0.068	0.0608	
		63.6885	-0.1314	0.2114	
		25.3625	0.2517	0.3944	
		10.7338	0.6433	0.398	
		3.764	0.2825	0.2251	
	sp	48.1434	0.0122	-0.0215	
		17.4579	-0.2278	-0.085	
		6.9972	-0.8801	0.201	
		3.0791	0.9755	1.3024	
	sp	1.2989	1.0	1.0	
	sp*	0.5430	1.0	1.0	
	d	31.3296			0.058
		8.7866			0.263
		3.1008			0.5017
		1.1377			0.5656
	d*	0.3594			1.0
O	s	8020.0	0.00108		
		1338.0	0.00804		
		255.4	0.05324		
		69.22	0.1681		
		23.90	0.3581		
		9.264	0.3855		
		3.851	0.1468		
		1.212	0.0728		
	sp	47.7145	-0.0102	0.0098	
		10.47	-0.0908	0.0692	
		3.2817	-0.0434	0.2052	
		1.241	0.3984	0.3263	
	sp*	0.466	1.0	1.0	
	sp*	0.183	1.0	1.0	

(a)

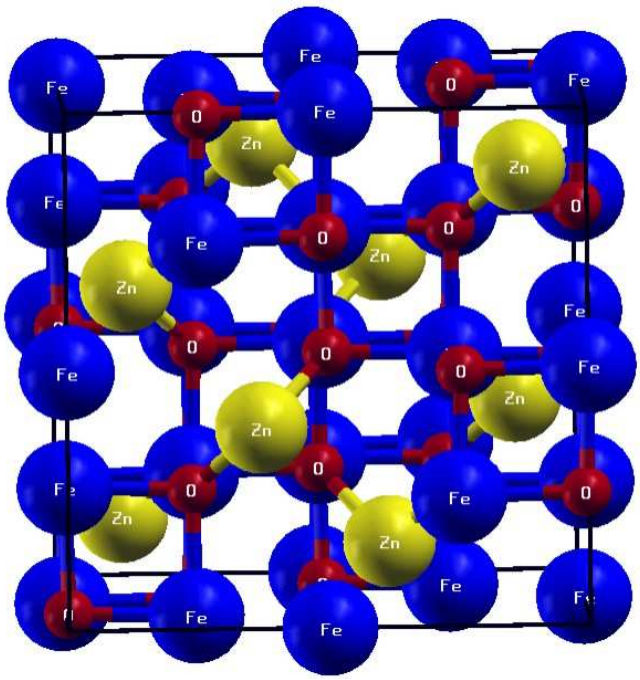

(b)

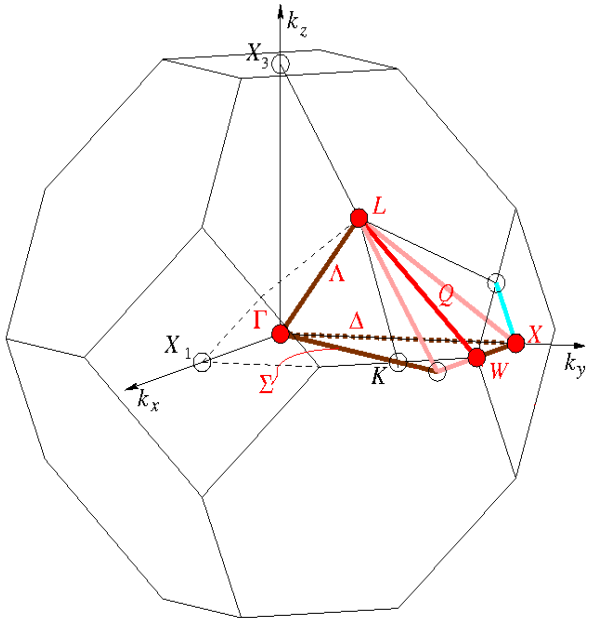

Fig. 4.1: Structural sketch of (a) $ZnFe_2O_4$ plotted using software tool of Kokalj [31]. For $CdFe_2O_4$ structure, Zn is replaced by Cd. (b) First BZ corresponding to structural sketch given in part 'a'.

4.3. Results and Discussion:

4.3.1. MP analysis:

MP data of charge transfer for $TMFe_2O_4$ (TM = Zn and Cd) using LCAO-DFT-LDA, LCAO-DFT-GGA, LCAO-B3LYP and LCAO-PBE0 schemes have been presented in Table 4.3. Here, the transition metal atoms (Zn/Cd and Fe) in $TMFe_2O_4$ (TM = Zn/Cd) donate charge to the oxygen atoms and total charge from donor is equally distributed among O atoms for both the compounds. The total numerical values of charge transfer in $ZnFe_2O_4$ ($CdFe_2O_4$) are 4.12 (4.32), 4.16 (4.40), 4.44 (4.60) and 4.52 (4.72) e^- using LCAO-DFT-LDA, LCAO-DFT-GGA, LCAO-B3LYP and LCAO-PBE0 schemes, respectively. It is observed that the charge transfer in $CdFe_2O_4$ is higher than that in $ZnFe_2O_4$ for each approximation (LCAO-DFT-LDA/LCAO-DFT-GGA/LCAO-B3LYP/LCAO-PBE0). Such trend of MP data indicates more ionic (or less covalent) character in $CdFe_2O_4$ than that in $ZnFe_2O_4$, as larger value of charge transfer in any compound reflects more ionicity. Also, in all the adopted approximations, contribution of Fe atom in total charge transfer data is found to be approximately similar for both the compounds. However, difference in total charge transfer exists due to the contribution of Zn/Cd atom in $TMFe_2O_4$ environment. In addition to MP data for charge transfer, we have also calculated overlap population (OP) between the nearest neighbour atoms in both the compounds. The OP value of identical Fe-O in $TMFe_2O_4$ (TM = Zn/Cd) are found to be 0.051, 0.051, 0.049 and 0.048 e^- using LCAO-DFT-LDA, LCAO-DFT-GGA, LCAO-B3LYP and LCAO-PBE0, respectively, for both the compounds. While these values for Zn-O (Cd-O) in case of $ZnFe_2O_4$ ($CdFe_2O_4$) are observed as 0.127 (0.047), 0.126 (0.045), 0.124 (0.039) and 0.120 (0.035) e^- using LCAO-DFT-LDA, LCAO-DFT-GGA, LCAO-B3LYP and LCAO-PBE0, respectively. The OP values of Zn-O in case of $ZnFe_2O_4$ are higher than that for Cd-O in $CdFe_2O_4$ using all the LCAO approximations. It indicates more covalent (or less ionic) character of $ZnFe_2O_4$ than that in $CdFe_2O_4$ because large value of OP indicates more covalent character of the compound. It is worth mentioning that MP analysis of charge transfer is bound to be quite reliable as we have included large number of atomic orbitals in each LCAO computation using DFT-

Table 4.3: Mulliken's population (MP) data for $TMFe_2O_4$ (TM=Zn and Cd) using LCAO-DFT-LDA, LCAO-DFT-GGA, LCAO-B3LYP and LCAO-PBE0 schemes as mentioned in the text. Here, TM (Zn and Cd) and Fe atoms are the donor atoms while O atoms are the acceptor atoms. The numbers of equivalent atoms are shown in the brackets.

Scheme	Amount of charge transfer (e^-)		
	Donor atoms		Acceptor atoms
	Zn/Cd (2)	**Fe (4)**	**O (8)**
(a) $ZnFe_2O_4$			
LCAO-DFT-LDA	1.04	1.54	1.03
LCAO-DFT-GGA	1.06	1.55	1.04
LCAO-B3LYP	1.16	1.64	1.11
LCAO-PBE0	1.18	1.67	1.13
(b) $CdFe_2O_4$			
LCAO-DFT-LDA	1.18	1.57	1.08
LCAO-DFT-GGA	1.22	1.59	1.10
LCAO-B3LYP	1.30	1.65	1.15
LCAO-PBE0	1.32	1.70	1.18

LDA, DFT-GGA, B3LYP and PBE0 prescriptions. Such MP analysis have successfully been reported in various other oxides, viz. $TMWO_4$ (TM=Co, Ni, Cu, Zn and Cd) [36,37], Ag_2TMO_4 (TM= Cr and Mo) [38] and $BaTiO_3$ [39].

4.3.2. Energy bands and density of states:

Majority (spin-up) and minority (spin-down) energy bands of LCAO-B3LYP scheme are presented in Figs. 4.2-4.3 for $ZnFe_2O_4$ and $CdFe_2O_4$, respectively. Except some fine structures, the energy bands of LCAO-B3LYP are in consonance with LCAO-DFT-LDA, LCAO-DFT-GGA and LCAO-PBE0 schemes hence energy bands are shown only for B3LYP scheme (which performed well in reproducing EMDs, as discussed later). Also, our energy bands of $ZnFe_2O_4$ and $CdFe_2O_4$ reasonably resemble with the available data [6,7,14]. From Figs. 4.2-4.3, a significant energy gap between the valence band maximum (VBM) and conduction band minimum (CBM) are observed in both the majority- and minority-spin channels of both the compounds. Present band structures indicate a direct band gap (E_g) semiconducting nature of $ZnFe_2O_4$ and $CdFe_2O_4$, as VBM and CBM are found at the same Γ point. The band gap value for both the compounds is lower in case of minority-spin bands channels than that in majority-spin channel (Figs. 4.2-4.3). In Table 4.4, we have collated band gap values derived using various approximation (LCAO-DFT-LDA, LCAO-DFT-GGA, LCAO-B3LYP and LCAO-PBE0) along with available theoretical and experimental data [7,12,13,14,18,40,41,42] for $TMFe_2O_4$. Our band gap values using LCAO-DFT-LDA and LCAO-DFT-GGA schemes underestimate the experimental band gap [40-42] for both the compounds, while a reverse trend is found for LCAO-B3LYP and LCAO-PBE0 schemes. It is seen that B3LYP approach shows a closer agreement with the experimental band gap than other schemes considered within the periphery of LCAO prescription. It is worthwhile to mention that most of the theoretical prescriptions using pure LDA and GGA schemes have underestimated the band gap values than the experimental band gaps, as evident from Table 4.4. This trend is consistent with the general observation that the HF calculations overestimate the band gap (because of lack of screening in the exchange term leading to an over stabilization of occupied states) and the DFT based LDA and GGA theories underestimate the band gap. It is quite

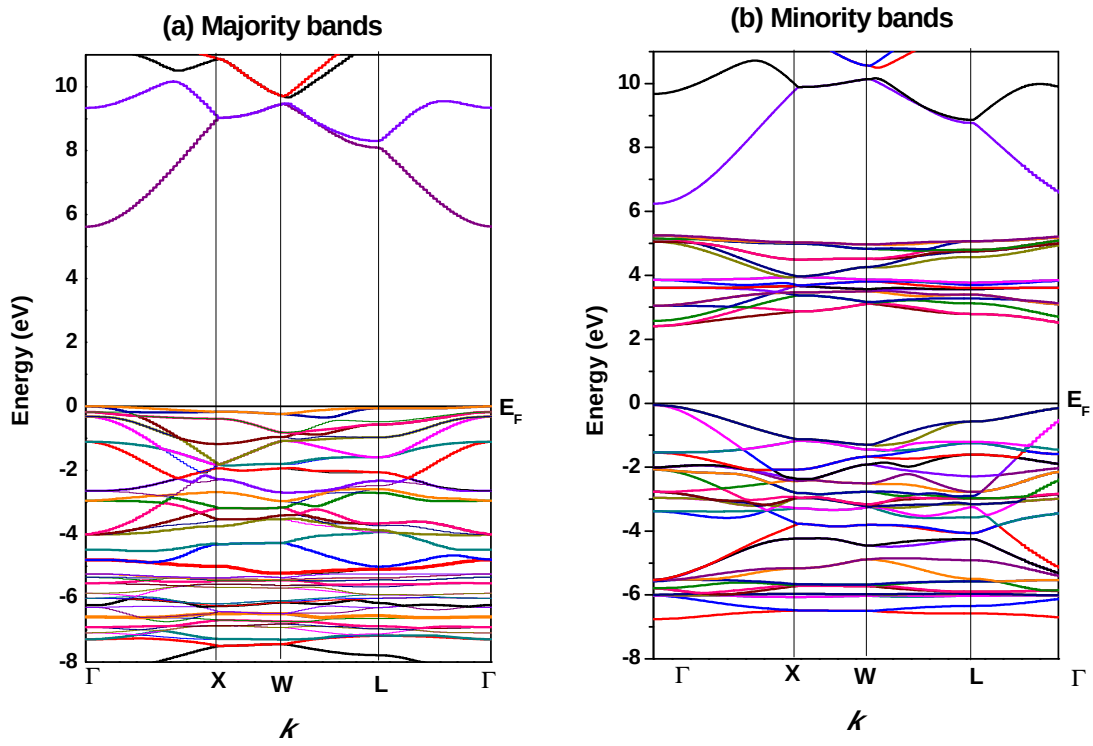

Fig. 4.2: (a) Majority- and (b) minority-spin energy bands of $ZnFe_2O_4$ using LCAO-B3LYP scheme along the high symmetry directions of BZ. The positions of Γ, X, W and L vertices are (0,0,0), (1/2,0,1/2), (1/2,1/4,3/4) and (1/2,1/2,1/2), respectively.

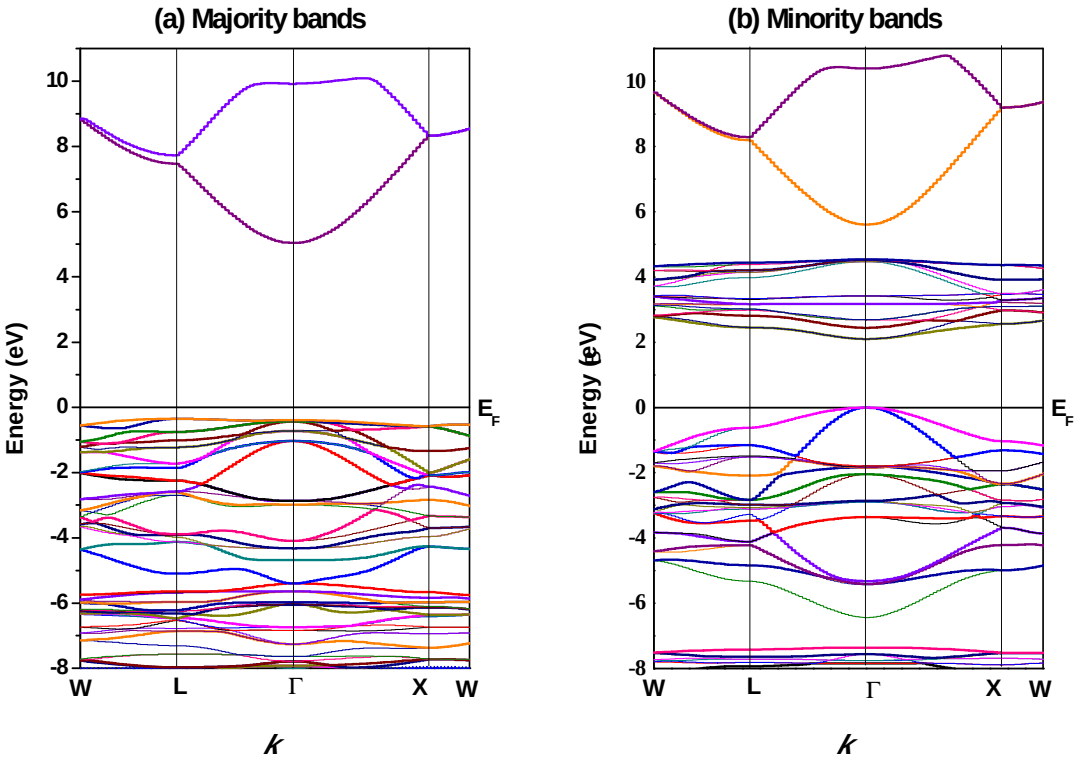

Fig. 4.3: (a) Majority- and (b) minority-spin energy bands of $CdFe_2O_4$ using LCAO-B3LYP scheme along the high symmetry directions of BZ.

Table 4.4: Band gap (Eg) for $ZnFe_2O_4$ and $CdFe_2O_4$ using various combinations of exchange-correlation potentials within LCAO schemes as mentioned in the text along with the available data.

Approach	Band gap (Eg) in eV	
	$ZnFe_2O_4$	$CdFe_2O_4$
(i) Present computations		
LCAO-DFT-LDA	1.06	0.52
LCAO-DFT-GGA	1.37	0.40
LCAO-B3LYP	2.40	2.10
LCAO-PBE0	3.22	3.26
(ii) Available theories		
(a) Plane wave pseudopotential (PWP) [7] with		
LDA-CA-PZ	0.87	---
GGA-PBE	0.84	---
GGA-RPBS	0.93	---
GGA-PW91	0.79	---
GGA-WC	0.87	---
GGA-PBESOL	0.80	---
(b) FP-LAPW + lo [12]	2.20	---
(c) FP-LAPW + lo with GGA+U [13]		
Non inverted	2.00	---
Inverted	2.10	---
(d) Projector-augmented wave (PAW) [40] with		---
GGA+U (spinel)	1.68	---
PBE0 (spinel)	3.68	---
GGA+U (inverse)	1.91	---
PBE0 (inverse)	3.37	---
(e) FP-LAPW with PBESOL+mBJ [14]	---	1.86
(f) FP-LAPW-DFT [18] with		
GGA+U	---	1.56
TB-mBJ	---	1.88
(iii) Available experiment		
Yao et al. [7]	1.90	---
Valeznuela et al. [41]	1.92	---
Akamatsu et al. [42]	---	1.46

satisfying that in this situation the hybrid method (mixing of HF to DFT) like B3LYP minimizes the deviation of band gap from the experimental values and leads to reasonable electronic response for such compounds.

In Fig. 4.4 (a-d), we have shown DOS for spin-up (↑) and spin-down (↓) states using LCAO-B3LYP scheme for 3d, 4s states of Zn; 3d, 4s states of Fe; 2s, 2p states of O and total DOS for $ZnFe_2O_4$. Similarly spin projected DOS for $CdFe_2O_4$ environment are plotted in Figs. 4.5(a-d). The Fermi energy (E_F) is shifted to 0 eV. The majority-spin and minority-spin DOS for both the compounds unambiguously reconfirm the semiconducting nature of both the compounds. In Fig. 4.4 (Fig. 4.5), the DOS in energy range −8.34 (−8.65) eV to the E_F level are mostly contributed by the 3d (4d) electrons of Zn (Cd) and 3d electrons of Fe atom along with a small contribution of 2p electrons of O atoms. In Fig. 4.4(d), the majority-spin states dominate in the formation of the DOS in the energy range −8.34 to −6.77 eV, while the DOS in the energy range +2.40 to +5.23 eV are majorly contributed by the minority-spin states of $ZnFe_2O_4$. In case of $CdFe_2O_4$ (Fig. 4.5d), contribution of minority-spin (majority-spin) DOS are found to be absent in the energy range −7.36 to −6.46 (+2.10 to 4.52) eV. In Fig. 4.4(a), the majority-spin DOS of Zn-3d states are dominated in the energy range −8.34 to −6.60 eV while the trend becomes reverse and dominancy of minority-spin DOS of 3d states of Zn prevails between −6.60 to −5.53 eV. Similarly major role of majority-spin states of Fe is found between the energy range −8.34 to −3.30 eV (Fig. 4.4b). In the conduction band region between +2.40 to +5.23 eV, the DOS are majorly governed by 3d minority-spin states of Fe atom along with a small contribution of minority-spin states of 2p electrons of O atom (Figs. 4.4b,c). In Fig. 4.5(a), major contribution of majority-spin states of 4d electrons of Cd is seen between −8.65 to −7.89 eV and a reverse trend is observed between −7.89 to −7.38 eV. For 3d electrons of Fe (Fig. 4.5b), the majority-spin contribution dominates in the valence band region (−8.65 to −0.36 eV) and minority-spin contribution dominates in conduction band region (+2.10 to +4.52 eV) of $CdFe_2O_4$. From Fig. 4.4c for $ZnFe_2O_4$ and Fig. 4.5c for $CdFe_2O_4$, a small contribution below the VBM is found from majority- and minority-spin states of

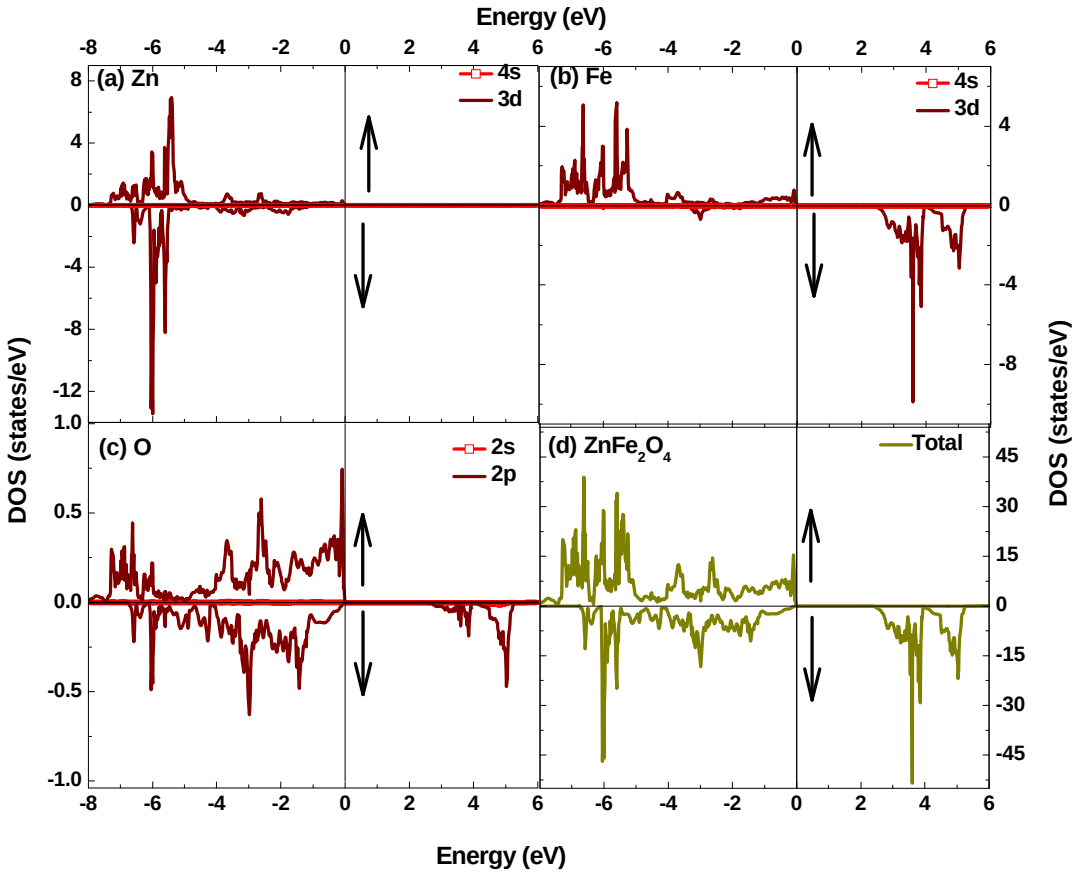

Fig. 4.4: Majority-spin (↑) and minority-spin (↓) density of states (DOS) for (a) 3d and 4s states of Zn, (b) 3d and 4s states of Fe, (c) 2s and 2p states of O and (d) total $ZnFe_2O_4$ using LCAO-B3LYP approximation.

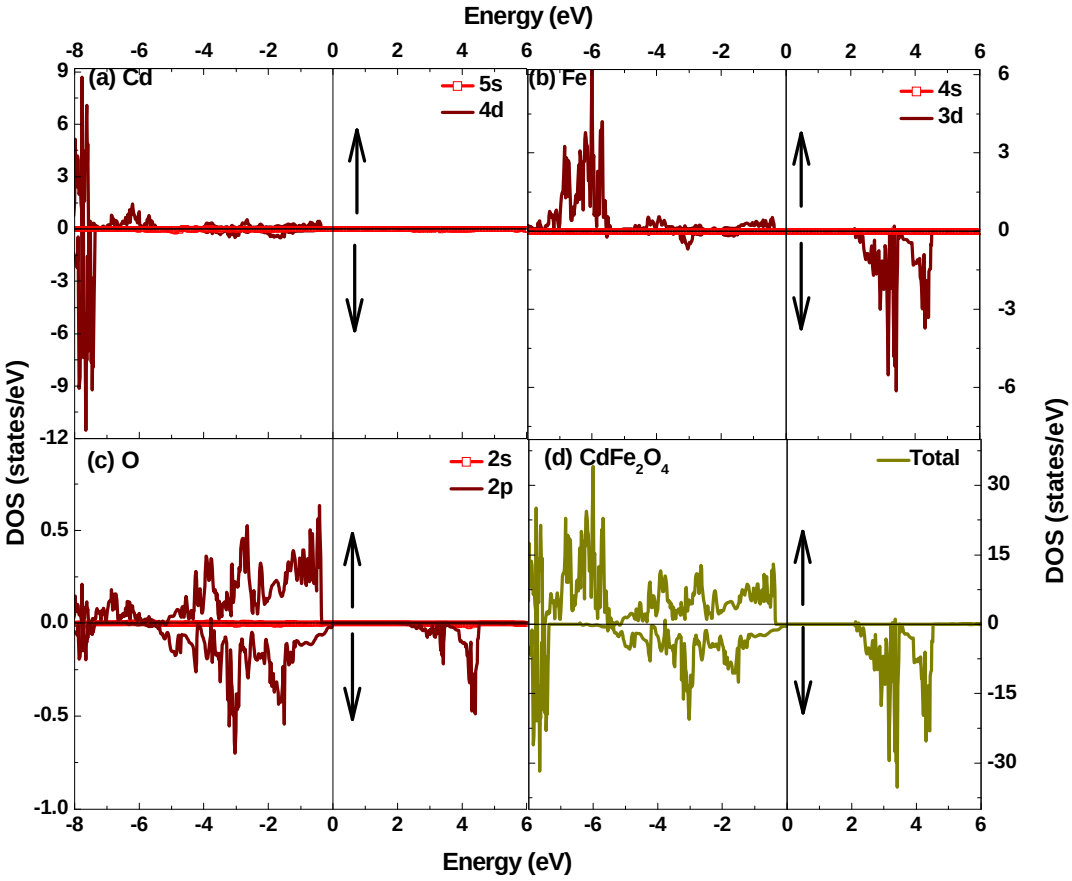

Fig. 4.5: Majority-spin (↑) and minority-spin (↓) density of states (DOS) for (a) 4d and 5s states of Cd, (b) 3d and 4s states of Fe, (c) 2s and 2p states of O and (d) total $CdFe_2O_4$ using LCAO-B3LYP approximation. The range of DOS is different than that in energy bands for a clear visualization.

O, while the contribution of only minority-spin states of O atoms in CBM is witnessed. It is observed that the VBM is formed by the majority-spin states of 3d (4d) of Zn (Cd) and 3d states of Fe along with the a small contribution of majority-spin O-2p states for $ZnFe_2O_4$ ($CdFe_2O_4$). Also, the CBM is built mainly by minority-spin of 3d (4d) states of Fe along with a small contribution of minority-spin of 2p states of O atom in $ZnFe_2O_4$ ($CdFe_2O_4$).

4.3.3. Compton profiles:

In Figs. 4.6 (a-b), the anisotropies between unconvoluted theoretical CPs (J_{110}-J_{100}, J_{111}-J_{100} and J_{111}-J_{110}) using LCAO-DFT-LDA, LCAO-DFT-GGA, LCAO-B3LYP and LCAO-PBE0 schemes are presented for $ZnFe_2O_4$ and $CdFe_2O_4$, respectively. An overall trend of oscillations in the anisotropies (J_{110}−J_{100}, J_{111}−J_{100} and J_{111}−J_{110}) for $TMFe_2O_4$ (TM = Zn and Cd) using LCAO computations (DFT-LDA, DFT-GGA, B3LYP and PBE0) are found to be similar. In the higher momentum region ($p_z \geq 4.0$ a.u.), negligible anisotropic effects in momentum densities of both the compounds has been observed for all the considered schemes (LCAO-DFT-LDA, LCAO-DFT-GGA, LCAO-B3LYP and LCAO-PBE0). In high momentum region, such observations are quite expected as core electrons which contribute to formation of CPs in this region remain unaffected in directional momentum densities. Anisotropic effects are observed in the low momentum region ($p_z \leq 4.0$ a.u.), which are dictated by dispersive nature of energy bands and their degeneracy in different branches of BZ. In low momentum side, the trend of anisotropies in hybrid schemes (LCAO-B3LYP and LCAO-PBE0) are almost similar, while it differs from the overall trend seen for LCAO-DFT-LDA and LCAO-DFT-GGA schemes. Such a trend in hybrid calculations may be due to the incorporation of HF exchange energy component in B3LYP and PBE0 schemes, which was absent in DFT with LDA and GGA. As expected, the oscillations in CP anisotropies in Figs. 4.6 (a-b) are also in consonance with the cross-overs and degenerate states of majority- and minority-spin energy bands (Fig. 4.2 and 4.3) for both the compounds. The positive values of anisotropies (J_{111}-J_{100} and J_{111}-J_{110}) in Figs. 4.6(a,b) near p_z = 0.0 a.u. are due to the large degenerate states along [111] direction as compared to [100] and [110] directions.

(a) (b)

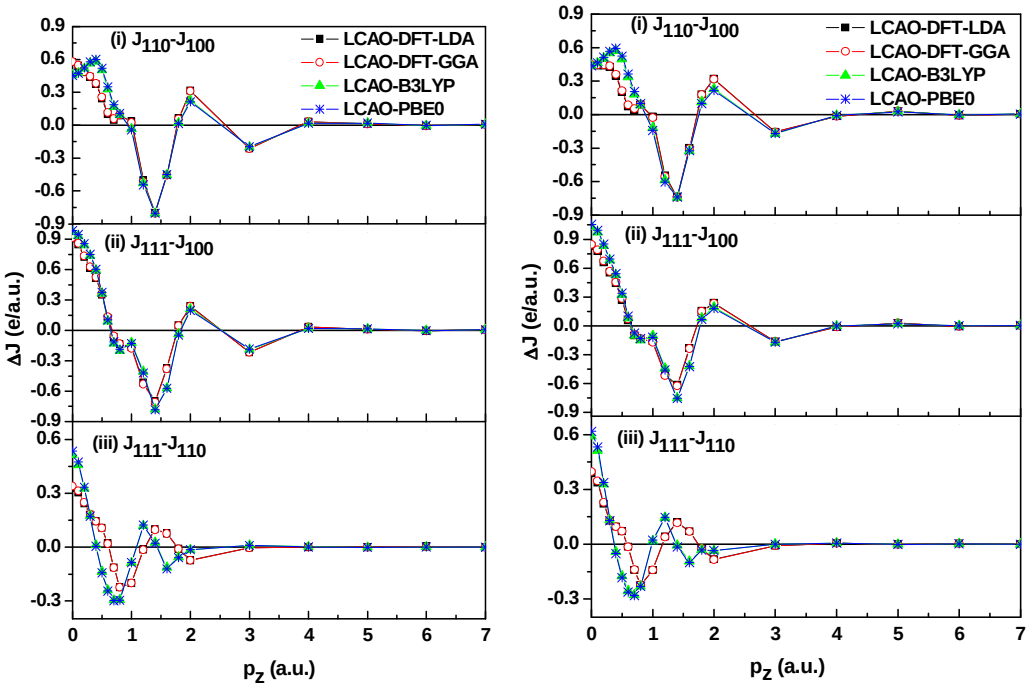

Fig. 4.6: Anisotropies in the unconvoluted theoretical Compton profiles of (a) $ZnFe_2O_4$ and (b) $CdFe_2O_4$ calculated using LCAO-DFT-LDA, LCAO-DFT-GGA, LCAO-B3LYP and LCAO-PBE0 approximations for the directional pairs (i) J_{110}–J_{100}, (ii) J_{111}–J_{100} and (iii) J_{111}–J_{110}. The solid lines are drawn for a quick view of trend.

Decreasing order of J(p_z=0.0 a.u.) values for the three crystallographic directions is found to be [111]→[110]→[100] for both the compounds which shows signatures of atomic density effects in different principal orientations. Also, the negative amplitude near p_z = 1.5 a.u. along J_{111}-J_{100} in Fig. 4.6(a,b) arises due to zone boundary of Γ-X (0.39 a.u.; n=4 for $ZnFe_2O_4$ and 0.38 a.u.; n=4 for $CdFe_2O_4$) branch. It may be noted that some fine structures may be invisible in the anisotropies (Fig. 4.6) because of cancellation effect on taking the differences of CPs. Anisotropic measurements of CPs for $ZnFe_2O_4$ and $CdFe_2O_4$ are necessitated to validate the theoretical anisotropic effects in momentum densities (Fig. 4.6). The numerical values of directional CPs using LCAO-DFT-LDA, LCAO-DFT-GGA, LCAO-B3LYP and LCAO-PBE0 schemes for $ZnFe_2O_4$ and $CdFe_2O_4$ are also listed in Tables 4.5-4.6, respectively.

The difference in CPs between convoluted theoretical (LCAO-DFT-LDA, LCAO-DFT-GGA, LCAO-B3LYP and LCAO-PBE0) and experimental data have been plotted in Figs. 4.7 (a-b) for $ZnFe_2O_4$ and $CdFe_2O_4$, respectively. The numerical values of unconvoluted theoretical (LCAO-DFT-LDA, LCAO-DFT-GGA, LCAO-B3LYP and LCAO-PBE0) and experimental CPs for $ZnFe_2O_4$ and $CdFe_2O_4$ (with statistical errors) have been collated in Tables 4.7-4.8, respectively. In Tables 4.7-4.8, total CPs for each approximation is calculated by adding the FA core CP contribution [35] to the respective LCAO based CP data of valence electrons. Also, to mimic experimental resolution, each theoretical data is convoluted with fwhm of 0.34 a.u. (momentum resolution of present experimental setup) before taking the difference between theoretical and experimental CPs. From Tables 4.7-4.8 and Figs. 4.7 (a-b), it is observed that experimental CP data of both the compounds underestimate the momentum densities in the low momentum region ($p_z \leq 1.0$. a.u.). This trend reverse in the region $1.0 \leq p_z \leq 4.0$ a.u. Also, the difference in the higher momentum region ($p_z \geq 4.0$. a.u.) is very small (within the experimental error) for $CdFe_2O_4$. Such trend in high momentum region is expected because of contribution of core electrons whose wave functions are well defined by HF approximation. For quantitative conclusions related to goodness of agreement between theoretical CP with the experimental data for

Table 4.5: The directional CPs (unconvoluted) of $ZnFe_2O_4$ along [100], [110] and [111] using LCAO-DFT-LDA, LCAO-DFT-GGA, LCAO-B3LYP and LCAO-PBE0 schemes.

p_z (a.u.)	J (p_z) (e/a.u.)											
	LCAO-DFT-LDA			LCAO-DFT-GGA			LCAO-B3LYP			LCAO-PBE0		
	[100]	[110]	[111]	[100]	[110]	[111]	[100]	[110]	[111]	[100]	[110]	[111]
0.0	25.698	26.274	26.604	25.671	26.250	26.590	25.499	25.956	26.471	25.525	25.978	26.512
0.1	25.684	26.226	26.531	25.658	26.204	26.518	25.474	25.948	26.406	25.500	25.973	26.447
0.2	25.454	25.936	26.179	25.434	25.921	26.170	25.234	25.751	26.078	25.261	25.783	26.117
0.3	25.026	25.464	25.645	25.010	25.456	25.638	24.832	25.397	25.571	24.859	25.437	25.609
0.4	24.372	24.746	24.889	24.359	24.742	24.885	24.238	24.819	24.830	24.263	24.863	24.867
0.5	23.682	23.926	24.033	23.669	23.925	24.031	23.604	24.105	23.968	23.627	24.148	24.004
0.6	22.855	22.958	22.979	22.845	22.961	22.980	22.815	23.145	22.904	22.834	23.183	22.938
0.7	21.852	21.899	21.785	21.847	21.905	21.791	21.847	22.016	21.720	21.861	22.049	21.750
0.8	20.614	20.701	20.477	20.618	20.711	20.487	20.651	20.744	20.451	20.662	20.770	20.475
1.0	17.965	18.000	17.799	17.988	18.013	17.813	18.009	17.975	17.888	18.026	17.983	17.897
1.2	15.712	15.207	15.194	15.736	15.222	15.207	15.710	15.184	15.304	15.719	15.175	15.298
1.4	13.729	12.928	13.029	13.745	12.940	13.037	13.792	12.987	13.012	13.778	12.975	12.996
1.6	11.586	11.133	11.210	11.595	11.138	11.213	11.689	11.234	11.120	11.670	11.220	11.099
1.8	9.684	9.745	9.735	9.688	9.745	9.735	9.758	9.778	9.722	9.748	9.761	9.702
2.0	8.236	8.550	8.477	8.237	8.548	8.475	8.309	8.536	8.520	8.305	8.518	8.504
3.0	4.975	4.762	4.759	4.972	4.759	4.756	4.951	4.753	4.763	4.941	4.746	4.755
4.0	2.976	3.009	3.009	2.976	3.008	3.008	2.992	3.010	3.012	2.990	3.008	3.010
5.0	2.081	2.093	2.093	2.081	2.093	2.093	2.078	2.097	2.095	2.078	2.096	2.094
6.0	1.549	1.542	1.545	1.549	1.542	1.545	1.549	1.545	1.546	1.548	1.545	1.546
7.0	1.160	1.167	1.167	1.160	1.167	1.167	1.160	1.168	1.168	1.160	1.168	1.168

Table 4.6: Same as Table 4.5 except the sample which is $CdFe_2O_4$.

p_z (a.u.)	J (p_z) (e/a.u.)											
	LCAO-DFT-LDA			LCAO-DFT-GGA			LCAO-B3LYP			LCAO-PBE0		
	[100]	[110]	[111]	[100]	[110]	[111]	[100]	[110]	[111]	[100]	[110]	[111]
0.0	28.019	28.461	28.848	27.984	28.432	28.829	27.695	28.134	28.726	27.715	28.152	28.770
0.1	27.972	28.410	28.746	27.939	28.384	28.729	27.661	28.122	28.634	27.682	28.144	28.677
0.2	27.694	28.132	28.353	27.666	28.112	28.340	27.433	27.938	28.268	27.457	27.970	28.308
0.3	27.222	27.647	27.775	27.199	27.634	27.765	27.038	27.590	27.723	27.064	27.631	27.760
0.4	26.539	26.886	26.982	26.520	26.879	26.974	26.415	26.987	26.946	26.438	27.032	26.981
0.5	25.828	26.028	26.099	25.811	26.024	26.094	25.735	26.232	26.058	25.753	26.277	26.094
0.6	24.962	25.033	25.018	24.948	25.032	25.018	24.896	25.232	24.977	24.909	25.273	25.011
0.7	23.869	23.910	23.768	23.862	23.913	23.772	23.845	24.027	23.748	23.854	24.060	23.779
0.8	22.540	22.627	22.402	22.544	22.635	22.411	22.568	22.653	22.421	22.577	22.676	22.445
1.0	19.763	19.745	19.604	19.787	19.758	19.617	19.807	19.687	19.704	19.830	19.689	19.711
1.2	17.353	16.806	16.848	17.379	16.822	16.860	17.375	16.788	16.932	17.385	16.779	16.925
1.4	15.120	14.386	14.505	15.139	14.398	14.515	15.218	14.472	14.466	15.201	14.464	14.448
1.6	12.726	12.424	12.494	12.737	12.431	12.499	12.860	12.534	12.441	12.844	12.522	12.421
1.8	10.661	10.841	10.816	10.668	10.844	10.818	10.756	10.869	10.838	10.753	10.854	10.821
2.0	9.144	9.465	9.381	9.148	9.466	9.381	9.222	9.453	9.416	9.222	9.436	9.401
3.0	5.450	5.294	5.286	5.448	5.292	5.283	5.456	5.285	5.285	5.446	5.278	5.277
4.0	3.570	3.553	3.558	3.570	3.552	3.557	3.559	3.551	3.557	3.556	3.548	3.554
5.0	2.618	2.649	2.647	2.617	2.648	2.647	2.624	2.650	2.648	2.624	2.649	2.647
6.0	2.051	2.042	2.046	2.050	2.042	2.046	2.046	2.044	2.046	2.044	2.043	2.045
7.0	1.584	1.588	1.588	1.584	1.588	1.588	1.585	1.589	1.588	1.584	1.589	1.588

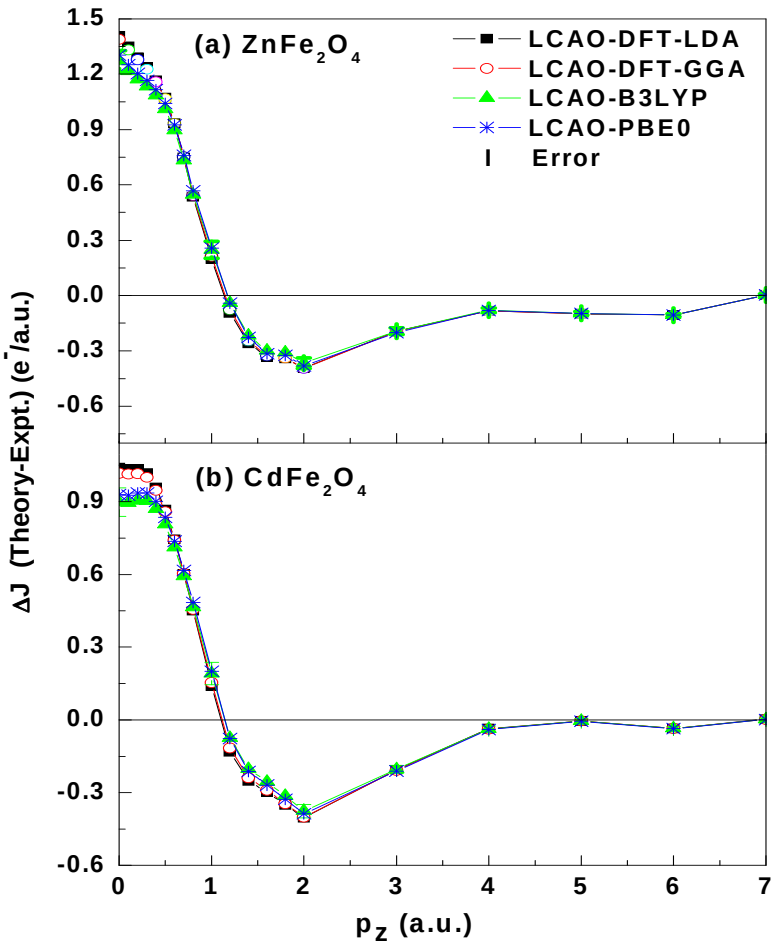

Fig. 4.7: The difference profiles deduced from isotropic convoluted theoretical (LCAO-DFT-LDA, LCAO-DFT-GGA, LCAO-B3LYP and LCAO-PBE0 approximations) and experimental Compton profiles for (a) $ZnFe_2O_4$ and (b) $CdFe_2O_4$. The solid lines are drawn for a quick view of trend.

Table 4.7: Unconvoluted theoretical (LCAO-DFT-LDA, LCAO-DFT-GGA, LCAO-B3LYP and LCAO-PBE0) and experimental Compton profiles along with statistical errors (±σ) for $ZnFe_2O_4$.

p_z (a.u.)	J (p_z) (e/a.u.)				
	Theory				Expt.
	LCAO-DFT-LDA	LCAO-DFT-GGA	LCAO-B3LYP	LCAO-PBE0	
0.0	26.136	26.117	25.996	26.029	24.659±0.058
0.1	26.098	26.080	25.960	25.993	24.571±0.058
0.2	25.831	25.816	25.700	25.734	24.341±0.057
0.3	25.394	25.382	25.280	25.314	23.954±0.057
0.4	24.728	24.719	24.643	24.676	23.407±0.056
0.5	23.955	23.950	23.900	23.932	22.714±0.054
0.6	22.990	22.988	22.953	22.982	21.905±0.053
0.7	21.878	21.882	21.858	21.884	21.003±0.052
0.8	20.621	20.630	20.631	20.653	20.014±0.050
1.0	17.952	17.968	18.018	18.030	17.772±0.046
1.2	15.341	15.357	15.395	15.392	15.540±0.042
1.4	13.143	13.155	13.183	13.170	13.484±0.038
1.6	11.248	11.254	11.281	11.265	11.678±0.035
1.8	9.718	9.720	9.751	9.735	10.134±0.031
2.0	8.468	8.467	8.495	8.480	8.920±0.029
3.0	4.794	4.791	4.793	4.785	5.002±0.018
4.0	3.006	3.006	3.010	3.007	3.099±0.012
5.0	2.092	2.091	2.093	2.092	2.193±0.010
6.0	1.542	1.542	1.543	1.543	1.651±0.007
7.0	1.167	1.167	1.167	1.167	1.183±0.005

Table 4.8: Unconvoluted theoretical (LCAO-DFT-LDA, LCAO-DFT-GGA, LCAO-B3LYP and LCAO-PBE0) and experimental Compton profiles along with statistical errors (±σ) for $CdFe_2O_4$.

p_z (a.u.)	J (p_z) (e/a.u.)				
	Theory				Expt.
	LCAO-DFT-LDA	LCAO-DFT-GGA	LCAO-B3LYP	LCAO-PBE0	
0.0	28.354	28.329	28.211	28.243	27.237±0.059
0.1	28.308	28.285	28.162	28.194	27.089±0.059
0.2	28.042	28.021	27.897	27.929	26.792±0.058
0.3	27.586	27.569	27.460	27.492	26.347±0.058
0.4	26.874	26.861	26.784	26.816	25.750±0.056
0.5	26.051	26.042	25.997	26.027	25.008±0.055
0.6	25.039	25.035	25.006	25.034	24.128±0.054
0.7	23.859	23.861	23.844	23.869	23.123±0.052
0.8	22.534	22.542	22.550	22.570	22.009±0.050
1.0	19.726	19.742	19.793	19.802	19.599±0.046
1.2	16.961	16.978	17.019	17.015	17.192±0.042
1.4	14.589	14.602	14.637	14.625	14.918±0.038
1.6	12.502	12.510	12.546	12.532	12.898±0.034
1.8	10.789	10.793	10.825	10.812	11.221±0.031
2.0	9.386	9.387	9.412	9.400	9.854±0.028
3.0	5.317	5.315	5.319	5.312	5.543±0.017
4.0	3.555	3.554	3.554	3.552	3.601±0.012
5.0	2.646	2.646	2.647	2.645	2.653±0.009
6.0	2.042	2.042	2.042	2.041	2.079±0.007
7.0	1.587	1.587	1.587	1.587	1.609±0.006

both the compounds, we have undertaken χ^2 fitting. For this purpose, we have used the following formula,

$$\chi^2 = \sum_{p_z=0}^{7} \left[\frac{J^{LCAO-DFT-LDA/LCAO-DFT-GGA/LCAO-B3LYP/LCAO-PBE0}(p_z) - J^{Experiment}(p_z)}{\sigma(p_z)} \right]^2 \quad (4.6)$$

Here $\sigma(p_z)$ is the statistical error at each p_z value. The χ^2 value for $ZnFe_2O_4$ ($CdFe_2O_4$) using LCAO-DFT-LDA, LCAO-DFT-GGA, LCAO-B3LYP and LCAO-PBE0 approximations are computed as 4540.14 (2847.40), 4484.60 (2776.84), 3951.46 (2356.82) and 4189.12 (2534.73), respectively. Hence, the lowest value of χ^2 indicates an overall better agreement by LCAO-B3LYP scheme for both the compounds. Further similar type of performance of both the hybridized approximations (LCAO-B3LYP and LCAO-PBE0) is due to an incorporation of HF exchange effects in such computations. The difference in LCAO-B3LYP and LCAO-PBE0 data may be due to the different contribution of hybridization in exchange and correlation potentials and the percentage of mixing of HF with DFT (being 20 and 25 % in B3LYP and PBE0 schemes). In the low momentum side differences between theoretical and experimental CPs may be due to non-inclusion of relativistic effects and Lam-Platzman (LP) correlation [19] in LCAO calculations and further possibility for improvement in the quality of Gaussian basis sets used in the present computations.

4.3.4. EVED:

To highlight relative nature of bonding in the present iso-electronic compounds, we have rescaled the LCAO-B3LYP based CP and experiment profile on EVED (p_z/p_F) parameters (Fig. 4.8). Values of Fermi momentum (p_F) for $ZnFe_2O_4$ and $CdFe_2O_4$ were taken as 1.48 and 1.42 a.u., respectively. The outer electrons configurations of Zn (Cd), Fe and O atoms in $TMFe_2O_4$ (TM = Zn and Cd) environment are considered as $3d^{10}4s^2$ ($4d^{10}5s^2$), $3d^64s^2$ and $2s^22p^4$, respectively. Since the total valence electrons in both the iso-electronic compounds are 52, therefore each EVED profile has been normalized to 26 e^- in the major p_z range of 0-2 a.u. From Fig. 4.8, EVED (p_z/p_F =0) value of $CdFe_2O_4$ using LCAO-B3LYP (experiment) is found to be 2.61 (0.76) %

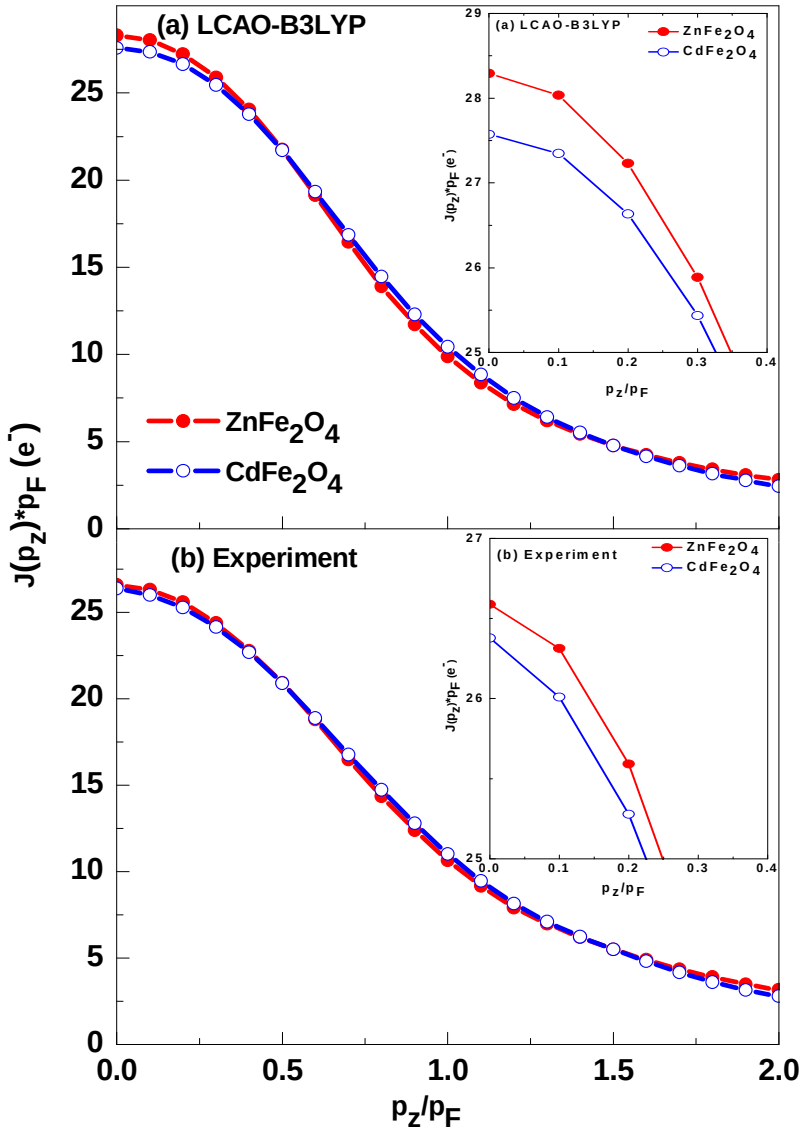

Fig. 4.8: Equal-valence-electron-density (EVED) profiles of iso-electronic $ZnFe_2O_4$ and $CdFe_2O_4$ for (a) LCAO-B3LYP and (b) experimental. In the inset, the values of $J(p_z/p_F)$ near $p_z/p_F=0$ are shown.

lesser than that of $ZnFe_2O_4$. Such a trend indicates more ionic (or less covalent) character of $CdFe_2O_4$ than $ZnFe_2O_4$. This is admittedly due to a fact that the lower value of $J(p_z/p_F=0.0)$ indicates the lesser sharing of the electrons along the bond directions which further leads to lesser covalent (or higher ionic) character in the compound. Trend shown by present theoretical (B3LYP) and experimental EVED profiles is also in accordance with earlier discussed MP and OP analysis. Such type of confirmation of charge transfer and overlap populations (as deduced from MP analysis) was also quite successful in other compounds like $TMWO_4$ (TM= Zn and Cd) [37], Ag_2TMO_4 (TM= Cr and Mo) [38], $TMTiO_3$ (TM = Ba, Sr and Ca) [39].

4.3.5. LCAO based Magnetization:

Local magnetic moments for Fe ions in $ZnFe_2O_4$ ($CdFe_2O_4$) have been calculated using LCAO-DFT-LDA, LCAO-DFT-GGA, LCAO-B3LYP and LCAO-PBE0 schemes and the values are found to be 3.47 (3.87), 3.99 (4.07), 4.24 (4.24) and 4.31 (4.32) μ_B per formula unit, respectively. Here, the unit cell magnetic moment for $ZnFe_2O_4$ ($CdFe_2O_4$) are also calculated as 7.87 (9.23), 9.57 (9.93), 9.99 (9.99) and 10.01 (10.01) μ_B from LCAO-DFT-LDA, LCAO-DFT-GGA, LCAO-B3LYP and LCAO-PBE0 schemes, respectively. Our LCAO-B3LYP formulation based magnetic moments of Fe ions for both the ferrites are in accordance with the available data [3,8,9,12,13,14]. In case of LCAO-B3LYP, the magnetic moment of Fe ions is approximately equal to the experimental value of 4.22 μ_B. Also, our unit cell magnetic moment using LCAO-B3LYP scheme for $ZnFe_2O_4$ is found to be same as reported by Soliman et al. [8] using FP-LAPW approach.

4.4. Conclusions:

MP analysis, energy bands, DOS, band gaps and CPs computed using DFT-LDA, DFT-GGA, B3LYP and PBE0 within LCAO approximations along with Compton profile measurements for $ZnFe_2O_4$ and $CdFe_2O_4$ are presented. Further, MP analysis shows the charge transfer from zinc/cadmium and iron to oxygen atoms. On the basis of EVED CPs and MP data, more ionic character in $CdFe_2O_4$ than that in $ZnFe_2O_4$ was observed. The magnetic moments are well explored by the LCAO-B3LYP

approximation. A closer agreement of LCAO-B3LYP based Compton profiles with the experimental CPs, reproducibility of band gaps, confirmation of trend of B3LYP based MP and OP data together with electronic response and magnetization data unambiguously warrants use of hybrid functionals for exchange and correlation potentials in the spinel ferrites, as reported here.

References

1. B.J. Evans, S.S. Hafner, H.P. Weber, J. Chem. Phys. 55 (1971) 5282–5288.

2. A.F. Pasquevich, J. Shitu, Hyperfine Interactions 120/121 (1999) 463–468.

3. C. Cheng, Phys. Rev. B 78 (2008) 132403-1–132403-4.

4. C. Cheng, C.-S. Liu, J. Phys.: Conf. Ser. 145 (2009) 012028-1–012208-4.

5. M. Pénicaud, B. Siberchicot, C.B. Sommers, J. Kübler, J. Mag. Mag. Mat. 103 (1992) 212–220.

6. D.J. Singh, M. Gupta, R. Gupta, Phys. Rev. B 63 (2001) 205102-1–205102-5.

7. J. Yao, X. Li, Y. Li, S. Le, Integrated Ferroelectrics 145 (2013) 17–23.

8. S. Soliman, A. Elfalaky, G.H. Fecher, C. Felser, Phys. Rev. B 83 (2011) 085205-1–085205-6.

9. W. Schiessl, W. Potzel, H. Karzel, M. Steiner, G.M. Kalvius, A. Martin, M.K. Krause, I. Halevy, J. Gal, W. Schäfer, G. Will, M. Hillberg, R. Wäppling, Phys. Rev. B 53 (1996) 9143–9152.

10. W.B. Cross, L. Affleck, M.V. Kuznetsov, I.P. Parkin, Q.A. Pankhurst, J. Mater. Chem. 9 (1999) 2545–2552.

11. K. Rama Krishna, D. Ravinder, K. Vijaya Kumar, Ch. Abraham Lincon, World J. Condens. Mater. Phys. 2 (2012) 153–159.

12. J.J.M. Quintero, K.L.S. Rodríguez, G.A. Pasquevich, P.M. Zélis, S.J. Stewart, C.E.R. Torres, L.A. Errico, Hyperfine Interact. 237 (2016) 63-1–63-7.

13. J.J.M. Quintero, K.L.S. Rodríguez, C.E.R. Torres, L.A. Errico, J. Alloys Compounds 775 (2019) 1117–1128.

14. Q. Mahmood, M. Yaseen, K.C. Bhamu, A. Mahmood, Y. Javed, S.M. Ramay, Chin. Phys. B 27 (2018) 037103-1-037103-8.

15. A.K. Nikumbh, A.V. Nagawade, G.S. Gugale, M.G. Chaskar, P.P. Bakare, J. Mater. Sci. 37 (2002) 637–647.

16. K. Kamazawa, S. Park, S.-H. Lee, T.J. Sato, Y. Tsunoda, Phys. Rev. B 70 (2004) 024418-1-024418-5.

17. S. Noor, M.M. Rahman, S.S. Sikder, M.A. Hakim, Jahangirnagar Univ. J. Sci. 34 (2011) 1-11.

18. H. Zaari, A.G. El hachimi, A. Benyoussef, A. El Kenz, J. Mag. Mag. Mat. 393 (2015) 183–187.

19. M.J. Cooper, P.E. Mijnarends, N. Shiotani, N. Sakai, A. Bansil, X-ray Compton Scattering, Oxford University Press, New York, 2004.

20. N.L. Heda, B.L. Ahuja, Recent Trends in Radiation Physics Research, in: B.L. Ahuja (Ed.), Himanshu Publications, New Delhi, India, 2010, 25–30.

21. R. Dovesi, V.R. Saunders, C. Roetti, R. Orlando, C.M. Zicovich-Wilson, F. Pascale, B. Civalleri, K. Doll, N.M. Harrison, I.J. Bush, Ph. D'Arco, M. Llunell, M. Causa, Y. Neol. CRYSTAL14 User's Manual, University of Torino, Torino, 2014, and references therein.

22. J.P. Perdew, A. Zunger, Phys. Rev. B 23 (1981) 5048–5079.

23. J.P. Perdew, A. Ruzsinszky, G.I. Csonka, O.A. Vydrov, G.E. Scuseria, L.A. Constantin, X. Zhou, K. Burke, Phys. Rev. Lett. 100 (2008) 136406-1–136406-4.

24. J. Muscat, C. Klauber, Surf. Sci. 491 (2001) 226–238.

25. C. Adamo, V. Barone, J. Chem. Phys. 110 (1999) 6158–6170.

26. A.D. Becke, Phys. Rev. A 38 (1988) 3098–3100.

27. J.P. Perdew, K. Burke, M. Ernzerhof, Phys. Rev. Lett. 77 (1996) 3865–3868

28. C. Lee, W. Yang, R.G. Parr, Phys. Rev. B 37 (1988) 785–789.

29. S.H. Vosko, L. Wilk, M. Nusair, Can. J. Phys. 58 (1980) 1200–1211.

30. http://www.crystal.unito.it/basis-sets.php (2019).

31. A. Kokaji, Comput. Mater. 28 (2003) 155–168.

32. B.L. Ahuja, M. Sharma, S. Mathur, Nucl. Instrum. Methods B 244 (2006) 419–426.

33. D.N. Timms, Compton Scattering Studies of Spin and Momentum Densities (Ph.D. thesis), University of Warwick, UK, 1989 (Unpublished).

34. J. Felsteiner, P. Pattison, M.J. Cooper, Philos. Mag. 30 (1974) 537–548.

35. F. Biggs, L.B. Mendelsohn, J.B. Mann, At. Data Nucl. Data Tables 16 (1975) 201–308.

36. B.S. Meena, N.L. Heda, K. Kumar, S. Bhatt, H.S. Mund, B.L. Ahuja, Physica B 484 (2016) 1-6.

37. B.S. Meena, N.L. Heda, H.S. Mund, B.L. Ahuja, Rad. Phys. Chem. 117 (2015) 93-101.

38. S.K. Meena, N.L. Heda, G. Arora, L. Meena, B.L. Ahuja, Physica B 560 (2019) 236-243.

39. S.K. Meena, A. Dashora, N.L. Heda, B.L. Ahuja, Rad. Phys. Chem. 158 (2019) 46-52.

40. D. Fritsch, J. Phys.: Condens. Mater. 30 (2018) 095502-1-095502-5.

41. M.A. Valenzuela, P. Bosch, J. Jiménez – Becerrill, O. Quiroz, A.I. Páez, J. Photochem. Photobiol. A Chem. 148 (2002) 177–182.

42. H. Akamatsu, Y. Zong, Y. Fujiki, K. Kamiya, K. Fujita, S. Murai, K. Tanaka, IEEE Trans. Mag. 44 (2008) 2796–2799.

Chapter 5

Structural, Magnetic and Electronic Properties of Nickel Ferrites: Experiment and LCAO Calculations

Based on:

Kalpana Panwar, S. Tiwari, K. Bapna, K. Kumar, N.L. Heda, D.M. Phase, B.L. Ahuja, J. Alloys Compounds (2020) Revised

5.1. Introduction:

The transition metal (TM) doped ferrimagnetic spinel oxides, such as $TMFe_2O_4$ (TM = Co, Ni, Zn, Cd and Mn) are newly engineered materials. Such materials are quite useful in advanced electronic and magnetic devices, like microwave-integrated and magnetoelectric devices and spin filters. Among these oxides, $NiFe_2O_4$ (NFO) is of immense interest due to its peculiar technological and fundamental properties. NFO is known to exhibit an inverse spinel structure, where Ni^{+2} cations occupy octahedral (B) sites and Fe^{+3} ions are equally divided among the tetrahedral (A) and octahedral (B) sites. Theoretically, the magnetic moments of antiferromagnetically coupled Fe^{+3} ions are cancelled from the tetrahedral and octahedral sites in the inverse spinel structure. Accordingly, the Ni^{+2} ions on the octahedral sites majorly contribute for the magnetization with a moment of about 2 μ_B/f.u. [1-3]. The structural, magnetic and electronic response of NFO have been explored in the past years [4-13]. It is reported that the properties of NFO hugely rely upon the cationic distribution of Ni and Fe ions between A and B sites, which in turn depends upon the doping parameters and the method of sample preparation. Earlier, the magnetocrystalline anisotropies were studied using density functional theory (DFT) [4,5]. Local spin density approximation (LSDA) and generalized gradient approximation (GGA) within DFT schemes were employed for structural and electronic properties for NFO [6]. Few studies of epitaxial strain effects, magnetoelastic, magnetoristriction and p-d hybridization in NFO using DFT with LSDA+U and GGA+U are also available in literature [7-9]. Pénicaud et al. [10] have reported the electronic spin-density functional based energy bands, density of states (DOS) and magnetic moments for NFO. Further, fully relativistic Dirac linear muffin-tin orbital (LMTO) with LSDA and LSDA+U formalism were considered for electronic properties, x-ray absorption and magnetic circular dichroism spectra [11]. NFO was also studied in spinel and inverse spinel structures using self-interaction corrected LSDA method [12]. Among different dopants, Cr doping in NFO is of further interest due to presence of three magnetically active Ni^{2+}, Fe^{3+} and Cr^{2+} ions [13-18]. Patange et al. [14] suggested that $NiCr_xFe_{2-}$

$_xO_4$ (x = 0 to 1) prepared by chemical co-preparation method has mixed spinel structure and the electric field values required for switching properties increase with increasing Cr concentration. Rais et al. [15] fabricated $NiCr_xFe_{2-x}O_4$ (x = 0 to 1.4) ferrites by double sintering ceramic technique and revealed an occurrence of magnetic compensation with Cr doping. Although the effect of Cr doping in NFO has been studied by many authors, only a few have studied the doping of Cr at Ni site. Lang at el. [16] studied $M_xNi_{1-x}Fe_2O_4$ (M=Cr, Co and $0.0 \leq x \leq 0.3$) prepared by chemical co-precipitation method. It was found that magnetic moment decreases with Cr doping, while it increases with Co doping, in spite of the fact that Co^{2+} and Cr^{2+} both have higher magnetic moment than Ni^{2+}. They have proposed a quantum – mechanical potential barrier to explain this discrepancy. Also the cation distribution analysis using x-ray diffraction (XRD) measurement, magnetic and Mössbauer effect for Cr doped NFO are available in the literature [17-18].

In this chapter, which is also communicated by us in J. Alloys Compounds (2020) revised, we have reported structural, electronic and magnetic properties of NFO and $Ni_{0.95}Cr_{0.05}Fe_2O_4$ (NCFO) due to the fact that Cr at Ni site has not been explored much in ferrites. Linear combination of atomic orbitals (LCAO) scheme with DFT [19] was also employed for the first time to compute magnetic moments, Mulliken's population (MP), majority- and minority-spin DOS and Compton profiles (CPs) for NFO. In addition, Compton profile (CP) measurements were attempted for NFO using 740 GBq ^{137}Cs Compton spectrometer [20] to validate the theoretical CPs. Due to the small component (5 %) of Cr doping (leading to large unit cell formation) for NCFO and limitations of computational parameters, we could not extend LCAO based computation for $Ni_{0.95}Cr_{0.05}Fe_2O_4$ and also CP measurements were restricted due to non -availability of theoretical data for validation of measurements.

5.2. Methodologies:

5.2.1. Structural and magnetic properties:

NFO and NCFO were prepared by solid state reaction method using requisite amounts of high purity oxides, namely Cr_2O_3, Fe_2O_3 and NiO. Each mixture was

calcined at 900°C for 24 h and calcined powder was thoroughly grounded in an agate mortar and thereafter palletized under the high pressure. The pellet was sintered at 1050°C for 24 h. We have repeated this process again and the pallet was grounded and pelletized under high pressure and sintered at 1100°C for 12 h. Further θ-2θ XRD was carried out using Brooker D2-Phaser with Cu-K_α source to identify phase of the prepared samples. The crystal structures were refined using the Rietveld profile refinement program FULLPROF [J. Rodriguez-Carvajal, FULLPROF Version 3.0.0, Laboratorie Leon Brillouin, CEACNRS, 2003]. Fourier transform infrared (FTIR) spectroscopy was performed using Bruker model vertex 70. Raman spectra were registered at room temperature. Further, magnetic measurements (M-H) were carried out employing a 7-Tesla SQUID-vibrating sample magnetometer (SVSM; Quantum Design Inc., USA).

5.2.2. CP measurements:

In Compton spectroscopy measurements, CP, $J(p_z)$, is basically a projection of electron momentum density along the z-axis (scattering vector direction) [21,22 and chapter 1]. Experimentally, we measure double differential Compton scattering cross-section $\left(d^2\sigma / d\Omega\, dE_2\right)$ and $J(p_z)$ is calculated as:

$$J(p_z) = \frac{1}{C(E_1, E_2, \theta, p_z)} \times \frac{d^2\sigma}{d\Omega\, dE_2} \qquad (5.1)$$

Here E_1 and E_2 are the energies of incident and scattered photons. Further θ and p_z are scattering angle and component of linear momentum of electron along z-axis, respectively. The factor $C(E_1, E_2, \theta, p_z)$ can be deduced from the formalism of Eisenberger and Reed [23]. Present, CP measurements for NFO were performed using 740 GBq ^{137}Cs Compton spectrometer at a momentum resolution of 0.34 a.u. (full width at half maximum) [20 and chapter 2]. For CP measurements, we have used circular pellet of NFO and placed it vertically in the sample chamber. The diameter, thickness and bulk density of the sample were 1.05 cm, 0.137 cm, and 2.89 gm/cm^3, respectively. In the present measurements, photons of energy 661.65 keV were allowed to impinge on the sample pellet and the scattered photons were detected at a

scattering angle of 160±0.6° by a high purity Germanium (HPGe) detector (Canberra made, Model GL0510P). The cross sectional area and thickness of Ge crystal were 500 mm^2 and 10 mm, respectively. We have ensured about the stability of the associated electronics throughout the measurements using two weak calibration sources namely ^{57}Co and ^{133}Ba. Total 5.22×10^7 integrated Compton counts were collected during acquisition periods 401.0 h. Now, the raw data (as reported in Fig. 2.5b of chapter 2) were handled for systematic corrections like background, detector efficiency (limited to stripping-off the low-energy tail), sample absorption and Compton cross-section corrections using standard computer codes [24]. Further multiple scattering correction (terminated upto triple scattering) using Monte Carlo simulation was also applied, following the mathematical formulation of Felsteiner et al. [25]. Finally, the CP data were normalized to corresponding free atom (FA) CP area of 50.85 e^- in the momentum range 0–7 a.u. [26].

5.2.3. LCAO calculations:

MP data, magnetic moments, majority- and minority-spin DOS and CPs have been computed using LCAO scheme [19 and chapter 2]. Present LCAO calculations have been accomplished in DFT framework within LDA and second order GGA (SOGGA) along with peculiar hybridized (HF+DFT) schemes (B3LYP and PBE0) as prescribed by Dovesi et al. [19]. Combinations of exchange-correlations potentials can be chosen in terms of various exchange-correlation energy (E_{XC}) models available in literature [19]. Different exchange-correlations energies chosen in the present computation are summarized below:

(i) DFT-LDAVBH: Dirac–Slater [19] exchange and von Barth and Hedin (VBH) [27] correlation energies.

(ii) DFT-SOGGA: Exchange and correlation energies of Zhao et al. [28] and Perdew et al. [29], respectively.

(iii) B3LYP: Exchange energies of Dirac-Slater [19], Becke gradient correction [30] and Hartree-Fock (HF) [19] along with correlation energies of Vosko et al. [31] and Lee et al. [32].

(iv) PBE0: Exchange energies of Perdew et al. [29] and HF [19] along with Perdew et al. [29] correlation energies.

The basis sets of Fe, Ni and O atoms were taken from http://www.crystal.unito.it/basis-sets.php and were re-optimized for minimum energy using BILLY code in the NFO environment and reported in Table 5.1. In this work, our XRD (discussed in Section. 5.3.1) based lattice parameter for NFO were used. Self consistent field computations were performed using 95 **k** points in the irreducible Brillouin zone (BZ). Total CP of DFT-LDAVBH, DFT-SOGGA, B3LYP and PBE0 have been calculated by adding the FA core contribution [26] to the presently computed normalized CP data for valence electrons. In Fig. 5.1, we have plotted the structure sketch of NFO using plotting tools of Kokalj [33].

5.3. Results and Discussion:

5.3.1. XRD measurements:

The room temperature (RT) Rietveld refined XRD pattern of NFO and NCFO samples are represented in Fig. 5.2(a,b), respectively. We have employed pseudo-Voigt function for refining the peaks. It is clear from the Fig. 5.2 that the peaks corresponding to (111), (220), (311), (222), (400), (422), (333), (511), (440), (531), (442), (620), (444) and (551) are reflection of the cubic structure of the spinel with the space group Fd-3m. The fitted curves match well with the experimental data, which unanimously depict structure with space group Fd-3m of inverse spinel arrangement. It is worth mentioning that all the peaks observed in XRD spectra are totally generated by the spinel structure and there is no extra peak of any impurity phase. The refined parameters of samples are given in Table 5.2 along with weighted pattern R_{wp}, Bragg factor R_{Bragg}, structure factor R_F and χ^2 to support the quality of present fitting. Our lattice parameter for NFO (8.338 Å**)** is in accordance with those reported by Pubby et al. [34] and Ahlawat et al. [35]. The distribution of divalent and trivalent cation among tetrahedral and octahedral sites in the $Ni_{0.95}Cr_{0.05}Fe_2O_4$ was $[Ni_{0.937}Cr_{0.049}Fe_1]_{oct}[Fe_{0.997}]_{tet.}O_4$. The lattice constant of NCFO calculated using

Table 5.1: Optimized basis-sets, Gaussian exponents (in $a.u.^{-2}$) and contraction coefficients for Ni, Fe and O in case of $NiFe_2O_4$. Asterisks represent unoccupied atomic orbitals at the beginning of the self consistent field (SCF) process.

Atom	Orbitals	Exponents	Coefficients		
			S	p	d
Ni	s	367916.0	0.000227		
		52493.9	0.001929		
		11175.8	0.0111		
		2925.4	0.05		
		882.875	0.1703		
		305.538	0.369		
		119.551	0.4035		
		49.9247	0.1426		
	sp	924.525	-0.0052	0.0086	
		223.044	-0.0679	0.0609	
		74.4211	-0.1319	0.2135	
		29.6211	0.2576	0.3944	
		12.4721	0.6357	0.3973	
		4.2461	0.2838	0.2586	
	sp	56.6581	0.0124	-0.018	
		21.2063	-0.2218	-0.08	
		8.4914	-0.8713	0.2089	
		3.6152	1.0285	1.255	
	sp	1.417	1.0	1.0	
	sp*	0.4812	1.0	1.0	
	d	41.0800			0.041
		11.4130			0.2063
		3.8561			0.428
		1.3017			0.4805
	d*	0.3719			1.0
Fe	s	315379.0	0.000227		
		45690.0	0.0019		
		9677.3	0.0111		
		2520.88	0.0501		
		759.746	0.1705		
		262.964	0.36924		
		102.801	0.4033		
		42.9733	0.1434		

	sp	798.262	-0.0052	0.00850	
		191.162	-0.068	0.0608	
		63.6885	-0.1314	0.2114	
		25.3625	0.2517	0.3944	
		10.7338	0.6433	0.398	
		3.764	0.2825	0.2251	
	sp	48.1434	0.0122	-0.0215	
		17.4579	-0.2278	-0.085	
		6.9972	-0.8801	0.201	
		3.0791	0.9755	1.3024	
	sp	1.2989	1.0	1.0	
	sp*	0.5430	1.0	1.0	
	d	31.3296			0.058
		8.7866			0.263
		3.1008			0.5017
		1.1377			0.5656
	d*	0.3594			1.0
O	s	8020.0	0.00108		
		1338.0	0.00804		
		255.4	0.05324		
		69.22	0.1681		
		23.90	0.3581		
		9.264	0.3855		
		3.851	0.1468		
		1.212	0.0728		
	sp	47.7145	-0.0102	0.0098	
		10.47	-0.0908	0.0692	
		3.2817	-0.0434	0.2052	
		1.241	0.3984	0.3263	
	sp*	0.466	1.0	1.0	
	sp*	0.183	1.0	1.0	

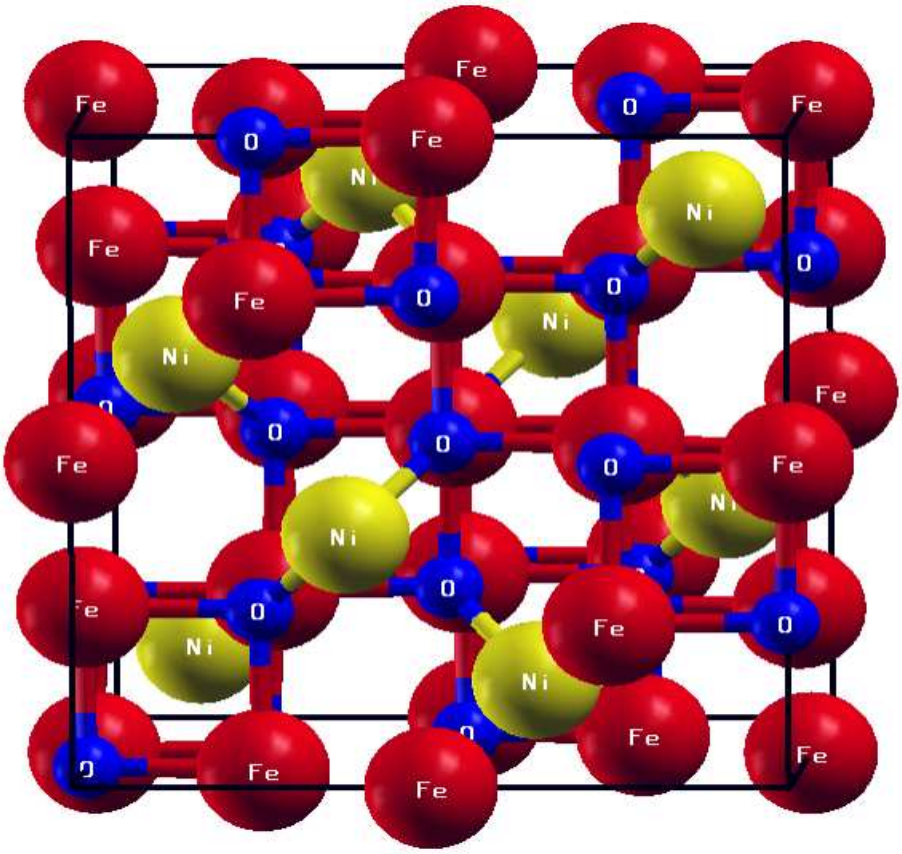

Fig. 5.1: Structural sketch of NFO plotted using software tool of Kokalj [33].

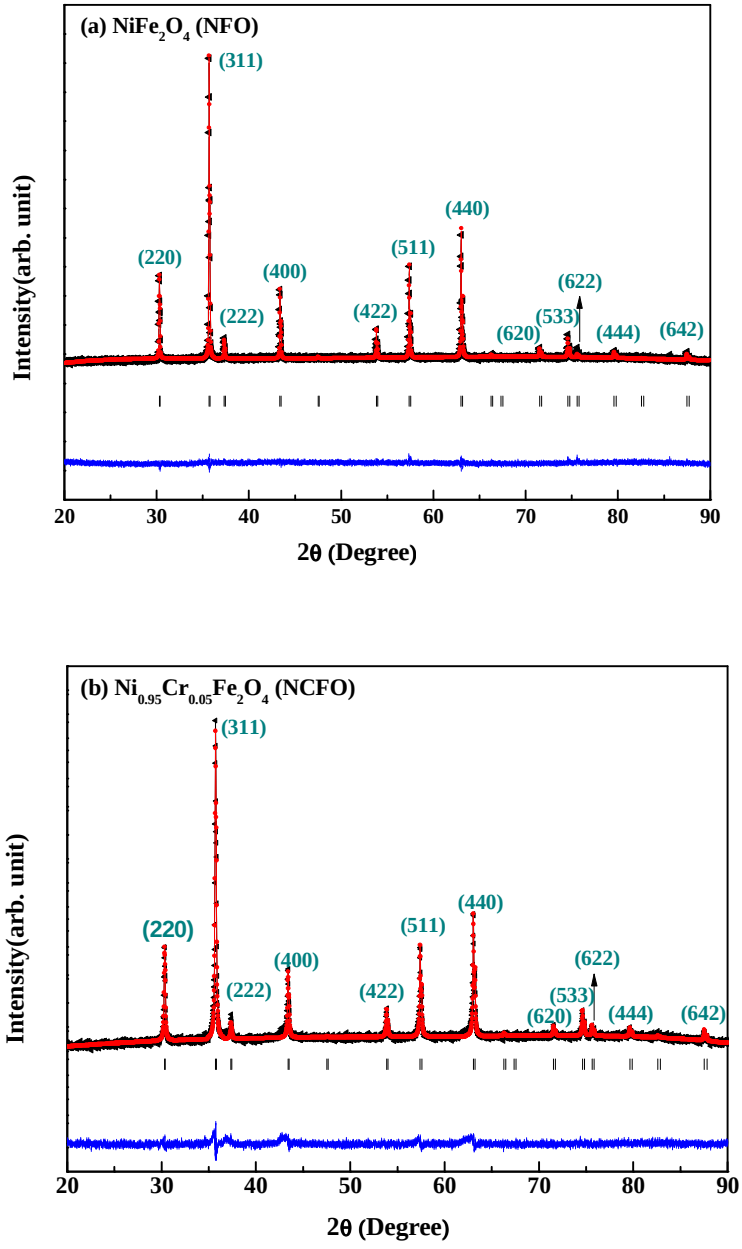

Fig. 5.2: XRD patterns for (a) $NiFe_2O_4$ (NFO) and (b) $Ni_{0.95}Cr_{0.05}Fe_2O_4$ (NCFO).

Table 5.2: XRD lattice constant and other parameters of $NiFe_2O_4$ (NFO) and $Ni_{0.95}Cr_{0.05}Fe_2O_4$ (NCFO).

Sample	**a (Å)**	χ^2	R_{wp}	R_{exp}	R_F	R_{Bragg}	**Volume ($Å^3$)**	**Grain size (Å)**
NFO	8.338	1.82	17.7	13.09	9.320	7.398	579.68	1263.61 Å
NCFO	8.334	1.70	21.9	16.77	9.177	9.212	578.95	660.51 Å

Rietveld refinement is found to be approximately same to the parent compound, which is understandable due to similar ionic radii of Ni^{+2} and Cr^{+3} ions. After confirming the single phase nature of these samples, we determined their grain sizes using following Debye-Scherrer formula,

$$D = 0.94 * \lambda/(B \cos\theta) \quad (5.2)$$

In Eq.5.2, λ is the wavelength of the incident x-rays, θ is the Bragg diffraction angle and B is the FWHM of corresponding peak in XRD spectra. It is observed that the grain size for NFO is larger than NCFO, which may be due to the strain produced in the lattice due to small difference in ionic radii of Ni^{+2} and Cr^{+2} (although small difference) hindering the grain growth.

5.3.2. Raman spectroscopy and FTIR measurements:

To further assess local disorder in FeO_6 octahedral induced by Jahn–Teller distortion due to the local geometry of the structure and other interaction, we performed Raman spectroscopy and FTIR measurements. According to the group theory, NFO with cubic spinel structure is predicted to have following modes of vibration [36],

$$A_{1g}(R)+E_g(R)+T_{1g}(in)+3T_{2g}(R)+2A_{2u}(in)+2E_u(in)+4T_{1u}(IR)+2T_{2u}(in) \quad (5.3)$$

In Eq. 5.3, A_{lg}, E_g and T_{2g} are Raman active modes, T_{1u} type mode is infrared mode and all others are silent modes. Figs. 5.3 and 5.4(a,b) show FTIR and Raman spectra of NFO and NCFO, respectively. Besides this, in NFO the higher frequency mode above 700 cm^{-1} (A_{1g}) corresponds to the motion of oxygen (symmetric stretch along Fe-O bond) in tetrahedral site, while the lower frequency modes ($T_{2g}(2)$ ~ 490.85 cm^{-1}, E_g ~ 335.61 cm^{-1} and $T_{2g}(3)$ ~ 581.07 cm^{-1}) depict the characteristics of the motion of oxygen in octahedral sites. NCFO Raman spectra also show a shoulder like feature at lower wave number around ~ 660 cm^{-1}, which is due to the difference in the local cation distribution between tetrahedral and octahedral sites. The shoulder is slightly broader in NCFO due to further amendment in Fe/Ni-O bond distance caused by Cr doping. The effect of Cr doping in NFO on the microstructure is clearly evident from Table 5.3 where the position and FWHM of Raman modes have been compiled. All the observed modes are in consonance with the earlier reports [34,35]. As we dope Cr at Ni sites, the bands shift towards lower wave number which is attributed to

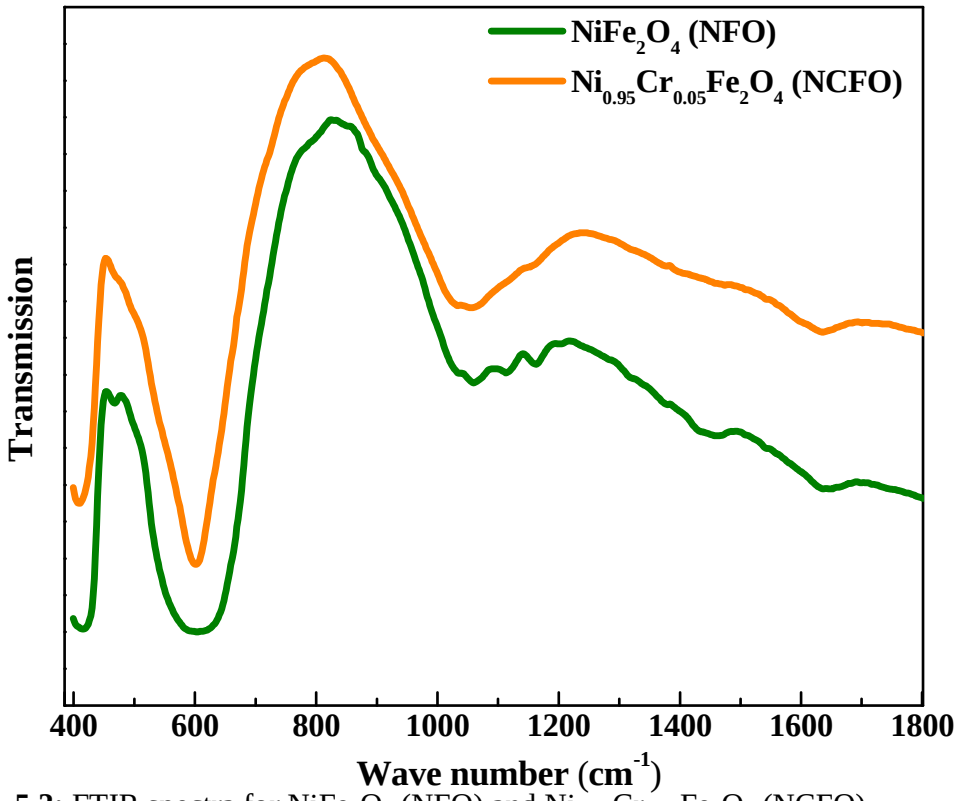

Fig. 5.3: FTIR spectra for $NiFe_2O_4$ (NFO) and $Ni_{0.95}Cr_{0.05}Fe_2O_4$ (NCFO).

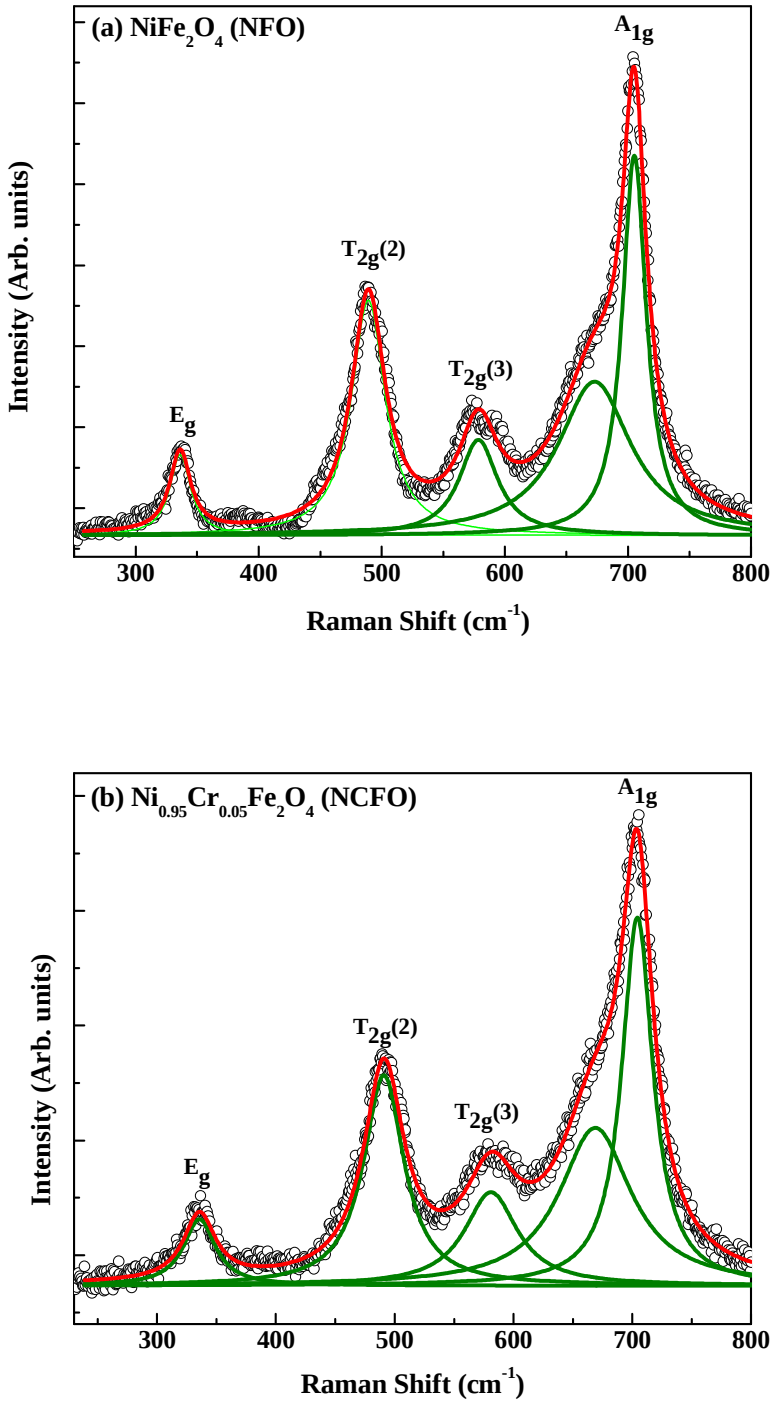

Fig. 5.4: Raman spectra for (a) $NiFe_2O_4$ (NFO) and (b) $Ni_{0.95}Cr_{0.05}Fe_2O_4$ (NCFO).

Table 5.3: Raman parameters (different band positions together with FWHM of Raman peaks in cm^{-1}) of $NiFe_2O_4$ (NFO) and $Ni_{0.95}Cr_{0.05}Fe_2O_4$ (NCFO).

Sample	**E_g**	**$T_{2g}(2)$**	**$T_{2g}(3)$**	**Shoulder peak**	**A_{1g}**
(i) NFO	336.28	489.16	578.16	672.88	705.20
FWHM	20.64	33.27	37.89	72.75	23.55
(ii) NCFO	335.61	490.85	581.07	668.86	704.33
FWHM	32.72	41.27	54.41	73.35	31.94

the compression of Fe-O bonds. Observed increase in line width of Raman modes suggest a higher electronic disorder in Cr doped sample which is in consensus with smaller grain size as revealed from XRD. Moreover, the blue shift in Raman modes for octahedral site indicates the incorporation of Cr dominantly into octahedral sites.

5.3.3. Magnetization:

M-H loops of NCFO measured at RT are shown in Fig. 5.5. We have also measured the M-H loop of NFO at RT and shown in the inset of Fig. 5.5. It is observed that the magnetic moment of NCFO is reduced to almost half of NFO. It is also seen that NFO exhibits a steep M-H loop with coercivity of few Oe magnetic field, while the coercivity of NCFO increases to ~800 Oe. The reduction in magnetic moment in NCFO can be understood in terms of the modified exchange interaction between Ni^{2+} and Fe^{3+} ions when doped with Cr^{2+}. It has been reported that when Ni^{2+} is replaced by Cr^{2+}, the Cr^{2+} ions prefer to sit at octahedral site only [15,37]. As Cr^{2+} has less than half filled 3d states, while Fe^{3+}/Ni^{2+} 3d states are half filled or more than half filled, the magnetic moment of Cr^{2+} must align antiferromagnetically with those of Fe^{3+}/Ni^{2+} ions. The coercivity is increased due to increased disorders arising from the ionic radii mismatch between Cr^{2+}/Ni^{2+} and Fe^{3+} ions.

It is known that the magnetic properties of ferrites hugely depend upon on the cation distribution. In the present study, it is found that the M-H loop shows a pinched shape (sudden slope change near origin), suggesting the presence of two magnetic phases: hard magnetic phase (with higher coercivity) and soft magnetic phase (with smaller coercivity) [38]. It is to be noted here that appearance of two-phase-like hysteresis loop was also found in $Co_xNi_{1-x}Fe_2O_4$ system by Lang et al. [16], though it remained unnoticed there. The same was the case for $CoCr_xFe_{2-x}O_4$ where Raghasudha et al. [39] have observed pinched hysteresis in $CoCrFe_2O_4$ but this feature again remained unobserved.

In Table 5.4, we have collated our experimental (M-H) and theoretical (DFT-LDAVBH, DFT-SOGGA, B3LYP and PBE0) based magnetic moments along with the available data [4,6,10-11] for NFO and NCFO. The magnetic moment at A site

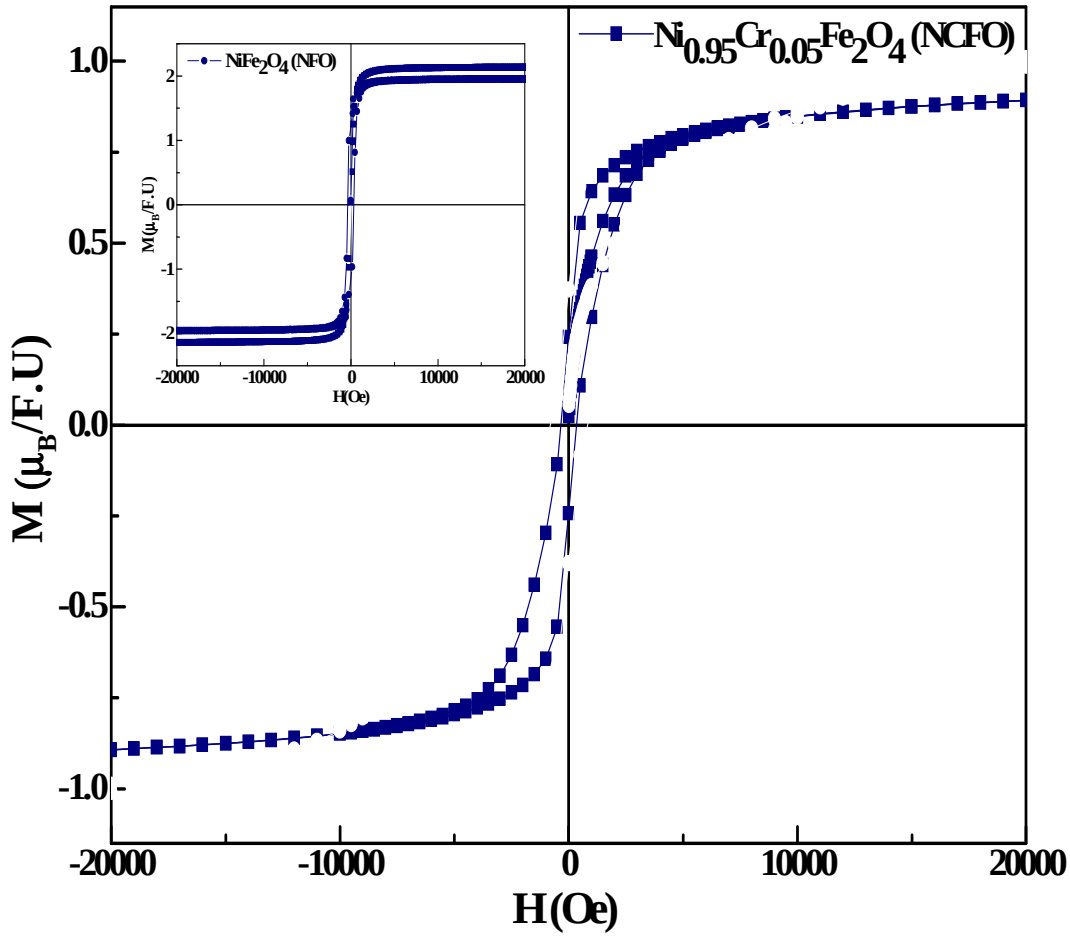

Fig. 5.5: The magnetic hysteresis loop of $Ni_{0.95}Cr_{0.05}Fe_2O_4$ (NCFO). In inset, M-H curves of $NiFe_2O_4$ (NFO) are shown.

Table 5.4: Experimental (M-H) and theoretical (DFT-LDAVBH, DFT-SOGGA, B3LYP and PBE0 scheme) based magnetic moments along with the available data for $NiFe_2O_4$ (NFO) and $Ni_{0.95}Cr_{0.05}Fe_2O_4$ (NCFO). Here, A and B denote the tetrahedral and octahedral sites as mentioned in the text.

Approach	Magnetic moment (μ_B)				
	Fe (A)	Ni (B)	Fe (B)	O	Total
(a) $NiFe_2O_4$ (NFO)					
(i) Present work					
• DFT-LDAVBH	–3.32	1.24	3.64	0.09	1.92
• DFT-SOGGA	–3.55	1.36	3.82	0.09	1.99
• B3LYP	–4.08	1.64	4.20	0.06	2.00
• PBE0	–4.17	1.69	4.28	0.05	2.00
• Experiment (M-H)	----	----	----	---	1.95
(ii) DFT with [4]					
• LSDA+U	–3.82	1.49	4.00	---	1.67
• GGA	–3.46	1.36	3.71	---	1.61
• GGA+U	–3.97	1.58	4.11	---	1.72
(iii) DFT-LSDA [6] with k-point sampling					
• $2 \times 2 \times 2$	–3.40	1.33	3.70	0.10	2.03
• $3 \times 3 \times 3$	–3.40	1.34	3.70	0.10	2.04
• $4 \times 4 \times 4$	–3.40	1.34	3.69	0.10	2.03
• $5 \times 5 \times 5$	–3.40	1.34	3.70	0.10	2.04
(iv) LSDF [10]	–3.24	1.38	3.70	0.04	2.00
(v) DFT-LSDA+U [11]	–4.01	1.81	4.12	---	1.92
(b) $Ni_{0.95}Cr_{0.05}Fe_2O_4$ (NCFO)					
• Present experiment (M-H)	----	----	----	---	0.96

(tetrahedral) of Fe and B site (octahedral) of Ni and Fe along with O atom component are also compiled in Table 5.4. Here, present LCAO based theoretical magnetic moments (DFT-LDAVBH, DFT-SOGGA, B3LYP and PBE0) are very close to the experimental (M-H) data than those reported using DFT with LSDA+U, GGA and GGA+U [4] and also DFT-LSDA [6]. Further, our B3LYP and PBE0 schemes based magnetic moments for NFO are same as reported by other workers [1-3]. It is also noticed that our DFT-LDAVBH based moments are close to the DFT-LSDA+U [11] which might be due to similar type of LDA approximation. Also, our B3LYP and PBE0 data are reconcile well with the LSDF [10]. Needless to mention that the magnetic moments of Fe atom at A and B sites majorly cancel due to the inverse spinel structure of NFO.

5.3.4. MP analysis:

MP charge transfer data of NFO have been incorporated in Table 5.5 using LCAO scheme (DFT-LDAVBH, DFT-SOGGA, B3LYP and PBE0). Here, Fe and Ni atoms at both sites (tetrahedral and octahedral) behave as donor atoms whereas O atoms are acceptor atoms. The total charge transfer for NFO using DFT-LDAVBH, DFT-SOGGA, B3LYP and PBE0 schemes are found to be 4.88, 5.06, 5.50 and 5.70 e^{-}, respectively. The large value of charge transfer indicates the dominancy of ionic bonding in NFO. Further, a small difference is observed in the amount of charge transfer in case of Fe atoms at tetrahedral and octahedral sites for all the schemes (DFT-SOGGA, B3LYP and PBE0 schemes). Also at octahedral site, Ni and Fe show different charge transfer in all the four approximations (DFT-LDAVBH, DFT-SOGGA, B3LYP and PBE0 schemes). Further, the amount of charge transfer using DFT-LDAVBH and DFT-SOGGA schemes are lower than those using B3LYP and PBE0 schemes. This may be due to the incorporation of 20 and 25 % HF hybrid components in case of B3LYP and PBE0 schemes, respectively. Needless to mention that such MP data are quite reliable as the present basis sets contains sufficient numbers of external atomic orbitals for NFO. Also, such MP analysis has successfully been applied to our earlier work on oxides like AWO_4 (A=Co, Ni, Cu, Zn and Cd) [40-41].

Table 5.5: Mulliken's population (MP) based charge transfer resulting from donor (Fe and Ni) to the acceptor (O) atoms for $NiFe_2O_4$ (NFO) using DFT-LDAVBH, DFTSOGGA, B3LYP and PBE0 schemes within LCAO approximations. The numbers of equivalent atoms are shown in the brackets.

Scheme	Amount of charge transfer (e^-)				
	Donor atoms			Acceptor atoms	
	Fe		**Ni**	**O**	
	A Site	**B site**	**B site**		
DFT-LDAVBH	1.72 (2)	1.75 (2)	1.41 (2)	1.24 (4)	1.20 (4)
DFT-SOGGA	1.77 (2)	1.46 (2)	1.83 (2)	1.29 (4)	124 (4)
B3LYP	1.96 (2)	1.52 (2)	2.02 (2)	1.40 (4)	1.35 (4)
PBE0	2.04 (2)	1.57 (2)	2.09 (2)	1.45 (4)	1.40 (4)

5.3.5. Majority- and minority-spin DOS:

In Fig. 5.6, we have presented total majority- (↑) and minority-spin (↓) DOS for NFO using B3LYP approximation. DFT-LDAVBH, DFT-SOGGA and PBE0 based DOS are not reported because of their similar topology as for B3LYP scheme. In Fig. 5.6, we have not observed crossovers of Fermi energy level (E_F) by DOS and also a significant region above E_F with non-existence of DOS is seen. Present DOS confirm wide band gap or almost insulating nature of NFO which is in agreement with the available data [2,11,12,42]. Here, the band gap values from majority- and minority-spin DOS using B3LYP scheme for NFO were observed as 3.41 and 2.59 eV, respectively. Our band gap values are in agreement with majority- (3.3 eV) and minority-spin (2.7 eV) values as reported by Sun et al. [2] using HSE06 approximation. This is expected because HSE0 and B3LYP both are hybrid (HF+DFT) approximations. Additionally in Figs. 5.7(a-d), we have plotted individual majority- (↑) and minority-spin (↓) DOS for 3d, 4s and total states of Fe atom at A site, 3d, 4s and total states of Ni atom at B site, 3d, 4s and total states of Fe atom at B site and 2s, 2p and total states of O atom, respectively. The silent features of DOS from Fig. 5.7(a-d) are:

(i) DOS in the energy range between –20.32 to –18.68 eV (not shown here): The contribution of 2s states of majority-spin electrons of O atom is observed while the contributions of 4s states of Fe atom (A and B sites) and Ni atom (B site) were missing.

(ii) DOS in the energy range between –8.18 eV to E_F level: The main contributors are 3d minority-spin states of Fe atom at A site and 3d majority- and minority-spin states of Ni atoms at B site and 3d majority spin state of atom at B along with a small component of 2p majority- and minority-spin states of O atoms. Here, hybridization of 3d states of minority-spin of Fe atom at A site and majority-spin of Fe atom at B site is observed between –7.62 to –5.56 eV. Also the hybridization of 3d states of majority-spin of Ni and Fe atoms at B site is seen between –5.99 to –4.42 eV. Here, a mixed hybridization of 3d states of Fe atom at A site (minority), Ni atom at B site

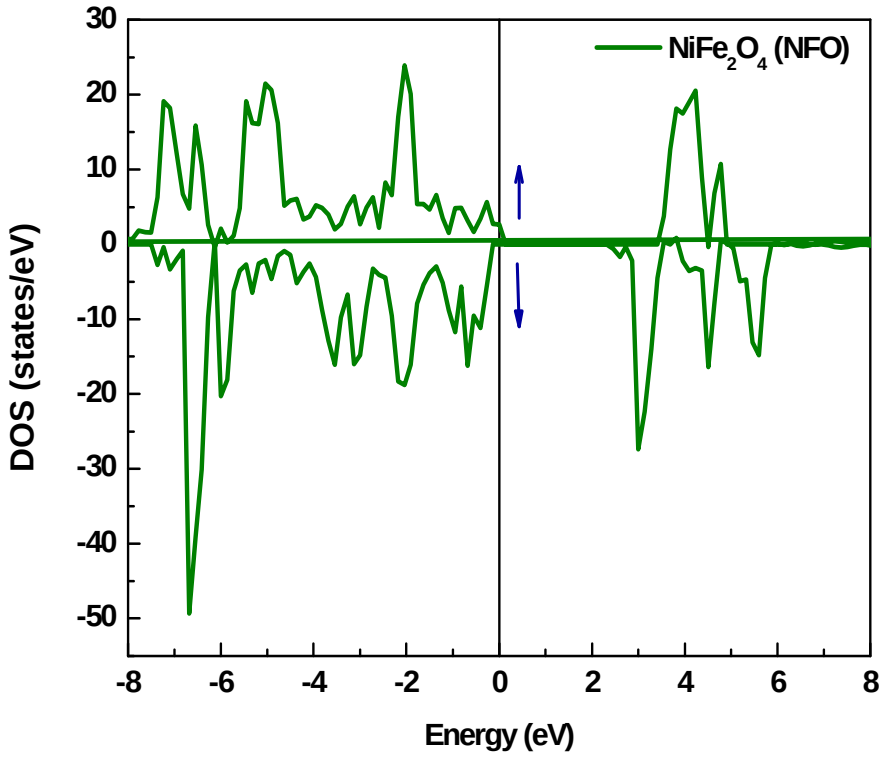

Fig. 5.6: Majority- (↑) and minority-spin (↓) total DOS for $NiFe_2O_4$ (NFO) using B3LYP scheme.

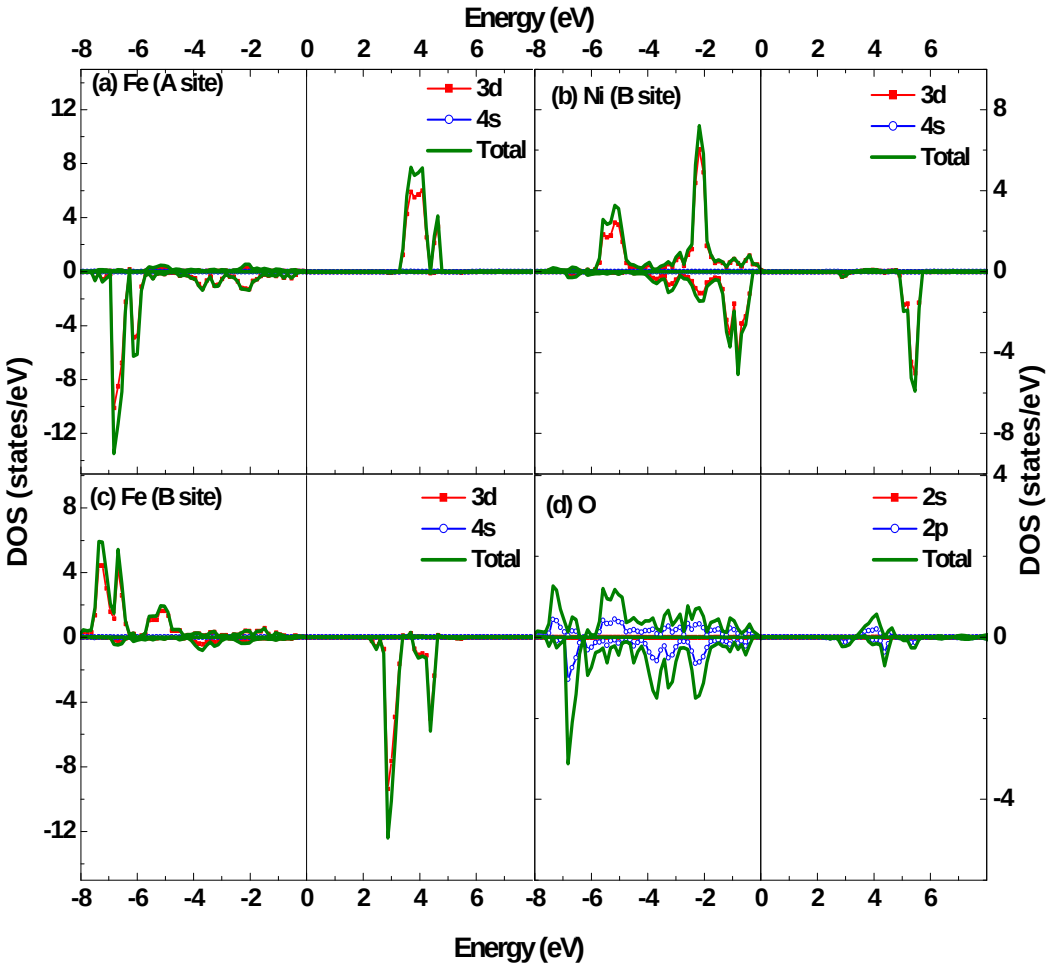

Fig. 5.7: Majority- (↑) and minority-spin (↓) DOS for (a) 3d, 4s states and their total of Fe atom at A site, (b) 3d, 4s states and their total of Ni atom at B site, (c) 3d, 4s states and their total of Fe atom at B site and (d) 2s, 2p states and their total of O atom, respectively.

(majority) and Fe atom at A site (majority) is seen between –5.99 to –5.56 eV. Below the E_F level, the major contribution is achieved from the majority-spin of 3d states of Ni atom (B site).

(iii) In the conduction band region, the DOS in the energy range between +2.59 to +3.41 eV is mainly contributed by minority-spin states of Fe atom at B site. Also, a hybridization of 3d states of majority- (A site) and minority-spin (B site) of Fe atom is achieved between +3.41 to +4.80 eV. While dominancy of minority-spin states of Ni atom (B site) is witnessed between +4.80 to +5.76 eV. Also a small contribution between +3.41 to +4.47 eV is visualized from 2p states of O atom. It is observed that B site majority-spin of 3d states of Ni atom and 3d minority-spin states of Fe atom are mainly responsible for the creation of valence DOS maxima and conduction DOS minima, respectively, with non crossovers of E_F level. Hence these states are majorly responsible for the wide band gap or insulating nature of NFO.

5.3.6. CP analysis:

Fig. 5.8 contains the directional differences between unconvoluted CPs (J_{111}–J_{110}, J_{111}–J_{100} and J_{110}–J_{100}) for NFO using DFT-LDAVBH, DFT-SOGGA, B3LYP and PBE0 schemes. While the numerical values of unconvoluted directional CPs ([100], [110] and [111]) using considered schemes for $NiFe_2O_4$ are incorporated in Table 5.6. It is easily visualized that the general trend of oscillations in these theoretical anisotropies in CPs (J_{111}–J_{110}, J_{111}–J_{100} and J_{110}–J_{100}) is quite similar for all the considered approximations (DFT-LDAVBH, DFT-SOGGA, B3LYP and PBE0 schemes). Also, the anisotropies in Fig. 5.8 in the momentum range $p_z \geq 4.0$ are approximately zero as the major contribution in this region is from identical core electrons, whose contribution in CPs is cancelled while taking the directional differences. In the low momentum region ($0.0 \leq p_z \leq 3$ a.u.), significant differences are observed which may be due to the difference in the electron densities along low indexed [100], [110] and [111] directions. Also, almost similar deviations in the anisotropies using DFT-LDAVBH and DFT-SOGGA are observed in the low momentum region, which can be understood in terms of similar performance of both

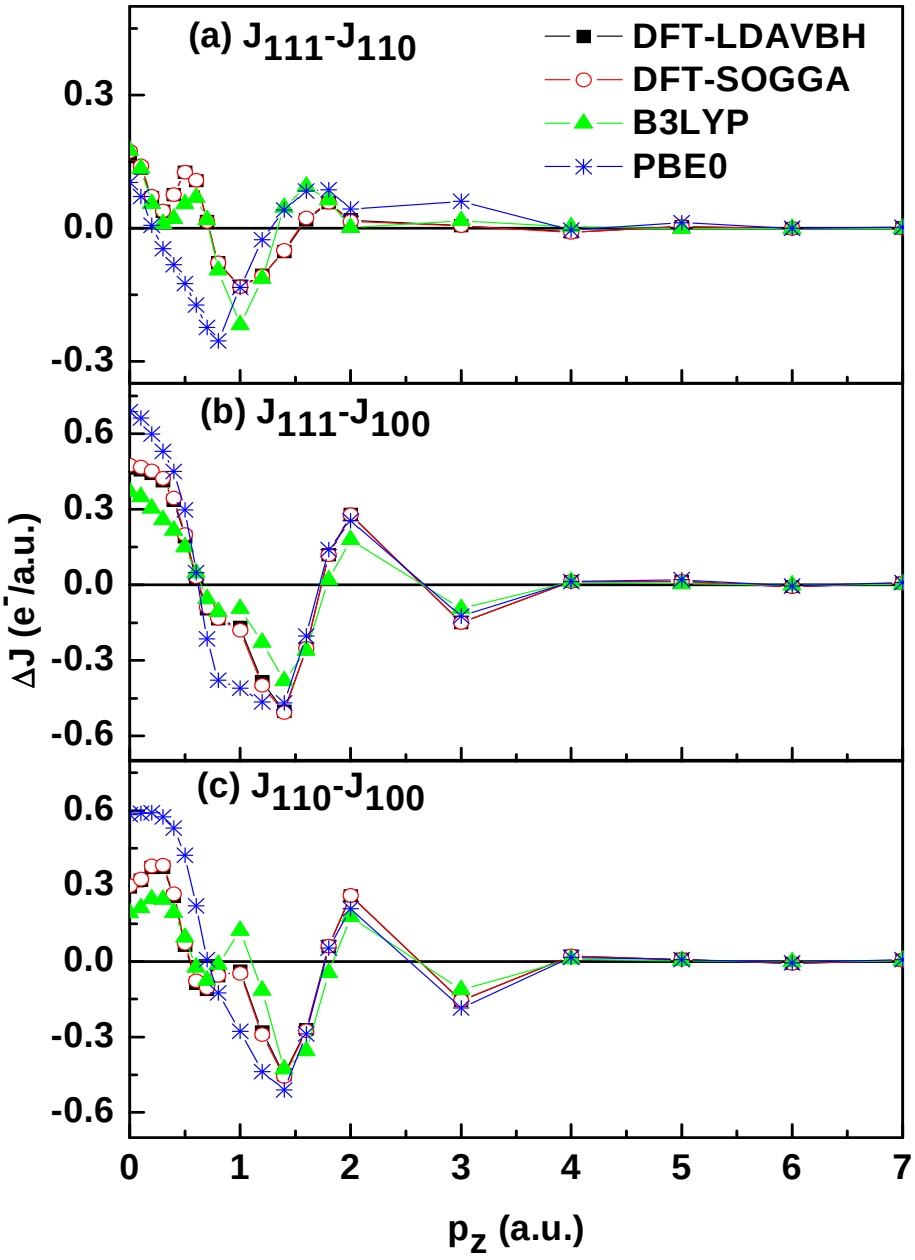

Fig. 5.8: Anisotropies in the unconvoluted theoretical Compton profiles for $NiFe_2O_4$ (NFO) calculated using DFT-LDAVBH, DFT-SOGGA, B3LYP and PBE0 schemes within LCAO approximations for (i) J_{111}–J_{110}, (ii) J_{111}–J_{100} and (iii) J_{110}–J_{100}. The solid lines are drawn for an overall guidance to eyes.

Table 5.6: The unconvoluted directional CPs of $NiFe_2O_4$ along [100], [110] and [111] using DFT-LDAVBH, DFT-SOGGA, B3LYP and PBE0 schemes within LCAO approximations.

p_z (a.u.)	J (p_z) (e/a.u.)											
	DFT-LDAVBH			DFT-SOGGA			B3LYP			PBE0		
	[100]	[110]	[111]	[100]	[110]	[111]	[100]	[110]	[111]	[100]	[110]	[111]
0.0	25.676	25.972	26.139	25.676	25.977	26.149	25.680	25.873	26.048	25.483	26.067	26.171
0.1	25.606	25.927	26.062	25.607	25.934	26.073	25.639	25.853	25.988	25.446	26.035	26.107
0.2	25.313	25.685	25.754	25.315	25.694	25.766	25.410	25.658	25.713	25.228	25.820	25.827
0.3	24.868	25.242	25.280	24.871	25.254	25.292	25.006	25.253	25.262	24.839	25.414	25.368
0.4	24.301	24.559	24.634	24.303	24.571	24.646	24.407	24.602	24.623	24.255	24.786	24.704
0.5	23.696	23.759	23.884	23.696	23.769	23.895	23.719	23.814	23.868	23.609	24.031	23.906
0.6	22.902	22.815	22.922	22.902	22.825	22.932	22.855	22.831	22.900	22.835	23.056	22.883
0.7	21.889	21.776	21.791	21.892	21.787	21.802	21.825	21.750	21.769	21.915	21.924	21.701
0.8	20.650	20.593	20.514	20.659	20.604	20.526	20.599	20.587	20.492	20.780	20.655	20.401
1.0	18.035	17.996	17.865	18.057	18.009	17.876	17.916	18.039	17.821	18.234	17.956	17.823
1.2	15.632	15.352	15.245	15.654	15.363	15.255	15.406	15.290	15.177	15.790	15.352	15.326
1.4	13.528	13.077	13.024	13.539	13.081	13.031	13.368	12.939	12.985	13.621	13.111	13.153
1.6	11.404	11.132	11.150	11.403	11.127	11.150	11.395	11.039	11.133	11.412	11.124	11.208
1.8	9.511	9.572	9.629	9.504	9.565	9.622	9.607	9.562	9.626	9.462	9.516	9.602
2.0	8.040	8.301	8.319	8.031	8.293	8.309	8.173	8.351	8.352	8.006	8.216	8.260
3.0	4.729	4.573	4.578	4.724	4.568	4.574	4.683	4.570	4.587	4.714	4.529	4.590
4.0	2.856	2.878	2.869	2.855	2.876	2.867	2.873	2.883	2.886	2.844	2.861	2.857
5.0	2.014	2.022	2.026	2.013	2.022	2.026	2.023	2.027	2.027	2.008	2.016	2.029
6.0	1.505	1.497	1.497	1.505	1.497	1.497	1.501	1.500	1.499	1.500	1.495	1.495
7.0	1.129	1.134	1.134	1.129	1.134	1.134	1.133	1.135	1.135	1.125	1.132	1.135

the schemes within DFT formalism. Also, a small difference in the low momentum region is observed in the anisotropies using B3LYP and PBE0 schemes which might be due to the different HF component in both the approximations. From all four approximations, the theoretical $J(p_z)$ near $p_z = 0$ along [111] direction is higher than that of [110] and [100], which is attributed to large degenerate states near E_F along [111] direction. Needless to mention that the directional CP measurements for NFO are required for a validation of theoretical anisotropic effects in momentum densities.

Differences between convoluted theoretical (DFT-LDAVBH, DFT-SOGGA, B3LYP and PBE0) and experimental CPs along with the statistical error (±σ) for NFO have also been presented in Fig. 5.9. To account the experimental resolution in theory, each theoretical CP has been convoluted with 0.34 a.u. (Gaussian FWHM). In Table 5.7, numerical values of the unconvoluted theoretical and experimental CPs along with the statistical error (±σ) for NFO are listed. We have employed χ^2 test to conclude about better reconciliation of a theoretical LCAO based approximations (DFT-LDAVBH, DFT-PBESol, B3LYP and PBE0) with the experimental data. The values of χ^2 are calculated using the following relation,

$$\chi^2 = \sum_{p_z=0.0}^{7} \left[\frac{J^{DFT-LDAVBH/DFT-SOGGA/B3LYP/PBE0}(p_z) - J^{Experiment}(p_z)}{\sigma(p_z)} \right]^2 \qquad (5.4)$$

Here the values of χ^2 for NFO using DFT-LDAVBH, DFT-SOGGA, B3LYP and PBE0 are 12267.85, 12403.54, 11095.96 and 11634.15, respectively. Such a trend indicates a better agreement of B3LYP scheme with Compton experimental data than other schemes namely DFT-LDAVBH, DFT-SOGGA and PBE0. Poor quality of basis sets along with non-inclusion of relativistic effects and Lam-Platzman (LP) electron-electron correlation corrections in the LCAO approximation are expected to be main cause for the deviations between the theoretical (DFT-LDAVBH, DFT-SOGGA, B3LYP and PBE0) and experimental CPs for NFO in the low momentum side. It may be noted that LP correction re-arranges the momentum densities just below the Fermi momentum (p_F) to above the p_F [21] which results to reduce values of $J(p_z)$ near $p_z = 0$, leading to better agreement between theoretical and experimental CP in the vicinity of p_z=0 a.u.

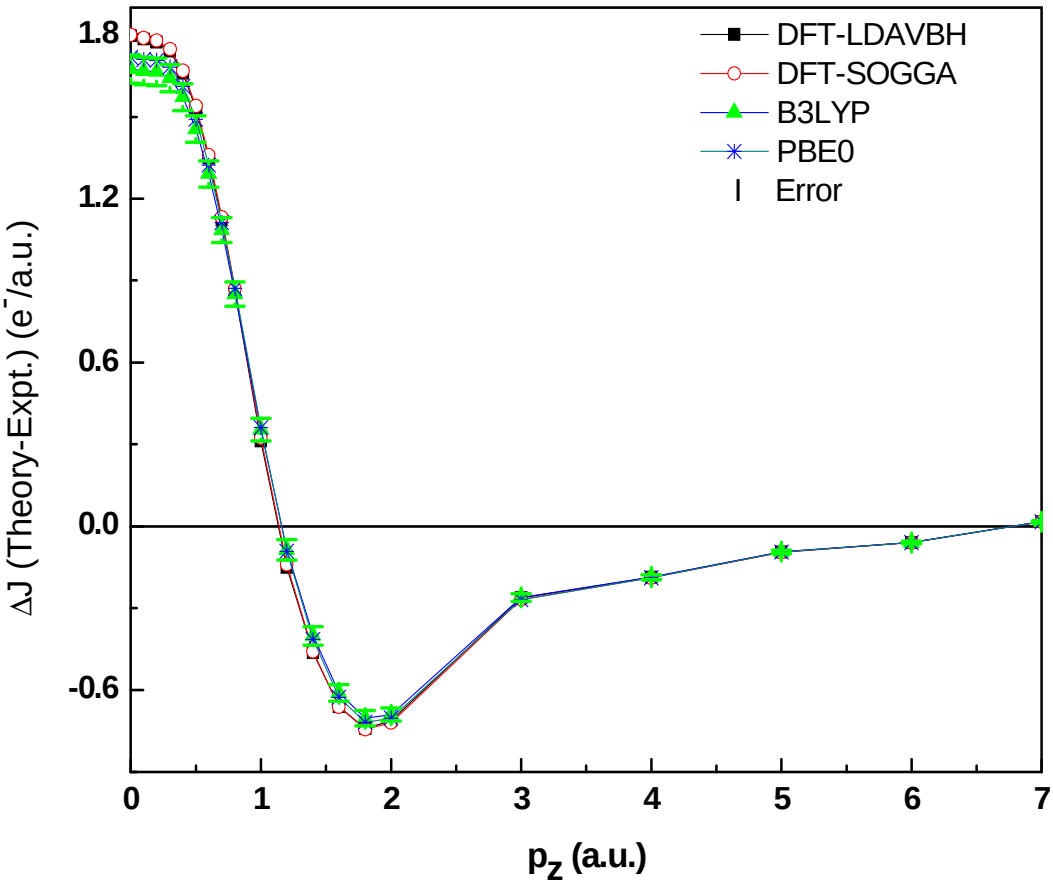

Fig. 5.9: Difference profiles deduced from isotropic convoluted theoretical (DFT-LDAVBH, DFT-SOGGA, B3LYP and PBE0 schemes within LCAO approximations) and experimental Compton profiles for $NiFe_2O_4$ (NFO). The statistical errors at all points are also included. Here, the solid lines are drawn for an overall guidance to eyes.

Table 5.7: Unconvoluted theoretical Compton profiles for $NiFe_2O_4$ (NFO) computed using DFT-LDAVBH, DFT-SOGGA, B3LYP and PBE0 approximations within LCAO schemes. The experimental data have also been listed along with the statistical error (±σ) at each point.

p_z (a.u.)	J (p_z) (e/a.u.)				
	Theory				Expt.
	DFT-LDAVBH	DFT-SOGGA	B3LYP	PBE0	
0.0	25.895	25.897	25.771	25.813	24.029±0.051
0.1	25.849	25.852	25.729	25.771	23.899±0.051
0.2	25.605	25.610	25.494	25.536	23.639±0.051
0.3	25.180	25.188	25.082	25.122	23.251±0.050
0.4	24.553	24.562	24.467	24.505	22.740±0.049
0.5	23.814	23.823	23.737	23.774	22.113±0.048
0.6	22.881	22.892	22.815	22.849	21.378±0.047
0.7	21.799	21.810	21.754	21.782	20.550±0.046
0.8	20.569	20.582	20.561	20.581	19.645±0.045
1.0	17.985	17.998	18.040	18.046	17.679±0.041
1.2	15.416	15.427	15.487	15.480	15.653±0.038
1.4	13.184	13.190	13.249	13.233	13.712±0.034
1.6	11.185	11.184	11.236	11.218	11.939±0.031
1.8	9.542	9.537	9.581	9.565	10.371±0.027
2.0	8.235	8.228	8.257	8.243	9.015±0.024
3.0	4.601	4.596	4.603	4.594	4.877±0.014
4.0	2.875	2.873	2.876	2.873	3.073±0.009
5.0	2.023	2.022	2.024	2.023	2.121±0.007
6.0	1.497	1.497	1.498	1.497	1.559±0.005
7.0	1.134	1.134	1.134	1.134	1.136±0.004

We emphasis to have many body wave functions based calculations with electron-electron correlation effect for a better comparison with the experimental data.

5.4. Conclusions:

Structural and functional properties of $Ni_{1-x}Cr_xFe_2O_4$ (x = 0 and 0.05) have been reported using XRD, Raman spectroscopy, FTIR and SQUID magnetometer. The changes in doublet like feature in A_{1g} mode of Raman spectra reflect the amendment of Fe/Ni–O bond distances due to Cr doping in the studied ferrites. An increase in line widths of Raman modes suggests higher electronic disorder in Cr doped sample which is also in accordance with reduction in grain size. The blue shift in Raman modes corresponding to octahedral sites suggests the presence of Cr dominantly into the octahedral lattice sites. In addition, magnetic moment, MP analysis, majority- and minority-spin DOS and CPs for NFO were calculated using DFT and hybrid (HF+DFT) schemes within LCAO approximation. Hybrid scheme namely B3LYP based momentum densities show a better agreement with the experimental CP of $NiFe_2O_4$, which has been measured using 20 Ci ^{137}Cs Compton spectrometer. Also, our LCAO based magnetic moments for $NiFe_2O_4$ are in accordance with the present M-H experiment and available data. Further, the majority- and minority-spin DOS predict an insulating character (wide band gap) in $NiFe_2O_4$, while MP data show charge transfer from Ni and Fe atoms to O atoms.

References

1. B.S. Holinsworth, D. Mazumdar, H. Sims, Q.–C. Sun, M.K. Yurtisigi, S.K. Sarker, A. Gupta, W.H. Butler, J.L. Musfeldt, Appl. Phys. Lett. 103 (2013) 082406-1–082406-4.

2. Q.–C. Sun, H. Sims, D. Mazumdar, J.X. Ma, B.S. Holinsworth, K.R. O'Neal, G. Kim, W.H. Butler, A. Gupta, J.L. Musfeldt, Phys. Rev. B 86 (2012) 205106-1–205106-5.

3. M. Pardavi-Horvath, J. Mag. Mag. Mat. 215–216 (2000) 171–183.

4. D. Fritsch, C. Ederer, Phys. Rev. B 82 (2010) 104117-1–104117-11.

5. H.-T. Jeng, G.Y. Guo, J. Mag. Mag. Mat. 240 (2002) 436–438.

6. H. Perron, T. Mellier, C. Domain, J. Roques, E. Simoni, R. Drot, H. Catlette, J. Phys.: Condens. Mater. 19 (2007) 346219-1–346219-10.

7. D. Fritsch, C. Ederer, Appl. Phys. Lett. 99 (2011) 081916-1–081916-3.

8. D. Fritsch, C. Ederer, Phys. Rev. B 86 (2012) 014406-1–014406-10.

9. U.-G. Jong, C.-J. Yu, Y.-S. Park, C.-S. Ri, Phys. Lett. A 380 (2016) 3302–3306.

10. M. Pénicaud, B. Siberchicot, C.B. Sommers, J. Kübler, J. Mag. Mag. Mat. 103 (1992) 212–220.

11. V.N. Antonov, B.N. Harmon, A.N. Yaresko, Phys. Rev. B 67 (2003) 024417-1–024417-14.

12. Z. Szotek, W.M. Temmerman, D. Ködderitzsch, A. Svane, L. Petit, H. Winter, Phys. Rev. B 74 (2006) 174431-1–174431-12.

13. S.E. Shirsath, S.S. Jadhav, B.G. Toksha, S.M. Patange, K.M. Jadhav, J. Appl. Phys. 110 (2011) 031914-1–031914-8.

14. S.M. Patange, S.E. Shirsath, S.S. Jadhav, K.S. Lohar, D.R. Mane, K.M. Jadhav, Mater. Lett. 64 (2010) 722–724.

15. A. Rais, A.M. Gismelseed, I.A. Al-Omari, Phys. Stat. Sol. (b) 242 (2005) 1497–1503.

16. L.L. Lang, J. Xu, W.H. Qi, Z.Z. Li, G.D. Tang, Z.F. Shang, X.Y. Zhang, L.Q. Wu, L.C. Xue, J. Appl. Phys. 116 (2014) 123901-1–123901-10.

17. S. Singhal, K. Chandra, J. Solid State Chem. 180 (2007) 296–300.

18. S. Winell, Ö. Amcoff, T. Ericsson, Phys. Stat. Sol. (b) 245 (2008) 1635–1640.

19. R. Dovesi, V.R. Saunders, C. Roetti, R. Orlando, C.M. Zicovich-Wilson, F. Pascale, B. Civalleri, K. Doll, N.M. Harrison, I.J. Bush, Ph D'Arco, M. Llunell, M. Causa, Y. Neol, CRYSTAL14 User's Manual, University of Torino, Torino, 2014, and references therein.

20. B.L. Ahuja, M. Sharma, S. Mathur, Nucl Instrum. Methods Phys. Rev. B 244 (2006) 419–426.

21. M.J. Cooper, P.E. Mijnarends, N. Shiotani, N. Sakai, A. Bansil, X-ray Compton Scattering, Oxford Science Publications, New York, 2004.

22. N.L. Heda, B.L. Ahuja, Role of in-house Compton spectrometer in probing the electronic properties, Recent Trends in Radiation Physics Research, in: B.L. Ahuja (Ed.), Himanshu Publications, New Delhi, India, 2010, 25–30.

23. P. Eisenberger, W.A. Reed, Phys. Rev. B 9 (1974) 3237–3241. .

24. D.N. Timms, Compton Scattering Studies of Spin and Momentum Densities, Ph.D. thesis, University of Warwick, UK, 1989 (Unpublished).

25. J. Felsteiner, P. Pattison, M.J. Cooper, Philos. Mag. 30 (1974) 537–548.

26. F. Biggs, L.B. Mendelsohn, J.B. Mann, At. Data Nucl. Data Tables 16 (1975) 201–308.

27. U. von Barth, L. Hedin, J. Phys. C: Solid State Phys. 5 (1972) 1629–1642.

28. Y. Zhao, D.G. Truhlar, J. Chem. Phys. 128 (2008) 184109-1–184109-8.

29. J.P. Perdew, K. Burke, M. Ernzerhof, Phys. Rev. Lett. 77 (1996) 3865–3868.

30. A.D. Becke, Phys. Rev. A 38 (1988) 3098–3100.

31. S.H. Vosko, L. Wilk, M. Nusair, Can. J. Phys. 58 (1980) 1200–1211.

32. C. Lee, W. Yang, R.G. Parr, Phys. Rev. B 37 (1988) 785–789.

33. A. Kokalj, Comput. Mater. Sci. 28 (2003) 155–168.

34. K. Pubby, S.S. Meena, S.M. Yusuf, S.B. Narang, J. Mag. Mag. Mat. 466 (2018) 430–445.

35. A. Ahlawat, V.G. Sathe, J. Raman Spectrosc. 42 (2011) 1087–1094.

36. K. Panwar, S, Tiwari, K. Bapna, N.L. Heda, R.J. Choudhary, D.M. Phase, B.L. Ahuja, J. Mag. Mag. Mat. 421 (2017) 25–30.

37. A.M. Gismelseed, A.A. Yousif, Physica B 370 (2005) 215–222.

38. K. Sharma, V.R. Reddy, A. Gupta, A. Banerjee, A.M. Awasthi, J. Phys: Condens. Matter 25 (2013) 076002-1–076002-9.

39. M. Raghasudha, D. Ravinder, P. Veerasomaiah, J. Nano Struct. Chem. 3:63 (2013) 1–6.

40. B.S. Meena, N.L. Heda, K. Kumar, S. Bhatt, H.S. Mund, B.L. Ahuja, Physica B 484 (2016) 1–6.

41. B.S. Meena, N.L. Heda, H.S. Mund, B.L. Ahuja, Rad. Phys. Chem. 117 (2015) 93–101.

42. X. Zuo, S. Yan, B. Barbiellini, V.G. Harris, C. Vittoria, J. Mag. Mag. Mat. 303 (2006) e432–e435.

Chapter 6

Part-I

(Based on 100 mCi ^{241}Am Compton spectrometer)

Electronic Properties of Fe_3O_4: LCAO Calculations and Compton Spectroscopy

Based on:

Kalpana Panwar, S. Tiwari, N.L. Heda, AIP Conf. Proc. 1942 (2018) 090032-1–090032-4

6.1. Introduction:

As discussed in chapter 1, it is well known fact the Compton spectroscopy (CS) have been used as a versatile tool for predicting the electronic properties of the materials [1,2]. In the CS experiments, the measured quantity is named as Compton profile, $J(p_z)$, which is basically the projection of electron momentum densities $[\rho(\vec{p})]$ along the scattering vector direction (usually considered along z-axis) as:

$$J(p_z) = \iint \rho(\vec{p})\, dp_x\, dp_y \tag{6.1}$$

where p_z is the momentum component of the electron along z-axis which shifts the energy of scattered photon from E_1 (incident energy) to E_2 (scattered energy) with photon scattering angle (ϕ) as:

$$\frac{p_z}{m_0 c} = \frac{\{E_2 - E_1 + E_1 E_2\,(1-\cos\phi)/m_0 c\}}{\left(E_1^2 + E_2^2 - 2E_1E_2\cos\phi\right)^{1/2}} \tag{6.2}$$

Fe_3O_4 is important Ferrites and used in several electronic and magnetic devices for different applications in radio frequency circuits, high quality filters, transformer cores, read or write heads for high-speed digital tapes and several operating devices [3-8]. Regarding the earlier studies, Szotek et al. [3] have applied the self-interaction corrected local spin density approximation to study the electronic structure and magnetic properties of the base spinel and inverse spinel ferrites. Penicaud et al. [4] have employed density functional calculations to study magnetic and electronic properties of $A_xFe_2O_4$ (A=Fe, Zn, Co, Ni and Mn) while Piekarz et al. [5] have studied the phase transformation in this compound and shown the monoclinic phase below the transition. The charge order in Fe_3O_4 has been explored by Szotek et al. [6] where as Masrour et al. [7] have observed the density of states (DOS) in Fe_3O_4 essentially originate from Fe atom. Regarding the CP measurements, the magnetic Compton profile of Fe_3O_4 has been measured at different temperature by Duffy et al. [8].

In this part of the chapter, which is also published by us in AIP Conf. Proc. 1942 (2018) 090032-1–090032-4, we have employed the 100 mCi ^{241}Am Compton spectrometer [9] to measure the CP of Fe_3O_4. In theoretical side, we have used the linear combination of atomic orbitals (LCAO) scheme within density functional theory (DFT) approximation [10] to compute the CP, Mulliken's populations

(MP) and DOS. The experimental CP has been used to check the performance of various exchange and correlation schemes within DFT approximations.

6.2. Experiment:

To measure the CP of Fe_3O_4, we have used the first ever shortest geometry and lowest intensity based 100 mCi ^{241}Am Compton spectrometer at a resolution of 0.55 a.u. (full width at half maximum) [9 and chapter 2]. A pallet of 25.4 mm diameter and 4.11 mm thickness of the sample was exposed by the photons of energy 59.54 keV and the scattered photons were detected by a high purity germanium (HPGe) detector at a scattering angle 165±1.5°. Here, the density of the pallet was found to be 0.6597 gm/cm^3 and the Ge crystal has 200 mm^2 cross sectional area with 10 mm thickness. The intrinsic character of Ge crystal was maintained by putting it at 77 K (i.e. liquid nitrogen temperature). The integrated Compton intensity of 2.2×10^7 counts was collected during the 140.87 h exposure time. Further, the measured raw data were corrected for some systematic corrections like background, stripping of low-energy tail in the spectrum, sample absorption, detector efficiency, Compton scattering cross-section, etc. using the softwares of Warwick group [11]. Afterwards, the data were also corrected for the multiple scattering (double and triple scattering) using the Monte Carlo simulations [12] and then the CP was normalized to the corresponding free-atom (FA) CP area 50.05 e^- in the momentum range 0-7 a.u. [13].

6.3. Theory:

The MP analysis, DOS and directional and isotropic CPs were calculated using LCAO approximations within DFT approximations [10 and chapter 2]. Here, the local density approximation (LDA) and generalized gradient approximation (GGA) were considered within DFT scheme. It is known that LCAO approximations compute the crystal wave function by solving the Schrodinger equation $(\hat{H}\Psi = E\Psi)$, where the Hamiltonian energy operator $(\hat{H})$ consists as:

$$\hat{H} = \hat{t} + \hat{\upsilon} + \hat{J}[\rho(\vec{r})] + \frac{\partial E_{xc}[\rho(\vec{r})]}{\partial \rho(\vec{r})} \qquad (6.3)$$

where $\hat{t}$, $\hat{v}$ and $\hat{J}$ are corresponding to the kinetic, external potential and Coulomb interaction, respectively, while E_{xc} is the exchange-correlation density functional energy defined as:

$$E_{xc}[\rho(\vec{r})]=\int \rho(\vec{r})\,\varepsilon_{xc}(\vec{r})\,d\vec{r} \quad (6.4)$$

here ε_{XC} is the exchange-correlation energy per particle in uniform electron gas and defined differently in LDA and GGA approximations as:

$$\varepsilon_{xc}^{LDA/GGA}=\varepsilon_{xc}[\rho(\vec{r})/\rho(\vec{r}),|\vec{\nabla}\rho(\vec{r})|] \quad (6.5)$$

In the DFT-LDA, we have used the Dirac-Slater [10] exchange along with correlations of Perdew and Zunger [14] while the exchange and correlations of Perdew et al. [15] have been considered for DFT-GGA scheme. For the present case, the lattice parameter of Fe_3O_4 (space group = 227) is taken as 8.377 Å [5]. The all electron basis sets for Fe and O atoms were taken after re-optimization up to standard tolerance limit using BILLY softwares [10]. Here, the self-consistent field (SCF) calculations have been performed using 29 **k** points in the irreducible Brillouin zone (BZ). The total CPs using DFT-LDA and DFT-GGA schemes have been calculated by adding the FA core contribution from Biggs et al. [13] to the corresponding theoretical valence CP. The optimized basis sets for Fe_3O_4 are listed in Table 6.1. While in Fig. 6.1, we have plotted the structure sketch of cubic Fe_3O_4 using plotting software of Kokalj [16].

6.4. Results and Discussions:

The MP charge transfer data of Fe_3O_4 using DFT-LDA and DFT-GGA scheme show the charge transfer from Fe to O atoms in Fe_3O_4. The value of total charge transfer using DFT-LDA and DFT-GGA schemes are 4.42 and 4.50 e^-, respectively. Here, it can be seen that a slight different amount of charge is being transferred from non-equivalent Fe atoms and is equally distributed among the O atoms. The value of charge transfer for 2 non-equivalent Fe atoms is found to be 1.495 (1.522) e^- using DFT-LDA (DFT-GGA) scheme while for 4 non-equivalent Fe atoms, this value comes out to be 1.462 (1.490) e^-. Further, the amount of chare shared by each O atom among the 8 equivalent atoms using DFT-LDA

Table 6.1: Optimized basis-sets, Gaussian exponents (in a.u.$^{-2}$) and contraction coefficients for Fe and O in case of Fe_3O_4. Asterisks represent unoccupied atomic orbitals at the beginning of the self consistent field (SCF) process.

Atom	Orbitals	Exponents	Coefficients		
			s	p	D
Fe	s	315379.0	0.000227		
		45690.0	0.0019		
		9677.3	0.0111		
		2520.88	0.0501		
		759.746	0.1705		
		262.964	0.36924		
		102.801	0.4033		
		42.9733	0.1434		
	sp	798.262	-0.0052	0.00850	
		191.162	-0.068	0.0608	
		63.6885	-0.1314	0.2114	
		25.3625	0.2517	0.3944	
		10.7338	0.6433	0.398	
		3.764	0.2825	0.2251	
	sp	48.1434	0.0122	-0.0215	
		17.4579	-0.2278	-0.085	
		6.9972	-0.8801	0.201	
		3.0791	0.9755	1.3024	
	sp	1.2989	1.0	1.0	
	sp*	0.5430	1.0	1.0	
	d	31.9488			0.0578
		8.8893			0.2664
		3.1008			0.5195
		1.1377			0.5863
	d*	0.3563			1.0
O	s	8020.0	0.00108		
		1338.0	0.00804		
		255.4	0.05324		
		69.22	0.1681		
		23.90	0.3581		
		9.264	0.3855		
		3.851	0.1468		
		1.212	0.0728		
	sp	48.5885	-0.0108	0.0098	
		10.6554	-0.0903	0.0701	
		3.2817	-0.0467	0.2051	
		1.241	0.4211	0.3356	
	sp*	0.4475	1.0	1.0	
	sp*	0.11073	1.0	1.0	

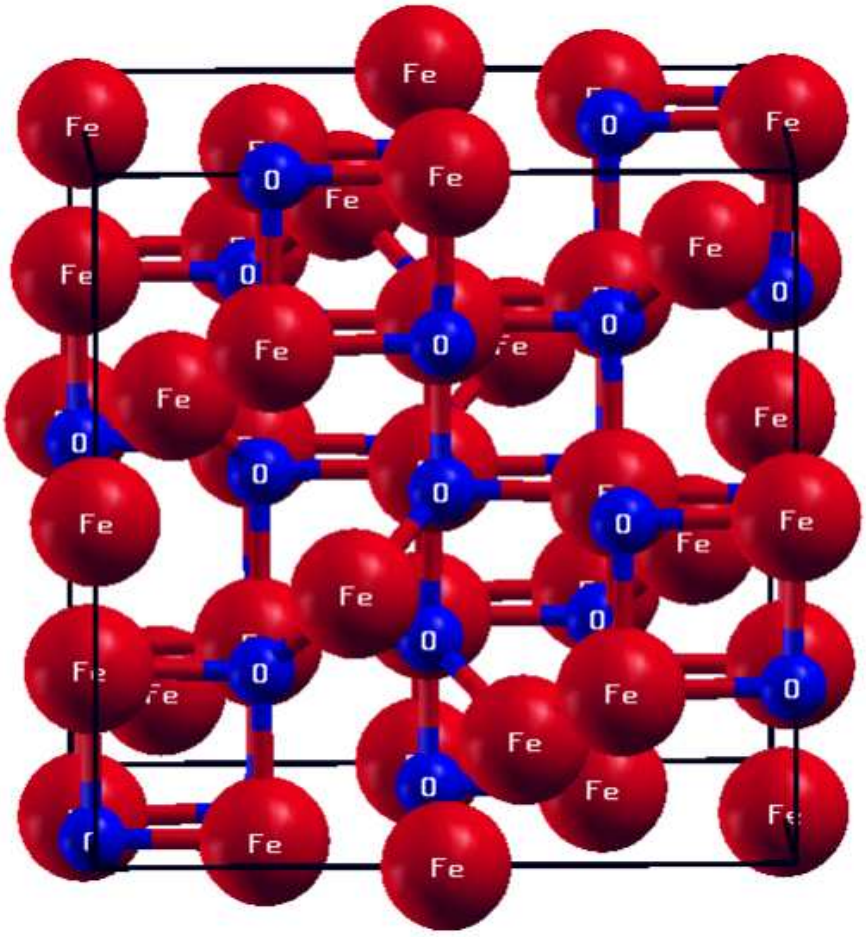

Fig. 6.1: Structural sketch of cubic Fe_3O_4 using software tool of Kokalj [16].

(DFT-GGA) scheme is 1.105 (1.126) e^-. Since the present computations of MP data are based on basis sets with sufficiently diffuse external atomic orbitals hence the data are expected to be quite reliable.

In Fig. 6.2, we have plotted the spin-up (↑) and spin down (↓) DOS for Fe_3O_4 using DFT-GGA scheme. Our computed DOS are in good agreement with the available data of Penicaud et al. [4]. Here, it can be seen that the band gap at Fermi energy (E_F) occurs in spin down state and non zero at the E_F level in spin-up state which predicts the half metallic character of Fe_3O_4. Here, we have also calculated the partial DOS of individual Fe and O atoms (not shown here) which shows that the DOS of Fe_3O_4 is mainly contributed by the Fe atoms which is in agreement with the DOS reported by Masrour et al. [7].

In Fig. 6.3, we have plotted the unconvoluted directional differences in the CPs for (a) J_{111}-J_{110}, (b) J_{111}-J_{100} and (c) J_{110}-J_{100} using DFT-LDA and DFT-GGA schemes for Fe_3O_4. The numerical values of directional CPs are also reported in Table 6.2. Here, almost zero anisotropic effect in the high momentum side ($p_z \geq 4$ a.u.) is seen which may be due to the dominance of the core electrons in this region and such identical contribution is cancelled while taking the directional differences. In the low momentum side, the anisotropies in CPs represent their characteristic effect and the similar trend in the low momentum side is occurred in case of DFT-LDA and DFT-GGA scheme. In Figs. 6.3 (a and b), the positive value of anisotropies at p_z=0.0 a.u. shows the dominance of electron density along [111] direction as compared to [110] and [100] directions. The single crystal measurements are required to explain more about these theoretical anisotropies. Further, the difference profiles between convoluted theoretical (DFT-LDA and DFT-GGA scheme) and experimental CPs have been reported in Fig. 6.4 along with the statistical error ($\pm\sigma$) at few points. Needless to mention that both the theoretical CPs have been convoluted at instrumental resolution of 0.55 a.u. to account the effects of experimental resolution in the theoretical CPs. Here, it can be seen that the theoretical CPs have overestimate the experimental data in the low momentum side while such difference in small in the high momentum side ($p_z \geq 5$ a.u.) which is again due to the dominancy of core electrons in this region. In

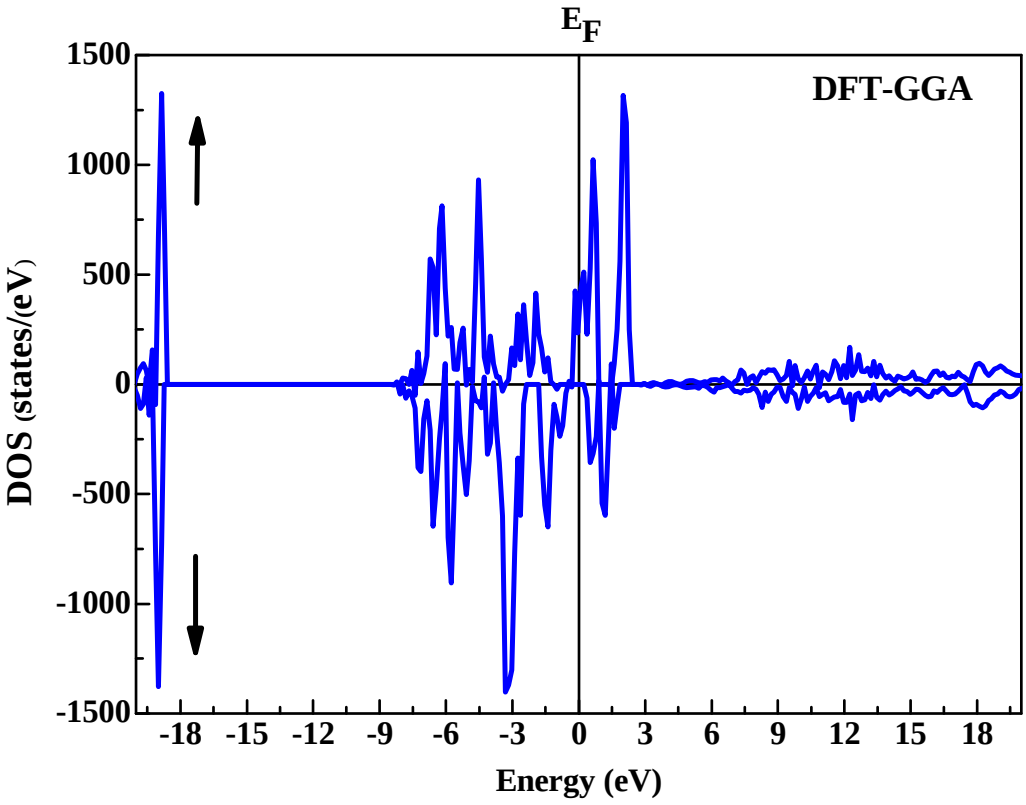

Fig. 6.2: The spin-up (↑) and spin down (↓) density of states (DOS) of Fe_3O_4 using DFT-GGA scheme.

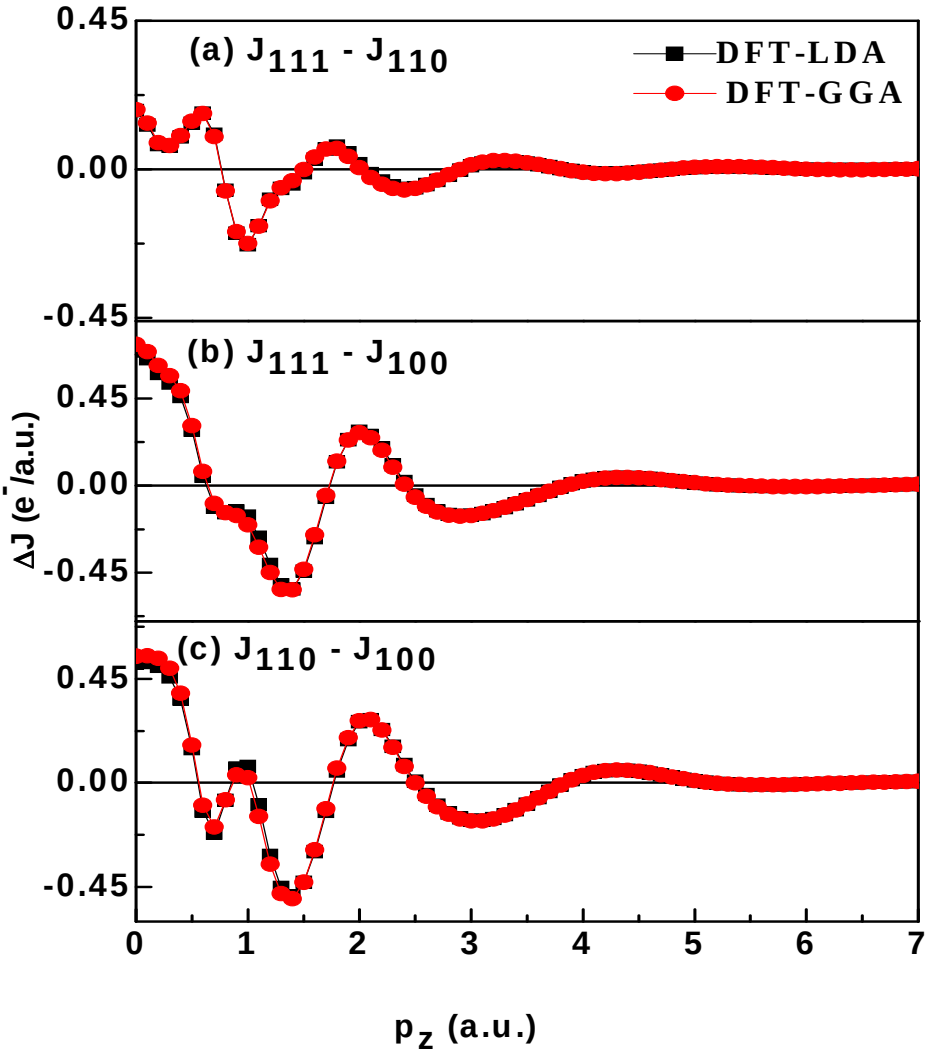

Fig. 6.3: Anisotropies in the unconvoluted theoretical CPs for Fe_3O_4 corresponding to the pairs (a) J_{111}-J_{110}, (b) J_{111}-J_{110} and (c) J_{110}-J_{100} within DFT-LDA and DFT-GGA approximations. The solid lines are drawn to dictate the eyes.

Table 6.2: The unconvoluted directional CPs of Fe_3O_4 along [100], [110] and [111] using DFT-LDA and DFT-GGA scheme within the LCAO approximations.

p_z	$J(p_z)$ (e^-/a.u.)					
(a.u.)	DFT-LDA			DFT-GGA		
	[100]	[110]	[111]	[100]	[110]	[111]
0.0	25.645	26.163	26.339	25.531	26.078	26.259
0.1	25.550	26.070	26.203	25.441	25.990	26.130
0.2	25.285	25.789	25.863	25.185	25.724	25.804
0.3	24.873	25.331	25.400	24.780	25.276	25.348
0.4.	24.331	24.692	24.789	24.247	24.635	24.736
0.5	23.694	23.840	23.979	23.618	23.782	23.927
0.6	22.932	22.809	22.978	22.860	22.764	22.932
0.7	21.929	21.710	21.816	21.869	21.678	21.776
0.8	20.654	20.578	20.513	20.626	20.552	20.486
1.0	17.878	17.949	17.719	17.928	17.949	17.724
1.2	15.456	15.141	15.048	15.530	15.177	15.081
1.4	13.270	12.781	12.736	13.323	12.820	12.785
1.6	11.139	10.840	10.870	11.162	10.871	10.908
1.8	9.226	9.278	9.347	9.238	9.302	9.364
2.0	7.769	8.033	8.049	7.782	8.050	8.054
3.0	4.527	4.365	4.374	4.536	4.370	4.382
4.0	2.732	2.764	2.755	2.734	2.766	2.756
5.0	1.946	1.955	1.959	1.948	1.957	1.962
6.0	1.456	1.450	1.450	1.458	1.452	1.452
7.0	1.091	1.096	1.096	1.092	1.098	1.098

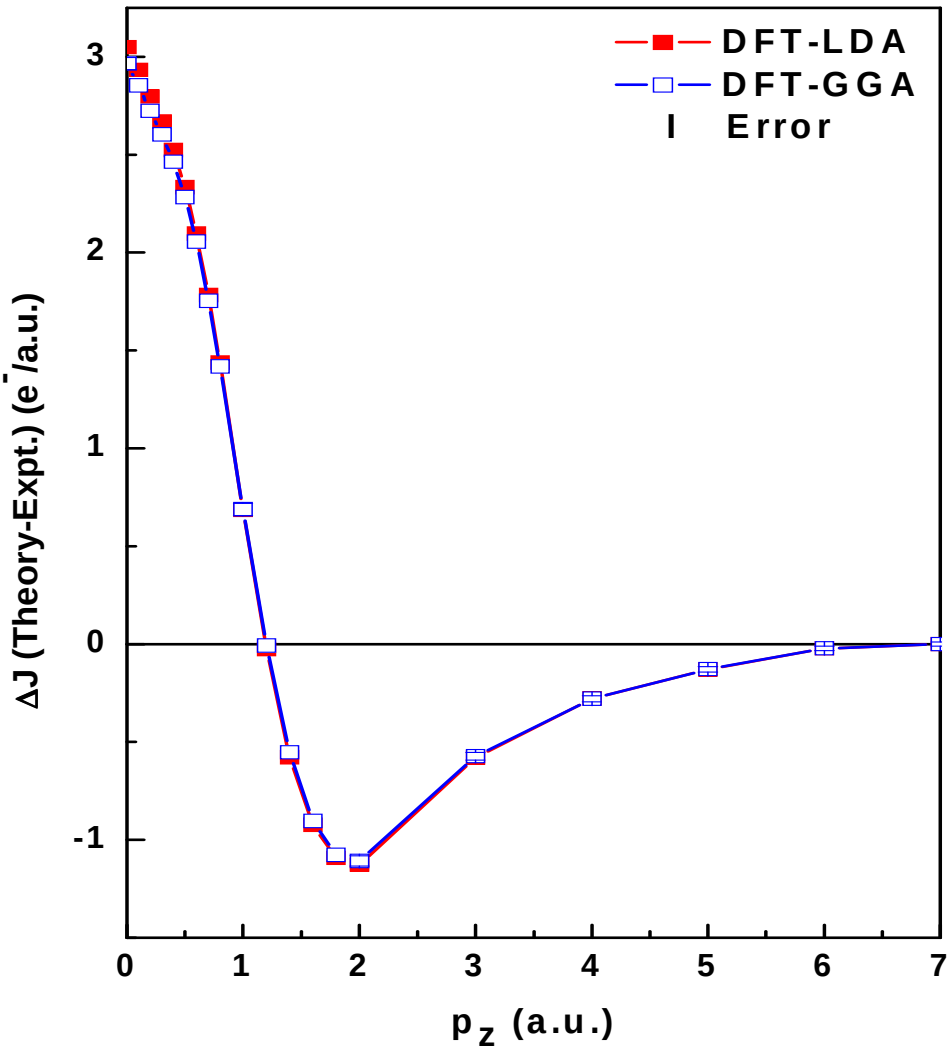

Fig. 6.4: Difference between isotropic convoluted theoretical (DFT-LDA and DFT-GGA) and experimental profiles along with the statistical errors (±σ) at few points for Fe_3O_4. The solid lines are drawn to dictate the eyes.

Table 6.3, we have also mentioned the numerical values of unconvoluted theoretical (DFT-LDA and DFT-GGA) and experimental CP along with statistical error (±σ) at few points. On the basis of the χ^2 fitting, it is found that the DFT-GGA scheme gives a slight better agreement with the experimental data as compared to the DFT-LDA scheme which shows the superiority of GGA over the LDA. The large difference between the theoretical and experimental data may be due to the non-inclusion of relativistic effects and Lam-Platzman (LP) correlation [1].

6.5. Conclusions:

The CP measurements using 59.54 keV of Fe_3O_4 have been used to test the DFT-LDA and DFT-GGA based CP under the framework of LCAO approximations. It is found that DFT-GGA scheme gives the better agreement as compared to the DFT-LDA scheme. Further, the MP charge transfer data shows the transfer of charge from Fe to O atoms while the DOS have confirmed the half metallic character of Fe_3O_4.

Table 6.3: Unconvoluted isotropic Compton profiles of Fe_3O_4 computed using DFT-LDA and DFT-GGA scheme within the LCAO approximations along with the experimental profile. The statistical errors (±σ) are also shown at few points.

p_z (a.u.)	$J(p_z)$ (e^-/a.u.)		
	Theory		Experiment
	DFT-LDA	DFT-GGA	
0.0	25.94	25.85	22.66 ± 0.031
0.1	25.88	25.80	22.56
0.2	25.62	25.54	22.35
0.3	25.20	25.13	22.02
0.4.	24.56	24.50	21.57
0.5	23.82	23.77	21.03
0.6	22.87	22.83	20.38
0.7	21.78	21.75	19.68
0.8	20.55	20.53	18.90
1.0	17.91	17.92	17.21 ± 0.030
1.2	15.23	15.26	15.45
1.4	12.95	12.99	13.73
1.6	10.94	10.96	12.09
1.8	9.29	9.30	10.60
2.0	7.97	7.98	9.29 ± 0.026
3.0	6.12	6.18	5.03 ± 0.020
4.0	4.40	4.41	3.06 ± 0.016
5.0	2.76	2.76	2.09 ± 0.013
6.0	1.96	1.96	1.48 ± 0.011
7.0	1.45	1.45	1.13 ± 0.010

Part-II

(Based on 20 Ci ^{137}Cs Compton spectrometer)

Electronic Structure of Magnetite: Ab-initio Computations and Electron Momentum Density Measurements

6.6. Introduction:

As discussed in part-I of the chapter, Magnetite (Fe_3O_4) belongs to inverse spinel cubic structure with two formula units (14 atoms) in a unit cell [5]. Magnetite has been studied by several workers due to its important electronic, magnetic and industrial applications. In addition to the earlier work of part I of the chapter, Chiba [17] has employed linear combination of atomic orbitals (LCAO) to study the momentum distributions for positron annihilation while Yanase and Siratori [18] have studied energy bands and density of states (DOS) using augmented plane wave (APW) method. Density functional theory (DFT) with local spin density approximation (LSDA) [19] and linearized muffin-tin orbital (LMTO) [20] were employed to discuss electronic and magnetic properties of the magnetite. Also, charge and orbital orders in Fe_3O_4 were discussed using Coulomb interaction correction (CIC) within local density approximation (LDA) [21,22]. Crystal structure, charge ordering and phonon analysis in Fe_3O_4 were also explained using DFT with generalized gradient approximation (GGA) and hybrid DFT (B3LYP) [23]. Fully-relativistic Dirac LMTO within LSDA and LSDA+U formalism were considered for electronic properties along with x-ray absorption and magnetic circular dichroism spectra [24]. In earlier Compton profile (CP) measurements, Lässer et al. [25] have reported CPs of Fe_3O_4 using 320.1 keV photons from ^{51}Cr radio-isotope at a poor resolution of 0.578 a.u. at 100 and 300 K and could not find significant differences between these two measurements.

As mentioned in chapter 1, Compton scattering (CS) technique has been marked as a definite tool to deduce information of fundamental ground state electron momentum density (EMD), $\rho(\mathbf{p})$, of the materials [1,2]. In CS, CP is the measured quantity and is defined as the projection of EMD along the conventionally chosen z-axis. If E_1 and E_2 are the incident and scattered photon energies, respectively, then CP from double differential Compton cross-section $\left(d^2\sigma/d\Omega\, dE_2\right)$ is calculated as,

$$\frac{d^2\sigma}{d\Omega\, dE_2} = C(E_1, E_2, \theta, p_z) \times \left[J(p_z) = \int\int \rho(\mathbf{p})\, dp_x dp_y\right] \tag{6.6}$$

Here θ and p_z are scattering angle and component of electron linear momentum along z-axis, respectively. The factor $C(E_1, E_2, \theta, p_z)$ can be computed using formalism of Eisenberger and Reed [26].

6.7. Methodologies:

6.7.1. Experiment:

CP measurements of Fe_3O_4 were performed employing 740 GBq ^{137}Cs Compton spectrometer [27 and chapter 2]. High purity sample, procured from M/s Sigma Aldrich, was pressurized to get circular pallet of diameter and thickness of 34.0 and 7.44 mm, respectively with bulk density as 0.39 g/cm^3. In the present experiment, pallet was exposed by the γ-rays (661.65 keV) and scattered radiations were detected by Canberra made (GL0510P) high purity Germanium (HPGe) detector. The Ge crystal was cooled at liquid nitrogen temperature (77 K). In the present measurements, the scattering angle and overall momentum resolution (full width at half maximum) were 160±0.6° and 0.34 a.u., respectively. During the exposure time of 265.4 h, we have collected 2.09×10^7 Compton counts. To obtain true Compton profile, first of all the raw data were processed for the background correction. Thereafter, the profile was corrected for the detector response function (limited to stripping off the low-energy tail), energy dependent detector efficiency, sample absorption and Compton cross-section corrections by using the computer codes of Warwick group [11]. Afterwards, the data were corrected for multiple scattering correction using the Monte Carlo simulation as prescribed by Felsteiner et al. [12]. The percentage of the multiple scattering in p_z range −10.0 to + 10.0 a.u. was found to be 10.21 %. Finally, the momentum scale CP was normalized to corresponding free atom (FA) CP area of Biggs et al. [13] which was found to be 50.07 e^- in the momentum range 0–7 a.u. for Fe_3O_4.

6.7.2. Theory:

MP data, DOS and CPs for Fe_3O_4 have been computed using LCAO formalism [10].

Here the LCAO calculations have been performed using DFT with GGA and B3LYP (hybridization of Hartree-Fock and DFT potentials) as prescribed by Dovesi et al. [10 and chapter 2]. In these approximations within LCAO scheme, the exchange-correlation energy (E_{XC}) is approximated as,

$$E_{XC}^{LCAO-DFT-GGA}[n(\mathbf{r})] = \int n(\mathbf{r})\,\varepsilon_{xc}[n(\mathbf{r}),|\nabla n(\mathbf{r})|]d\mathbf{r}, \tag{6.7}$$

where ε_{XC} is the exchange-correlation energy per particle in uniform electron gas.

For DFT-GGA, the exchange and correlation are taken form Perdew et al. [28]. While in B3LYP, E_{XC} is defined as,

$$E_{XC}^{LCAO-B3LYP} = 0.80 * \left(E_X^{LDA} + 0.90 * \Delta E_X^{BECKE}\right) + 0.20 * E_X^{HF} + 0.19 * E_C^{VWN} + 0.81 * E_C^{LYP} \quad (6.8)$$

Here $E_X^{LDA}, \Delta E_X^{BECKE}$ and E_X^{HF} are the exchange potentials of Dirac-Slater [21], Becke gradient correction [10,29] and HF [10], respectively, whereas E_C^{VWN} and E_C^{LYP} are the correlation potentials of Vosko et al. [30] and Lee et al. [31], respectively. The basis sets of Fe and O atoms were taken from Table 6.1. Lattice parameter for Fe_3O_4 is taken as 8.377 Å [5] along with self consistent field calculations with 95 **k** points in the irreducible Brillouin zone. Further, the total CP from DFT-GGA and B3LYP schemes have been calculated by adding the respective FA core contribution [12] to the normalized valence Compton profile of the respective scheme.

6.8. Results and Discussion:

6.8.1. MP analysis and density of states:

MP charge transfer data of Fe_3O_4 using DFT-GGA and B3LYP are listed in Table 6.4. Here, A and B denote tetrahedral and octahedral sites. MP data show that Fe atoms perform the role of donor atoms whereas O atoms act as acceptor atoms. Here, the total charge transfer using DFT-GGA and B3LYP schemes are 4.48 and 4.72 e^-, respectively. Our charge transfer data for Fe_3O_4 are lower than prediction of Zhang and Satpathy [19] (6 e^-) and Rowan et al. [23] (6.06 e^-). Also, charge transfer from DFT-GGA is lower than to B3LYP scheme, due to incorporation of 20 % HF component in B3LYP. Also, such MP analysis have successfully been applied to our earlier work on Sm_2O_3 [32] and B_2O_3 (B= Sc and Y) [33].

In Fig. 6.5 (a-d), we have reported the majority- and minority-spin DOS for 3d, 4s and total states at tetrahedral (A) site of Fe atom, 3d, 4s and total states at octahedral (B) site of Fe atom, 2s, 2p and total states of O atom and total states of Fe_3O_4, respectively. The DOS are in good agreement with available data of Pénicaud et al. [4]. We observed that there is no energy gap in spin-up states and band gap occurs in spin-down states, which confirm a half metallic character of Fe_3O_4.

Table 6.4: MP based charge transfer, from Fe to O atoms in Fe_3O_4 using DFT-GGA and B3LYP schemes within LCAO. The numbers of equivalent atoms are shown in the brackets. A and B represent tetrahedral and octahedral sites of inverse spinel structure, respectively.

Scheme	Amount of charge transfer (e^-)		
	Donor atoms (Fe)		Acceptor atoms (O)
	A site	B site	
DFT-GGA	1.50 (2)	1.49 (4)	1.12 (8)
B3LYP	1.68 (2)	1.52 (4)	1.18 (8)

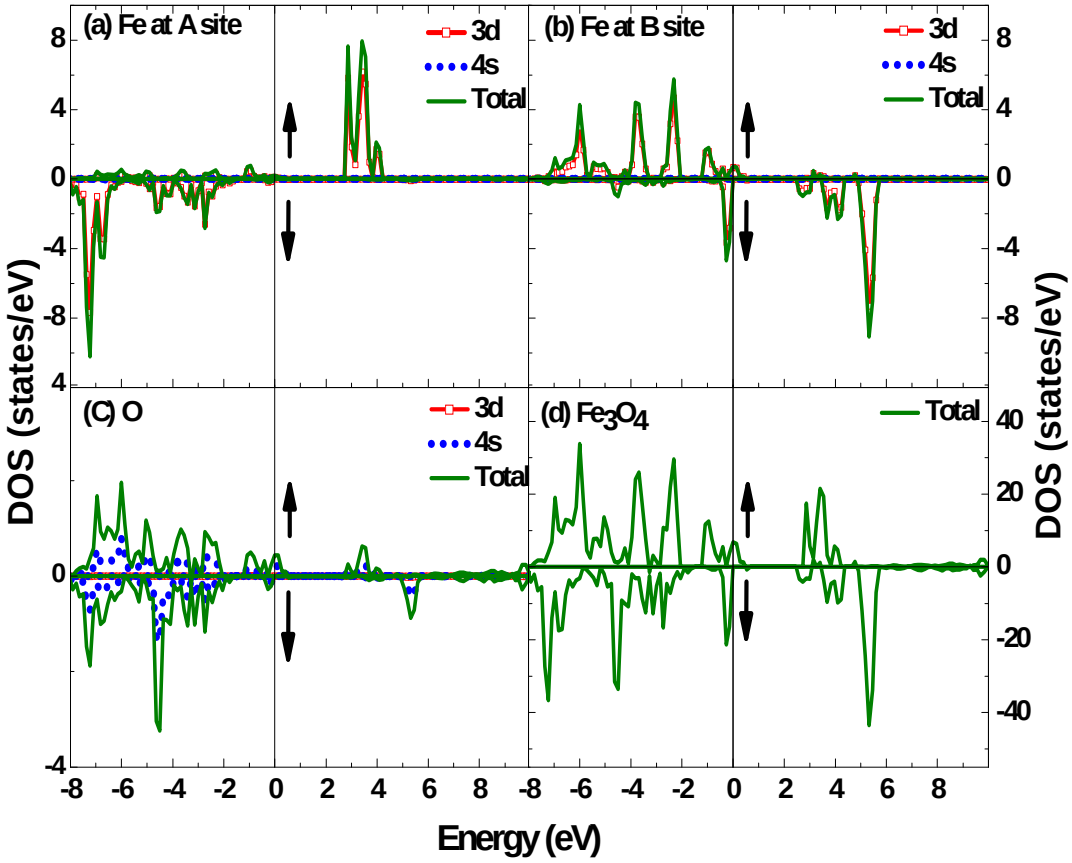

Fig. 6.5: Spin projected density of states (DOS) for (a) 3d, 4s states and their total of Fe at tetrahedral (A) site, (b) 3d, 4s states and total of Fe at octahedral (B) site, (c) 2s, 2p states and total of O and (d) total DOS for Fe_3O_4 using LCAO-B3LYP approximation.

6.8.2. Compton profile:

Differences between the unconvoluted directional CPs for Fe_3O_4 have been plotted using DFT-GGA and B3LYP schemes (Fig. 6.6). General trends of oscillations in these theoretical anisotropies ($J_{111}-J_{110}$, $J_{111}-J_{100}$ and $J_{110}-J_{100}$) are quite similar using DFT-GGA and B3LYP schemes. The numbers of directional CPs are reported in Table 6.5. The values of the anisotropies for the reported combinations in the high momentum range ($p_z \geq 4.0$ a.u.) are approximately zero as this region is formed by identical core electrons. The anisotropy in low momentum densities region using DFT-GGA is different from B3LYP, which is understandable due to incorporation of HF exchange energy in B3LYP scheme.

In Fig. 6.7, difference (convoluted theory − experimental) profiles along with the statistical errors ($\pm\sigma$) are reported. Numerical values of the unconvoluted theoretical (DFT-GGA and B3LYP) and experimental CPs along with the statistical errors ($\pm\sigma$) for Fe_3O_4 are also collated in Table 6.6.

Further, we have calculated sum of square of deviations between theory and experiment (Δ^2) to judge the best agreement between DFT-GGA or B3LYP and the experiment for Fe_3O_4. The lower value of Δ^2 for B3LYP than that from DFT-GGA scheme reflects a better agreement of B3LYP scheme with the experimental CP. It is worthwhile to mention that quality of basis sets, non-inclusion of relativistic effects and Lam-Platzman (LP) electron-electron correlation correction in LCAO approximation may be main reasons for deviations in low momentum region of Fig. 6.7.

6.9. Conclusions:

We have performed CP measurements of Fe_3O_4 using 661.65 keV γ-rays to validate the theoretical CPs derived using LCAO method. LCAO calculations have been attempted using DFT with GGA and the hybridization of HF and DFT scheme (so called B3LYP). It is found that B3LYP scheme gives a better agreement with experimental data than the DFT-GGA scheme. Further, spin dependent density of states using LCAO-B3LYP scheme have confirmed the half metallic character of Fe_3O_4, while large value of MP charge transfer (4.72 e^-) predicts the dominancy of ionic nature in the compound.

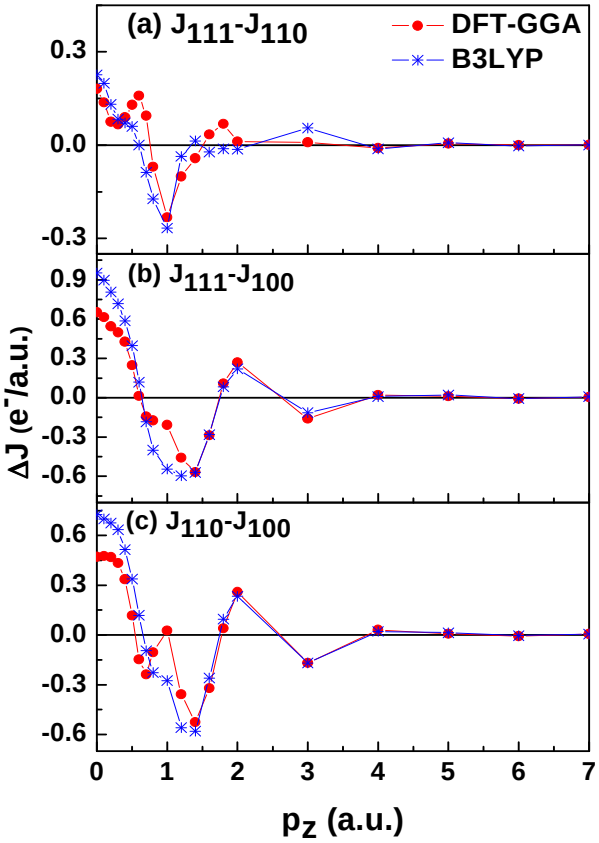

Fig. 6.6: Anisotropies in the unconvoluted theoretical Compton profiles of Fe_3O_4 using DFT-GGA and B3LYP schemes.

Table 6.5: The unconvoluted directional CPs of Fe_3O_4 along [100], [110] and [111] using DFT-GGA and B3LYP approximations within LCAO scheme.

p_z	$J(p_z)$ (e^-/a.u.)					
(a.u.)	DFT-GGA			B3LYP		
	[100]	[110]	[111]	[100]	[110]	[111]
0.0	25.563	26.035	26.216	25.178	25.903	26.130
0.1	25.507	25.983	26.120	25.168	25.868	26.066
0.2	25.253	25.722	25.797	24.993	25.670	25.801
0.3	24.855	25.289	25.354	24.657	25.293	25.376
0.4.	24.285	24.622	24.712	24.118	24.634	24.705
0.5	23.693	23.811	23.940	23.507	23.845	23.905
0.6	22.928	22.782	22.940	22.728	22.847	22.846
0.7	21.924	21.686	21.781	21.795	21.700	21.612
0.8	20.639	20.535	20.465	20.666	20.439	20.265
1.0	17.949	17.975	17.742	18.178	17.903	17.636
1.2	15.500	15.143	15.042	15.727	15.168	15.132
1.4	13.357	12.832	12.789	13.487	12.906	12.919
1.6	11.199	10.878	10.912	11.219	10.959	10.937
1.8	9.274	9.315	9.383	9.271	9.366	9.354
2.0	7.777	8.035	8.047	7.812	8.046	8.032
3.0	4.541	4.372	4.381	4.534	4.366	4.421
4.0	2.734	2.765	2.755	2.746	2.767	2.755
5.0	1.951	1.958	1.962	1.948	1.962	1.969
6.0	1.460	1.454	1.454	1.460	1.456	1.453
7.0	1.095	1.101	1.101	1.095	1.101	1.102

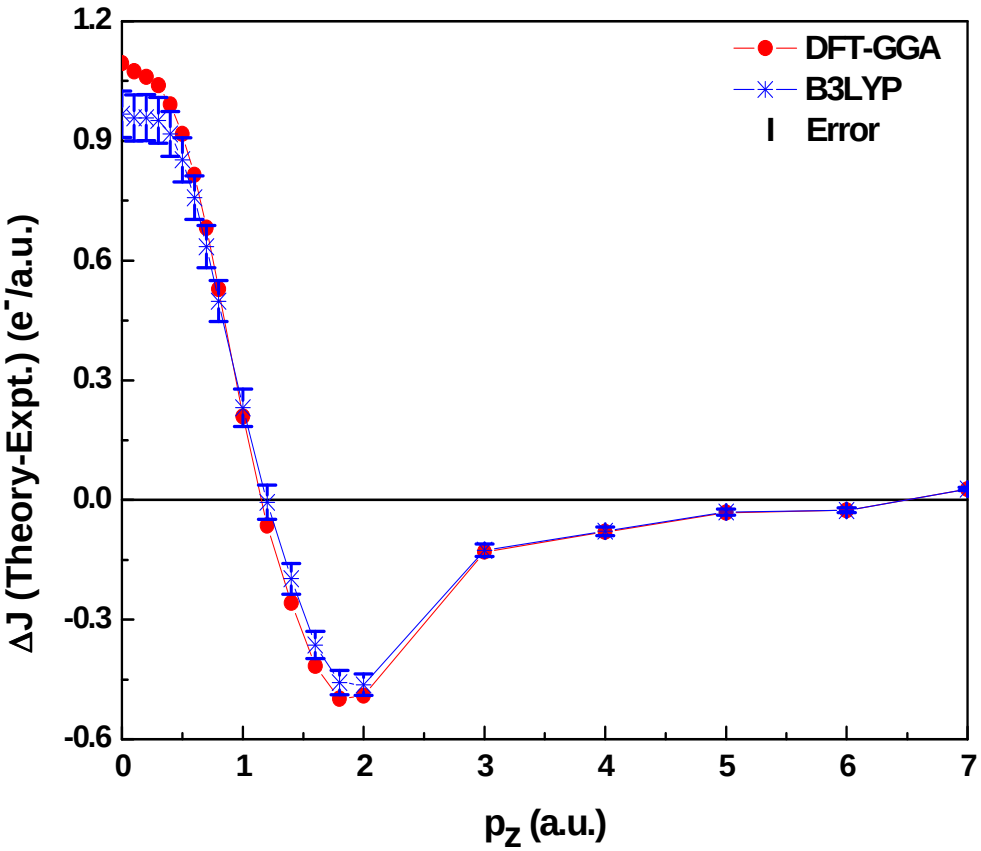

Fig. 6.7: Difference profiles deduced from isotropic convoluted theoretical (DFT-GGA and B3LYP schemes within LCAO approximations) and experimental Compton profiles of Fe_3O_4.

Table 6.6: Unconvoluted theoretical CPs of Fe_3O_4 using DFT-GGA and B3LYP approximations within LCAO scheme and experimental data. Statistical error (±σ) at each data point is also shown.

p_z (a.u.)	J (p_z) (e/a.u.)		
	Theory		Expt.
	DFT-GGA	B3LYP	
0.0	25.923	25.771	24.758±0.058
0.1	25.869	25.729	24.629±0.058
0.2	25.610	25.494	24.367±0.058
0.3	25.188	25.082	23.964±0.057
0.4	24.555	24.467	23.415±0.056
0.5	23.817	23.737	22.727±0.055
0.6	22.872	22.815	21.910±0.054
0.7	21.788	21.754	20.981±0.053
0.8	20.560	20.561	19.956±0.051
1.0	17.928	18.040	17.711±0.047
1.2	15.243	15.487	15.413±0.043
1.4	12.968	13.249	13.298±0.038
1.6	10.944	11.236	11.459±0.034
1.8	9.290	9.581	9.878±0.030
2.0	7.968	8.257	8.531±0.027
3.0	4.402	4.603	4.546±0.016
4.0	2.760	2.876	2.851±0.011
5.0	1.958	2.024	1.992±0.008
6.0	1.454	1.498	1.482±0.006
7.0	1.100	1.134	1.091±0.004

References

1. M.J. Cooper, P.E. Mijnarends, N. Shiotani, N. Sakai, A. Bansil, X-ray Compton Scattering, Oxford University Press, New York, 2004, and references therein.

2. N.L. Heda, B.L. Ahuja, Recent Trends in Radiation Physics Research, in: B.L. Ahuja (Ed.), Himanshu Publications, New Delhi, India, 2010, 25–30.

3. Z. Szotek, W.M. Temmerman, D. Ködderitzsch, A. Svane, L. Petit, H. Winter, Phys. Rev. B 74 (2006) 174431-1−174431-12.

4. M. Penicaud, B. Siberchicot, C.B. Sommers, J. Kübler, J. Mag. Mag. Mat. 103 (1992) 212–220.

5. P. Piekarz, K. Parlinski, A.M. Oles, Phys. Rev. B 76 (2007) 165124-1−165124-16.

6. Z. Szotek, W.M. Temmerman, A. Svane, L. petit, G.M. Stocks, H. Winter, Phys. Rev. B 68 (2003) 054415-1−054415-9.

7. R. Masrour, E.K. Hlil, M. Hamedoun, A. Benyoussef, O. Mounkachi, H.E. Moussaoui, J. Mag. Mag. Mat. 378 (2015) 37−40.

8. J.A. Duffy, J.W. Taylor, S.B. Dugdale, C.S. Taylor, M.W. Butchers, S.R. Giblin, M.J. Cooper, Y. Sakurai, M. Itou, Phys. Rev. B 81 (2010) 134424-1−134424-5.

9. B.L. Ahuja, N.L. Heda, Pramana J. Phys. 68 (2007) 843−850.

10. R. Dovesi, V.R Saunders, C. Roetti, R. Orlando, C.M. Zicovich-Wilson, F. Pascale, B. Civalleri, K. Doll, N.M. Harrison, I.J. Bush, Ph. D'Arco, M. Llunell, M. Causa, Y. Neol, CRYSTAL14 User's Manual, University of Torino, Torino, Italy (2014), and references therein.

11. D.N. Timms, Compton Scattering Studies of Spin and Momentum Densities, Ph.D. thesis, University of Warwick, UK, 1989 (Unpublished).

12. J. Felsteiner, P. Pattison, M.J. Cooper, Phil. Mag. 30 (1974) 537−548.

13. F. Biggs, L.B. Mendelsohn, J.B. Mann, At. Data Nucl. Data Tables 16 (1975) 201−308.

14. J.P. Perdew, A. Zunger, Phys. Rev. B 23 (1981) 5048–5079.

15. J.P. Perdew, K. Burke, M. Ernzerhof, Phys. Rev. Lett. 77 (1996) 3865–3868.

16. A. Kokalj, Comput. Mater. Sci. 28 (2003) 155−168.

17. T. Chiba, J. Chem. Phys. 64 (1976) 1182–1188.

18. A. Yanase, K. Siratori, J. Phys. Soc. Japan 53 (1984) 312–317.

19. Z. Zhang, S. Satpathy, Phys. Rev. B 44 (1991) 13319–13331.

20. H.-T. Jeng, G.Y. Guo, Phys. Rev. B 65 (2002) 094429-1–094429-9.

21. V.I. Anisimov, I.S. Elfimov, N. Hamada, K. Terakura, Phys. Rev. B 54 (1996) 4387–4390.

22. I. Leonov, A.N. Yaresko, V.N. Antonov, M.A. Korotin, V.I. Anisimov, Phys. Rev. Lett. 93 (2004) 146404-1–146404-4.

23. A.D. Rowan, C.H. Patterson, L.V. Gasparov, Phys. Rev. B 79 (2009) 205103-1–205103-18.

24. V.N. Antonov, B.N. Harmon, A.N. Yaresko, Phys. Rev. B 67 (2003) 024417-1–024417-14.

25. R. Lässer, R.M. Singru, B. Lengeler, Solid State Commun. 25 (1978) 345–347.

26. P. Eisenberger, W.A. Reed, Phys. Rev. B 9 (1974) 3237–3241.

27. B.L. Ahuja, M. Sharma, S. Mathur, Nucl Instrum. Methods B 244 (2006) 419–426.

28. J.P. Perdew, A. Ruzsinszky, G.I. Csonka, O.A. Vydrov, G.E. Scuseria, L.A. Constantin, X. Zhou, K. Burke, Phys. Rev. Lett. 100 (2008) 136406-1–136406-4.

29. A.D. Becke, Phys. Rev. A 38 (1988) 3098–3100.

30. S.H. Vosko, L. Wilk, M. Nusair, Can. J. Phys. 58 (1980) 1200–1211.

31. C. Lee, W. Yang, R.G. Parr, Phys. Rev. B, 37 (1988) 785–789.

32. S. Sharma, N.L. Heda, K.K. Suthar, S. Bhatt, K. Sharma, B.L. Ahuja, Comput. Mater. Sci. 104 (2015) 205–211.

33. B.L. Ahuja, S. Sharma, N.L. Heda, S. Tiwari, K. Kumar, B.S. Meena, S. Bhatt, J. Phys. Chem. Solids 92 (2016) 53–63.

Chapter 7

Conclusions and Future Scope

7.1. Conclusions:

The present thesis work is devoted to the preparation of $Ni_{1-x}Cr_xFe_2O_4$ (x= 0.0, 0.02 and 0.05) thin films and their characterization using X-ray diffraction (XRD), Raman spectroscopy (RS), X-ray photoemission spectroscopy (XPS), super-conducting quantum interference device (SQUID)-vibrating sample magnetometer (VSM) and Fourier transform infrared (FTIR) spectroscopy. Further, we have undertaken work on theoretical and experimental Compton profiles (CPs) of some ferrites namely Fe_3O_4, $NiFe_2O_4$, $ZnFe_2O_4$ and $CdFe_2O_4$ using 20 Ci ^{137}Cs Compton spectrometer. In addition, 100 mCi ^{241}Am Compton spectrometer is also employed to measure CP of Fe_3O_4. All the CP measurements have been performed at ML Sukhadia University, while other measurements were made at IUC-DAE-CSR, Indore. Going beyond experimental CPs, we have also computed the energy bands, density of states (DOS), Mulliken's populations (MP), band gap and magnetic moments using linear combination of atomic orbital (LCAO) scheme as embodied in CRYSTAL14 software.

Pulsed laser deposition method has been successfully applied to grow thin films of $Ni_{1-x}Cr_xFe_2O_4$ (NCFO) (x = 0.02 and 0.05) on Si (111) and Si (100) substrates. It is observed that thin films grown on Si (111) substrate have larger grain size than those films grown on Si (100) substrate. The XRD and FTIR measurements show single phase growth of the films. XPS measurements have uniquely revealed the mixed spinel structure which is in contrast to inverse spinel structure. Our XPS data suggest Ni and Fe ions in +2 and +3 states at octahedral (O_h) and tetrahedral ($T_{d)}$ sites, which shows decrease in saturation magnetization arising due to magnetic moment at O_h and T_d sites. It is suggested that different cationic distribution of Ni and Fe ions between O_h and T_d sites are due to different strains produced by the substrates and lattice distortion arising due to Cr doping. The present study unambiguously show that the magnetic property in NCFO is majorly controlled by the cationic distribution at different sites, and also its further control by defect density, strain in the film, doping of magnetic or non-magnetic ions.

Electronic response like MP, energy bands, DOS, band gaps and CPs of $ZnFe_2O_4$ and $CdFe_2O_4$ have been computed for the first time using density functional

theory (DFT) within LCAO scheme. Present DFT calculations have been undertaken within the scenario of local density approximation (LDA) and generalized gradient approximation (GGA). Going beyond pure DFT computations, we have also used the hybridized (DFT + Hartree-Fock) approximations for B3LYP and PBE0 prescriptions within LCAO method. The theoretical CPs have been compared with the measured electron momentum densities using 661.65 keV γ-rays and a better agreement between experimental and theoretical B3LYP based profiles was seen for both the spinel ferrites. MP analysis dictates charge transfer from Zn/Cd and Fe to O atoms. On the basis of spin dependent energy bands and DOS, semiconducting nature of the compounds is witnessed. On the basis of equal-valence-electron-density (EVED) scaled CPs and MP analysis for overlap population, more covalent character is found in $ZnFe_2O_4$ than that in $CdFe_2O_4$. Present computations on magnetic moments which are well explored by the LCAO-B3LYP scheme, indicate the applicability of hybrid functionals for such spinel ferrites.

Bulk $Ni_{1-x}Cr_xFe_2O_4$ (x = 0.00 and 0.05) which were prepared by solid state reaction method have been analyzed for structural and magnetic properties, etc. using XRD, RS, FTIR and SQUID measurements. Present data of XRD, RS and FTIR confirmed single phase without any impurity. Further, magnetic moment, MP, spin projected DOS and CPs for $NiFe_2O_4$ (NFO) using DFT and hybrid schemes within LCAO approximation are reported. Presently computed LCAO-B3LYP based CP shows a better agreement with our experimental CP for NFO, which was measured using ^{137}Cs Compton spectrometer. It is seen that present LCAO based magnetic moments for NFO are in tune with the present M-H data and also other available data. Presently deduced spin-projected DOS show an insulating nature of NFO in both the spin-channels, while charge reorganization from Ni/Fe→O atoms is found from MP analysis.

The CP measurements of Fe_3O_4 using 59.54 keV have been used to check the role of LDA and GGA schemes in producing the electron momentum densities. It is found that GGA scheme within LCAO-DFT method leads to a better agreement as compared to the LDA, which is understandable due to homogeneous electron density character considered in LDA scheme. Further, the MP reorganization data

shows the transfer of charge from Fe to O atoms. Present DFT-GGA based total DOS have confirmed the metallic character of Fe_3O_4. Further to revalidate role of hybrid functionals in ferrites at better resolution of instrument, we have remeasured the CP of Fe_3O_4 using 20 Ci ^{137}Cs Compton spectrometer. As seen in other ferrites reported in this thesis, it is seen that the hybrid scheme (B3LYP) predicts a better agreement with the experimental CP. Further, spin up and spin down DOS using LCAO-B3LYP scheme confirmed a half metallic character of the Fe_3O_4 compound. The MP analysis, which is quite reliable because of inclusion of diffused components in basis sets, has also predicted the dominancy of ionic character in Fe_3O_4. The present analysis on Fe_3O_4 also supports that DFT computations as such underestimate the band gap.

7.2. Future Scope:

The present work can be further extended to deduce more science on spinel ferrites:

- High resolution directional CP measurements for Fe_3O_4, $NiFe_2O_4$, $ZnFe_2O_4$ and $CdFe_2O_4$ may help to explore the present anisotropies in the CPs.
- High resolution magnetic Compton profile measurements of these ferrites using synchrotron radiations may be helpful to calculate site dependent magnetic moments and further validate the use of LCAO computations in predicting the magnetic response of such ferrites.
- Energy bands, DOS, CPs and magnetic moment using full-potential linearized augmented plane wave (FP-LAPW) and spin-polarized-relativistic Korringa-Kohn-Rostoker (SPR-KKR) method may be undertaken for comparison with the presently computed LCAO based profiles.

Appendix

(for additional work carried out)

Compton profiles of doped nickel ferrites

In this Appendix, we present the first ever Compton profile (CP) measurements for $Ni_{1-x}Cr_xFe_2O_4$ (x = 0.2 and 0.5) and $NiCr_xFe_{2-x}O_4$ (x = 0.2 and 0.5) using 20 Ci ^{137}Cs Compton spectrometer [1, Chapter 2] at 0.34 a.u. momentum resolution. As reported in the chapters 4 and 5, 661.65 keV γ-rays have been allowed to interact the sample pellet and the scattered photons have been energy analyzed at 160±0.6° scattering angle by high purity germanium (HPGe) detector. The experimental parameters like sample dimensions (pellet diameter, thickness and bulk density), exposure time, integrated counts under CPs, multiple scattering contribution (between −10 to +10 a.u.) and free atom (FA) for profile normalization [2] (between 0 to 7 a.u.) for $Ni_{1-x}Cr_xFe_2O_4$ (x = 0.2 and 0.5) and $NiCr_xFe_{2-x}O_4$ (x = 0.2 and 0.5) have been incorporated in Table A.1. We have also checked the stability of the spectrometer from time-to-time by weak calibrators (^{57}Co and ^{133}Ba). The measured raw data for $Ni_{0.8}Cr_{0.2}Fe_2O_4$, $Ni_{0.5}Cr_{0.5}Fe_2O_4$, $NiCr_{0.2}Fe_{1.8}O_4$ and $NiCr_{0.5}Fe_{1.5}O_4$ are reported in Fig. A.2 (a-d), respectively. The true CP for each sample has been deduced by processing the raw data for systematic corrections as reported in chapter 2, using computer code of Warwick group [3,4]. Finally the CPs have been normalized to corresponding free atom (FA) [2] area as mentioned in Table A.1. Further, the numerical values of true CP for $Ni_{1-x}Cr_xFe_2O_4$ (x = 0.2 and 0.5) and $NiCr_xFe_{2-x}O_4$ (x = 0.2 and 0.5) have been listed in Table A.2 along with the statistical errors (±σ) at each point. Due to the limitation of the computational facilities, we could not perform LCAO based computations of CPs for $Ni_{1-x}Cr_xFe_2O_4$ (x = 0.2 and 0.5) and $NiCr_xFe_{2-x}O_4$ (x = 0.2 and 0.5). Hence in Fig. A.2 (a-d), we have plotted the difference between convoluted free atom [2] and experimental CP for $Ni_{0.8}Cr_{0.2}Fe_2O_4$, $Ni_{0.5}Cr_{0.5}Fe_2O_4$, $NiCr_{0.2}Fe_{1.8}O_4$ and $NiCr_{0.5}Fe_{1.5}O_4$, respectively. It is clear from the Fig. A.2 (a-d) that the differences in the momentum range $p_z \geq 3.0$ are almost zero for all the studied samples ($Ni_{0.8}Cr_{0.2}Fe_2O_4$, $Ni_{0.5}Cr_{0.5}Fe_2O_4$, $NiCr_{0.2}Fe_{1.8}O_4$ and $NiCr_{0.5}Fe_{1.5}O_4$) which shows the accuracy of the measurements and data correction. This is because the fact that this region is contributed by the identical core electrons. Rigorous DFT calculations for CPs will more helpful for the validation of the present experimental CPs.

Table A.1: Experimental parameters for the Compton profile (CP) measurements for $Ni_{1-x}Cr_xFe_2O_4$ (x = 0.2 and 0.5) and $NiCr_xFe_{2-x}O_4$ (x = 0.2 and 0.5).

Sample	**Sample diameter (thickness) in cm**	**Bulk density in g/cm^3**	**Exposure time in hours**	**Integrated counts under CP (x 10^7)**	**Multiple scattering (-10 to +10 a.u.) %**	**Normalization of profile (0 to 7 a.u.) (e^-)**
$Ni_{0.8}Cr_{0.2}Fe_2O_4$	1.85 (0.53)	1.63	154.38	3.26	10.69	50.54
$Ni_{0.5}Cr_{0.5}Fe_2O_4$	1.93 (0.55)	3.48	182.23	2.14	11.47	50.07
$NiCr_{0.2}Fe_{1.8}O_4$	1.90 (0.50)	1.31	161.96	1.72	10.54	50.69
$NiCr_{0.5}Fe_{1.5}O_4$	2.01 (0.65)	1.33	154.86	1.82	10.64	50.46

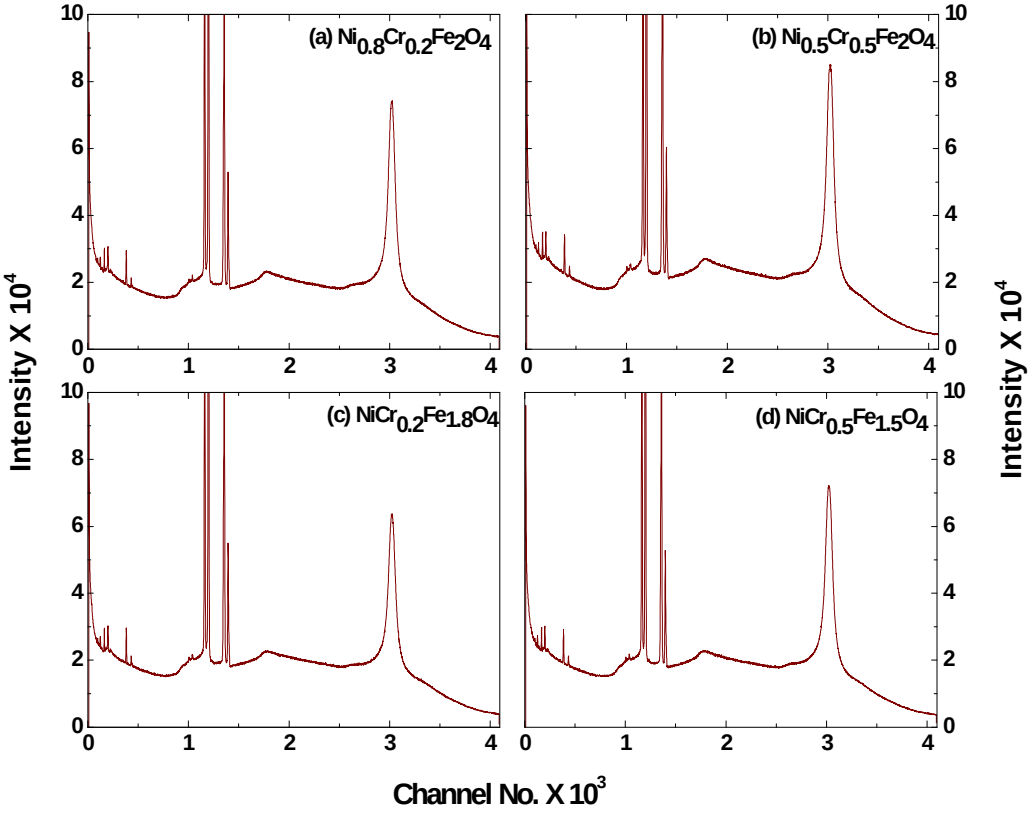

Fig. A.1: Raw data for (a) $Ni_{0.8}Cr_{0.2}Fe_2O_4$, (b) $Ni_{0.5}Cr_{0.5}Fe_2O_4$, (c) $NiCr_{0.2}Fe_{1.8}O_4$ and (d) $NiCr_{0.5}Fe_{1.5}O_4$ using 20 Ci ^{137}Cs Compton spectrometer. The peak on the right hand side of each panel corresponds to raw Compton profile.

Table A.2: Experimental Compton profiles along with statistical errors (±σ) for $Ni_{1-x}Cr_xFe_2O_4$ (x = 0.2 and 0.5) and $NiCr_xFe_{2-x}O_4$ (x = 0.2 and 0.5).

p_z	**J (p_z) (e/a.u.)**			
(a.u.)	**$Ni_{0.8}Cr_{0.2}Fe_2O_4$**	**$Ni_{0.5}Cr_{0.5}Fe_2O_4$**	**$NiCr_{0.2}Fe_{1.8}O_4$**	**$NiCr_{0.5}Fe_{1.5}O_4$**
0.0	24.402±0.052	24.547±0.049	24.299±0.056	24.522±0.053
0.1	24.319±0.052	24.429±0.048	24.208±0.056	24.418±0.053
0.2	24.104±0.051	24.183±0.048	23.991±0.055	24.177±0.053
0.3	23.726±0.051	23.799±0.048	23.630±0.055	23.789±0.052
0.4	23.191±0.050	23.270±0.047	23.127±0.054	23.256±0.052
0.5	22.525±0.049	22.606±0.047	22.489±0.053	22.595±0.051
0.6	21.742±0.048	21.821±0.046	21.734±0.052	21.813±0.050
0.7	20.854±0.047	20.927±0.044	20.857±0.050	20.915±0.049
0.8	19.874±0.046	19.941±0.043	19.863±0.049	19.919±0.048
1.0	17.704±0.042	17.750±0.040	17.709±0.046	17.735±0.044
1.2	15.448±0.039	15.445±0.037	15.535±0.042	15.478±0.041
1.4	13.334±0.036	13.274±0.034	13.489±0.038	13.388±0.037
1.6	11.512±0.032	11.390±0.030	11.659±0.034	11.544±0.034
1.8	9.980±0.029	9.840±0.028	10.080±0.031	9.940±0.031
2.0	8.656±0.027	8.534±0.025	8.753±0.028	8.626±0.028
3.0	4.779±0.017	4.608±0.016	4.799±0.018	4.756±0.018
4.0	2.988±0.012	2.871±0.011	3.007±0.012	2.996±0.012
5.0	2.107±0.009	2.038±0.008	2.110±0.009	2.094±0.009
6.0	1.582±0.007	1.506±0.006	1.556±0.007	1.502±0.007
7.0	1.109±0.005	1.094±0.005	1.113±0.005	1.106±0.005

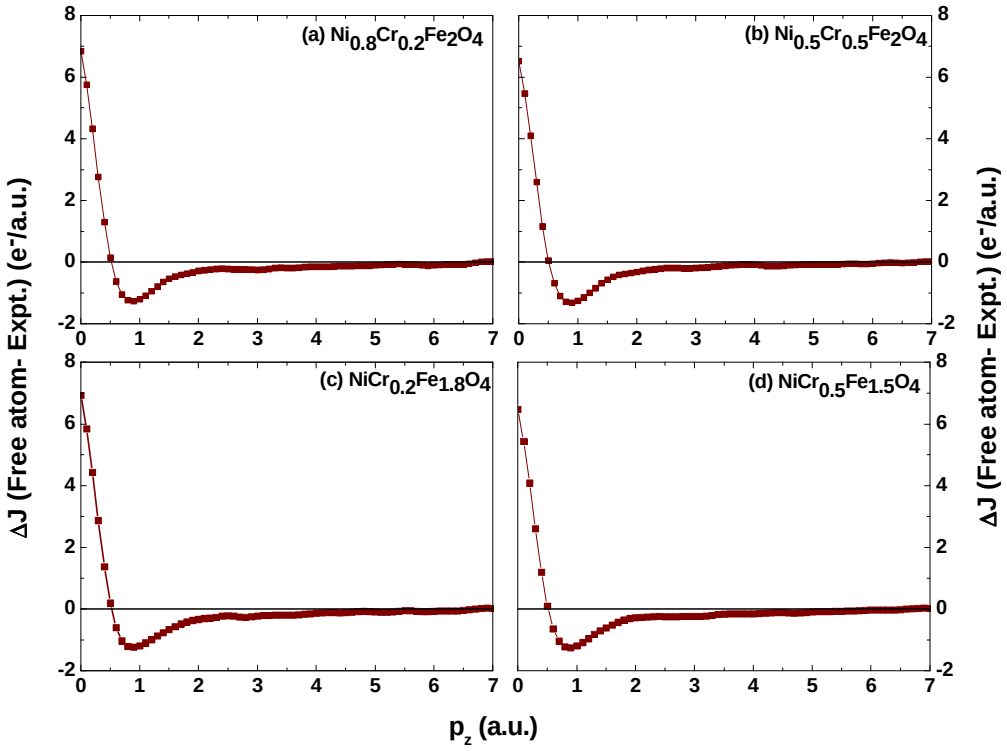

Fig. A.2: The difference profiles deduced from isotropic convoluted theoretical (free atom) and experimental (using 20 Ci ^{137}Cs Compton spectrometer) Compton profiles for (a) $Ni_{0.8}Cr_{0.2}Fe_2O_4$, (b) $Ni_{0.5}Cr_{0.5}Fe_2O_4$, (c) $NiCr_{0.2}Fe_{1.8}O_4$ and (d) $NiCr_{0.5}Fe_{1.5}O_4$. The solid lines are drawn for a quick view of trend.

References

1. B.L. Ahuja, M. Sharma, S. Mathur, Nucl Instrum. Methods Phys. Rev. B 244 (2006) 419–426.

2. F. Biggs, L.B. Mendelsohn, J.B. Mann, At. Data Nucl. Data Tables 16 (1975) 201–308.

3. D.N. Timms, Compton Scattering Studies of Spin and Momentum Densities, Ph.D. thesis, University of Warwick, UK, 1989 (Unpublished).

4. J. Felsteiner, P. Pattison, M.J. Cooper, Philos. Mag. 30 (1974) 537–548.

Summary

This section contains the summary of the research work carried out for the present thesis along with the future scope. The present work reports the systematic study of experimental and theoretical Compton profiles (CPs) of some ferrites namely Fe_3O_4, $NiFe_2O_4$, $ZnFe_2O_4$ and $CdFe_2O_4$. For the CP measurements, we have employed 20 Ci ^{137}Cs Compton spectrometer while the theoretical directional and isotropic CPs have been computed using linear combination of atomic orbitals (LCAO) approximations. In addition, we have also measured the CP of Fe_3O_4 using 100 mCi ^{241}Am Compton spectrometer and compared the results with LCAO based CPs. Here, we have prepared bulk $Ni_{1-x}Cr_xFe_2O_4$ (x= 0.00, 0.02 and 0.05) using solid state reaction (SSR) method and the thin films of $Ni_{1-x}Cr_xFe_2O_4$ (x= 0.02 and 0.05) using pulsed laser deposition (PLD) technique. The prepared samples have been characterized using X-ray diffraction (XRD), X-ray photoemission spectroscopy (XPS), Raman spectroscopy (RS), superconducting quantum interface device-vibration sample magnetometer (SQUID-VSM) and Fourier transform infrared (FTIR) spectroscopy measurements. In theoretical side, we have attempted pure and hybrid density functional theory (DFT) within LCAO approximations to compute spin dependent energy bands and density of states (DOS), charge organization using Mulliken population (MP), band gap and magnetic moment along with the CP data for Fe_3O_4, $NiFe_2O_4$, $ZnFe_2O_4$ and $CdFe_2O_4$. Due to the limitation of computational parameters, we could not extend LCAO scheme for $Ni_{1-x}Cr_xFe_2O_4$ (x= 0.02 and 0.05) and also CP measurements were restricted due to non-availability of theoretical data for validation of measurements. The present thesis has been divided into seven chapters as:

Chapter 1

In the first chapter, we have presented the theoretical aspects of the experimental techniques used in the present thesis namely XRD, XPS, RS and Compton scattering (CS) along with the detailed review of the earlier work of relevant ferrites of last 20 years with a sufficient number of research references. It is

worth while mentioning that reported ferrites, (MFe_2O_4; M = Cr, Fe, Ni, Zn and Cd), belong to a special class of magnetic materials consisting of metal oxides and ferric oxides as their main compositions and identified as important engineered materials for advanced applications like microwave-integrated and magnetoelectric devices, etc. The main interest in doped ferrite materials is due to their role in spin barriers used in conjunction with spin filters.

Chapter 2

The second chapter is divided into two parts. The first part contains the details of bulk sample preparation using SSR method and thin film growth using PLD technique along with the experimental details of characterized techniques like XRD, XPS, RS, SQUID-VSM and FTIR spectroscopy. We have also presented the details of two experimental set-ups for CS measurements namely 20 Ci ^{137}Cs and 100 mCi ^{241}Am Compton spectrometer along with the data correction process to deduce the true CP. In the second part, we have reported the details of ab-initio approximation namely LCAO to compute the CP, energy bands, DOS, MP, magnetic moment and band gap. The details of the local density approximation (LDA), generalized gradient approximation (GGA), second order GGA (SOGGA) and the hybrid schemes (B3LYP, B3PW, PBE0, PBESOL0, WC1LYP and B1WC) have also been reported.

Chapter 3

The third chapter describes the study of structural, electronic and magnetic properties of pulsed laser deposited thin films of $Ni_{1-x}Cr_xFe_2O_4$ (x = 0.02 and 0.05) on Si (111) and Si (100) substrates. The films reveal single phase, polycrystalline structure with a better crystalline quality on Si (111) substrate than that on Si (100) substrate. Contrary to the expected inverse spinel structure, XPS studies reveal the mixed spinel structure. XPS results suggest that Ni and Fe ions exist in 2+ and 3+ states, respectively, and they exist in tetrahedral as well as octahedral sites. The deviation from the inverse spinel leads to modified magnetic

properties. It is observed that saturation magnetization drastically drops compared to the expected saturation value for inverse spinel structure. Strain in the films and lattice distortion produced by the Cr doping also appear to influence the magnetic properties.

Chapter 4

In this chapter, pure and hybrid DFT schemes within LCAO have been employed to compute MP, energy bands, partial and total DOS and electron momentum densities (EMDs) of $TMFe_2O4$ (TM = Zn and Cd). Pure DFT calculations have been performed within LDA and GGA, while Hartree-Fock exchange contribution is added to DFT for hybrid calculations (B3LYP and PBE0). To validate the performance of hybrid functionals, we have also performed EMD measurements using 661.65 keV γ-rays from ^{137}Cs source for both the ferrites. Chi-square test predicts an overall better agreement of experimental CP data with LCAO-B3LYP scheme based momentum densities leading to usefulness of hybrid functionals in predicting electronic and magnetic response of such ferrites. Further, LCAO-B3LYP based majority- and minority-spin energy bands and DOS for $ZnFe_2O_4$ and $CdFe_2O_4$ predict semiconducting nature in both the compounds. In addition, MP data and equal-valence-electron-density scaled EMDs show more covalent character of $ZnFe_2O_4$ than that of $CdFe_2O_4$. A reasonable agreement of magnetic moments of both the ferrites with available data unambiguously promotes use of Gaussian-type orbitals in LCAO scheme in exploring magnetic properties of such ferrites.

Chapter 5

In this chapter, structural and magnetic response of $Ni_{1-x}Cr_xFe_2O_4$ (x = 0 and 0.05) have been presented using XRD, RS, FTIR spectroscopy and SQUID

magnetometer. The single phase of both the compositions is confirmed using Rietveld refinement method. The absence of any impurity is further cinched using structural sensitive techniques, namely FTIR and RS. Interestingly, a pinched shaped M-H behaviour is observed for the Cr doped ferrite. In addition, we have computed magnetic moment, MP, partial and total DOS and CPs for $NiFe_2O_4$ using LCAO scheme with and without hybrid functional for exchange and correlation potentials. Further, theoretical CPs have been validated using isotropic CP measurement with ^{137}Cs radio-isotope for $NiFe_2O_4$. Among the considered exchange-correlation potentials within LCAO, the hybrid B3LYP scheme based momentum densities give better agreement with the experimental CP. Majority- and minority-spin DOS have confirmed the insulating nature of $NiFe_2O_4$. Peculiarities of presently deduced MP data and magnetic moments are also discussed.

Chapter 6

The sixth chapter is also divided into two parts. The part-I is devoted to the CP measurements of Fe_3O_4 using 100 mCi ^{241}Am Compton spectrometer at momentum resolution of 0.55 a.u. The experimental CP has been compared with the LCAO data within DFT. The LDA and GGA schemes have been used within DFT scheme. It is found that the DFT-GGA scheme gives the better agreement than to DFT-LDA. In addition, we have also computed the MP and DOS using the DFT-GGA scheme. MP data predicts the charge transfer from Fe to O atoms whiles DOS have confirmed the half metallic character of the compounds. Whereas the part-II has been included with CP measurements of Fe_3O_4 using 661.65 keV γ-rays to validate the theoretical CPs derived using LCAO method. LCAO calculations have been attempted using DFT with GGA and the hybridization of Hartree-Fock and DFT scheme (so called B3LYP). It is found that B3LYP scheme gives a better agreement with experimental data than the DFT-GGA scheme. Further, spin dependent density of states using LCAO-B3LYP scheme have confirmed the half metallic character of

Fe_3O_4, while large value of Mulliken charge transfer (4.72 e^-) predicts the dominancy of ionic nature in the compound.

Chapter 7

The last chapter contains the chapter wise brief conclusions of present work and suggestions for future possibilities. Among the future possibilities, the high resolution directional CP measurements may be attempted to explore our reported theoretical anisotropies of the samples. Also, the high resolution magnetic Compton profile measurements of these ferrites using synchrotron radiations may be helpful to calculate site dependent magnetic moments to further validate our LCAO calculations. The energy bands, DOS, CPs and magnetic moment using full-potential linearized augmented plane wave (FP-LAPW) and spin-polarized-relativistic Korringa-Kohn-Rostoker (SPR-KKR) method may also be attempted.

In **Appendix**, we have reported the details of CP measurements for $Ni_{1-x}Cr_xFe_2O_4$ (x = 0.2 and 0.5) and $NiCr_xFe_{2-x}O_4$ (x = 0.2 and 0.5) using 20 Ci ^{137}Cs Compton spectrometer and compared the data with available free atom CP data. All most zero difference in CPs in the momentum range $p_z \geq 3.0$ a.u. show the accuracy of the measurement for all four samples. Here, we have also presented the relative nature of bonding in $ZnFe_2O_4$ and $CdFe_2O_4$ using hybrid approximations (B1WC and WC1LYP) within LCAO approximations. Both the observations predict $ZnFe_2O_4$ to be more covalent (or less ionic) than to $CdFe_2O_4$.

Bibliography

- A. Ahlawat, V.G. Sathe, J. Raman Spectrosc. 42 (2011) 1087–1094.
- A. Barone (Ed.), Principles and Applications of Superconducting Quantum Interference Devices, World Scientific Publishing 1992.
- A. Bengtson, D. Morgan, U. Becker, Phys. Rev. B 87 (2013) 155141-1–155141-13.
- A. Dashora, J. Sahariya, R.J. Choudhary, D.M. Phase, M. Itou, Y. Sakurai, B.L. Ahuja, Appl. Phys. Letts. 102 (2013) 142403-1–142403-4.
- A. Dashora, M. Suthar, K. Kumar, R.J. Choudhary, H. Sakurai, N. Tsuji, Y. Sakurai, B.L. Ahuja, J. Alloys Compounds 824 (2020) 153883.
- A. Kokaji, Comput. Mater. 28 (2003) 155–168.
- A. Raghunathan, D.C. Jiles, J.E. Synder, J. Appl. Phys. 109 (2011) 083922-1–083922-4.
- A. Rais, A.M. Gismelseed, I.A. Al-Omari, Phys. Stat. Sol. (b) 242 (2005) 1497–1503.
- A. Sharma, H.S. Mund, K. Bapna, S. Tiwari, M. Itou, Y. Sakurai, B.L. Ahuja, J. Mater. Sci. 52 (2017) 4568–4574.
- A. Ulpe, T. Bredow, Chem. Phys. Chem. 21 (2020) 1–7
- A. Yanase, K. Siratori, J. Phys. Soc. Japan 53 (1984) 312–317.
- A.D. Becke, Phys. Rev. A 38 (1988) 3098–3100.
- A.D. Rowan, C.H. Patterson, L.V. Gasparov, Phys. Rev. B 79 (2009) 205103-1–205103-18.
- A.F. Pasquevich, J. Shitu, Hyperfine Interactions 120/121 (1999) 463–468.
- A.H. Compton, Phys. Rev. 21 (1923) 409–413; ibid Phys. Rev. 21 (1923) 483–502.
- A.K. Nikumbh, A.V. Nagawade, G.S. Gugale, M.G. Chaskar, P.P. Bakare, J. Mater. Sci. 37 (2002) 637–647.
- A.M. El-Sayed, Ceram. Inter. 28 (2002) 651–655.

- A.M. El-Sayed, Mater. Chem. Phys. 82 (2003) 583–587.
- A.M. Gismelseed, A.A. Yousif, Physica B 370 (2005) 215–222.
- A.R. West, Solid State Chemistry and its Applications, John Wiley & Sons, Asia, 2003.
- A.V. Ramos, S. Matzen, J. Moussy, F. Ott, M. Viret, Phys. Rev. B 79 (2009) 014401-1–014401-8.
- B.D. Cullity (Ed.), Elements of X-ray Diffraction, Addison Wesley Publication Company, 1978.
- B.G. Williams, Compton Scattering, McGraw-Hill, London, 1977.
- B.J. Evans, S.S. Hafner, H.P. Weber, J. Chem. Phys. 55 (1971) 5282–5288.
- B.L. Ahuja, A. Dashora, Compton Scattering, Reference Module in Materials Science and Materials Engineering, Oxford: Elsevier; 2016, pp. 1–8.
- B.L. Ahuja, A. Dashora, N.L. Heda, S. Tiwari, N.E. Rajeevan, M. Itou, Y. Sakurai, R. Kumar, Appl. Phys. Lett. 97 (2010) 212502-1–212502-3.
- B.L. Ahuja, A. Dashora, N.L. Heda, S. Tiwari, R. Kumar, M. Itou, Y. Sakurai, AIP Conf. Proc. 1347 (2011) 202–205.
- B.L. Ahuja, H.S. Mund, S. Tiwari, J. Sahariya, A. Dashora, M. Itou, Y. Sakurai, Appl. Phys. Lett. 100 (2012) 132410-1–132410-4.
- B.L. Ahuja, M. Sharma, Pramana-J. Phys. 65 (2005) 137–145.
- B.L. Ahuja, M. Sharma, S. Mathur, Nucl. Instrum. Methods B 244 (2006) 419–426.
- B.L. Ahuja, N.L. Heda, Pramana J. Phys. 68 (2007) 843–850.
- B.L. Ahuja, P. Jain, J. Sahariya, N.L. Heda, P. Soni, J. Phys. Chem. A 117 (2013) 5685–5692.
- B.L. Ahuja, S. Sharma, N.L. Heda, S. Tiwari, K. Kumar, B.S. Meena, S. Bhatt, J. Phys. Chem. Solids 92 (2016) 53–63.

- B.L. Ahuja, S. Tiwari, A. Dashora, H.S. Mund, J. Sahariya, D.M. Phase, R.J. Choudhary, A. Banerjee, M. Itou, Y. Sakurai, Appl. Phys. Lett. 99 (2011) 062515-1–062515-3.
- B.L. Ahuja, V. Sharma, A. Rathor, A.R. Jani, B.K. Sharma, Nucl. Instrum. Methods B 262 (2007) 391–398.
- B.S. Holinsworth, D. Mazumdar, H. Sims, Q.–C. Sun, M.K. Yurtisigi, S.K. Sarker, A. Gupta, W.H. Butler, J.L. Musfeldt, Appl. Phys. Lett. 103 (2013) 082406-1–082406-4.
- B.S. Meena, N.L. Heda, B.L. Ahuja, AIP Conf. Proc. 1953 (2018) 140135-1–140135-4.
- B.S. Meena, N.L. Heda, H.S. Mund, B.L. Ahuja, AIP Conf. Proc. 1731 (2016) 090016-1–090016-3.
- B.S. Meena, N.L. Heda, H.S. Mund, B.L. Ahuja, Rad. Phys. Chem. 117 (2015) 93–101.
- B.S. Meena, N.L. Heda, K. Kumar, S. Bhatt, H.S. Mund, B.L. Ahuja, Physica B 484 (2016) 1–6.
- C. Adamo, V. Barone, J. Chem. Phys. 110 (1999) 6158–6170.
- C. Cheng, C.-S. Liu, J. Phys.: Conf. Ser. 145 (2009) 012028-1–012208-4.
- C. Cheng, J. Mag. Mag. Mat. 325 (2013) 144–146.
- C. Cheng, Phys. Rev. B 71 (2005) 052401-1–052401-4.
- C. Cheng, Phys. Rev. B 78 (2008) 132403-1–132403-4.
- C. Himcinschi, L. Vrejoiu, G. Salvan, M. Fronk, A. Talkenberger, D.R.T. Zahn, D. Rafaja, J. Kortus, J. Appl. Phys. 113 (2013) 084101-1–084101-8.
- C. Klewe, M. Meinert, A. Boehnke, K. Kuepper, E. Arenholz, A. Gupta, J.M. Schmalhorst, T. Kuschel, G. Reiss, J. Appl. Phys. 115 (2014) 123903-1–123903-7.
- C. Lee, W. Yang, R.G. Parr, Phys. Rev. B 37 (1988) 785–789.
- C.B.R. Jesus, E.C. Mendonça, L.S. Silva, W.S.D. Folly, C.T. Meneses, J.G.S.

Duque, J. Mag. Mag. Mat. 350 (2014) 47–49.

- C.D. Wagner, W.M. Riggs, L.E. Davis, J.F. Moulder, Handbook of X-ray Photoemission Spectroscopy, G.E. Muilenberg (Ed.), Perkin Elmer, Minnesota, USA, 1978.

- C.J. O'Brien, Z. Rák, D.W. Brenner, J. Phys.: Condens. Matter 25 (2013) 445008-1–445008-17.

- C.N. Benwell, E.M. McCash, Fundamental of Molecular Spectroscopy, Tata McGraw Hill, 4th addition, 1995.

- C.N. Chinnasamy, A. Narayanasamy, N. Ponpandian, K. Chattopadhyay, K. Shinoda, B. Jeyadevan, K. Tohji, K. Nakatsuka, T. Furubayashi, I. Nakatani, Phys. Rev. B 63 (2001) 184108-1–184108-8.

- C.N. Chinnasamy, A. Narayanasamy, N. Ponpandian, R.J. Joseyphus, B. Jeyadevan, K. Tohji, K. Chattopadhyay, J. Mag. Mag. Mat. 238 (2002) 281–287.

- C.N. Chinnasamy, S.D. Yoon, A. Yang, A. Baraskar, C. Vittoria, V.G. Harris, J. App. Phys. 101 (2007) 09M517-1–09M517-3.

- D. Fritsch, C. Ederer, Appl. Phys. Lett. 99 (2011) 081916-1–081916-3.

- D. Fritsch, C. Ederer, Phys. Rev. B 82 (2010) 104117-1–104117-11.

- D. Fritsch, C. Ederer, Phys. Rev. B 86 (2012) 014406-1–014406-10.

- D. Fritsch, J. Phys.: Condens. Matter 30 (2018) 095502-1-095502-5.

- D. Odkhuu, P. Taivansaikhan, W.S. Yun, S.C. Hong, J. Appl. Phys. 115 (2014) 17A916-1–17A916-3.

- D. Varshney, K. Verma, Mater. Chem. Phys. 140 (2013) 412–418.

- D.C. Kulkarni, S.P. Patil, V. Puri, Microelect. J. 39 (2008) 248–252.

- D.J. Huang, C.F. Chang, H.-T. Jeng, G.Y. Guo, H.-J. Lin, W.B. Wu, H.C. Ku, A. Fujimori, Y. Takahashi, C.T. Chen, Phys. Rev. Lett. 93 (2004) 077204-1–077204-4.

- D.J. Singh, M. Gupta, R. Gupta, J. Appl. Phys. 91 (2002) 7370–7372.

- D.J. Singh, M. Gupta, R. Gupta, Phys. Rev. B 63 (2001) 205102-1–205102-5.
- D.M. Phase, S. Tiwari, R. Prakash, A. Dubey, V.G. Sathe, R.J. Choudhary, J. Appl. Phys. 100 (2006) 123703-1–123703-5.
- D.N. Timms, Compton Scattering Studies of Spin and Momentum Densities (Ph.D. Thesis), University of Warwick, UK 1989 (unpublished).
- D.R. Patil, B.K. Chougule, Mater. Chem. Phys. 117 (2009) 35–40.
- E.N. Kaufmann, Characterization of Materials, John Wiley & Sons, 2003.
- F. Biggs, L.B. Mendelsohn, J.B. Mann, At. Data Nucl. Data Tables 16 (1975) 201–308.
- F. Zhang, Y. Kitamoto, M. Abe, M. Naoe, J. Appl. Phys. 87 (2000) 6881–6883.
- F. Zhou, G. Ceder, Phys. Rev. B 81 (2010) 205113-1–205113-6.
- F.L. Zabotto, A.J. Gualdi, J.A. Eiras, A.J.A. de Oliveira, D. Garcia, Mater. Res. 15 (2012) 428–433.
- F.M. Mohammed, A.M. Ghaleb, J. Sahariya, B.L. Ahuja, K.C. Bhamu, Nat. Sci. 4 (2012) 797–802.
- G. Choudhary, V. Raykar, S. Tiwari, A. Dashora, B.L. Ahuja, Phys. Stat. Sol. (b) 248 (2011) 212–219.
- G. Dixit, J.P. Singh, R.C. Srivastava, H.M. Agrawal, R.J. Choudhary, A. Gupta, Surf. Inter. Analysis 42 (2010) 151–156.
- G. Dixit, J.P. Singh, R.C. Srivastava, H.M. Agrawal, R.J. Choudhary, Adv. Mater. Lett. 3 (2012) 21–28.
- G.D. Tang, D.H. Ji, Y.X. Yao, S.P. Liu, Z.Z. Li, W.H. Qi, Q.J. Han, X. Hou, D.L. Hou, Appl. Phys. Lett. 98 (2011) 072511-1–072511-3.
- G.H. Jaffari, A.K. Rumaiz, J.C. Woicik, S.I. Shah, J. Appl. Phys. 111 (2012) 093906-1–093906-6.
- G.K.H. Madsen, P. Novak, Europhys. Lett. 69 (2005) 777–783.

- H. Akamatsu, Y. Zong, Y. Fujiki, K. Kamiya, K. Fujita, S. Murai, K. Tanaka, IEEE Trans. Mag. 44 (2008) 2796–2799.
- H. Perron, T. Mellier, C. Domain, J. Roques, E. Simoni, R. Drot, H. Catlette, J. Phys.: Condens. Matter 19 (2007) 346219-1–346219-10.
- H. Zaari, A.G. El hachimi, A. Benyoussef, A. El Kenz, J. Mag. Mag. Mat. 393 (2015) 183–187.
- H.S. Mund, B.L. Ahuja, Mater. Res. Bull. 85 (2017) 228–233.
- H.S. Mund, J. Sahariya, R.J. Choudhary, D.M. Phase, A. Dashora, M. Itou, Y. Sakurai, B.L. Ahuja, Appl. Phys. Letts. 102 (2013) 232403-1–232403-4.
- H.S. Mund, S. Tiwari, J. Sahariya, M. Itou, Y. Sakurai, B.L. Ahuja, J. Appl. Phys. 110 (2011) 073914-1–073914-4.
- H.-T. Jeng, G.Y. Guo, J. Mag. Mag. Mat. 240 (2002) 436–438.
- H.-T. Jeng, G.Y. Guo, Phys. Rev. B 65 (2002) 094429-1–094429-9.
- http://www.crystal.unito.it/basis-sets.php (2019).
- I. Leonov, A.N. Yaresko, V.N. Antonov, M.A. Korotin, V.I. Anisimov, Phys. Rev. Lett. 93 (2004) 146404-1–146404-4.
- İ. Sabikoğlu, L. Parali, O. Malina, P. Novak, J. Kaslik, J. Tucek, J. Pechousek, J. Navarik, O. Schneeweiss, Prog. Nat. Sci.: Mater. Inter. 25 (2015) 215–221.
- I.P. Yaremiy, V.S. Bushkova, N.I. Bushkov, S.I. Yaremiy, J. Nano Elect. Phys. 11 (2019) 04020-1–04020-8.
- J. Felsteiner, P. Pattison, M.J. Cooper, Philos. Mag. 30 (1974) 537–548.
- J. Jacob, M.A. Khadar, J. Appl. Phys. 107 (2010) 114310-1–114310-10.
- J. Kulawik, D. Szwagierczak, P. Guzdek, J. Mag. Mag. Mat. 324 (2012) 3052–3057.
- J. Li, Z. Yu, K. Sun, X. Jiang, Z. Xu, Z. Lan, J. Alloys Compounds 513 (2012) 606–609.

- J. Muscat, C. Klauber, Surf. Sci. 491 (2001) 226–238.
- J. Sahariya, H.S. Mund, A. Sharma, A. Dashora, M. Itou, Y. Sakurai, B.L. Ahuja, J. Mag. Mag. Mat. 360 (2014) 113–117.
- J. Shan, A.V. Singh, L. Liang, L.J. Cornelissen, Z. Galazka, A. Gupta, B.J. van Wees, T. Kuschel, Appl. Phys. Lett. 113 (2018) 162403-1–162403-5.
- J. Singh, S.K. Gupta, A.K. Singh, P. Kothari, R.K. Kotnala, J. Akhtar, J. Mag. Mag. Mat. 324 (2012) 999–1005.
- J. Yao, X. Li, Y. Li, S. Le, Integrated Ferroelectrics 145 (2013) 17–23.
- J.A. Duffy, J.W. Taylor, S.B. Dugdale, C. Shenton-Taylor, M.W. Butchers, S.R. Giblin, M.J. Cooper, Y. Sakurai, M. Itou, Phys. Rev. B 81 (2010) 134424-1–134424-5.
- J.A. Victoreen, J. Appl. Phys. 20 (1949) 1141–1147.
- J.J.M. Quintero, C.E.R. Torres, L.A. Errico, J. Alloys Compounds 741 (2018) 746–755.
- J.J.M. Quintero, K.L.S. Rodríguez, C.E.R. Torres, L.A. Errico, J. Alloys Compounds 775 (2019) 1117–1128.
- J.J.M. Quintero, K.L.S. Rodríguez, G.A. Pasquevich, P.M. Zélis, S.J. Stewart, C.E.R. Torres, L.A. Errico, Hyperfine Interact. 237 (2016) 63-1–63-7.
- J.J.M. Quintero, K.L.S. Rodríguez, G.A. Pasquevich, P.M. Zélis, S.J. Stewart, C.E.R. Torres, L.A. Errico, Hyperfine Interact. 63 (2016) 237-1–237-7.
- J.P. Perdew, A. Ruzsinszky, G.I. Csonka, O.A. Vydrov, G.E. Scuseria, L.A. Constantin, X. Zhou, K. Burke, Phys. Rev. Lett. 100 (2008) 136406-1–136406-4.
- J.P. Perdew, A. Zunger, Phys. Rev. B 23 (1981) 5048–5079.
- J.P. Perdew, J.A. Chevary, S.H. Vosko, K.A. Jackson, M.R. Pederson, D.J. Singh, C. Fiolhais, Phys. Rev. B 46 (1992) 6671–6686.
- J.P. Perdew, K. Burke, M. Ernzerhof, Phys. Rev. Lett. 77 (1996) 3865–3868.

- J.P. Perdew, Phys. Rev. B 33 (1986) 8822–8824.
- J.P. Perdew, Y. Wang, Phys. Rev. B 45 (1992) 13244–13249.
- J.P. Wright, J.P. Attfield, P.G. Radaelli, Phys. Rev. Lett. 87 (2001) 266401-1–266401-4.
- J.X. Ma, D. Mazumdar, G. Kim, H. Sato, N.Z. Bao, A. Gupta, J. Appl. Phys. 108 (2010) 063917-1–063917-5.
- K. Bapna, R.J. Choudhary, D.M. Phase, S. Shastri, R. Prasad, B.L. Ahuja, AIP Conf. Proc. 1728 (2016) 020462-1–020462-3.
- K. Bharathi, K. Balamurugan, P.N. Santhosh, M. Pattabiraman, G. Markandeyulu, Phys. Rev. B 77 (2008) 172401-1–172401-4.
- K. Kamazawa, S. Park, S.-H. Lee, T.J. Sato, Y. Tsunoda, Phys. Rev. B 70 (2004) 024418-1–024418-5.
- K. Kamazawa, Y. Tsunoda, H. Kadowaki, K. Kohn, Phys. Rev. B 68 (2003) 024412-1–024412-9.
- K. Panwar, S, Tiwari, K. Bapna, N.L. Heda, R.J. Choudhary, D.M. Phase, B.L. Ahuja, J. Mag. Mag. Mat. 421 (2017) 25–30
- K. Pubby, S.S. Meena, S.M. Yusuf, S.B. Narang, J. Mag. Mag. Mat. 466 (2018) 430–445.
- K. Rama Krishna, D. Ravinder, K. Vijaya Kumar, C.A. Lincon, World J. Condens. Matter Phys. 2 (2012) 153–159.
- K. Sharma, H.S. Mund, K. Kumar, S. Talreja, B.L. Ahuja, Phys. Stat. Sol. (b) 253 (2016) 1743–1753.
- K. Sharma, J. Sahariya, B.L. Ahuja, J. Alloys Compounds 645 (2015) 414–420.
- K. Sharma, V.R. Reddy, A. Gupta, A. Banerjee, A.M. Awasthi, J. Phys: Condens. Matter 25 (2013) 076002-1–076002-9.
- K.C. Bhamu, A. Dashora, G. Arora, B.L. Ahuja, Rad. Phys. Chem. 81 (2012) 728–734.

- K.K. Bharathi, J.A. Chelvane, G. Markandeyulu, J. Mag. Mag. Mat. 321 (2009) 3677–3680.
- K.K. Bharathi, R.S. Vemuri, C.V. Ramana, Chem. Phys. Lett. 504 (2011) 202–205.
- L. Horng, G. Chern, M.C. Chen, P.C. Kang, D.S. Lee, J. Mag. Mag. Mat. 270 (2004) 389–396.
- L. Li, X. Tu, L. Peng, X. Zhu, J. Alloy Compounds 545 (2012) 67–69.
- L. Zhu, K.L. Yao, Z.L. Liu, Phys. Rev. B 74 (2006) 035409-1–035409-10.
- L.C. Wilson, M. Levy, Phys. Rev. B 41 (1990) 12930–12932.
- L.L. Lang, J. Xu, W.H. Qi, Z.Z. Li, G.D. Tang, Z.F. Shang, X.Y. Zhang, L.Q. Wu, L.C. Xue, J. Appl. Phys. 116 (2014) 123901-1–123901-10.
- M. Atif, M. Nadeem, R. Grössinger, R.S. Turtelli, J. Alloys Compounds 509 (2011) 5720–5724.
- M. Birkholz, Thin Film Analysis by X-Ray Scattering, Wiley-VCH Weinheim, 2006.
- M. Hoppe, S. Döring, M. Gorgoi, S. Cramm, M. Muller, Phys. Rev. B 91 (2015) 054418-1–054418-7.
- M. Meinert, G. Reiss, J. Phys.: Condens. Matter 26 (2014) 115503-1–115503-4.
- M. Pénicaud, B. Siberchicot, C.B. Sommers, J. Kübler, J. Mag. Mag. Mat. 103 (1992) 212–220.
- M. Pardavi-Horvath, J. Mag. Mag. Mat. 215–216 (2000) 171–183.
- M. Raghasudha, D. Ravinder, P. Veerasomaiah, J. Nano Struct. Chem. 3:63 (2013) 1–6.
- M. Sorescua, L. Diamandescu, R. Swaminathan, M.E. McHenry, M. Feder, J. Appl. Phys. 97 (2005) 10G105-1–10G105-3.
- M.A. Gabal, Y.M. Al Angari, Mater. Chem. Phys. 115 (2009) 578–584.
- M.A. Valenzuela, P. Bosch, J. Jiménez – Becerrill, O. Quiroz, A.I. Páez, J.

Photochem. Photobiol. A Chem. 148 (2002) 177–182.

- M.A.F. Ramalho, L. Gama, S.G. Antonio, C.O. Paiva-Santos, E.J. Miola, R.H.G.A. Kiminami, A.C.F.M. Costa, J. Mater. Sci. 42 (2007) 3603–3606.
- M.J. Cooper, P.E. Mijnarends, N. Shiotani, N. Sakai, A. Bansil, X-ray Compton Scattering, Oxford Science Publications, Oxford University Press, New York, 2004 and references therein.
- M.J. Cooper, Rep. Prog. Phys. 48 (1985) 415–481 and references therein.
- M.N. Iliev, D. Mazumdar, J.X. Ma, A. Gupta, F. Rigato, J. Fontcuberta, Phys. Rev. B 83 (2011) 014108-1–014108-6.
- M.S.R. Prasad, B.B.V.S.V. Prasad, B. Rajesh, K.H. Rao, K.V. Ramesh, J. Mag. Mag. Mat. 323 (2011) 2115–2121.
- Magnetic Property Measurement System SQUID-VSM, User's Manual, Quantum Design, USA, 2010.
- N. Jahan, F. Chowdhury, A.K.M. Zakaria, Mater. Sci. Poland 34 (2016) 185–191.
- N.L. Heda, A. Dashora, J. Sahariya, B.L. Ahuja, Solid State Phenomena 209 (2014) 156–159.
- N.L. Heda, B.L. Ahuja, Comp. Mater. Sci. 72 (2013) 49–53.
- N.L. Heda, B.L. Ahuja, Role of in-house Compton spectrometer in probing the electronic properties, Recent Trends in Radiation Physics Research, in: B.L. Ahuja (Ed.), Himanshu Publications, New Delhi, India, 2010, 25–30.
- N.L. Heda, U. Ahuja, Rad. Phys. Chem. 106 (2015) 33–39.
- N.M. Caffrey, D. Fritsch, T. Archer, S. Sanvito, C. Ederer, Phys. Rev. B 87 (2013) 024419-1–024419-7.
- O.F. Caltun, J. Optoelectro. Adv. Mater. 6 (2004) 935–938.
- O.F. Caltun, J. Optoelectro. Adv. Mater. 7 (2005) 739–744.
- P. Eisenberger, W.A. Reed, Phys. Rev. B 9 (1974) 3237–3241.

- P. Guzdek, J. Kulawik, K. Zaraska, A. Bienkowski, J. Mag. Mag. Mat. 322 (2010) 2897–2901.
- P. Guzdek, J. Mag. Mag. Mat. 349 (2014) 219–223.
- P. Piekarz, K. Parlinski, A.M. Oles, Phys. Rev. B 76 (2007) 165124-1–165124-16.
- P. Piekarz, K. Parlinski, A.M. Oles, Phys. Rev. Lett. 97 (2006) 156402-1–156402-4.
- Q. Mahmood, M. Yaseen, K.C. Bhamu, A. Mahmood, Y. Javed, S.M. Ramay, Chin. Phys. B 27 (2018) 037103-1-037103-8.
- Q.-C. Sun, H. Sims, D. Mazumdar, J.X. Ma, B.S. Holinsworth, K.R. O'Neal, G. Kim, W.H. Butler, A. Gupta, J.L. Musfeldt, Phys. Rev. B 86 (2012) 205106-1–205106-5.
- R. Datta, S. Kanuri, S.V. Karthik, D. Mazumdar, J.X. Ma, A. Gupta, Appl. Phys. Lett. 97 (2010) 071907-1–071907-3.
- R. Dovesi, V.R Saunders, C. Roetti, R. Orlando, C.M. Zicovich-Wilson, F. Pascale, B. Civalleri, K. Doll, N.M. Harrison, I.J. Bush, Ph. D'Arco, M. Llunell, M. Causa, Y. Neol, CRYSTAL14 User's Manual, University of Torino, Torino, Italy (2014), and references therein.
- R. Eason (Ed.), Pulsed Laser Deposition of Thin Films, Wiley Inter Science, New Jersey, 2007.
- R. Ghasemi, J. Echeverría, J.I. Pérez-Landazábal, J.J. Beato-Lopez, M. Naseri, C. Gómez-Polo, J. Mag. Mag. Mat. 499 (2020) 166201.
- R. Lässer, R.M. Singru, B. Lengeler, Solid State Commun. 25 (1978) 345–347.
- R. Masrour, E.K. Hlil, M. Hamedoun, A. Benyoussef, O. Mounkachi, H. El Moussaoui, J. Mag. Mag. Mat. 378 (2015) 37–40.
- R. Sharma, S. Singhal, Physica B 414 (2013) 83–90.
- R.C. Kambale, P.A. Shaikh, S.S. Kamble, Y.D. Kolekar, J. Alloys Compounds 478 (2009) 599–603.

- R.C. Rai, S. Wilser, M. Guminiak, B. Cai, M.L. Nakarmi, Appl. Phys. A 106 (2012) 207–211.
- R.C.H. Cheng, B.G. Williams, M.J. Cooper, Phil. Mag. 23 (1971) 115–133.
- R.N. Singh, J.P. Singh, B. Lal, M.J.K. Thomas, S. Bera, Electrochim. Acta 51 (2006) 5515–5523.
- R.S. Devan, Y.D. Kolekar, B.K. Chougule, J. Phys.: Condens. Matter 18 (2006) 9809–9821.
- S. Abdul Khader, S. Mohamed Shariff, N. Firdous, J. Basawaraja, H. Madanakumara, M.S. Thyagaraj, J. Chem. Pharm. Sci. 9 (2016) 993–997.
- S. Anjum, G.H. Jaffari, A.K. Rumaiz, M.S. Rafique, S.I. Shah, J. Phys. D: Appl. Phys. 43 (2010) 265001-1–265001-7.
- S. Ikram, J. Jacob, M.I. Arshad, K. Mahmood, A. Ali, N. Sabir, N. Amin , S. Hussain, Ceram. Inter. 45 (2020) 3563–3569.
- S. Matzen, J.-B. Moussy, P. Wei, C. Gatel, J.C. Cezar, M.A. Arrio, P. Sainctavit, J.S. Moodera, Appl. Phys. Lett. 104 (2014) 182404-1–182404-5.
- S. Nakashima, K. Fujita, K. Tanaka, K. Hirao, T. Yamamoto, I. Tanaka, Phys. Rev. B 75 (2007) 174443-1–174443-8.
- S. Noor, M.M. Rahman, S.S. Sikder, M.A. Hakim, Jahangirnagar Univ. J. Sci. 34 (2011) 1–11.
- S. Phumying, S. Labuayai, E. Swatsitang, V. Amornkitbamrung, S. Maensiri, Mater. Res. Bull. 48 (2013) 2060–2065.
- S. Seifikar, A. Tabei, E. Sachet, T. Rawdanowicz, N. Bassiri-Gharb, J. Schwartz, J. Appl. Phys. 112 (2012) 063908-1–063908-6.
- S. Sharma, J. Sahariya, G. Arora, B.L. Ahuja, Physica B 450 (2014) 25–29.
- S. Sharma, N.L. Heda, K.K. Suthar, S. Bhatt, K. Sharma, B.L. Ahuja, Comp. Mater. Sci. 104 (2015) 205–211.
- S. Singhal, K. Chandra, J. Solid State Chem. 180 (2007) 296–300.
- S. Soliman, A. Elfalaky, G.H. Fecher, C. Felser, Phys. Rev. B 83 (2011)

085205-1–085205-6.

- S. Tiwari, D.M. Phase, R.J. Choudhary, Appl. Phys. Lett. 93 (2008) 234108-1–234108-3.
- S. Tiwari, D.M. Phase, R.J. Choudhary, H.S. Mund, B.L. Ahuja, J. Appl. Phys. 109 (2011) 033911-1–033911-5.
- S. Tiwari, R. Master, R.J. Choudhary, D.M. Phase, B.L. Ahuja, J. Appl. Phys. 111 (2012) 083905-1–083905-6.
- S. Tiwari, R. Prakash, R.J. Choudhary, D.M. Phase, J. Phys. D: Appl. Phys. 40 (2007) 4943–4947.
- S. Tiwari, R.J. Choudhary, D.M. Phase, Thin Solid Films 517 (2009) 3253–3256.
- S. Tiwari, R.J. Choudhary, R. Prakash, D.M. Phase, J. Phys.: Condens. Matter 19 (2007) 176002-1–176002-7.
- S. Winell, Ö. Amcoff, T. Ericsson, Phys. Stat. Sol. (b) 245 (2008) 1635–1640.
- S. Zhi-Feng, Q. Wei-Hua, J. Deng-Hui, X. Jing, T. Gui-De, Z. Xaio-Yun, L. Zhuang-Zhi, L. Li-Li, Chin. Phys. B 10 (2014) 107503-1–107503-10.
- S.D. Bhame, P.A. Joy, J. Phys. D: Appl. Phys. 40 (2007) 3263–3267.
- S.E. Shirsath, B.G. Toksha, K.M. Jadhav, Mater. Chem. Phys. 117 (2009) 163–168.
- S.E. Shirsath, S.S. Jadhav, B.G. Toksha, S.M. Patange, K.M. Jadhav, J. Appl. Phys. 110 (2011) 013914-1–013914-8.
- S.F. Mohammed, F.M. Mohammed, J. Sahariya, H.S. Mund, K.C. Bhamu, B.L. Ahuja, App. Rad. Isotopes. 72 (2013) 64–67.
- S.H. Vosko, L. Wilk, M. Nusair, Can. J. Phys. 58 (1980) 1200–1211.
- S.K. Meena, A. Dashora, N.L. Heda, B.L. Ahuja, Rad. Phys. Chem. 158 (2019) 46–52.
- S.K. Meena, K. Bapna, N.L. Heda, B.L. Ahuja, AIP Conf. Proc. 1942 (2018)

090033-1–090033-4.

- S.K. Meena, N.L. Heda, G. Arora, L. Meena, B.L. Ahuja, Physica B 560 (2019) 236–243.
- S.M. Patange, S.E. Shirsath, K.S. Lohar, S.S. Jadhav, N. Kulkarni, K.M. Jadhav, Physica B 406 (2011) 663–668.
- S.M. Patange, S.E. Shirsath, S.S. Jadhav, K.M. Jadhav, Phys. Stat. Sol. A 209 (2012) 347–352.
- S.M. Patange, S.E. Shirsath, S.S. Jadhav, K.S. Lohar, D.R Mane, K.M. Jadhav, Mater. Lett. 64 (2010) 722–724.
- T. Chiba, J. Chem. Phys. 64 (1976) 1182–1188.
- U. Lüders, M. Bibes, J.-F. Bobo, M. Cantoni, R. Bertacco, J. Fontcuberta, Phys. Rev. B 71 (2005) 134419-1–134419-7.
- U. von Barth, L. Hedin, J. Phys. C: Solid State Phys. 5 (1972) 1629–1642.
- U.-G. Jong, C.-J. Yu, Y.-S. Park, C.-S. Ri, Phys. Lett. A 380 (2016) 3302–3306.
- V. Sepelak, I. Bergmann, A. Feldhoff, P. Heitjans, F. Krumeich, D. Menzel, F.J. Letterst, S.J. Campobell, K.D. Becker, J. Phys. Chem. C 111 (2007) 5025 –5033.
- V.G. Ivanov, M.V. Abrashev, M.N. Iliev, M.M. Gospodinov, J. Meen, M.I. Aroyo, Phys. Rev. B 82 (2010) 024104-1–024104-8.
- V.I. Anisimov, I.S. Elfimov, N. Hamada, K. Terakura, Phys. Rev. B 54 (1996) 4387–4390.
- V.N. Antonov, B.N. Harmon, A.N. Yaresko, Phys. Rev. B 67 (2003) 024417-1–024417-14.
- V.N. Antonov, B.N. Harmon, V.P. Antropov, A.Ya. Perlov, A.N. Yaresko, Phys. Rev. B 64 (2001) 134410-1–134410-12.
- W. Schiessl, W. Potzel, H. Karzel, M. Steiner, G.M. Kalvius, A. Martin, M.K. Krause, I. Halevy, J. Gal, W. Schäfer, G. Will, M. Hillberg, R. Wäppling, Phys. Rev. B 53 (1996) 9143–9152.

- W. Schülke, Electron Dynamics by Inelastic X-ray Scattering, Oxford Science Publications, Oxford University Press, New York, 2007.
- W.B. Cross, L. Affleck, M.V. Kuznetsov, I.P. Parkin, Q.A. Pankhurst, J. Mater. Chem. 9 (1999) 2545–2552.
- W.H. McMaster, G.N. KerrDel, J.H. Mallett, J.H. Hubble, Compilation of X-ray Cross Sections, Section I, Lawrence Radiation Laboratory, University of California, Livermore, USA, UCRL-50174, Sec. I, 1979.
- X. Yu, C.-F. Huo, Y.-W. Li, J. Wang, H. Jiao, Surf. Sci. 606 (2012) 872–879.
- X. Zuo, S. Yan, B. Barbiellini, V.G. Harris, C. Vittoria, J. Mag. Mag. Mat. 303 (2006) e432–e435.
- Y. Yamada, K. Kamazawa, Y. Tsunoda, Phys. Rev. B 66 (2002) 064401-1–064401-7.
- Y. Zhao, D.G. Truhlar, J. Chem. Phys. 128 (2008) 184109-1–184109-8.
- Y.C. Wang, J. Ding, J.B. Yi, B.H. Liu, T. Yu, Z.X. Shen, Appl. Phys. Lett. 84 (2004) 2596–2598.
- Z. Szotek, W.M. Temmerman, A. Svane, L. Petit, G.M. Stocks, H. Winter, Phys. Rev. B 68 (2003) 054415-1–054415-9.
- Z. Szotek, W.M. Temmerman, D. Ködderitzsch, A. Svane, L. Petit, H. Winter, Phys. Rev. B 74 (2006) 174431-1–174431-12.
- Z. Wu, R.E. Cohen, Phys. Rev. B 73 (2006) 235116-1–235116-6.
- Z. Zhang, S. Satpathy, Phys. Rev. B 44 (1991) 13319–13331.

List of Publications

Publication list of Kalpana Panwar

1. The effect of Cr substitution on the structural, electronic and magnetic properties of pulsed laser deposited $NiFe_2O_4$ thin films, **Kalpana Panwar**, Shailja Tiwari, Komal Bapna, N.L. Heda, R.J. Choudhary, D.M. Phase, B.L. Ahuja, J. Mag. Mag. Mat. 421 (2017) 25–30 **[Impact Factor: 2.683] (It forms chapter 3).**

2. Performance of hybrid functional in linear combination of atomic orbitals scheme in predicting electronic response in spinel ferrites $ZnFe_2O_4$ and $CdFe_2O_4$, N.L. Heda, **Kalpana Panwar,** Kishor Kumar, B.L. Ahuja, J. Mater. Sci. 55 (2020) 3912–3925 **[Impact Factor: 3.442] (It forms chapter 4).**

3. Structural, magnetic and electronic properties of nickel ferrites: Experiment and LCAO calculations, **Kalpana Panwar**, Shailja Tiwari, Komal Bapna, Kishor Kumar, N.L. Heda, D.M. Phase, B.L. Ahuja, J. Alloys Compounds (2020) Revised **[Impact Factor: 4.175] (It forms chapter 5).**

4. Electronic properties of Fe_3O_4: LCAO calculations and Compton spectroscopy, **Kalpana Panwar,** Shailja Tiwari, N.L. Heda, AIP Conf. Proc. 1942 (2018) 090032-1–090032-4 **[SJR: 0.182] (It forms part-I of chapter 6).**

5. Structural and magnetic studies of Cr doped nickel ferrite thin films, **Kalpana Panwar**, N.L. Heda, Shailja Tiwari, Komal Bapna, R.J. Choudhary, D.M. Phase, B.L. Ahuja, AIP Conf. Proc. 1731 (2016) 080025-1–080025- **[SJR: 0.182].**

6. Energy Bands and density of states of $B_{1-X}TM_XP$ (TM= Cr, Fe and Co; X = 0 and 0.25) using FP-LAPW scheme, **Kalpana Panwar**, N.L. Heda, AIP Conf. Proc. 1953 (2018) 110034-1–110034-4 **[SJR: 0.182].**

7. Stable growth of Cr doped nickel ferrite thin films on Si (100) and (111) substrates, **Kalpana Panwar**, Shailja Tiwari, Komal Bapna, N.L. Heda, R.J. Choudhary, D.M. Phase, B.L. Ahuja, Proceedings of National Conference on "Advanced Functional Materials and Their Applications (AFMA-2015), 55–57 (2015) **[ISBN: 978-81-7233-976-0].**

8. Relative nature bonding in $ZnFe_2O_4$ and $CdFe_2O_4$ using hybrid B1WC and WC1LYP within LCAO approximations, **Kalpana Panwar**, Shailja Tiwari, N.L. Heda, Presented in National Conference on Advances in Materials Science and Technology (NCMAST-2020) during February 2020 at University of Rajasthan, Jaipur, Book of Abstracts, Page No. 60 (2020).

9. Electronic structure of magnetite: Ab-initio computations and electron momentum density measurements, N.L. Heda, **Kalpana Panwar,** B.L. Ahuja, Presented in 22nd National Symposium on Radiation Physics (NSRP-22) during November 2019 at Jawaharlal Nehru University (JNU), New Delhi, Abstracts Book, Page No. 114 (2019).

10. Electron momentum density and Mulliken population of $NiFe_2O_4$, N.L. Heda, **Kalpana Panwar**, Shailja Tiwari, B.L. Ahuja, Presented in 21st National Symposium on Radiation Physics (NSRP-21) during March 2018 at Raja Ramanna Centre for Advanced Technology (RRCAT), Indore, Book of Abstracts, Page No. 168 (2018).

11. Compton profile and Mulliken population of $ZnFe_2O_4$, B.S. Meena, **Kalpana Panwar,** N.L. Heda, B.L. Ahuja, Presented in NSRP-21 during March 2018 at RRCAT, Indore, Book of Abstracts, Page No. 173 (2018).

Copy of Published Papers in Journal